

**NRC HIGH-LEVEL RADIOACTIVE
WASTE RESEARCH AT CNWRA
JANUARY — JUNE 1994**

Prepared for

**Nuclear Regulatory Commission
Contract NRC-02-93-005**

Contributors

**M.P. Ahola, R.G. Baca, F.P. Bertetti, A.H. Chowdhury, C.B. Connor, G.A. Cragolino,
D.S. Dunn, R.T. Green, D.A. Ferrill, D.B. Henderson, B.E. Hill, S.M. Hsiung,
P.C. Lichtner, S. Mohanty, A.P. Morris, W.M. Murphy, G.I. Ofoegbu, R.T. Pabalan,
E.C. Percy, N. Sridhar, G.L. Stirewalt, S.A. Stothoff, D.R. Turner,
G.W. Wittmeyer, S.R. Young**

Edited by

Budhi Sagar

**Center for Nuclear Waste Regulatory Analyses
San Antonio, Texas**

September 1994

(THIS PAGE INTENTIONALLY LEFT BLANK)

PREVIOUS REPORTS IN SERIES

Number	Name	Date Issued
CNWRA 90-01Q	First Quarterly Research Report for 1990 January 1–March 30	May 1990
CNWRA 90-02Q	Second Quarterly Research Report for 1990 April 1–June 30	August 1990
CNWRA 90-03Q	Third Quarterly Research Report for 1990 July 1–September 30	November 1990
NUREG/CR-5817 Volume 1 CNWRA 90-01A	Report on Research Activities for Calendar Year 1990	December 1991
CNWRA 91-01Q	First Quarterly Research Report for 1991 January 1–March 30	May 1991
CNWRA 91-02Q	Second Quarterly Research Report for 1991 April 1–June 30	August 1991
CNWRA 91-03Q	Third Quarterly Research Report for 1991 July 1–September 30	November 1991
NUREG/CR-5817 Volume 2 CNWRA 91-01A	NRC High-Level Radioactive Waste Research at CNWRA Calendar Year 1991	May 1993
NUREG/CR-5817 Volume 3, No. 1 CNWRA 92-01S	NRC High-Level Radioactive Waste Research at CNWRA January–June 1992	May 1993
NUREG/CR-5817 Volume 3, No. 2 CNWRA 92-02S	NRC High-Level Radioactive Waste Research at CNWRA July–December 1992	July 1993
CNWRA 93-001S	NRC High-Level Radioactive Waste Research at CNWRA January–June 1993	August 1993
CNWRA 93-02S	NRC High-Level Radioactive Waste Research at CNWRA July–December 1993	February 1994

(THIS PAGE INTENTIONALLY LEFT BLANK)

PREFACE

The Center for Nuclear Waste Regulatory Analyses (CNWRA), a Federally Funded Research and Development Center (FFRDC), conducts research on behalf of the Nuclear Regulatory Commission (NRC). The NRC-funded research at the CNWRA is focused on activities related to the NRC responsibilities defined under the Nuclear Waste Policy Act (NWPA), as amended. Progress for the period of January 1, 1994 to June 30, 1994 on nine (see page 1) of 12 research projects that are currently active is described in this report. Three research projects not reported here are the Stochastic Analysis of Flow and Transport, Unsaturated Mass Transport (Geochemistry), and Thermohydrology. Final reports for the Stochastic Analysis of Flow and Transport and Unsaturated Mass Transport (Geochemistry) have been prepared, subjected to peer review, and submitted to the NRC. The Thermohydrology research project is scheduled for completion in December, 1994 when a final report on this project will be prepared. For a brief summary of the work in the reporting period, the reader is referred to the Executive Summary beginning on page 1.

In addition to disseminating research results through publications in appropriate open literature (e.g., CNWRA topical reports, NRC documents, and journals) and at technical meetings, workshops, and symposia; the CNWRA produces these research reports twice yearly. See page iii for a list of previous reports in this series.

Each chapter in this semi-annual report summarizes the progress made in a particular research project and is authored by the researchers in that project. Since readers of this report may be interested only in a particular topic, each chapter is self-contained and can be read without reference to other chapters. Coverage in the semi-annual reports is limited to only the key aspects of progress made; greater detail is provided in topical reports that are produced during the course of the research or at its conclusion, as appropriate. The editor of this report ensures that each chapter is reviewed for its technical and programmatic content and that some uniformity as to the depth of descriptions is maintained across the various chapters.

The NRC evaluates its research needs continually as the research progresses. The research needs are based on user needs identified jointly by the NRC Offices of Nuclear Material Safety and Safeguards (NMSS) and Nuclear Regulatory Research (RES). Generally, the NMSS is the user in the sense that its staff applies the research results to strengthen its reviews of the submittals by the U.S. Department of Energy (DOE), including the License Application for the first High-Level Nuclear Waste (HLW) Repository. In their turn, the user needs are based on Key Technical Uncertainties (KTUs) that are identified during the process of developing strategies and methods for determining compliance with the applicable regulations—in this case, 10 CFR Part 60. Thus, the research is directed toward evaluation of the KTUs.

(THIS PAGE INTENTIONALLY LEFT BLANK)

CONTENTS

Section	Page
FIGURES	xiii
TABLES	xxiii
ACKNOWLEDGMENTS	xxv
QUALITY OF DATA	xxv
1 EXECUTIVE SUMMARY	1
1.1 INTRODUCTION	1
1.2 SEISMIC ROCK MECHANICS	1
1.3 INTEGRATED WASTE PACKAGE EXPERIMENTS	4
1.4 GEOCHEMICAL NATURAL ANALOG RESEARCH	5
1.5 SORPTION MODELING FOR HLW PERFORMANCE ASSESSMENT	5
1.6 PERFORMANCE ASSESSMENT RESEARCH	6
1.7 VOLCANIC SYSTEMS OF THE BASIN AND RANGE	7
1.8 TECTONIC PROCESSES IN THE CENTRAL BASIN AND RANGE REGION	8
1.9 FIELD VOLCANISM	9
1.10 REGIONAL HYDROLOGY	10
1.11 REFERENCES	11
2 SEISMIC ROCK MECHANICS	13
2.1 TECHNICAL OBJECTIVES	13
2.2 SIGNIFICANT TECHNICAL ACCOMPLISHMENTS	14
2.2.1 Dynamic Scale Model Experiment on a Jointed Rock Mass	14
2.2.2 Field Site Investigation: Effect of Mine Seismicity on Groundwater	19
2.2.2.1 Background	19
2.2.2.2 Observed Seismo-Hydrologic Response at Lucky Friday Mine	22
2.2.2.3 Data Analysis and Conclusions	23
2.2.3 Thermal-Mechanical-Hydrological Coupled Modeling (DECOVALEX)	24
2.2.3.1 DECOVALEX Phase III Experimental and Modeling Studies	24
2.2.3.2 Direct Shear-Flow Test (TC5)	25
2.3 ASSESSMENT OF PROGRESS TOWARD MEETING PROJECT OBJECTIVES	30
2.4 PLANS FOR NEXT REPORTING PERIOD	31
2.5 REFERENCES	32
3 INTEGRATED WASTE PACKAGE EXPERIMENTS	35
3.1 OVERALL TECHNICAL OBJECTIVES	35
3.2 SIGNIFICANT TECHNICAL ACCOMPLISHMENTS	36
3.2.1 Background	36
3.2.2 Previous Reports	37

CONTENTS (Cont'd)

Section		Page
3.2.3	Present Report	37
3.3	CREVICE CORROSION	37
3.3.1	Experimental Procedures	37
3.3.2	Results and Discussion	38
3.3.2.1	Repassivation	38
3.3.2.2	Crevice Corrosion Propagation.	38
3.3.2.3	Mechanism of Repassivation	40
3.4	LONG-TERM LOCALIZED CORROSION TEST RESULTS	41
3.4.1	Experimental Procedure	41
3.4.2	Results and Discussion	41
3.5	STRESS CORROSION CRACKING STUDIES.	44
3.5.1	Experimental Procedures	44
3.5.2	Results.	45
3.5.2.1	Slow Strain Rate Tests	45
3.5.2.2	Constant-Deflection Tests.	46
3.5.3	Discussion.	49
3.6	CONCLUSIONS AND RECOMMENDATIONS.	51
3.6.1	Localized Corrosion	51
3.6.2	Stress Corrosion Cracking	51
3.7	ASSESSMENT OF PROGRESS TOWARDS MEETING PROJECT OBJECTIVES.	51
3.8	PLANS FOR THE NEXT REPORTING PERIOD	52
3.9	REFERENCES	52
4	GEOCHEMICAL NATURAL ANALOG RESEARCH	57
4.1	TECHNICAL OBJECTIVES	57
4.2	SIGNIFICANT TECHNICAL ACCOMPLISHMENTS	58
4.2.1	Methods	59
4.2.2	Results.	59
4.2.3	General Transport Through Fractured Tuff Surrounding the Deposit	61
4.2.4	Transport Along a Major Fracture Set	63
4.2.5	Relative Effectiveness of Mesofracture, Microfracture, Matrix Retardation and Retention of Uranium	68
4.2.6	Conclusions.	72
4.3	ASSESSMENT OF PROGRESS TOWARD MEETING PROJECT OBJECTIVES.	73
4.4	PLANS FOR NEXT REPORTING PERIOD	74
4.5	REFERENCES	74
5	SORPTION MODELING FOR HLW PERFORMANCE ASSESSMENT.	77

CONTENTS (Cont'd)

Section		Page
5.1	TECHNICAL OBJECTIVES	77
5.2	SORPTION EXPERIMENTS	77
5.2.1	Uranium Sorption on Montmorillonite	78
5.2.1.1	Preparation of Na-montmorillonite	78
5.2.1.2	Experimental Procedure	78
5.2.1.3	Experimental Results and Discussion	79
5.2.2	Uranium Sorption on Containers	81
5.2.2.1	Experimental Procedure	81
5.2.2.2	Container Sorption Results and Discussion	82
5.3	SORPTION MODELING	86
5.3.1	Model Description	86
5.3.2	Geochemical Modeling of Uranium (6+)-Montmorillonite Sorption	86
5.3.3	Geochemical Modeling of Carbon Sorption on Fe-(hydr)oxides	89
5.3.4	Model Results and Discussion	89
5.4	ASSESSMENT OF PROGRESS TOWARD MEETING PROJECT OBJECTIVES	92
5.5	PLANS FOR NEXT REPORT PERIOD	93
5.6	REFERENCES	94
6	PERFORMANCE ASSESSMENT RESEARCH	97
6.1	TECHNICAL OBJECTIVES	97
6.2	SIGNIFICANT TECHNICAL ACCOMPLISHMENTS	98
6.2.1	Review of Scenario Selection Methodologies	98
6.2.1.1	Nuclear Regulatory Commission/Sandia National Laboratories Scenario Method-ology	100
6.2.1.2	Department of Energy Yucca Mountain Project	100
6.2.1.3	Waste Isolation Pilot Plant	101
6.2.1.4	Scenario Analysis in Electric Power Research Institute Studies for Yucca Mountain	101
6.2.1.5	Atomic Energy of Canada Laboratory Scenario Selection Approach	101
6.2.1.6	Swedish Scenario Selection Approach	102
6.2.1.7	United Kingdom Nirex Ltd. Scenario Selection Approach	102
6.2.1.8	French Scenario Selection Approach	103
6.2.1.9	British Environmental Simulation Approach	103
6.2.1.10	Open Issues In Scenario Selection	104
6.2.2	Percolation Simulation Evaluation	104
6.2.2.1	Model Development	105
6.2.2.2	Simulation Results	108
6.3	ASSESSMENT OF PROGRESS	113
6.4	PLANS FOR NEXT REPORTING PERIOD	114

CONTENTS (Cont'd)

Section	Page
6.5	REFERENCES 115
7	VOLCANISM RESEARCH 117
7.1	TECHNICAL OBJECTIVES 117
7.2	SIGNIFICANT TECHNICAL ACCOMPLISHMENTS 118
7.2.1	Volcanism Geographic Information System 120
7.2.1.1	Coso Volcanic Field 121
7.2.1.2	Cima Volcanic Field 121
7.2.1.3	Big Pine Volcanic Field 123
7.2.1.4	Lunar Crater Volcanic Field 126
7.2.2	Critical Review of Compiled Volcanic and Tectonic Data 127
7.2.2.1	Assessment of Accuracy and Completeness 127
7.2.2.2	Assessment of Data Uncertainties 128
7.2.2.3	Assessment of Model Uncertainties 130
7.2.3	Peer Review of CNWRA Volcanism Research 131
7.3	ASSESSMENT OF PROGRESS 132
7.4	PLANS FOR NEXT REPORTING PERIOD 134
7.5	REFERENCES 134
8	Tectonic processes in the central basin and range region 139
8.1	TECHNICAL OBJECTIVES 139
8.2	SIGNIFICANT TECHNICAL ACCOMPLISHMENTS 140
8.2.1	Earthquake Distribution in Southern Nevada and Southern California 140
8.2.2	Landers Earthquake Sequence 142
8.2.3	Reconnaissance Field Investigations in the Black Mountains and Vicinity 148
8.2.4	Natural Selection of Faults 150
8.2.5	Stress, Brittle Deformation, and Effects on Transmissivity 152
8.3	ASSESSMENT OF PROGRESS TOWARD MEETING PROJECT OBJECTIVES 155
8.4	PLANS FOR NEXT REPORTING PERIOD 155
8.5	REFERENCES 156
9	FIELD VOLCANISM RESEARCH 161
9.1	TECHNICAL OBJECTIVES 161
9.2	SIGNIFICANT TECHNICAL ACCOMPLISHMENTS 162
9.3	DIFFUSE DEGASSING AT PARÍCUTIN VOLCANO, MEXICO 162
9.3.1	Background 162
9.3.2	Field Work at Parícutin Volcano 166
9.3.3	Preliminary Conclusions of the Parícutin Soil Gas Survey and Implications for the Volcanism Disruptive Scenario 169
9.4	AMPHIBOLES IN ALKALINE BASALTS 173

CONTENTS (Cont'd)

Section		Page
9.5	APPLICATIONS OF GEOPHYSICAL DATA TO ISSUES IN BASALTIC VOLCANISM	180
9.6	ASSESSMENT OF PROGRESS	182
9.7	PLAN FOR NEXT REPORTING PERIOD	183
9.8	REFERENCES	184
10	REGIONAL HYDROGEOLOGIC PROCESSES OF THE DEATH VALLEY REGION	189
10.1	TECHNICAL OBJECTIVES	189
10.2	SIGNIFICANT TECHNICAL ACCOMPLISHMENTS	190
10.2.1	Relation of Geologic Structure to the Regional Carbonate Aquifer	190
10.2.2	Hydraulic Properties of the Paleozoic Carbonate Aquifer	191
10.2.3	Evidence of Local Channeling in the Paleozoic Carbonate Aquifer	192
10.2.4	Flow in Fractured Rock and the Effect of In Situ Stress	193
10.2.4.1	Conductivity and Transmissivity of Fractured Rock Masses	193
10.2.4.2	Effect of In Situ Stress on Transmissivity	195
10.2.5	Effect of Anisotropy on Flow in the Paleozoic Carbonate Aquifer in Yucca Flat, Death Valley Regional Flow System	197
10.2.5.1	Geologic and Hydrogeologic Setting of Yucca Flat	197
10.2.5.2	Contemporary In Situ Stress in Yucca Flat	198
10.2.5.3	The Effect of Anisotropic Transmissivity on Flow in Yucca Flat	198
10.2.6	Implications of Stress and Transmissivity Anisotropy on Conceptual Models of Regional Flow	201
10.2.7	Calcite and Channeling in the Tuffaceous Aquifer Near Yucca Mountain ...	204
10.3	ASSESSMENT OF PROGRESS	208
10.4	PLAN FOR NEXT REPORTING PERIOD	209
10.5	REFERENCES	210

(THIS PAGE INTENTIONALLY LEFT BLANK)

FIGURES

Figure		Page
1-1	Relationship of the NRC HLW Research Program to licensing needs	2
2-1	Schematic drawing of scale model experiment	15
2-2	Two-dimensional UDEC model for the scaled rock mass experiment	17
2-3	Scaled earthquake velocity time history for the UDEC analysis	18
2-4	Equilibrium displacements after pretensioning of cables and excavation of the tunnel	19
2-5	Displacement field around the tunnel after 4 sec of dynamic loading	20
2-6	Horizontal cable tensions after 0.5 s of dynamic loading	21
2-7	Vertical cable tensions after 0.5 s of dynamic loading	21
2-8	Relative shear displacement along two joints intersecting the tunnel (i.e., Points A and B)	22
2-9	Groundwater pressure history observed with Zone 3 piezometer, September 18 through 20, 1991	23
2-10	Groundwater pressure history observed for Zone 3 piezometer, March 21 through April 10, 1991.	24
2-11	Relationship between steady-state pressure drop and flow rate in the nitrogen flow experiment using apparatus i. Cubic data fit. Corrected data account for the pressure drops in the tubings.	27
2-12	Faulty transducer reading mimics hysteretic effect	27
2-13	Repeatability of the pressure measurements after correction while going sequentially up and down the flow rate	28
2-14	Fully saturated water flow experiment using apparatus ii. Quadratic data fit (data: Mdata 5/5/94)	28
2-15	Time history of imposed normal load and corresponding pressure drop across the fully saturated fracture	29
2-16	Initial ABAQUS model of TC5 experiment.	30
2-17	ABAQUS results for closure versus normal stress response between monitoring points	31
3-1	Schematic diagram of the crevice corrosion specimen and PTFE serrated washer. The shaded areas indicate the crevice areas. A Hastelloy alloy C-276 bolt and nut was used for tightening the crevice device.	38
3-2	Repassivation potentials for crevice and pitting corrosion of alloy 825 in a 1,000 ppm chloride solution at 95 °C. The scan-rate was 5 mV/sec.	39
3-3	The maximum depth of crevice corrosion versus charge density for alloy 825 in 1,000 ppm chloride solution at 95 °C. The inset figure shows the current and potential versus time during one of the experiments.	40
3-4	The current density and weight-loss versus time for a specimen of alloy 825 totally immersed in a 1,000 ppm chloride solution at 95 °C and potentiostatically held at 0 mVSCE (about 100 mV below the repassivation potential)	42

FIGURES (Cont'd)

Figure	Page
3-5	The current density and weight-loss versus time for a specimen of alloy 825 totally immersed in a 1,000 ppm chloride solution at 95 °C and potentiostatically held at 200 mVSCE (about 100 mV above the repassivation potential). 43
3-6	The current density and weight-loss versus time for a specimen of alloy 825 totally immersed in a 300 ppm chloride solution containing 1,000 ppm nitrate and 1,000 ppm sulfate at 95 °C and potentiostatically held at 300 mVSCE (about 300 mV below the repassivation potential). 44
3-7	Result of slow strain rate tests of alloy 825 in concentrated chloride solutions of different cations (MgCl ₂ , LiCl, and NaCl) at temperatures ranging from 95 to 120 °C, with and without the addition of Na ₂ S ₂ O ₃ . Data points are shown in relation to the lowest values of pitting (E _p) and repassivation (E _{rp}) potentials, measured independently through cyclic polarization curves, as a function of chloride concentration. 46
3-8	SEM fractograph showing the transgranular SCC area of the alloy 825 specimen fractured in a slow strain rate test at an applied potential of -260 mVSCE in 40-percent MgCl ₂ solution at 120 °C. 47
3-9	Side surface of alloy 825 specimen tested at -260 mVSCE in 40-percent MgCl ₂ solution at 120 °C. 47
3-10	Results of constant-deflection tests of alloy 825 in concentrated chloride solutions of difference cations (LiCl and NaCl) at 95 °C. Data points are shown in relation to the lowest values of pitting (E _p) and repassivation (E _{rp}) potentials, measured independently through cyclic polarization curves, as a function of chloride concentration. 49
4-1	Fracture mapping of the Nopal I deposit was carried out at a scale of 1:25. Original field data were digitized and were manipulated using ARC/INFO software. This map includes 11,374 individual fractures. The visible uranophane line indicates the limit of visible U mineralization and marks the nominal edge of the deposit. Level +00 is 10 m lower in elevation than Level +10. The gap between the levels corresponds to the horizontal component of the slope of the face separating the levels and to large debris piles at the base of that face. Perimeter scales are in meters. 60
4-2	This map gives the results of a contact gamma survey conducted of the cleared areas of the Nopal I deposit with measurements made on a 1×1-m grid. The curved, shaded line indicates the limit of visible U mineralization and marks the nominal edge of the deposit. Contours have units of mR/hr. The areas of highest gamma intensity are well defined and, on Level +10, have a semiannular form. Anomalous gamma values are asymmetrically distributed around the deposit with a broader area of high-gamma values extending on Level +10 to the N than to the W and on Level +00 extending preferentially to the SE. 62

FIGURES (Cont'd)

Figure	Page
4-3	<p>This map shows that fracture density calculated by length appears randomly distributed across the map area; there is no apparent correspondence to areas of U occurrence. The curved, shaded line indicates the limit of visible U mineralization and marks the nominal edge of the deposit. Contours have units of meters of fracture length per meters² 64</p>
4-4	<p>This map shows that there is a broad tendency for increased fracture frequency density in areas close to the Nopal I deposit as opposed to those areas farther away. This broad correspondence is not supported by a detailed comparison; there is no significant statistical correlation between fracture density by frequency and gamma intensity. The curved, shaded line indicates the limit of visible U mineralization and marks the nominal edge of the deposit. Contours have units of number of fractures per meters² 65</p>
4-5	<p>Concentration of U in the fracture-filling material along the major EW fracture at 13.5 m N. The vertical dashed line indicates the edge of the Nopal I deposit. Uncertainties in U concentration are much less than the plot symbol size. 66</p>
4-6	<p>This plot shows the concentrations of U in the fracture-filling material along the major EW fracture at 13.5 m N outside the edge of the Nopal I deposit. A linear fit to these data predicts the concentration of U in the fracture-filling will reach local background levels (about 30 ppm) at 26.3 m from the edge of the deposit. Uncertainties in U concentration are much smaller than the plot symbol dimension. . . . 67</p>
4-7	<p>This drawing schematically illustrates the spatial relationships among the major EW fracture at 13.5 m N, the sample transects collected perpendicular to the fracture, and the edge of the Nopal I deposit. NS arrows give the distances of anomalous U concentrations from the major fracture; locations for each traverse are the distance from the edge of the deposit. U concentrations are given as the average for the microfractured areas N and S of the major fracture for each interval. Note that the drawing is scaled so that distances NS are expanded 10 times compared to distances. EW. 69</p>
4-8	<p>This model schematically illustrates variations in U concentrations along the major fracture at 13.5 m N and along transects perpendicular to the major fracture (i.e., Figure 4-7). Note that distances NS are expanded about 12 times compared to distances EW. Data which this surface approximates are given in Table 4.1. 70</p>
5-1	<p>U solution concentration versus equilibrium pH for U sorption experiments at an M/V ratio equal to 2.5 g/L. The diamond symbols represent measured values for solutions without montmorillonite. The curve represents an equation which was best fit to these data and was used to calculate the initial U concentrations, U_i, of experimental solutions. Open and closed circles represent data at the termination of forward and reverse experiments, respectively. Error bars were calculated based on 2% 2s</p>

FIGURES (Cont'd)

Figure	Page
	counting errors in liquid scintillation analysis. 80
5-2	U solution concentration versus equilibrium pH for U sorption experiments at an M/V ratio equal to 0.25 g/L. The diamond symbols represent measured values for solutions without montmorillonite. The curve represents an equation which was best fit to these data and was used to calculate the initial U concentrations, U_i , of experimental solutions. Circles represent data at the termination of forward experiments. Error bars were calculated based on 2% 2s counting errors in liquid scintillation analysis. 80
5-3	U solution concentration versus equilibrium pH for U sorption experiments at an M/V ratio equal to 0.25 g/L. The diamond symbols represent measured values for solutions without montmorillonite. The curve represents an equation which was best fit to these data and was used to calculate the initial U concentrations, U_i , of experimental solutions. Circles represent data at the termination of forward experiments. Error bars were calculated based on 2% 2s counting errors in liquid scintillation analysis. 81
5-4	Percent U sorbed by Teflon-FEP and polypropylene containers at uranium concentrations of approximately 5 and 50 ppb. Data points represent average values from three experimental solutions for each container type. Error bars represent 1s variation between experimental solutions. 83
5-5	Percent U sorbed by Teflon-FEP and polycarbonate containers at uranium concentrations of approximately 5 and 50 ppb. Data points represent average values from four experimental solutions for each container type. Error bars represent 1s variation between experimental solutions. 83
5-6	Comparison of percent U lost from solution in Teflon-FEP and polycarbonate (PC) containers at an initial U concentration of approximately 50 ppb. A Mann-Whitney rank sum test shows no significant difference in the sorption peaks of Teflon-FEP and PC containers (PC exp #2 and FEP exp #1) between pH 4.5 and 7. 84
5-7	Comparison of percent U initially sorbed and percent U desorbed due to competitive sorption at a uranium concentration of approximately 5 ppb for polycarbonate containers. Error bars represent 2s error for replicate samples. 85
5-8	Comparison of percent U initially sorbed and percent U desorbed due to competitive sorption at a uranium concentration of approximately 50 ppb for polycarbonate containers. Error bars represent 2s error for replicate samples. 85
5-9	Diffuse-Layer Model (DLM) model results for Uranium(6+)-Montmorillonite sorption. The model parameters and experimental conditions are given in Table 5-1. The binding constants were determined using FITEQL to interpret the sorption data for M/V=0.25 g/L. 88
5-10	DLM model results for carbon-ferrihydrite sorption. The model parameters and experimental conditions are given in Table 5-2. The binding constants were determined using FITEQL to interpret the sorption data for M/V=0.77 g/L (data from Zachara et al., 1987). 91

FIGURES (Cont'd)

Figure		Page
5-11	Diffuse-Layer Model (DLM) model results for uranium(6+)-montmorillonite sorption as a function of M/V and pH. Total uranium = 50 ppb. The model parameters and experimental conditions are given in Table 5-1.....	93
6-1	Model dimensions and boundary conditions	106
6-2	Retention data and calculated retention curves for nrg5, a generic tuff sample (Nitao, 1988b), and a fracture (Klavetter and Peters, 1986).....	107
6-3	Permeability versus bulk gas saturation for the composite model with a matrix permeability of 1.0×10^{-13} m ² and fracture permeabilities of 1.0×10^{-9} m ² (solid curve), and 1.0×10^{-11} m ² (dotted curve), and homogeneous matrix-only model with the same matrix permeability (dashed curve). The dotted curve with the lower fracture permeability gives effectively the same permeability as the matrix alone.....	109
6-4	Liquid saturation contours for a simulation time of 0.5 days of infiltration for a matrix/fracture composite medium with a matrix permeability of 1.0×10^{-11} m ² and (a) a fracture permeability of 1.0×10^{-11} m ² , and (b) a fracture permeability of 1.0×10^{-9} m ²	110
6-5	Liquid saturation contours for a simulation time of 1.0 day of infiltration for a matrix/fracture composite medium with a matrix permeability of 1.0×10^{-11} m ² and (a) a fracture permeability of 1.0×10^{-11} m ² , and (b) a fracture permeability of 1.0×10^{-9} m ²	111
6-6	Liquid saturation contours for a simulation time of 2.0 days of infiltration for a matrix/fracture composite medium with a matrix permeability of 1.0×10^{-11} m ² and (a) a fracture permeability of 1.0×10^{-11} m ² , and (b) a fracture permeability of 1.0×10^{-9} m ²	112
7-1	Overview of the relationship between the Volcanic Systems of the Basin and Range research project and other research and technical assistance activities. Projection is Universal Transverse Mercator, Zone 11.	119
7-2	Distribution of basaltic vents, lava flows, and faults in and around the Coso Volcanic Field. Epoch age is based on K/Ar dates and stratigraphic relationships. Data sources are summarized in Connor and Hill (1994a). Projection is Universal Transverse Mercator, Zone 11.....	122
7-3	Distribution of basaltic vents, lava flows, and faults in and around the Cima Volcanic Field. Epoch age is based on K/Ar dates and stratigraphic relationships. Data sources are summarized in Connor and Hill (1994a). Note that Quaternary volcanoes erupted on a topographic highland and that the volcanoes are distributed over 450 m of vertical relief. Projection is Universal Transverse Mercator, Zone 11.....	124

FIGURES (Cont'd)

Figure	Page
7-4	Distribution of basaltic vents, lava flows, and faults in and around the Big Pine Volcanic Field. Data sources are summarized in Connor and Hill (1994a). Note that Quaternary volcanoes erupted from about 1,200 m elevation on the Owen's Valley floor to 2,000 m on the eastern slopes of the Sierra Nevada Mountains. Projection is Universal Transverse Mercator, Zone 11. 125
7-5	Distribution of basaltic vents, lava flows, and faults in and around the Lunar Crater Volcanic Field. Data sources are summarized in Connor and Hill (1994a). Projection is Universal Transverse Mercator, Zone 11. 126
7-6	Histogram of the number of votes received by all peer-review panel nominees and those nominees who have expressed direct interest and availability for panel participation 133
8-1	Earthquake hypocenters in southern California, southern Nevada, and western Arizona are colored by date, sized by magnitude, and stacked by depth. Earthquake data are from PDE Catalog/National Earthquake Information Center. Magnitudes are assigned a value from one of the following fields in order of preference: Ms (average surface-wave magnitude), mb (average body-wave magnitude), contributed magnitude 1, or contributed magnitude 2. Fault traces are from Jennings (1991) in California; and Dohrenwend (1982), Dohrenwend and Moring (1991 a,b,c), Dohrenwend et al. (1991 a-f, 1992 a,b), and Nakata et al. (1982) in Nevada. The white rectangle indicates the boundary of the nine 7.5 minute USGS topographic quadrangles that comprise the Yucca Mountain area. 141
8-2	Earthquake activity belts of southern California and southern Nevada. 143
8-3	Landers earthquake sequence in plan view. Earthquake hypocenters are colored by date, sized by magnitude, and stacked by depth. Earthquake data are from PDE Catalog/National Earthquake Information Center. Magnitudes are assigned a value from one of the following fields in order of preference: Ms (average surface-wave magnitude), mb (average body-wave magnitude), contributed magnitude 1, or contributed magnitude 2. Fault traces are from Jennings (1992) in California; and Dohrenwend (1982), Dohrenwend and Moring (1991 a,b,c), Dohrenwend et al. (1991 a-f, 1992 a,b), and Nakata et al. (1982) in Nevada. The white rectangle indicates the boundary of the nine 7.5-minute USGS topographic quadrangles that comprise the Yucca Mountain area. 144
8-4	Landers sequence in profile view. Earthquake hypocenters are shaded by date and sized by magnitude. Earthquake data are from PE Catalog/National Earthquake Information Center. Magnitudes are assigned a value from one of the following fields in order of preference: Ms (average surface-wave magnitude), mb (average body-wave magnitude), contributed magnitude 1, or contributed magnitude 2. 145

FIGURES (Cont'd)

Figure	Page
8-5	<p>Field photographs of Emerson Fault rupture at the Galway Lake Road site. Right-lateral-dominated oblique slip of 7 m was measured at this site. (a) View towards NW displays fault scarp in foreground (1.5–2 m high) and trace of rupture crossing desert toward eastern end of distant ridge. (b) View toward NE shows main scarp (1.5–2 m high) dipping southwestward and subsidiary normal faults that form horsts and grabens in hangingwall of main fault. Photographs taken by D. Ferrill on 24 March 1994.</p>
8-6	<p>Graphical representation of solutions to Eq. (8-3) for the case where s_1 is vertical, s_2 is horizontal and oriented N-S, and s_3 is horizontal and E-W. The inset circles are lower hemisphere, equal-angle stereographic projections of the poles to surfaces in a three-space. The poles are coded according to their slip tendency (t/s): the large dots are those surfaces for which the slip tendency exceeds 80 percent of the maximum slip tendency developed in that stress condition; the medium dots are those surfaces for which slip tendency is between 60 and 79 percent of the maximum slip tendency in that stress condition; and the small dots represent surfaces that have slip tendencies lower than 59 percent of the maximum. The stereographic projections are positioned in s_1/s_2, s_2/s_3 space appropriately for the stress conditions that they represent.</p>
8-7	<p>Lower hemisphere, equal-angle projection of the poles to surfaces within a three-space representing the solution to Eq. (8-3) for the case where s_1 is vertical and equal to 100 units; s_2 is horizontal and oriented N-S, equal to 90 units, and s_3 is horizontal and oriented E-W, equal to 18 units. The poles are coded according to their slip tendency (t/s); large dots are those surfaces for which the slip tendency exceeds 80 percent of the maximum slip tendency developed in that stress condition; the medium dots are those surfaces for which slip tendency is between 60 and 79 percent of the maximum slip tendency in that stress condition; the small dots represent surfaces that have lower slip tendencies than 59 percent of the maximum. Surfaces that have high slip tendencies form a population that includes pure dip-slip normal faults with dips of 60° to 70° trending NS, oblique-slip faults with dips of 70° to 80° trending NW-SE and NE-SW, and vertical strike-slip faults trending WNW-ESE and ENE-WSW.</p>
8-8	<p>Regional groundwater flow and maximum horizontal stress. Flow directions are from Wittmeyer et al. (1994) and are represented by white arrow. Horizontal stress data are from Zoback et al. (1992). Fault traces are from Jennings (1992) in California; and Dohrenwend (1982), Dohrenwend and Moring (1991 a,b,c), Dohrenwend et al. (1991 a-f, 1992 a,b), and Nakata et al. (1982) in Nevada.</p>
9-1	<p>Overview of the relationship between tasks in the Field Volcanism Project and other research and technical assistance projects.</p>

FIGURES (Cont'd)

Figure		Page
9-2	Parícutin is surrounded by numerous Quaternary cinder cones. Ash isopachs are in meters.	165
9-3	Fumarole temperatures measured at the Ahuan vent, Parícutin volcano. Time is in days since January 1, 1994.	167
9-4	Fumarole temperatures (a) correlate with atmospheric temperatures (b), especially in the lower temperature fumaroles.	168
9-5	Fumarole temperatures (a) do not correlate with atmospheric pressure (b).	169
9-6	Soil He concentrations at Parícutin. Collected during January 1994.	171
9-7	Soil Radon concentrations at Parícutin. Collected during January 1994.	172
9-8	Soil CO ₂ concentrations at Parícutin. Collected during January 1994.	173
9-9	Variations in total Al and Ti (formula units) for amphibole from alkaline basalt x enocrysts and basalt crystallization experiments. Amphiboles from 5- and 10- kbar experiments are from Green (unpublished analyses, 1994), 20 kbar from Adam et al. (1993), and 23 kbar from Allen and Boettcher (1983).	178
9-10	Variations in Al(IV) versus Al(VI) in amphiboles are sensitive to variations in temperature, pressure, and water contents. Crater Flat amphiboles appear transitional between experimentally derived and xenocrystic amphiboles. Same symbols as in Figure 9-9.	179
10-1	Orientation of the principal axes of anisotropy in a fractured medium in two dimensions (After Maini and Hocking, 1977)	194
10-2	Physiography of the WIPP Site, New Mexico, with directions of inferred maximum horizontal in situ regional stress.	196
10-3	Hydrostratigraphic map of Yucca Flat with topographic contours (m), locations of boreholes with water level measurements in the Paleozoic rocks, inferred orientation of maximum in situ horizontal stress, and Quaternary faults.	199
10-4	Rose diagram of orientation of inferred maximum horizontal in situ stress at Yucca Flat, Nevada	200
10-5	Orientation of Darcy flux for transmissivity anisotropy ratio shown by long arrow. Orientation of driving force is shown by short arrow.	201
10-5	Contours of hydraulic heads (interval is 50 m except in southeastern portion where interval is 10 m) measured in Paleozoic units with orientation of driving force depicted by arrows	201
10-6	Orientation of Darcy flux for transmissivity anisotropy ratio shown by long arrow. Orientation of driving force is shown by short arrow.	202
10-6	Orientation of Darcy flux for transmissivity anisotropy ratio $T_x/T_y=2$ shown by long arrow. Orientation of driving force by short arrow.	202
10-7	Orientation of Darcy flux for transmissivity anisotropy ratio shown by long arrow. Orientation of driving force is shown by short arrow.	203
10-7	Orientation of Darcy flux for transmissivity anisotropy ratio $T_x/T_y=3$ shown by long arrow. Orientation of driving force is shown by short arrow.	203

FIGURES (Cont'd)

Figure		Page
10-8	Orientation of Darcy flux for transmissivity anisotropy ratio shown by long arrow. Orientation of driving force is shown by short arrow	204
10-8	Orientation of Darcy flux for transmissivity anisotropy ratio $T_x/T_y=4$ shown by long arrow. Orientation of driving force is shown by short arrow.	204
10-9	Angle between direction of driving force and direction of resulting Darcy flux in Paleozoic aquifer in Yucca Flat for: (a) anisotropy ratio of 2, (b) anisotropy ratio of 3, (c) anisotropy ratio of 4, and (d) anisotropy ratio of 5.	205
10-9	Orientation of Darcy flux for transmissivity anisotropy ratio $T_x/T_y=5$ shown by long arrow. Orientation of driving force is shown by short arrow.	205
10-10	Angle between direction of driving force and direction of resulting Darcy flux in Paleozoic aquifer in Yucca Flat for: (a) anisotropy ratio of 1, (b) anisotropy ratio of 2, (c) anisotropy ratio of 3, and (d) anisotropy ratio of 5	206
10-11	Angle between Darcy flux direction in Paleozoic carbonate aquifer and orientation of maximum horizontal stress in Yucca Flat for: (a) anisotropy ratio of 1, (b) anisotropy ratio of 2, (c) anisotropy ratio of 3, and (d) anisotropy ratio of 5	207
10-12	Calcite solubility limits for water samples from the tuffaceous aquifer at YM.	209

(THIS PAGE INTENTIONALLY LEFT BLANK)

TABLES

Table		Page
2-1	Material property data for the scale model blocks and interfaces	16
3-1	Summary of U-bend test results for alloy 825 in concentrated chloride solutions at 95 °C	48
4-1	Uranium content of microfractured tuff measured along traverses perpendicular to the EW fracture at 13.5 m N.	71
5-1	DLM parameters used to model Uranium (6+) sorption on Montmorillonite	87
5-2	DLM parameters used to model carbon sorption on ferrihydrite.	90
6-1	Scenario selection methodologies reviewed.	99
6-2	Hydraulic properties of a rock sample nrg5 from Peña Blanca compared to a YM tuff and fracture samples (Nitao, 1988a; Klavetter and Peters, 1986)	113
7-1	Compilation of published dates for Little Bear Peak, Nevada.	130
9-1	Fumarole temperature at Parícutin	170
9-2	Comparison of Crater Flats with basalts used in hydrous crystallization experiments.	174
9-3	Compositions of amphiboles from Crater Flat, Lunar Crater, western Grand Canyon Volcanic Fields, and analyses of Green and Draper (unpublished research). Formula units calculated using the method of Spear and Kimball (1984) with average Fe ³⁺ . Nomenclature of Hawthorne (1981).	176
9-3	Compositions of amphiboles from Crater Flat, Lunar Crater, western Grand Canyon Volcanic Fields, and analyses of Green and Draper (unpublished research). Formula units calculated using the method of Spear and Kimball (1984) with average Fe ³⁺ . Nomenclature of Hawthorne (1981).	177

(THIS PAGE INTENTIONALLY LEFT BLANK)

ACKNOWLEDGMENTS

This report was prepared to document work performed by the Center for Nuclear Waste Regulatory Analyses (CNWRA) for the Nuclear Regulatory Commission (NRC) under Contract NRC-02-93-005. The activities reported herein were performed on behalf of the NRC Office of Nuclear Regulatory Research (RES), Division of Regulatory Applications. The report is an independent product of the CNWRA and does not necessarily reflect the views or regulatory position of the NRC.

Active support from several people during the production of this report is thankfully acknowledged. First and foremost, this report is possible only because of the wholehearted cooperation from the principal investigators and researchers within each project who kept to the tight schedule of the editor. Technical reviewers—R.G. Baca, D.A. Ferrill, A. Gureghian, P.C. Lichtner, H.L. McKague, W.M. Murphy, W. Patrick, J.L. Russell, D. Turner, and S. Young—provided substantive comments that materially improved the quality of the report. Programmatic reviews were performed by W.C. Patrick and the editor. Able secretarial support was provided by E.F. Cantu, L.F. Gutierrez, M.A. Gruhlke, A. Ramos, and L. Selvey. The overall support from R.A. Sanchez and S.M. McCowan in producing this document using FrameMaker is especially appreciated.

Southwest Research Institute (SwRI) Publications Services staff provided illustration, editorial, and format adherence support.

Finally, the valued interaction with NRC project officers—G.F. Birchard, L.A. Kovach, T.J. McCartin, M.B. McNeil, T.J. Nicholson, J. Philip, and J.D. Randall—is gratefully acknowledged.

QUALITY OF DATA

DATA: Sources of data are referenced in each chapter. CNWRA-generated laboratory and field data contained in this report meet quality assurance requirements described in the CNWRA Quality Assurance Manual. Data from other sources however, is freely used. For data from non-CNWRA sources, their referenced sources should be consulted for determining their level of quality assurance.

ANALYSES AND CODES: Scientific/engineering computer codes used in analyses contained in this report are: UDEC and ABAQUS (Chapter 2), FITEQL and MINTEQA2 (Chapter 5), VTOUGH (Chapter 6), and ARC/INFO Geographic Information System (GIS) (Chapters 8 through 10). The computer codes UDEC, FITEQL, and MINTEQA2 are presently controlled under the CNWRA Software Configuration Procedure TOP-018. The ABAQUS and ARC/INFO are commercial software and only their object codes are available to the CNWRA.

(THIS PAGE INTENTIONALLY LEFT BLANK)

1 EXECUTIVE SUMMARY

1.1 INTRODUCTION

Progress from January 1 to June 30, 1994, on nine out of 12 research projects under way at the Center for Nuclear Waste Regulatory Analyses (CNWRA) is discussed in this report. Two of the three research projects not reported, namely Stochastic Hydrology and Unsaturated Mass Transport (Geochemistry), have been completed with final peer-reviewed project reports (Bagtzoglou et al., 1994, Bagtzoglou and Muller, 1994, and Murphy and Pabalan, 1994). Thermohydrology is the third unreported project which is scheduled to be completed in December 1994.

All research projects at the CNWRA are sponsored by the Nuclear Regulatory Commission (NRC) to fulfill its mandate under the Nuclear Waste Policy Act (NWPA), as amended. To understand the role of NRC funded research, it is important to recognize that the NRC regulatory responsibilities are distinct from those of the U.S. Department of Energy (DOE), which is responsible for siting, constructing, and operating a repository for the permanent disposal of high-level waste (HLW). The DOE has undertaken the development and implementation of a broad range of techniques and methods to obtain information and produce analyses necessary to determine site suitability, design the engineered portions of the repository, and complete a license application for review by the NRC. In fulfilling its responsibilities for assuring the radiological health and safety of the public, the NRC conducts confirmatory and exploratory (also referred to as anticipatory) research to

- Develop the licensing tools and technical bases necessary to judge the adequacy of the DOE license application
- Ensure a sufficient independent understanding of the basic physical processes taking place at the proposed geologic repository site
- Maintain an independent, but limited, confirmatory research capability to be used in evaluating DOE prelicensing and license application submittals

Figure 1-1 depicts the basic relationship between the NRC research program and licensing needs.

Regulations applicable to the licensing of a HLW repository (primarily 10 CFR Part 60) are translated into regulatory requirements, each of which must be met before the NRC staff can recommend the issuance of a license. Strategies and methods for determining if DOE demonstration of compliance with the regulatory requirements is acceptable are currently being developed and documented in the NRC License Application Review Plan (LARP). Key Technical Uncertainties (KTUs) are defined based on the risk to compliance determination. Evaluation and reduction of those aspects of the KTUs which are NRC's responsibility are the primary objectives of the research undertaken by the NRC. Each chapter of this report outlines the specific KTUs being addressed by the research described in that chapter.

Each of the research projects discussed herein is being conducted in accordance with approved Research Project Plans, which were developed consistent with an associated NRC statement of work. These plans are the vehicle for establishing the objectives, technical approach, justification, and funding for each of the studies. They also describe the interrelationships among the various projects, which provide a sound basis for integrating research results across disciplines. Because the plans primarily address planning and management matters, they are not discussed further in this report.

This document provides an executive summary that covers, in capsule form, the progress of each research project over the past 6 mo. The executive summary is followed by Chapters 2 through 10, representing each of the nine currently active research projects. Project objectives and a report of research activities and results to date, as appropriate, are given in each chapter. Progress toward fulfillment of identified research needs and development of particular regulatory products are addressed in cases where such progress has been significant. In addition, commentary is provided on anticipated progress for each project in the ensuing 6 mo period.

1.2 SEISMIC ROCK MECHANICS

Long-term deterioration of emplacement drifts and potentially enhanced near-field fluid flow resulting from coupled processes are among the important

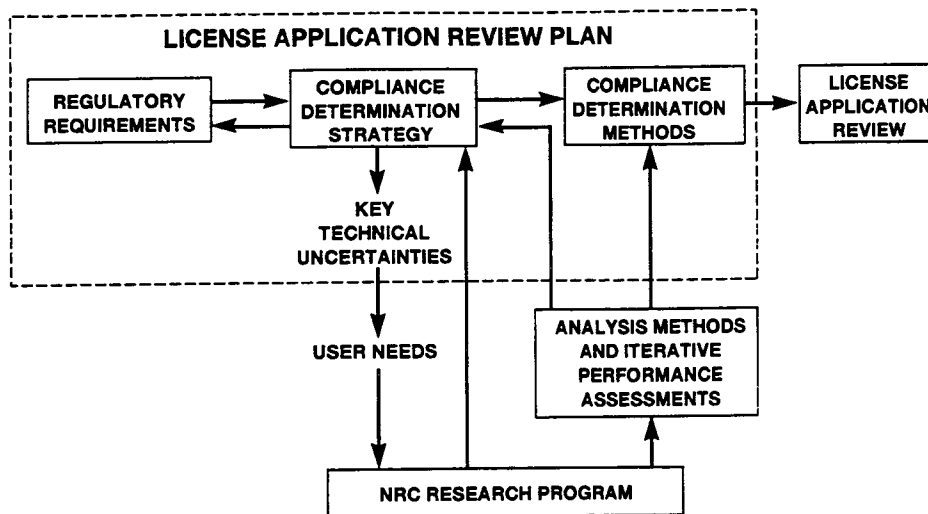


Figure 1-1. Relationship of the NRC HLW Research Program to licensing needs

concerns for safe high-level nuclear waste (HLW) disposal. Repetitive seismic loads and thermal loads generated by decay of the emplaced waste are among the factors that could potentially cause rock degradation or change near-field flow patterns due to joint normal and shear deformations. Evidence in the literature indicates that the most likely significant effect of earthquakes on hydrology is changes in fracture permeability.

A key technical uncertainty (KTU) has been identified that could pose a high risk of noncompliance with the performance objectives of 10 CFR Part 60. This KTU is the ability to predict the long-term effects of repetitive seismic load and high temperatures on the degradation of emplacement drifts. These long-term effects may have implications on the performance of the Engineered Barrier Systems (EBS), retrievability of waste, and long-term waste isolation, especially if some of the openings to the HLW repository are left unfilled at closure. The objective of the Seismic Rock Mechanics Research Project is to develop techniques that could be used to predict the response of the near-field rock mass at the proposed repository at the Yucca Mountain (YM) site when it is subjected to repetitive seismic loads and high temperature conditions. The knowledge gained through laboratory, field, and theoretical analyses in this project has supported the

development and implementation of portions of the License Application Review Plan (LARP) and precicensing activities, including reviews of Exploratory Studies Facility (ESF) design packages. The results of ongoing activities in Tasks 4, 5, 7, and 9 are reported herein.

Task 4 activities during this reporting period included construction of a small-scale model of jointed rock mass for dynamic tests. This scale model consisted of approximately 670 cast simulated-rock ingots aligned within a testing frame at 45 degrees to the horizontal. In the center of the simulated rock mass was a 6-in. (15.2-cm) circular tunnel. Thin steel cables were used to apply a portion of the scaled *in situ* loadings. Detailed instrumentation was placed around the tunnel as well as at other locations, some of which were determined from pretest computer analysis using the Universal Distinct Element Code (UDEC). The entire test specimen was loaded onto a shaking table and a horizontal (i.e., shear) earthquake input motion was applied to the base. Both the amplitude and time duration of the input signal were appropriately scaled. The laboratory experiments involved the application of four earthquake motions using the same input signal characterized by the peak input displacement. Measurements were recorded after each experimental run. The input signal was then increased in amplitude, and another four runs were

made. The process was continued until significant displacement had occurred or the tunnel collapsed. The purpose of these experiments was to study the impact of repetitive motion on the stability of the tunnel.

Pretest modeling analysis of the first input earthquake motion was conducted with the UDEC. This input motion consisted of a peak displacement of 0.15 in. (0.38 cm). Due to the long computer run times for the 7.5-s dynamic signal, some geometric simplifications within the model were necessary. These simplifications involved using the actual size [i.e., 2-in. (5.08-cm)] experimental rock blocks within a few diameters of the opening and 4-in. (10.16-cm) square blocks further away. It was determined that this simplification would not result in much difference in the predicted results. Maximum shear displacements on the order of 4.0×10^{-3} in. (0.1 mm) were predicted along certain joints intersecting the tunnel. The shear displacement response along joints was in the form of step changes rather than continuous shear displacements. The 7.5-s signal required approximately 6 d of computer run time on a Sun Sparc 10 workstation using the UDEC code.

Task 5 activity during this reporting period involved the analysis of field data on the effects of mining-induced small magnitude earthquakes on groundwater pressure distribution, based on field work conducted by the Center for Nuclear Waste Regulatory Analyses (CNWRA) at the Lucky Friday Mine, Idaho. The groundwater pressure in three fracture zones was monitored for 24 mo. In addition, the magnitude, source location, and associated ground motions of mining-induced seismic events were noted. It was observed that, in general, the magnitude of earthquake-induced groundwater pressure change varied with the earthquake magnitude and distance of the observation point from the source location. This relationship may be modeled by fitting a regression curve to the observed data. However, use of such a model for predictions may be limited to earthquake magnitudes that fall within the range of the fitted data. Mechanistic modeling is likely to be more reliable but such models are not available at this time.

Task 9, the **DE**velopment of **CO**upled models and their **VA**lida**TI**on against **EX**periments (DECOVALEX), is currently in its third phase. The Big-Ben Experiment (TC3) is one of five test cases (TCs) for this phase and is currently being modeled by the NRC/CNWRA using the finite element code

ABAQUS. The Big-Ben Experiment consists of an EBS involving coupled thermal-mechanical-hydrological (TMH) processes. The EBS incorporates a partially saturated bentonitic buffer material surrounding the heater system within the simulated rock (concrete). Simulated fractures were also present in the system in which water injection took place. Thus, the purpose of the test was to evaluate the water uptake within the buffer as well as determine the degree of moisture-induced swelling under heated conditions and water injection. The ABAQUS code was chosen due to its capabilities for modeling partially saturated flow and mechanical swelling of the buffer. ABAQUS does not have all the degrees-of-freedom for modeling fully coupled TMH processes within a single element. Thus, two separate analyses are required, namely a thermal analysis, followed by a poroelastic analysis. To date, the thermal analysis has been completed. The predicted nodal temperatures will be input into a model for analyzing the mechanical swelling and thermo-mechanical stresses, as well as the partially saturated flow. Final results will be presented in the next reporting period.

Both experimental and modeling work are continuing on the Direct Shear-Flow Test (TC5), proposed by the NRC/CNWRA for Phase 3 of DECOVALEX. TC5 was designed to study both saturated and unsaturated flow in a single natural welded tuff joint under both normal and direct shear loading. To date, saturated tests using water have been conducted under pure normal loading conditions. Prior to conducting the test, the rock matrix on either side of the fracture was fully saturated with water. At each increment in normal load, the fracture injection flow rate was held constant while the pressure difference between the inlet and outlet of the fracture was measured. During the next reporting period, saturated flow experiments will be conducted under shear loading conditions. Initial progress has been made in modeling the experiment using the code ABAQUS. The fracture is modeled using gap elements that can conduct fluid flow. As a first attempt, only a two-dimensional (2D) vertical cross-section through the joint was modeled, taking into account the actual rough surface profile. It was found that the nonlinear normal stress versus joint closure response could be reasonably simulated using a softened contact option within ABAQUS. This approach was necessary since ABAQUS lacks sophisticated joint models, having only the standard Mohr-Coulomb friction model.

1.3 INTEGRATED WASTE PACKAGE EXPERIMENTS

The Nuclear Regulatory Commission (NRC) regulation 10 CFR 60.113 requires waste packages to provide substantially complete containment of radionuclides for a minimum period of 300 to 1,000 yr. As stated in the License Application Review Plan (LARP) Sections 5.4, 2.2.2, and 2.2.3, the key technical uncertainties (KTUs) in the assessment of Engineered Barrier System (EBS) compliance with performance objectives include the prediction of environmental effects on the performance of waste packages and the EBS, and the extrapolation of short-term laboratory and prototype tests results to predict long-term performance of EBS components. The goal of the Integrated Waste Package Experiments (IWPE) program is to provide a critical evaluation of the information available for the assessment of compliance with regulatory requirements pertaining to EBS by a suitable combination of literature surveys and critical experiments. To achieve its objectives, the IWPE program is divided into six tasks: Task 1 — Corrosion, Task 2 — Stress Corrosion Cracking, Task 3 — Materials Thermal Stability, Task 4 — Microbiologically Influenced Corrosion, Task 5 — Other Degradation Modes, and Task 6 — General Reporting. The results of ongoing activities in Tasks 1 and 2 are reported here.

The general approach to long-term life prediction of container materials in environments promoting localized corrosion is pointed out along with the role of experimental investigations. Two of the parameters in this approach are the initiation and repassivation potential. In performance assessment (PA) calculations, a single critical potential, which is the experimentally determined repassivation potential, is used to predict the occurrence of localized corrosion of waste package containers. The assumption of a single critical potential is supported by the results reported in this chapter. The repassivation potential for crevice corrosion is found to be similar to that for pitting corrosion. The propagation rate of crevice corrosion is found to be only slightly faster than that of pitting, and the maximum depth of crevice corrosion is similar to that of pitting for the same charge density. These findings can be qualitatively explained by the available mechanistic models, which are based on the changes in chloride concentration and pH inside the crevice or pit.

Long-term localized corrosion tests (up to 9 mo) show that the use of repassivation potential for deep

pits or crevices is more conservative in comparison to other parameters, such as pit initiation potential. Specimens held at potentials more positive than the repassivation potential, but more negative than the pit initiation potential, exhibit crevice corrosion after a few months. However, specimens held at potentials more negative than the repassivation potential have not yet shown any indication of localized corrosion. Further tests along this line are recommended to gain greater confidence in the use of this parameter for PA.

The applicability of critical potentials for localized corrosion for predicting stress corrosion cracking (SCC) is being studied using slow strain rate and constant deflection tests on type 316L stainless steel (SS) and alloy 825. The results generated thus far are consistent with the assumption that the repassivation potential for localized corrosion constitutes a lower bound for the critical potential for SCC in the case of type 316L. However, the occurrence of SCC is apparently dependent on test technique. In slow strain rate tests, SCC of type 316L SS was promoted by concentrated chloride solution (>9.0 mol/kg water) above 100 °C, and at lower chloride concentrations and temperatures by the presence of thiosulfate. However, no SCC was observed with the slow strain rate test technique at chloride concentrations lower than 6 mol/kg water, even in the presence of thiosulfate. In contrast, SCC of type 316L SS was observed using U-bend specimens in constant-deflection tests conducted in solutions with chloride concentration as low as 1,000 ppm. In dilute solutions, cracking was found to be confined to the region above the liquid water-vapor interface. In the case of alloy 825, no apparent discrepancies were observed by comparing the results of the slow strain rate tests with those of constant-deflection tests under environmental conditions similar to those used for testing type 316L SS. For alloy 825, SCC was only observed in tests at 120 °C in highly concentrated chloride solutions. However, since alloy 825 is far more resistant to SCC than type 316L SS, additional studies are needed to reach a conclusion regarding the effect of test technique. The need to study the effects of crevice conditions and concentration processes at the vapor/solution interface on the initiation of cracks is emphasized to explore the full range of environmental conditions and electrochemical potentials that can cause cracking of these alloys in chloride-containing solutions at temperatures close to the boiling point.

1.4 GEOCHEMICAL NATURAL ANALOG RESEARCH

The Geochemical Natural Analog Research Project is being conducted to develop a better understanding of the usefulness and limitations of natural analog studies when employed to support a license application for a high-level waste (HLW) repository and to provide fundamental data on the long-term behavior of HLW within a repository environment to support Performance Assessment (PA) models. Field and literature data were used to select two sites for analog research: the Nopal I uranium (U) deposit in the Peña Blanca district, Chihuahua, Mexico, and the Akrotiri archaeological site on Thera (Santorini), Greece. This report describes recent results from the Peña Blanca site.

At the Nopal I U deposit, U has been transported under conditions comparable to those that could occur at the candidate HLW repository at Yucca Mountain (YM), Nevada. This investigation focused on approximately 1,400 m² of essentially continuous bedrock outcrop spanning the Nopal I deposit and surrounding host tuff. Analysis and interpretation of the data collected provide estimates of: (i) the distributions of U within and around the Nopal I deposit, (ii) the distribution and characteristics of the fracture network within and surrounding the deposit, and (iii) the transport of U away from the deposit mainly along fracture paths. U-series isotopic measurements indicate mobilization of U along the margin of the deposit within the last 1 Ma and significant U transport at about 54 ka.

Greater transport distances were observed along a few relatively continuous mesofractures (i.e., fractures with apertures >1 mm and traces extending more than 10 m) than through the general fracture network composed of thousands of less continuous microfractures (i.e., fractures with apertures <1 mm and trace lengths on the order of centimeters) within and surrounding the deposit. U transport away from the deposit appears to be largely independent of variations in the general fracture network pattern. Analyses reported here place semi-quantitative constraints on U transport distances along paths with distinct fracture characteristics. Movement of U away from the Nopal I deposit, measured as net horizontal transport vectors along mesofracture paths, achieved maximum distances at least 20 times greater than transport of U through tuff with a complex network of microfractures. Transport of U away from individual microfractures into

homogeneous, unfractured (at optical microscopy scales) tuff matrix appears limited to distances less than 1 mm.

Uranium distributions are interpreted as relative inventories of transported U within distinct portions of the transport system. The U content of a complex microfracture network is five times greater than the U content of the mesofracture through which U was introduced into the microfracture network. Data from individual microfractures with high U concentrations (e.g., 5.6×10^5 ppm) indicate that the amount of U transported out of a microfracture into the tuff matrix adjacent to a microfracture and retained to the present is only 5 percent of the U retained within a microfracture (mainly by precipitation as uranophane). This analysis suggests a relative ranking for transported U inventories: (i) microfracture network U content >> mesofracture U content, and (ii) individual microfracture U content >> adjacent matrix U content.

These results comprise significant progress toward a better understanding of performance issues important for a YM repository. NRC/CNWRA Iterative Performance Assessment (IPA) has identified substantial conceptual uncertainties regarding appropriate implementation of fracture transport and fracture retardation, and the relationship between fracture flow and matrix diffusion remains indeterminate in transport models. Results reported here provide semi-quantitative constraints on U fracture transport distances and identify the portions of a complex fracture-matrix system that have retained (under conditions comparable to those anticipated for a YM repository, for a time period of at least 10^4 yr) the greatest proportion of transported U. Future versions of PA models can use these results to reduce conceptual uncertainties regarding U transport.

1.5 SORPTION MODELING FOR HLW PERFORMANCE ASSESSMENT

To develop an understanding of radionuclide sorption processes and the important physical and chemical parameters that affect sorption behavior in the Yucca Mountain (YM) environment, experimental and modeling activities are being conducted to investigate the sorption behavior of uranium (U) and other actinides on geologic media. During the first half of 1994, experiments were completed to determine the possible effects of pH and solid-mass to solution-volume (M/V)

ratio on the sorption of U(6+) on montmorillonite, which is an important alteration mineral occurring at YM, Nevada. The experiments were conducted using initial solution concentrations of approximately 50 ppb, solution pH from 2 to 9, and M/V equal to 0.25 or 2.5 g/L. The results show that U sorption on montmorillonite is strongly dependent on pH; at an M/V ratio equal to 2.5 g/L, U sorption increases sharply at pH values above about 3.0 (adsorption edge), reaches almost 100 percent at pH ~ 6.3, and decreases sharply at pH greater than about 8.0 (desorption edge). Sorption data at M/V equal to 0.25 g/L indicate that, at lower M/V, the sorption envelope collapses, that is, the adsorption edge shifts to higher pH, the desorption edge moves to lower pH, and the sorption maximum decreases to lower values. Data from reverse experiments indicate that U sorption on montmorillonite is reversible.

Because of the low concentrations of U used in the experiments, potential U sorption by the container walls was a major concern. Therefore, experiments were conducted to determine the dependence of container sorption on the type of container used and the impact of sorption competition between the container walls and the mineral sorbent. The results of these experiments indicate that significant amounts of U are lost from solution due to sorption on container walls and that different types of containers have different affinities for U (polypropylene >> Teflon-FEP > polycarbonate). The results also indicate that desorption of U from the container occurs upon the introduction of a competitive substrate, such as a mineral phase. Thus experimental studies of radionuclide sorption must account not only for the effects of sorption on container material but also the effects of sorption competition between the mineral sorbent of interest and the container material.

Using simple conceptual models, a Diffuse-Layer Model (DLM) is able to predict complex sorption behavior reasonably well. For U sorption on montmorillonite, binding constants determined using the data for M/V = 0.25 g/L were able to reproduce the observed sorption behavior for M/V = 2.5 g/L quite well. The DLM was also able to model sorption of aqueous carbon as a function of pH and M/V. The performance of the DLM suggests that surface complexation models (SCM) can be used to predict sorption behavior for conditions beyond those used in sorption experiments. The DLM could be used to create an array of sorption coefficients as a function of system

chemistry for use in contaminant transport calculations. It may be difficult, however, to unambiguously define some of the necessary chemical variables in a natural groundwater system.

Results of these laboratory experiments and modeling activities provide us with an understanding of the important parameters that control the sorption behavior of an actinide element. Because of the strong dependence on pH and sorbent-surface-area/solution-volume ratio, modeling of sorption processes will likely require that changes in groundwater chemistry and in rock/fluid ratio be properly accounted for in performance assessment calculations if retardation by sorption processes is included. However, the success of the surface-complexation model in describing and predicting U sorption on montmorillonite and other minerals suggests that SCMs offer a scientifically defensible approach that may be useful for performance assessment calculations.

The similarity in the pH-dependence of U sorption on montmorillonite observed in these experiments and those observed for clinoptilolite and α -alumina reported previously is important. It may help identify simplified approaches to modeling sorption and thus help in the development of Compliance Determination Methods (CDMs) that will appropriately address the key technical uncertainties (KTUs) identified in Section 5.1 of the LARP and in the development of conceptual models related to the Performance Assessment Research (PA) Project and the Iterative Performance Assessment (IPA) Phase 3. The information derived from the laboratory experiments may also help interpret data on U distribution and migration at the Peña Blanca field site of the Geochemical Natural Analog Research Project.

1.6 PERFORMANCE ASSESSMENT RESEARCH

There are three primary objectives of this project. The first objective is to provide modeling technology that will benefit the Nuclear Regulatory Commission (NRC) Iterative Performance Assessment (IPA) activity and the development of methodologies that will be used in Compliance Determination Methods (CDMs). A second, and equally important, objective is to address key technical uncertainties (KTUs) associated with conceptual models, mathematical models, model parameters, future system states (i.e., disruptive scenarios), and model validation. The third objective is

to provide the technical basis for formulating guidance to the U.S. Department of Energy (DOE) in the specific areas of Performance Assessment (PA) modeling approaches and validation strategies. Research conducted under the PA Research Project is divided among three major tasks: Task 1—Conceptual Model Development; Task 2—Computational Model Development, and Task 3—Model Evaluation. In this reporting period, a strong emphasis was placed on Task 1, which includes research on hydrologic conceptual models and disruptive event scenarios. Major effort was made in reviewing scenario selection methodologies, and in analyzing hydrologic data from the Peña Blanca site, both under Task 1. A reduced level of research was performed on: (i) development of a conceptual model, based on thin-film approximations, for flow in a fracture (Task 1); (ii) documentation of a time-dependent, nonisothermal infiltration model (Task 2); and (iii) examination of the effects of data filtering on unsaturated flow model predictions (Task 3). In addition, research on conceptual models of flow and transport in fractured tuff was performed jointly with the Geochemical Analog of Contaminant Transport in Unsaturated Rock Research Project.

Work on disruptive event scenarios (i.e., future system states) was given high priority. Disruptive event scenarios are an important element of NRC IPA exercises and provide the basis for estimating how well the geologic repository may perform under combinations of adverse events and processes. In this reporting period, a major portion of the staff effort was devoted to a review of the state-of-the art in scenario-selection approaches. This activity produced a technical report (Bonano and Baca, 1994) that may be published as a NUREG/CR. The report shows that, despite differing terminology, many countries are using approaches similar to the NRC/Sandia National Laboratories (SNL) scenario methodology used in IPA; only in the United Kingdom is another distinct approach being used based on environmental simulation. The two approaches are shown to be complementary, with both approaches having strong and weak points. In addition, a number of open issues in scenario-selection are identified, including the role of expert judgment, the uniqueness and completeness of scenarios, and the implementation of scenarios.

The other task given high priority was the analysis of hydrologic data from the Peña Blanca Natural Analog Site, including both the measurement of

field-sample hydraulic properties and the simulation of field-scale percolation using these measured properties. These analysis activities have the dual purpose of supporting the planning for proposed field experimentation examining water percolation at the Peña Blanca site, and augmenting the understanding of the mathematical and numerical models used to simulate transport and represent the source term in studies of the natural analog. The proposed field experiment, in turn, is intended to address the dearth of experimental results examining field-scale percolation in the partially saturated, fractured tuffs which are characteristic of both the Peña Blanca site and YM. In this reporting period, hydraulic properties were obtained for five Nopal Formation core samples, representing differing degrees of hydrothermal alteration, which were collected from the Peña Blanca Site as part of the Natural Analog Research Project and measured as part of the PA Research Project. The measured hydraulic properties include porosity, bulk density, saturated hydraulic conductivity, and the soil-moisture retention curve. Samples of highly altered tuff have measured porosities on the order of 25 to 30 percent and permeabilities on the order of $1.0 \times 10^{-12} \text{ m}^2$, whereas the least altered rock has porosities on the order of 5 to 8 percent and permeabilities on the order of $1.0 \times 10^{-14} \text{ m}^2$. Numerical model simulations were performed to estimate how long an infiltration front would be expected to take to arrive at the existing adit, with and without the presence of fractures, under experimental ponding conditions. Based on these simulations, the total useful duration for an equivalent field experiment is anticipated to be on the order of a few days.

1.7 VOLCANIC SYSTEMS OF THE BASIN AND RANGE

Characterization of the frequency and nature of past volcanic events in the Yucca Mountain region (YMR), and assessment of the probability and consequences of future volcanism, are critical aspects of precicensing scientific investigations. The technical objectives of the Volcanic Systems of the Basin and Range research project are to (i) assess the probability of continued magmatic activity in the YMR, (ii) evaluate the quality and quantity of uncertainties in volcanological data for the YMR and nearby volcanic fields, and (iii) develop models that better predict the interaction between crustal tectonics and volcanism in the western Great Basin (WGB). These studies will provide a basis for precicensing guidance to the U.S.

Department of Energy (DOE) and are critical to license application review, as evinced in specific sections of the License Application Review Plan (LARP) (Section 3.2.1.9, evidence of igneous activity as a potentially adverse condition, Section 3.2.27, impact of volcanism on groundwater movement, and Section 6.1, assessment of compliance with the requirement for cumulative releases of radioactive materials). The Volcanic Systems of the Basin and Range research project has been designed to assess the probability of future volcanism in the YMR, taking into account the range of activity and structural controls on activity that are an inherent part of WGB volcanism.

During the last 6 mo, work has concentrated on development of the Volcanism Geographic Information System (GIS). Published geological data for the Reville Range-Lunar Crater Volcanic Field of Nevada and the Cima, Coso, and Big Pine Volcanic Fields of California, have been linked to common geographic coordinates in the GIS. Because of this linkage, volcanism models that relate tabular (e.g., volcano age) and spatial (e.g., fault location) data can be developed and tested at different areas and scales. In addition, the Volcanism GIS provides an effective tool for the review of prelicensing documents and the DOE license application.

A peer review of both the Volcanic Systems of the Basin and Range and Field Volcanism research programs was initiated as part of Task 3 review activities. This review will examine the scope and focus of Center for Nuclear Waste Regulatory Analyses (CNWRA) volcanism research and provide specific recommendations for improvement of these projects. Nominations for panel membership have been solicited from 150 active researchers in numerous volcanism sub-disciplines. To date, 12 candidates have indicated a general willingness to serve on the review panel and have a relatively high number of nominations. The review is tentatively scheduled for late September 1994, in San Antonio, Texas.

Work also began on developing a strategy for the critical review of volcanic and tectonic data compiled in the Volcanism GIS and an assessment of conceptual magmo-tectonic models for the WGB. In addition, this task will review the completeness and accuracy of data in the Volcanism GIS. All geological data have some level of uncertainty. To the extent possible this uncertainty must be quantified and propagated through geological models, so that model

results are presented with appropriate levels of uncertainty. Data uncertainties must reflect both the precision and accuracy of the method used to collect the data. Model uncertainties must reflect both the uncertainties in the data used to construct the model and the accuracy of the model in representing geological processes.

1.8 TECTONIC PROCESSES IN THE CENTRAL BASIN AND RANGE REGION

The objectives of the Tectonics Research Project are: (i) to compile and integrate tectonic data for the central Basin and Range and Yucca Mountain (YM) regions, and (ii) to develop and assess models of tectonic processes. The purpose of the project is to evaluate the adequacy of existing data, methods, and models for demonstrating and determining compliance with regulatory requirements. Of particular concern is the adequacy of existing and anticipated data for quantitatively assessing compliance with waste-isolation performance objectives.

Data and references compiled by Tectonics Research project staff have been used to develop Compliance Determination Strategies (CDSs) on Structural Deformation [License Application Review Plan (LARP) Section 3.2.1.5], Evidence of Igneous Activity (LARP Section 3.2.1.9), and Structural Deformation and Groundwater (LARP Section 3.2.2.8). Digital terrain and boundary data, and visualization methods developed for tectonics research are also being used in the regional and subregional hydrogeology research projects.

A Geographic Information System (GIS) is being used to compile data from disparate sources into an integrated management, review, and analysis environment. Significant technical accomplishments to date consist of: (i) development of digital terrain models of the YM and central Basin and Range regions; (ii) production of integrated maps of Quaternary faults, Quaternary basaltic volcanic fields, historic earthquake seismicity, and *in situ* stress orientations; and (iii) compilation of an initial database of geodetically measured regional strain and geologically determined slip rates for individual fault systems.

Significant accomplishments since the last report include: (i) evaluation of the National Earthquake Information Center (NEIC) hypocenter database, with

emphasis on the temporal and spatial clustering of earthquakes, relationships between earthquakes and mapped faults, and the 3-dimensional (3D) distribution of earthquakes through time in the sequence of earthquakes associated with the Ms 7.6 Landers earthquake (1992); (ii) reconnaissance field work in the Black Mountains; (iii) analysis of fault slip in 3D stress fields; and (iv) collaborative research, with the Regional Hydrology Research, on the geometry of the regional carbonate aquifer system and the effects of *in situ* stress on transmissivity and regional groundwater flow.

Evaluation of the NEIC hypocenter database reveals that, during the relatively brief period of the earthquake record (<200 yr), spatial and temporal clustering of major earthquake activity has occurred in the central Basin and Range region. Therefore, a tectonically active fault system in the Basin and Range province that is seismically quiet (e.g., the right-lateral strike-slip Death Valley-Furnace Creek system) should not be assumed to be aseismic. The Ms 7.6 Landers earthquake (1992) is similar to the type and magnitude of a large earthquake that would potentially occur on the Death Valley-Furnace Creek fault system. The Landers earthquake sequence produced approximately 75 km of surface rupture (with right-lateral strike-slip displacement) along mapped and previously unmapped faults, and triggered earthquakes as far as 1,250 km north of the Landers mainshock.

Field observations of extensional detachment-zone deformation indicate that detachment faulting in carbonate rocks is capable of producing tremendous fracture permeability which could have a major impact on groundwater flow in the regional carbonate aquifer. A new approach to analysis of fault slip tendency in 3D stress fields shows great potential for predicting orientations of faults (and sense of slip) expected in contemporary stress fields of southern California and Nevada. Collaborative work with Regional Hydrology Research has identified fairly close agreement between direction of maximum horizontal stress and direction of groundwater flow in the greater Death Valley region. A model is suggested wherein *in situ* stress produces anisotropic transmissivity by either forming new fractures (which act as groundwater conduits) at a low angle to the maximum horizontal stress, or preferentially closing existing fractures that are oriented at a high angle to the maximum horizontal stress.

1.9 FIELD VOLCANISM

The primary goals of the field volcanism project are to better characterize the effect of this type of volcanic activity on repository performance and, as a result, better constrain probability models of disruption of the repository. This characterization will be possible through investigation of the: (i) mechanics of mafic cinder cone eruptions, (ii) extent and characteristics of shallow hydrothermal systems and diffuse degassing associated with small-volume mafic eruptions, and (iii) nature of mafic intrusive geometries at repository depths. Successful completion of the Field Volcanism project, which began in April 1993, will require study of Plio-Quaternary cinder cones in the western Great Basin and comparison with modern, recently active cinder cones located elsewhere. Key Technical Uncertainties (KTUs) related to the Field Volcanism Project are (i) low resolution of exploration techniques to detect and evaluate igneous features, (ii) inability to sample igneous features, and (iii) development and use of conceptual tectonic models as related to igneous activity.

Several specific research activities were initiated or completed during the last 6 mo. These activities are designed to address issues related to the probability and consequences of igneous activity in the Yucca Mountain region (YMR). These include:

- Completion of a review of the seismic tomographic and magnetic methods and their application to the study of small-volume basaltic cinder cone fields
- Development of a research strategy to use tomographic and magnetic methods to investigate basaltic cinder cone alignments
- Completion of a simple model for dike-fracture interaction
- Preliminary study of diffuse degassing at Parícutin volcano, Mexico
- Comparison of xenocrystic and phenocrystic amphiboles in alkaline basalts
- Acquisition of basaltic rocks collected during the 1975-1976 eruption of the Tolbachik cinder cones

- Continuing major element and petrographic analysis of basaltic lavas of the western Great Basin

These activities resulted in a Major Milestone (MM), Geophysical Topical Report: Application of Seismic Tomographic and Magnetic Methods to Issues in Basaltic Volcanism, and an abstract A Simple Model of Dike-Fracture Interaction, presented at the Spring Meeting of the American Geophysical Union. In addition, a position paper was prepared during this period on the technical and regulatory basis for the study of recently active cinder cones, in support of an earlier Intermediate Milestone on this topic.

Soil gas and temperature data collected at Parícutin cinder cone in January and February, 1994, provide bounds on models for diffuse degassing at cooling cinder cones. Very high temperature zones are limited in areal extent to former vents, covering areas of several thousand square meters. Even after a long period of time, these vents are superheated; however, there is little or no condensable phase associated with fumaroles in these high-temperature regions, indicating that they act as dry-out zones. The high Rn and He fluxes observed in these areas indicate transport from depth with comparatively little mixing. These zones are surrounded by lower temperature regions in which there is high vapor flow at temperatures of 45–100 °C. At Parícutin, this region of elevated vapor flow covers 1.5–2 km². Gas flow is high throughout this area. A working hypothesis is that these zones cause areas of convective upwelling due to the cooling rock beneath the cone, and that there is very little or no magmatic component to gases at Parícutin. At depth, a broader area is likely affected by convective flow. Modeling of convective flow and cooling is planned, which will be constrained by gas flow and temperature data collected at Parícutin, with the objective of determining the likely areas affected by gas flow during and following cinder cone eruptions.

During the next 6 mo, research will focus on studies at the Tolbachik cinder cones, Kamchatka, Russia. These studies will include surveys of diffuse degassing, temperature monitoring, and collection of rock specimens for characterization of eruption mechanisms at these cinder cones. Following field work at Tolbachik, initial surveys of the three cinder cones used for analog studies, Parícutin, Mexico, Cerro Negro, Nicaragua, and Tolbachik, will be complete. During the

Fall of 1994, initial modeling studies of the degassing data will be made.

In addition to these activities, it is anticipated that a new task will be developed in the Field Volcanism Project. This task will involve seismic tomographic and magnetic investigations of a selected cinder cone alignment for the purpose of delineating intrusion geometry and the relationship of the alignment to regional structure. Based on results from Task 4, it is clear that this geophysical investigation will provide an auspicious approach to reduction of uncertainty related to exploration of igneous features, especially intrusions at repository depths and the relationship between tectonism and volcanism in the western Great Basin. It is anticipated that, in collaboration with NRC RES staff, this Task will be developed in the next 6 mo.

1.10 REGIONAL HYDROLOGY

Yucca Mountain (YM) has been proposed as a potential high-level nuclear waste (HLW) repository in part because of the favorable geochemical and hydrologic environment provided by its 700-m-thick unsaturated zone. Siting the repository in the unsaturated zone may limit the potential for waste canister corrosion and dissolution of the waste form. Low water fluxes that are postulated to exist in the unsaturated zone limit the likelihood that dissolved radionuclides will be rapidly transported to the accessible environment. One mechanism that may saturate the repository horizon and compromise favorable conditions at the YM site would be an increase in the elevation of the regional water table. Elevation of the water table may occur due to increased recharge to the regional hydrogeologic system from areas up to 100 km to the north and northeast of YM. Even if elevation of the regional water table does not saturate the repository block, the reduced thickness of the unsaturated zone may significantly diminish travel times in the vadose zone. The research project on Regional Hydrogeologic Processes of the Death Valley region was initiated to improve understanding of the saturated groundwater flow regime at YM and to assess the influence of the regional flow system on the height of the water table beneath YM. The objectives of this research project are to: (i) analyze existing conceptual models and develop new conceptual models of the regional hydrogeologic flow regime in the Death Valley region that contains YM, and (ii) construct numerical models of regional flow that may be used to assess the

potential for the water table beneath YM to rise in response to wetter climatic conditions.

Predictions made with numerical models will be used by the U.S. Department of Energy (DOE) in its license application to demonstrate that the YM site meets the overall performance standards outlined in 10 CFR 60.112 and the geologic subsystem performance standard defined in 10 CFR 60.113(a)(2). In addition, the DOE may choose to use numerical models to demonstrate the absence or influence of potentially adverse conditions including: (i) the effects of future pumping on the regional flow system [10 CFR 60.122(c)(2)]; the potential for deleterious changes to the hydrologic system [10 CFR 60.122(c)(5)]; (ii) the potential for changes to the hydrologic conditions resulting from climate change [10 CFR 60.122(c)(6)]; (iii) the potential for water table rise [10 CFR 60.122(c)(22)]; and (iv) the presence and influence of favorable conditions, including the clear absence of fully saturated pathways connecting the repository to the water table [10 CFR 60.122(b)(8)(ii)]. Understanding of the regional hydrogeologic system developed from this project will be used to guide the review of the DOE license application and to assess the adequacy of the models used by the DOE to demonstrate compliance with the regulatory requirements and environmental standards.

During the past 6 mo, efforts have continued within Task 1 on: (i) review of literature characterizing the hydrogeology and hydrogeochemistry of subbasins within the Death Valley region; (ii) collection of hydraulic, geologic, and geochemical data; and (iii) integration of data into a GIS database. However, most of the work conducted during the past 6 mo, as well as all the work presented in this research report, has been in Task 2. Efforts within Task 2 have been focused on developing and assessing methods for delineating high permeability flow channels within both the Paleozoic carbonate aquifer, which connects the topographically closed basins of the Death Valley region at depth, and the fractured welded tuff aquifer in the vicinity of YM. Understanding the potential for, and consequences of, flow channeling is essential for evaluating the potential for future climate changes to affect the performance of the repository. Local hydrogeologic studies of the Paleozoic carbonate aquifer suggest that channeling does occur along solution widened faults and fracture zones. Research presented here suggests that the contemporary regional stresses may affect the hydraulic

properties of fractures and fault zones and lead to anisotropy of the transmissivity. Simple models of flow in fractured rock aquifers based on parallel plate theory are developed to demonstrate the physical relationship between the orientation of the horizontal contemporary stress tensor and the orientation of the transmissivity tensor. This model indicates that the orientation of the maximum principal component of the transmissivity tensor in a fractured rock aquifer is parallel to the orientation of the maximum horizontal stress. This theoretical result is partially supported by stress measurements and multiple well hydraulic test data from the fractured Culebra dolomite unit at the Waste Isolation Pilot Plant (WIPP) near Carlsbad, New Mexico. Estimates of the orientation of the maximum horizontal stress in Yucca Flat were inferred from borehole breakout data. Incorporating the effects of transmissivity anisotropy into flow maps of Yucca Flat shows that the direction of the Darcy flux differs significantly from the direction of the driving force. Anisotropy will be used in computational models developed in Task 3 to quantitatively demonstrate the effects of flow channeling. Channelization may also characterize flow in the tuffaceous aquifer between the repository horizon and the regional carbonate aquifer; and nonisostatic stress effect may also be influential. Evidence for channelization in the tuffaceous aquifer is provided by the occurrence and isotope chemistry of calcite and the groundwater chemistry in the vicinity of YM. The carbon isotope chemistry of calcite is indicative of precipitation from water derived from the Paleozoic aquifer, which may have occurred millions of years ago. Tuffaceous zone groundwaters extracted from boreholes are chemically undersaturated with respect to calcite. The occurrence of calcite in core from these same boreholes indicates that the flow system supplying water to wells is channelized and isolated from rock containing calcite.

1.11 REFERENCES

- Bagtzoglou, A.C, and M. Muller. 1994. *Stochastic Analysis of Large-Scale Unsaturated Flow and Transport in Layered, Heterogeneous Media*. CNWRA 94-012. San Antonio, TX: Center for Nuclear Waste Regulatory Analyses.
- Bonano, E.J., and R.G. Baca. 1994. *Review of Scenario Selection Approaches for Performance Assessment of High-Level Waste Repositories and*

Related Issues. CNWRA 94-002. San Antonio, TX: Center for Nuclear Waste Regulatory Analyses.

Murphy, W.M., and R.T. Pabalan. 1994. *Geochemical Investigations Related to the Yucca Mountain Environment and Potential Nuclear Waste Repository.* CNWRA 94-006. San Antonio, TX: Center for Nuclear Waste Regulatory Analyses.

Bagtzoglou, A.C., S. Mohanty, A. Nedungadi, T-C.J. Yeh, and R. Ababou. 1994. *Effective Hydraulic Property Calculations for Unsaturated, Fractured Rock with Semi-Analytical and Direct Numerical Techniques: Review and Applications.* CNWRA 94-007. San Antonio, TX: Center for Nuclear Waste Regulatory Analyses.

2 SEISMIC ROCK MECHANICS

by Simon M. Hsiung, Mikko P. Ahola, Sitakanta Mohanty, Goodluck I. Ofoegbu, and Asadul H. Chowdhury

Investigators: Mikko P. Ahola, Asadul H. Chowdhury, Amitava Ghosh, Simon M. Hsiung, Sitakanta Mohanty, Goodluck I. Ofoegbu (CNWRA); Daniel D. Kana (SwRI)

NRC Project Officer: Jacob Philip

2.1 TECHNICAL OBJECTIVES

The technical objective of the Seismic Rock Mechanics Research Project is to develop techniques that could be used to predict the response of the near-field jointed rock mass at the proposed high-level waste (HLW) repository at Yucca Mountain (YM), Nevada, when it is subjected to repetitive seismic conditions (including earthquakes and nuclear explosions at the Nevada Test Site) and thermal loads. The near-field response includes the response both at the emplacement borehole and the emplacement drift scales. The laboratory, field, and theoretical analyses conducted as a part of this project are designed to develop a better understanding of near-field rock mass behavior under repetitive seismic and thermally induced loads. The analyses are also designed to obtain fundamental data on the seismic and thermal effects that can be used to validate predictive models and to verify computer codes for review of repository design [10 CFR 60.131(b)(1), 60.133(e)(1), 60.133(e)(2), 60.133(i), and 60.134], waste retrievability [10 CFR 60.111, 60.133(c), 60.133(e)(1), 60.133(i), and 60.134], and postclosure performance assessment [10 CFR 60.112, 60.113, 60.122(c)(5), 60.122(c)(12), 60.122(c)(14), and 60.122(c)(23)]. Many factors that control the effect of seismic and thermally induced loads on the near-field jointed rock mass behavior of the proposed repository are poorly understood. The problem is further complicated when the potential coupled effects of thermal loads are considered.

Information developed within the Seismic Rock Mechanics Research Project is being used to support specific portions of the License Application Review Plan (LARP) and prelicensing activities, including reviews of Exploratory Studies Facility (ESF) design packages. Detailed laboratory and field studies on the stability of underground openings were used to provide a basis for development and implementation of portions of the LARP relating to Section 4.3,

Assessment of Compliance with Design Criteria for Shafts and Ramps and will be used for Section 4.4, Assessment of Compliance with Design Criteria for Underground Facility; Section 4.5.2, Assessment of Integrated Geologic Repository Operations Area (GROA) Compliance with the Performance Objectives—Retrievability of Waste; and Section 5.3, Assessment of Compliance with the Design Criteria for the Postclosure Features of the Underground Facility. Knowledge regarding the prediction of long-term stability of vertical emplacement boreholes and emplacement drifts (for in-drift emplacement) and potential near-field fluid flow resulting from the coupled effects (including repetitive seismic effects) will support implementation of Section 5.4, Assessment of Compliance with the Engineered Barrier System (EBS) Performance Objectives. Furthermore, knowledge of effects of repetitive seismic and thermal loads (including long-term deterioration of underground openings in the emplacement area) on near-field hydraulic conductivity changes and on the potential to create preferential pathways that may compromise the waste isolation capability of the proposed repository will provide input for Iterative Performance Assessment (IPA).

The Compliance Determination Strategies (CDSs) for the LARP sections noted previously have been identified as type 4 or 5. It is clear that the Seismic Rock Mechanics Research Project is important in addressing uncertainties raised in CDSs 4.3, 4.4, 4.5.2, 5.3, 5.4, and 6.1, requiring an independent review capability for assessing Key Technical Uncertainties (KTUs) that pose a high risk of noncompliance with performance objectives of 10 CFR Part 60. Specific KTU topics that will be addressed by the Seismic Rock Mechanics Research Project include the ability to predict the effects of thermal and repetitive seismic loads on the stability of emplacement drifts and emplacement boreholes that may affect the performance of the EBS, retrievability of waste, and long-term

isolation of waste. For instance, it has already been determined through field experimental studies that repetitive lower magnitude seismic events can have a much greater influence on the degree of damage to underground openings than a single large-magnitude event (Hsiung et al., 1992).

The Seismic Rock Mechanics Research Project is an integrated effort combining expertise in rock mechanics, mining engineering, engineering geology, and hydrology. The integration includes the exchange of research results between Seismic, Thermohydrology, Integrated Waste Package Experiments (IWPE), and Performance Assessment (PA) Research Projects in the prediction of opening stability and changes in near-field hydraulic conductivity. The seismic and thermohydrology projects will complement each other developing techniques to predict near-field hydraulic conductivity and flow and transport environment, taking into account matrix flow and mechanical effect-dependent fracture flow under thermal conditions. The seismic research will assist in evaluating the mechanical loads that may cause stress/crevice corrosion or structural failure of waste packages, which is a component of EBS evaluations. The combined research and modeling efforts of Seismic and Thermohydrology projects will be useful to evaluate the presence of aqueous environments near the waste package for IWPE research and the near-field flow and transport environment for PA research.

Specific Nuclear Regulatory Commission (NRC) research needs that may be met through this project include: attainment of a better understanding of dynamic response of a jointed rock mass; evaluation of existing rock-joint constitutive models; evaluation of scale effects such that laboratory results can be applied to the field; assessment of potential effects of repetitive seismic loads on change of hydrological properties; identification, through a better understanding, of coupled TMH processes that are relevant to the unsaturated environment; and verification of selected computer code(s) that will be used in the LARP for seismic analyses and prediction of coupled TMH effects on near-field rock mass response. Research within the Seismic Rock Mechanics Research Project includes: characterization of dynamic behavior of single-joint rock in the laboratory using tuff natural joint specimens from Apache Leap near Superior, Arizona; performance of scale model experiments of a jointed rock mass; assessment of analytical models and computer codes;

performance of field studies on the effects of mining-induced seismicity on the rock mass near underground openings and local hydrology; collection of ground shock data; participation in the **DE**velopment of **CO**upled models and their **VAL**idation against **EX**periments (DECOVALEX) program for evaluation of computer codes capable of simulating coupled TMH processes; and identification and understanding of important thermally induced coupled processes in an unsaturated environment through laboratory studies. Earlier reports in this series documenting progress to date include: Hsiung et al. (1992, 1993a-e), Ahola et al. (1992, 1993), Hsiung and Chowdhury (1991, 1993), Kana et al. (1990, 1991), Brady et al. (1990), and Brandshaug et al. (1990). This report describes the results of activities in the Seismic Rock Mechanics Research Project during the first half of 1994.

2.2 SIGNIFICANT TECHNICAL ACCOMPLISHMENTS

2.2.1 Dynamic Scale Model Experiment on a Jointed Rock Mass

In this study, a scale model consisting of an aggregate of simulated rock material blocks was used to study the earthquake response of a larger segment of the reference repository rock mass. This model followed the direct shear experiments on single, naturally jointed, welded tuff fractures to determine the joint normal and shear response under both cyclic pseudostatic and dynamic loadings. The direct shear tests on single, natural welded tuff joints have been discussed fully in previous reports (e.g., Hsiung et al., 1993d-e, 1994) including the comparison with numerical predictions obtained from the distinct element code UDEC. For this period of reporting, a brief description of the scale model experiment as well as the numerical simulation of the experiment are presented, including how the numerical analysis was used in determining appropriate boundary loadings for the actual scale model experiment.

A schematic diagram of the scale model experiment is shown in Figure 2-1. This scale model experiment consisted of approximately 670 simulated rock ingots, each with a dimension of 2x2x24 in. (5.08x5.08x60.8 cm). The overall size of the 1/15 scale model was 4x4x2 ft (121.6x121.60x60.8 cm). The simulated rock ingots consisted of a mixture of portland cement, barite, bentonite, air entraining agent, soap

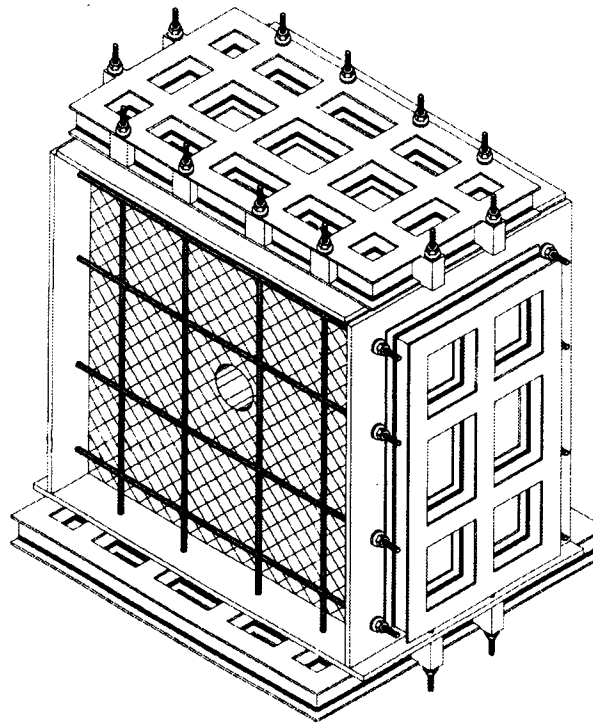


Figure 2-1. Schematic drawing of scale model experiment

agent, and water. The strength of the simulated rock ingots was about 1/15 to 1/10 that of the Apache Leap tuff rock. The placement of the ingots in the testing apparatus was such that two joint sets are created at 45 degrees to the horizontal. A circular tunnel 6 in. (15.2 cm) in diameter was created in the center of the model, perpendicular to the 4×4-ft (121.6×121.6-cm) sides. This tunnel was created by stacking ingots with curved surfaces against circular steel membranes which were used to support the opening until the boundary loadings were applied. Upon application of the boundary forces, these circular steel supports were removed prior to the dynamic testing. The instrumentation, not shown in Figure 2-1, consisted of Bentley transducers to monitor the normal and shear displacements along joints in the immediate vicinity of the tunnel opening. Strain gauges and accelerometers were installed on the face of the specimens around the opening to measure the block deformation and accelerations. In addition, linear variable differential transformers (LVDT) and accelerometers were installed at various distances along the axis of the tunnel to measure the tunnel closure and acceleration, respectively.

The horizontal boundary forces were simulated using thin steel cables anchored to the loading plates, whereas the overburden load was simulated through a combination of scale model weight, dead weight at the top of the specimen, and thin steel cables. Sixteen cables were used, 8 cables uniformly spaced in the horizontal direction on the front and back faces and 8 cables uniformly spaced in the vertical direction on the same two faces (see Figure 2-1). In addition to the top plate through which the vertical cables were attached, four additional plates were added, each having a weight of 310 lb (140.7 kg) to contribute to the overburden load. These plates are not shown in Figure 2-1. Each of the two vertical end plates was attached via a hinge assembly to the bottom plate, thus allowing rotation of these plates about the hinges. Contact between the top plate and the side plates was allowed through a roller assembly. The top plate was allowed to slide freely up and down along the end plates, and could also be detached from the end plates, if necessary, during the dynamic testing. Each vertical cable was tensioned to 236 lb (1.05 kN), to simulate the appropriately scaled overburden pressure. The horizontal cable tensions were determined through numerical simulation in which the

lateral displacement/joint slip was minimized during stacking of the rock ingots, top plate, and dead weights, and tensioning of the vertical cables. The horizontal cable tensions were thus determined to be 180 (0.8), 234 (1.04), 275 (1.22), and 293 lb (1.3 kN) for the top, midhigh, midlow, and bottom horizontal cables, respectively, on both the front and back of the scale model apparatus. The modeling exercise was used to establish the proper horizontal cable tensions at each stage of the assembly process in order to eliminate any lateral displacement along the joints. Six donut-shaped load cells were used to monitor the cable tensions in the horizontal and vertical cables on both the front and back of the test apparatus during the dynamic test. The load cells were also used to set the appropriate pretension on those cables prior to the dynamic test. The cable tension versus cable vibration frequency calibration curves were used to set the pretensions in the remaining horizontal and vertical cables that were without load cells. In order to input the dynamic loading, the entire assembly as shown in Figure 2-1 is mounted on a large shaking table. For this particular scale model test, only a horizontal seismic loading was applied to the base of the apparatus in the direction perpendicular to the axis of the tunnel. The particular earthquake time history is presented elsewhere in this section.

Prior to casting the simulated rock ingots, the batch mix proportion was established such that the uniaxial compressive strength was approximately 1/15 of the prototype based on tests results from the 28-d curing time. In pouring the ingots, a uniform surface roughness was maintained on all sides of the 2-ft (60.8-cm) long blocks. This roughness was created by lining the molds with a rubber material having a known roughness. In order to determine the joint properties, rock blocks were poured to the dimensions that could be tested within the existing direct shear apparatus. Corresponding to some batches of ingots, cylindrical samples were also prepared to determine the material property data for the mixture such as the Young's modulus, Poisson's ratio, and uniaxial compressive strength. Rectangular specimen pairs for simulated joints were also prepared for a determination of properties for simulated interface. Table 2-1 shows the

preliminary test results of the interface and material property data for a selected number of ingots.

Table 2-1. Material property data for the scale model blocks and interfaces

Bulk modulus (K)	1.475×10^3 MPa
Shear modulus (G)	1.020×10^3 MPa
Density (ρ)	2,053 kg/m ³
Joint friction angle (ϕ)	26 degrees
Joint normal stiffness (k_n)	1.0×10^4 MPa/m
Joint shear stiffness (k_s)	1.0×10^4 MPa/m
Joint cohesion (C)	0.0

For the pretest numerical simulation, the distinct element code UDEC was utilized. The distinct element approach was necessary because the dominant mode of deformation of the jointed rock mass system would take place along the joints. The two-dimensional (2D) plane strain model used for the UDEC analysis is shown in Figure 2-2. The model chosen did not incorporate the 2x2-in. (5.08x5.08-cm) blocks throughout the entire region, but only within the region extending approximately two tunnel diameters from the tunnel boundary. In the remainder of the model, 4-in. (10.16-cm) square blocks were utilized. An additional case was set up in which 2-in. (5.08-cm) square blocks were utilized within the entire model domain; however, the results still appeared to compare reasonably well even though there were some discrepancies as will be mentioned later in this section. Thus, in order to minimize the computer run time, the coarser model as shown in Figure 2-2 was used. To calculate responses to the 7.5-s earthquake time history developed for the scale model test, the computer run time for even this coarser model took approximately 7 d on a Sun Sparc 10 workstation.

Figure 2-2 shows the horizontal and vertical cable elements used in the UDEC analysis. These cables are anchored only in the bounding support plates, and thus interact with the scaled rock mass only through these plates, as in the actual experiment. Since a 2D plane strain model is used for the UDEC analysis, the cable force represents a force per unit depth (i.e., lb/in.).

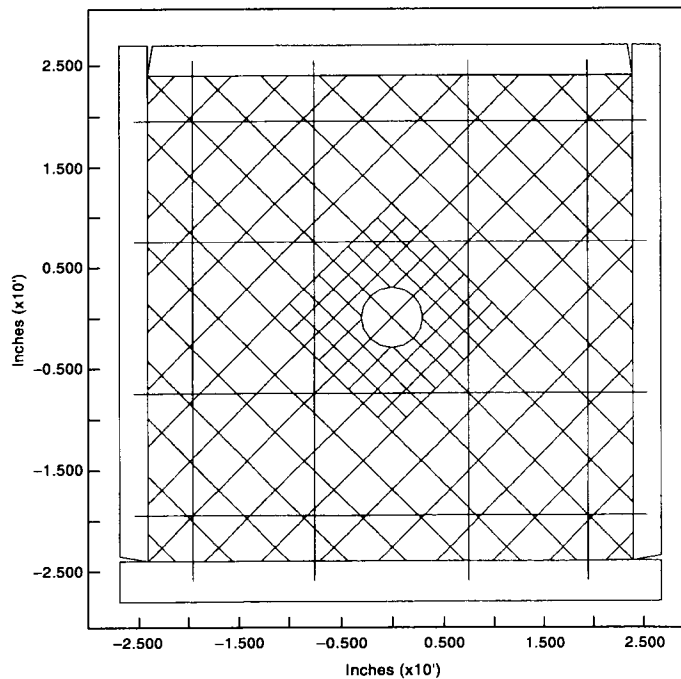


Figure 2-2. Two-dimensional UDEC model for the scaled rock mass experiment

Thus, the cable tensions in the UDEC model were set equal to the actual cable force specified in pounds divided by the cable spacing of 12 in. (30.4 cm). This was done because the actual depth of the scale model was 24 in. (60.8 cm), and cables were placed on both the front and rear faces of the actual apparatus. In the UDEC model, the end plates are pinned to the bottom plate at one point of contact to simulate the hinge in the actual experiment. The top plate, however, is not pinned to either of the two end plates. The points of contact are assigned values of zero for the friction, cohesion, and tension such that the top plate can slide freely along the end plates during the dynamic loading.

The scaled earthquake velocity time history representing the horizontal motion of the base plate is shown in Figure 2-3. The earthquake signal used for scaling was from the acceleration response recorded from the Guerrero accelerograph array for the earthquake of September 19, 1985, in Mexico. A 1/15 geometric scaling was used for the velocity amplitude, and duration was scaled by $1/\sqrt{15}$ based on the Riabucinski-Buckingham theorem (Fumagalli, 1968). The peak input velocity corresponds to a value of about 3.27 in./s (8.31 cm/s). This value corresponds to a peak

displacement of 0.15 in. (0.38 cm) and a peak acceleration of approximately 0.4 g. The duration of the dynamic motion is 7.5 s. This time history, representing a peak displacement of 0.15 in. (0.38 cm), was used in the UDEC simulation and was also the first motion applied to the actual experimental test apparatus. In addition, the actual experiment ran this particular time history several times to simulate the effect of repetitive seismic motion with the same peak amplitude. The displacement amplitude was then increased and a second series of repetitive motions was applied to the experimental apparatus. It is expected that the tunnel will likely collapse after several repetitive motions, with or without increasing the peak displacement amplitude. Experimental results on the small-scale rock mass model will be discussed in the future. In the following discussion, the results of the UDEC analysis are presented. Only one cycle of earthquake time history loading was applied to the UDEC model. No repetitive motions were simulated in the UDEC analysis.

Figure 2-4 shows the computed displacement field around the circular opening after removal of the tunnel blocks. The displacements shown include both those induced by removal of the blocks representing the

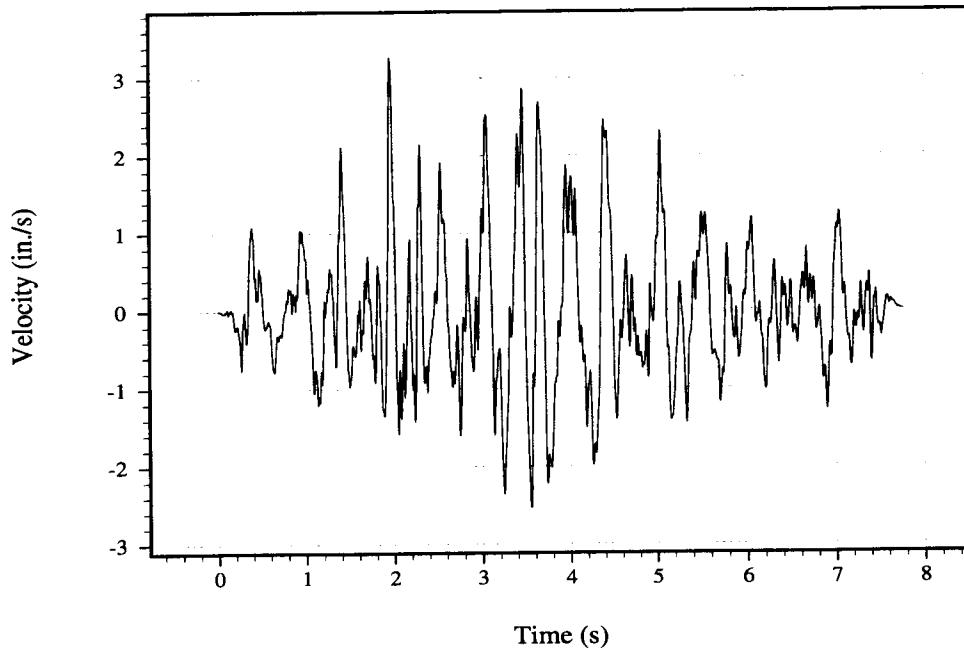


Figure 2-3. Scaled earthquake velocity time history for the UDEC analysis

tunnel as well as those caused by tensioning of the vertical cables. As shown in Figure 2-4, the maximum displacement is approximately 0.0036 in. (0.091 mm). During tensioning of the vertical cables, the horizontal cable tensions were adjusted to minimize any horizontal displacement. The numerical modeling simulation is somewhat different from the actual experiment in that during the actual construction of the scale model test, the circular tunnel is created while stacking the ingots prior to cable tensioning. However, in the numerical simulation, the tunnel is created after tensioning of the cables. This difference is not expected to cause significant variations in the results but will have to be verified.

Figure 2-5 shows the computed total displacement field after 4 s of dynamic loading, approximately halfway through the earthquake time history signal as shown in Figure 2-3. This figure shows higher block motion into the tunnel from the upper right and left portions of the tunnel due to slippage along the joints. Maximum total displacements are now on the order of 0.0513 in. (1.303 mm). There is also a significant drop in the stresses in the two block regions experiencing motion in the upper portion of the tunnel and a

significant increase in the stress state below the floor of the tunnel. It should be noted that in plotting the total displacements as shown in Figure 2-5, the small component of displacement due to excavation and preloading has not been subtracted out. Figure 2-5 shows some amount of detachment or displacement discontinuity occurring along the interface between the 2-in. (5.08-cm) and 4-in. (10.16-cm) blocks. This appears to be solely due to the coarse model assumption used, as this detachment was not present in the finer model. The maximum relative shear displacements between the two models was, however, approximately the same.

The horizontal and vertical cable tensions computed during the first 0.5 s of dynamic loading are shown in Figures 2-6 and 2-7, respectively. At the start of the dynamic loading, the time was initialized to zero. Thus, the initial starting cable tensions in both figures represent equilibrium after excavation of the tunnel blocks. As shown in Figure 2-6, the lower horizontal cable at the start of the dynamic loading has approximately 24.5 lb/in. (2.77 N/m) tension, whereas the upper horizontal cable has approximately 16 lb/in. (1.81 N/m) tension. However, soon after initiation of

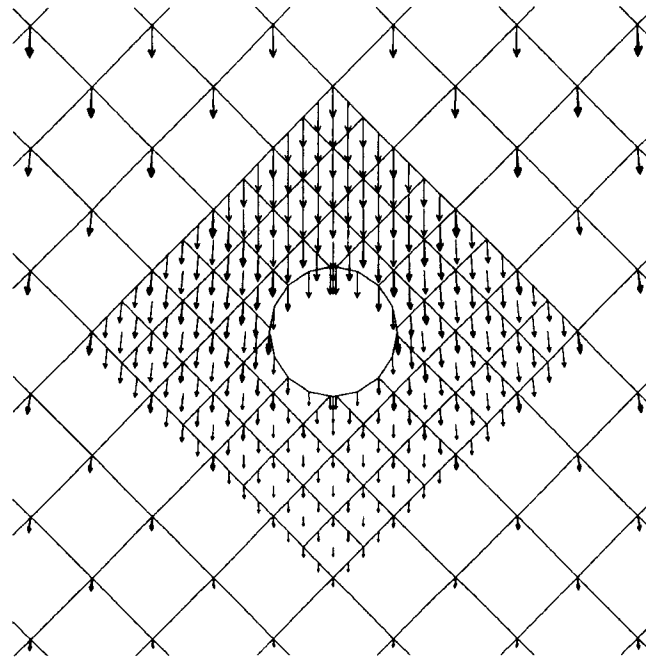


Figure 2-4. Equilibrium displacements after pretensioning of cables and excavation of the tunnel

the horizontal earthquake motion to the base plate, the upper horizontal cable tensions increased beyond that of the bottom horizontal cable, which remained relatively unchanged. As shown in Figure 2-7, the outermost vertical cables experienced the greatest fluctuations in tension. In addition, they are out of phase with each other, as would be expected. As one outer cable increases in tension, the other goes slack. At times during the dynamic loading, the numerical simulation shows the outer vertical cables going completely slack.

Relative shear displacements along the joints were monitored at various locations around the tunnel. Figure 2-8 shows the relative shear displacements at two points, A and B, as marked on the figure. It is interesting to note the stick slip type behavior for the relative shear displacement along the joints. For instance, at approximately 2 s, a large step change in the shear displacement occurs at point B, which directly correlates with the large peak in velocity applied at the base plate as shown in Figure 2-3. A decrease in peak input velocities from 2 to 3 s shows little or no change in the shear displacements at the two points. However, again at approximately 3 s, rapid step change in shear displacement occurs, this time at both points A and B,

apparently due to the fairly large velocity peak at 3 s. Subsequent velocity peaks show no change in shear displacement. The relative shear displacements at both points appear to stabilize at these values [approximately 0.040 in. (1.02 mm)] throughout the remaining earthquake motion.

2.2.2 Field Site Investigation: Effect of Mine Seismicity on Groundwater

2.2.2.1 Background

Field data on the nature and magnitude of groundwater response generated by mining-induced small-magnitude earthquakes were obtained and analyzed. The field studies were conducted during January 1991 through December 1992 at the Lucky Friday Mine, a silver mine located in Precambrian metasediments of the Couer d'Alene Mining District of Idaho. This mine experiences frequent seismic activity as a result of rockbursts and slippage on steeply dipping beddings and joints. Fluid flow in the rock mass is controlled by a series of fracture zones associated with major faults or mineralized veins. The water pressure in sections of four such fracture zones below the water

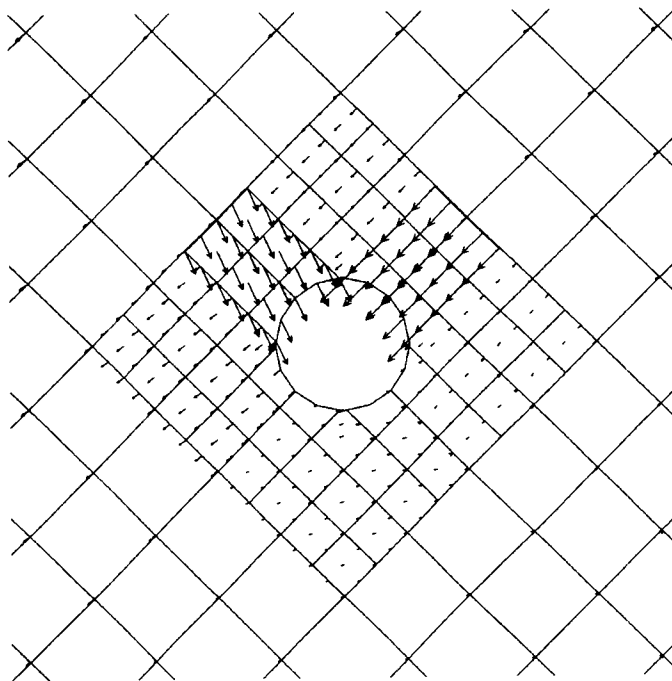


Figure 2-5. Displacement field around the tunnel after 4 sec of dynamic loading

table was monitored during the 24-mo period. The magnitude, source location, and associated ground motion of seismic events at the mine were also monitored during that period.

Water-pressure monitoring was conducted using vibrating wire piezometers installed in a 1,180-ft (360-m) long inclined borehole drilled from the 5,700-level station of the mine. The piezometers were installed in four fracture zones, which were isolated using straddle packers. Mining-induced seismicity was monitored using an existing seismic instrumentation network installed by the U.S. Bureau of Mines, augmented by additional instrumentation installed specifically for the project by the Center for Nuclear Waste Regulatory Analyses (CNWRA).

The hydrologic effects of earthquakes are related to changes in the hydraulic conductivity and storage capacity of rocks, which result from rock deformations caused by stress changes associated with the earthquake. The effects include changes in groundwater pressure and discharge rate through springs, wells, and streams. They can be classified into two general categories: (i) short-term effects (on the order of hours), which are believed to be caused by

changes induced directly by the seismic waves (generally, short-term effects build up and dissipate rapidly); and (ii) long-term effects (on the order of months or years) which develop more slowly and persist for a longer time following the earthquake. Long-term effects are believed to be caused by changes in tectonic stress that occur prior to and after the earthquake. Both of these modes of earthquake-induced hydrologic changes ought to be considered in numerical modeling and field measurement of the phenomena.

Numerical models that are based on a direct application of seismic energy to the model boundaries will predict mainly the short-term effects, unless the seismic waves are strong enough to cause permanent changes in permeability, in which case some long-term effects may also be predicted. On the other hand, those effects that account for both the release of seismic energy and the preceding and consequent stress changes may predict both long- and short-term effects. Similarly, the type of earthquake-induced hydrologic response observed through field measurements depends on the frequency and duration of measurement. Because the short-term response lasts only for a short duration of time (e.g., 1 hr) following the earthquake, it is best

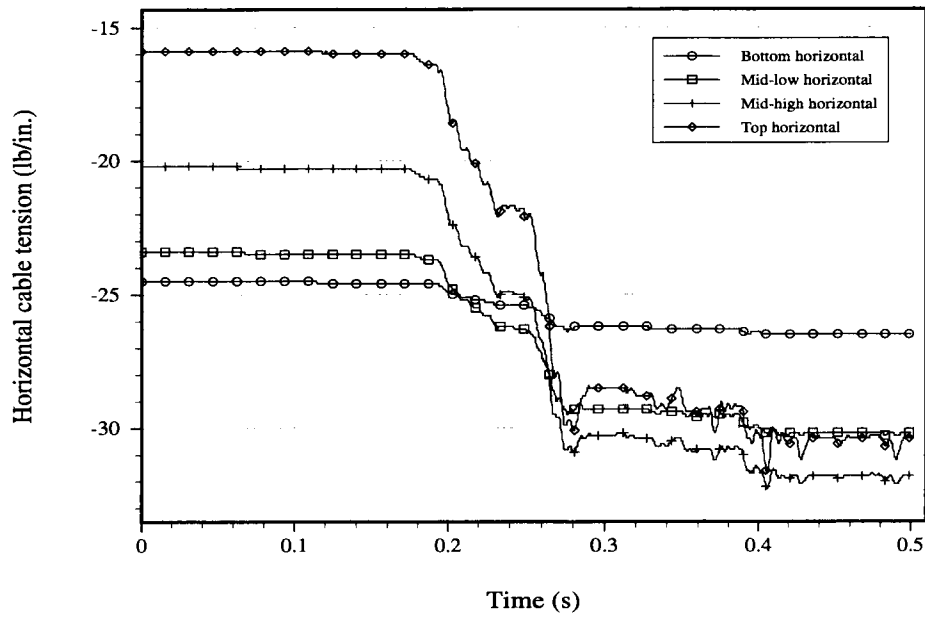


Figure 2-6. Horizontal cable tensions after 0.5 s of dynamic loading

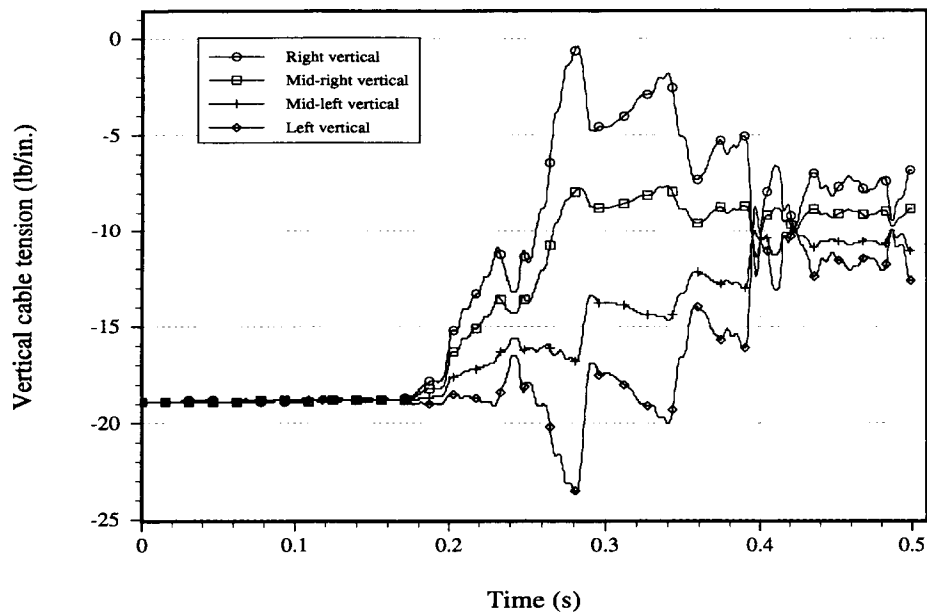


Figure 2-7. Vertical cable tensions after 0.5 s of dynamic loading

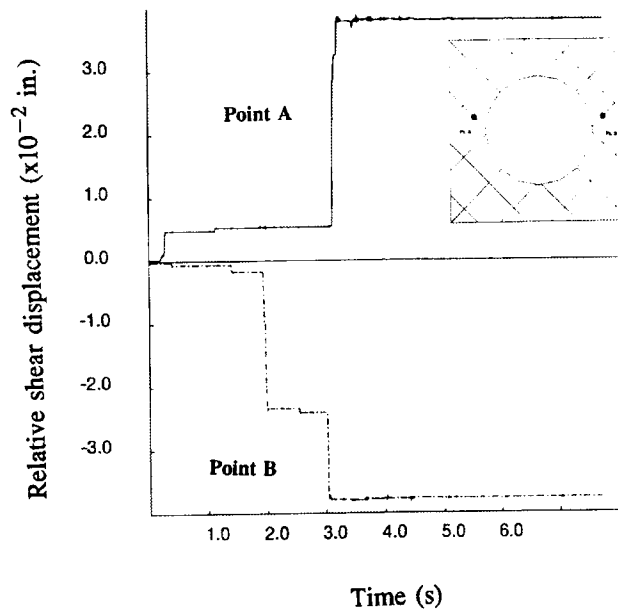


Figure 2-8. Relative shear displacement along two joints intersecting the tunnel (i.e., Points A and B)

observed through frequent (e.g., minute-by-minute) sampling. On the other hand, because the long-term response develops at almost the same rate as the ambient hydrologic changes, it is necessary to collect data over several years in order to separate the earthquake-induced response from the ambient response resulting from such processes as diurnal and barometric pressure fluctuation and mine dewatering.

2.2.2.2 Observed Seismo-Hydrologic Response at Lucky Friday Mine

The Lucky Friday Mine hydrologic pressure measurements were made over a 24-mo period, during which time the hydrologic response included the normal seasonal variations, mining-induced watertable drawdown, and the earthquake-induced changes. The data collected were not sufficient to permit the separation of possible earthquake-induced long-term effects from the ambient response (due to normal seasonal variation and mining-induced watertable drawdown). On the other hand, the data were sampled frequently enough to permit recognition of several episodes of earthquake-induced short-term effects.

More than 50 seismic events of Richter magnitude 1.0 or larger occurred during the monitoring period, the largest event being of magnitude 3.5. The majority of the events were of magnitude 2.5 or less. Most of the events caused the groundwater pressure to increase, but some caused it to decrease. Most of the observed hydrologic changes were of the short-term category, developing rapidly, almost at the same time as the causal seismic event, and dissipating within 24 hr thereafter. Some of the observed changes display the characteristics of long-term effects although it was not possible to determine that seismicity was the cause.

Figure 2-9 shows the groundwater pressure history observed for the Zone 3 piezometer, for September 18 through 20, 1991. An event of magnitude 3.5 on the Richter scale occurred at 0920 hr on September 19, 1991. As the figure shows, an increase in groundwater pressure occurred (almost instantaneously) at about the time of the event. The increase dissipated completely within 24 hr; more than half the increase dissipated during the first 3 hr following the event. The groundwater pressure history shown in this plot displays the typical characteristics of short-term seismic effects (i.e., rapid build-up and dissipation).

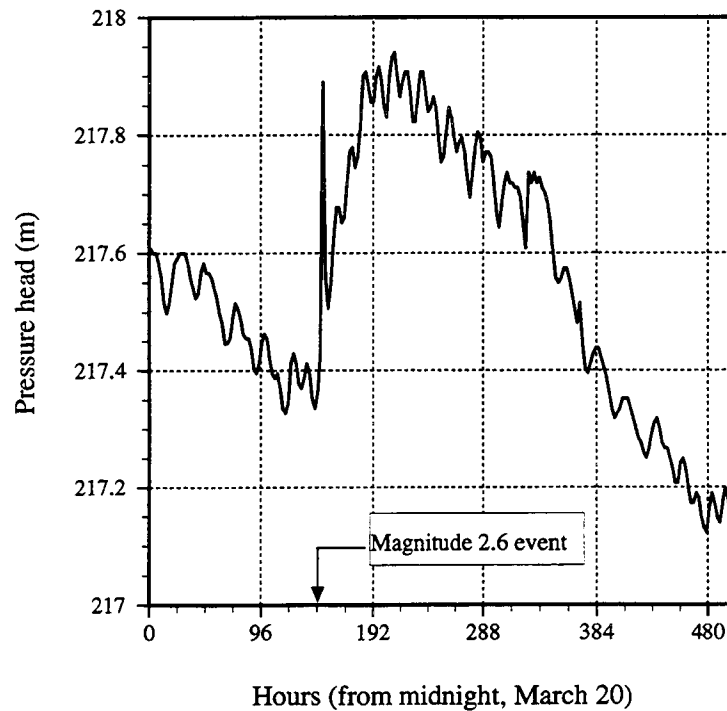


Figure 2-9. Groundwater pressure history observed with Zone 3 piezometer, September 18 through 20, 1991

The next example, shown in Figure 2-10, displays the characteristics of combined short- and long-term seismic effects, with the long-term effects probably dominant. The groundwater pressure history in the figure, which was observed with the Zone 3 piezometer, is associated with a magnitude 2.6 seismic event which occurred at 0458 hr on March 27, 1991. The figure shows an increase in groundwater pressure, with a build-up time of about 3 d and dissipation time of about 9 d. The increase in groundwater pressure shown in the figure is attributed to the seismic event because it was superimposed on a general trend of decreasing groundwater pressure. This superimposition implies that it was caused by an event with hydrologic consequences counter to the ambient hydrologic trend.

2.2.2.3 Data Analysis and Conclusions

An examination of the data obtained in this study showed that, in general, the groundwater pressure change increased as the earthquake magnitude increased; for a given earthquake magnitude, the groundwater pressure change decreased as the distance of the observation point from the earthquake source increased. An attempt to model this relationship

statistically was not successful: the majority of the data obtained were for earthquakes of magnitude 2.5 or smaller, and the regression model obtained could predict the effect of such earthquakes much better than that of larger magnitude earthquakes. Detailed treatment of the statistical analysis is provided in a separate report (Ofogebu et al., 1994). Pressure predicted for the larger-magnitude earthquakes using the model is consistently smaller than the measured change. This suggests that a statistical model such as this, which was derived mainly from small-magnitude earthquake data, would not be appropriate for predicting the groundwater pressure effects of larger-magnitude earthquakes.

The effect of earthquakes on groundwater flow should probably be evaluated through mechanistic modeling instead of the statistical modeling approach discussed above. The mechanical processes and material behavior that would need to be incorporated in the mechanistic model should be examined. An improved formulation of some of the processes and material behavior will need to be developed, and possibly incorporated in an existing numerical code, in order to develop the analytical capabilities required for the mechanistic modeling.

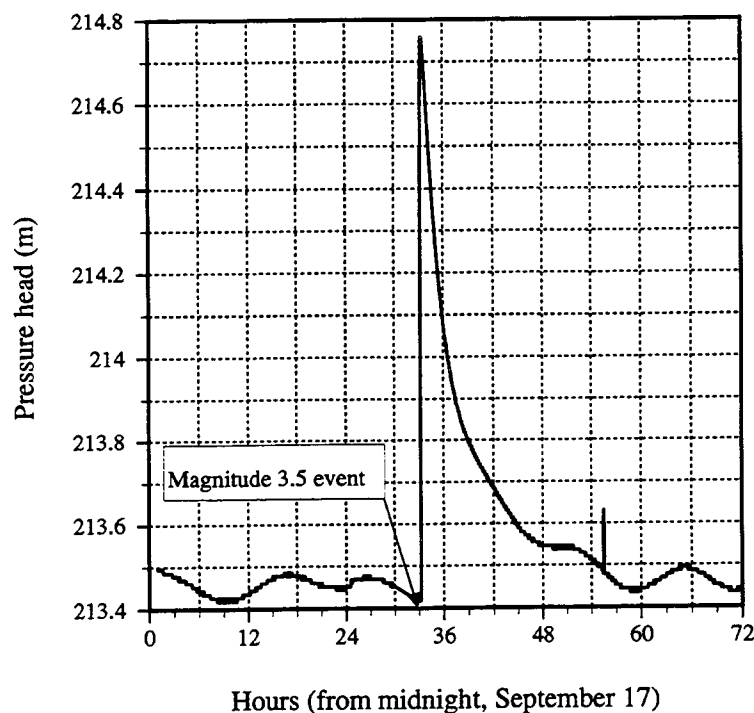


Figure 2-10. Groundwater pressure history observed for Zone 3 piezometer, March 21 through April 10, 1991

2.2.3 Thermal-Mechanical-Hydrological Coupled Modeling (DECOVALEX)

The purpose of this research activity is to increase the understanding of TMH processes for rock mass stability and radionuclide release and transport from a geologic repository through NRC/CNWRA participation in an international project called DECOVALEX. DECOVALEX was organized by the Swedish Nuclear Power Inspectorate (SKI) to increase the understanding of coupled TMH processes applied to the underground disposal and isolation of HLW. Eleven funding organizations are currently involved, each supporting one or more research teams. In the DECOVALEX project, modeling is being used to develop and design validation tests of TMH-coupled processes. DECOVALEX is expected to lead to the development and validation of coupled TMH models that are believed to be important to the licensing of a HLW repository.

The final report for Phase II of DECOVALEX is currently being finalized and will be published as an SKI Technical Report. This Phase II report will present detailed comparison of results among the various research teams, including the CNWRA, for one

benchmark test (BMT) and one Test Case (TC) problem. These study problems for Phase II were the Near-Field Repository Model (BMT3) and the revised Coupled Stress-Flow Model (TC1).

2.2.3.1 DECOVALEX Phase III Experimental and Modeling Studies

The experimental and modeling work for Phase III of DECOVALEX is continuing. The results of DECOVALEX Phases I and II were reported elsewhere (Ahola et al., 1992 and 1993). Of the five TC problems proposed for Phase III, the CNWRA has proposed one, namely, the Direct Shear-Flow Test (TC5). In addition to conducting the experiment, the CNWRA team will use the computer code ABAQUS to model the TC5 experiment. Also, the CNWRA team will use ABAQUS to model the Big-Ben Experiment (TC3) as proposed by the Japanese group. ABAQUS results from modeling the Big-Ben Experiment will be presented during the next reporting period. The following sections briefly summarize the experimental and modeling work conducted to date for TC5.

2.2.3.2 Direct Shear-Flow Test (TC5)

The coupled TMH experimental research has been organized to progress from simple to the more complex activities. In FY93, the experimental program was initiated with the study of the mechanical-hydrological (MH) coupling effects of single-jointed specimens. For this experiment, tests were conducted on single-jointed welded tuff specimens collected from Apache Leap, Arizona. These specimens, consisting of upper and lower blocks, have 8×8 in. (20.32×20.32 cm) of joint surface area, with the lower block having a dimension of 8×12 in. (20.32×30.48 cm). This experiment was designed to study the effects of mechanical loading on fluid flow patterns and the joint hydraulic conductivities.

This coupled MH experiment was designed to make maximum utilization of the existing equipment. The existing direct shear test apparatus has both pseudostatic and dynamic shear testing capabilities. This apparatus is capable of applying mechanical loads of up to 8-MPa normal and up to 7.5-MPa shear. Measurements of normal joint displacement at four locations around the joint and relative shear displacement at two locations were obtained.

An apparatus was designed originally to promote radial flow of fluid injected into a joint through a vertical hole at the top block. The fluid was collected as it exited from the joints. A flowmeter was attached to the inlet line in order to maintain a constant liquid flow rate. A manometer was used to monitor the fluid pressure at the injection point within the joint, and to record any changes in pressure at various normal loading conditions. Flow rates were varied between 0.5 and 400 mL/min. In order to measure the fluid outflow from the joint surface, troughs were made in the grout, below the surface of the joint, along all four sides of the bottom block. The troughs were partitioned and tubing attached such that outflow from each side was collected and measured separately. The outflow measurements were designed to determine how the flow changed through various preferential channels as a function of normal stress and inlet flow rate.

These experiments confirmed observations of other investigators that the fluid flow takes place along preferential channels from the injection point to the edges of the block where it exits the joint. Such preferential flow is believed to be due to factors such as low fluid injection rate, sloping fracture surface in the

natural joints, and spatial distribution of aperture widths. The concept of hydraulic conductivity based on Darcy's law is dependent upon the assumption of laminar flow, which requires low water injection rates. Low fluid rates resulted in low-pressure gradients, which were more difficult to measure. It was therefore necessary to conduct the experiments at higher pressure gradients. To be able to conduct experiments at high-flow rates and thus a high-pressure gradient and to maintain laminar flow, higher viscosity fluids such as a water and glycerol mixture were required. It may be pointed out that joint permeability can be calculated from hydraulic conductivity by taking into consideration the viscosity of the fluid. In spite of a 30-fold increase in water viscosity due to the addition of glycerol, the whole joint face could not be completely saturated. The details of the findings will be reported in a DECOVALEX letter report.

The determination of saturated and unsaturated conductivity values from the radial flow experiments requires that the effective external hydraulic radius be known. The hydraulic radius could trivially be obtained in the absence of channel flow, but when channel flow is predominant, no standard technique is available to determine the external hydraulic radius. As noted above, the preferential channel flow can be partly attributed to small injection rates which are necessary to keep the fluid velocity low at the injection port. Since the channeling effect could not be eliminated by using higher viscosity fluids, it was necessary to implement a linear flow method so that, for the same injection rate, a large cross-sectional area would be available, thereby maintaining the lower velocity. It must be emphasized here that the main motivation for using a radial flow geometry was to conduct the flow experiments with the minimum possible modifications to the existing direct shear test apparatus.

For the linear hydrologic flow method to be applicable, the apparatus was modified to provide seals to confine the flow to one direction. The faces parallel to the overall flow direction were sealed. Special modifications were necessary for the grouted faces. The fluid was injected across one entire cross-section using a positive displacement pump, and the fluid produced from the entire cross-section of the opposite end was collected. In order to distribute fluid uniformly across the inlet end of the specimen, a manifold consisting of a stainless steel tubing with holes 0.2 in. (0.5 cm) apart was used. All the holes were aligned and pointed toward

the fracture face. The tubing was split into two halves, and one half was laid against the fracture at the outlet end. This splitting was to ensure that the fluid would be collected from across the outlet end of the fracture. The split tube was attached to flexible tubing through which the fluid drained out. The pressure drop across the specimen was measured by using a pressure transducer. In order to determine air permeability, experiments were conducted using N_2 when the specimen was completely dry. N_2 was used instead of air because dry N_2 was more readily available. N_2 was injected at a constant rate from a high-pressure supply tank. The flow rate was controlled with a pressure regulator. The pressure drop at the inlet end was measured with a U-tube manometer, and the N_2 flow rate was measured with rotameters and digital bubble flowmeters. A typical relationship between the N_2 flow rate and the pressure drop before and after correcting for tubing pressure drop is presented in Figure 2-11. The q - ΔP for N_2 seems to have a better cubic fit than a quadratic fit.

In order to conduct fully water-saturated experiments, the rock specimen was evacuated down to 29.3 in. (74.2 cm) Hg and was saturated with water. The system was left under positive pressure head for about 3 d to reach pressure equilibrium. After steady state was established, the pressure drop across the system was read from a differential pressure transducer. The measurements were taken at various flow rates. The relationship between flow rates and steady-state pressure drops is presented in Figure 2-12. This figure indicates a substantial hysteresis between the pressure drop curve for increasing flow rate and that for decreasing flow rate. This hysteresis is considered not acceptable. Some corrective measures were taken, notably eliminating air in tubing connecting the specimen assembly to the transducer. The readings were improved as demonstrated in Figure 2-13.

The q - ΔP for fully saturated waterflow experiment shows a quadratic fit (Figure 2-14). Once the method for measuring steady state was deemed correct, steady-state flow experiments were conducted at various normal loads. A flow rate of $4 \text{ cm}^3/\text{min}$ was chosen on the basis of Reynold's number requirement and was kept fixed at all normal loads. At each normal load, steady state was reached before ΔP readings were taken. A typical variation in the pressure drop and hence hydraulic conductivity with the cycle of normal load is presented in Figure 2-15.

The experiment was impaired by leaks, transducer malfunctions for water-saturated experiments, breakdown of a cylinder switching valve, and a failure of the piston movement to synchronize with the driving motor. Difficulties were also experienced in the airflow measurements at both high and low flow rates. At low flow rates, the bubble flowmeter was affected by the interfacial tension at the glass wall; at high flow rates, creation of multiple bubbles forced the experiment to be repeated several times. While these difficulties dictated many repetitions of the same experiment, only those datasets that were devoid of influences were deemed acceptable.

Work is in progress to test the repeatability of the normal load experiment. Preparation is also continuing to study the pressure drop at a steady-flow rate under shear load conditions at various normal loads. The data presented in the figures are currently under analysis to extract saturated hydraulic conductivity and thus the effective joint aperture.

Since conducting experiments with more than a limited number of samples is prohibitively expensive, a mathematical/computer model is often needed to predict the hydraulic conductivity from the joint surface properties and to develop or identify scaling parameters. An effort is proceeding to correlate the joint roughness to flow channeling and joint permeability. The roughnesses of the rock joint surfaces have been characterized by using a laser profilometer. Since the top and bottom rocks are of different sizes, and profiling is done separately for the top and bottom joint surfaces, their profiles must be appropriately matched in order to determine the aperture data. A numerical matching exercise was conducted by moving the upper block on the lower block, which was held fixed. The movement was mostly translational, and there is evidence that rotational movement is necessary to obtain closer matching. The mathematical minima in the sum of the square differences in the surface heights resulted in aperture values on the order of 5–10 mm at some locations. The aperture data calculated to date using this matching approach have been unacceptable even after the use of a numerical technique to obtain the best match. A better technique must be developed to estimate apertures more accurately.

Preliminary modeling of the TC5 experiment using ABAQUS was initiated during this reporting period. A 2D model of the rock block assemblage containing the single natural fracture was generated and

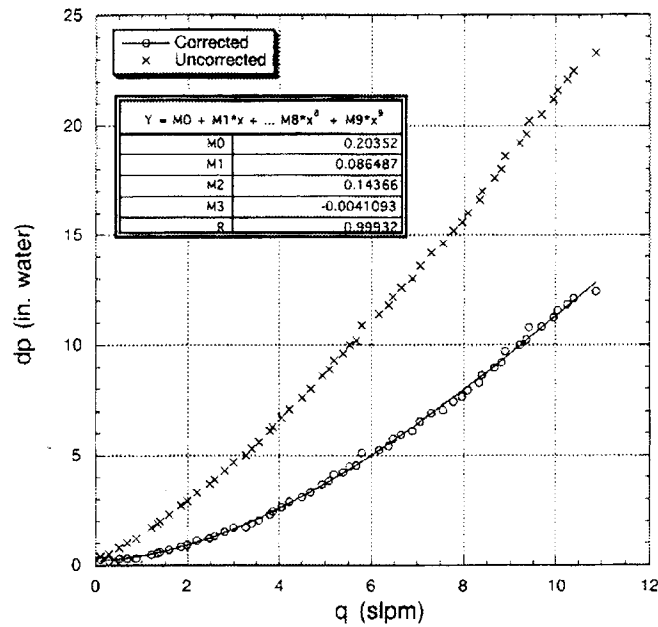


Figure 2-11. Relationship between steady-state pressure drop and flow rate in the nitrogen flow experiment using apparatus i. Cubic data fit. Corrected data account for the pressure drops in the tubings.

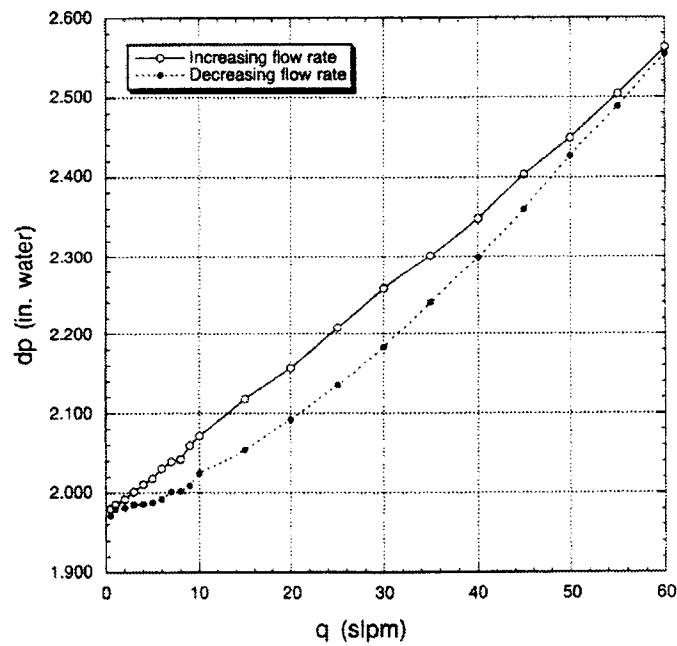


Figure 2-12. Faulty transducer reading mimics hysteretic effect

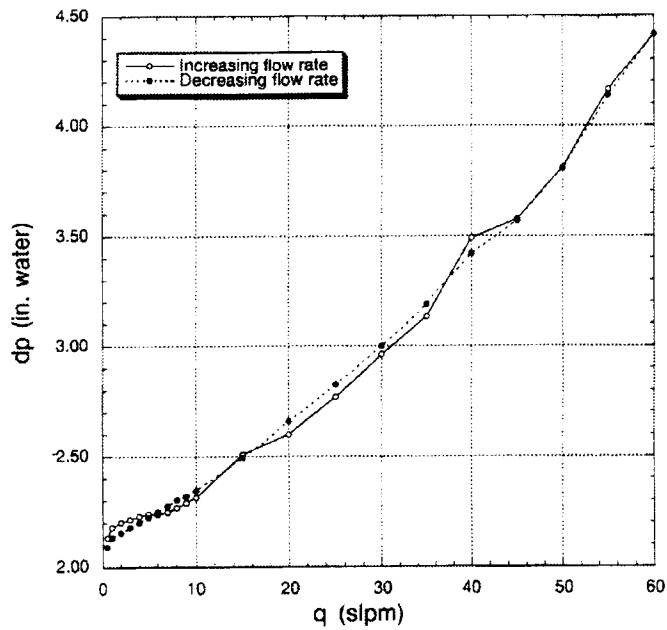


Figure 2-13. Repeatability of the pressure measurements after correction while going sequentially up and down the flow rate

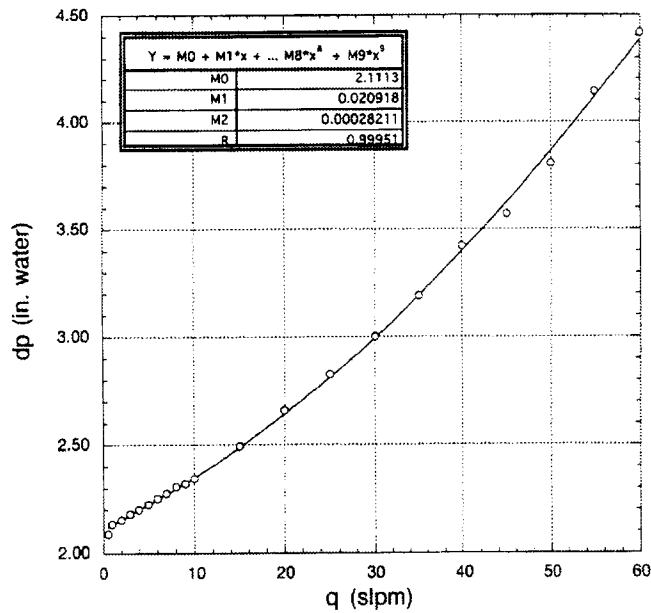


Figure 2-14. Fully saturated water flow experiment using apparatus ii. Quadratic data fit (data: Mdata 5/5/94)

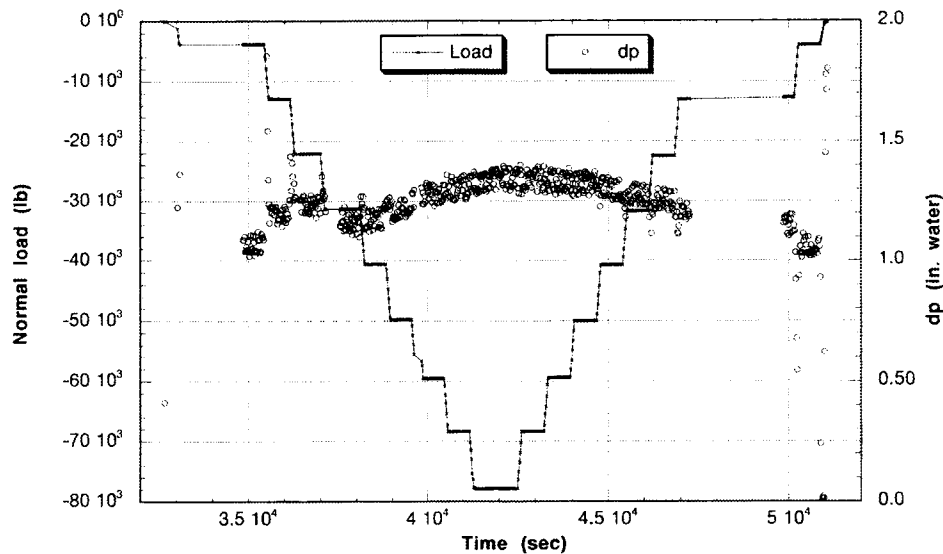


Figure 2-15. Time history of imposed normal load and corresponding pressure drop across the fully saturated fracture

is shown in Figure 2-16. For simplicity, the experimental loading frame was left out of the model. The joint surface irregularity was simulated in the 2D ABAQUS model as shown in Figure 2-16. At the time of the analysis, the initial aperture distribution for the joint to be determined from joint profile measurements was not available. As a result, an average initial aperture value was experimentally determined from the results of the saturated flow tests and is approximately 0.8 mm. Thus for the preliminary modeling analysis, the upper block was shifted vertically upward by this amount. Since, in the model, apertures along the joint are measured perpendicular to the local position along the joint, a variation in aperture distribution along the joint was incorporated into the model.

The main purpose of this preliminary ABAQUS analysis was to determine a better approach for simulating highly nonlinear joint closure deformation and fluid flow through joints. The main problem with ABAQUS, which uses interface or gap elements for simulating the hydromechanical response of a joint in 2D, is that as soon as any contact is made between any two upper and lower nodes along the joint, the flow through the joint is automatically set to zero. In

order to overcome this problem, a softened contact option was used in conjunction with the gap elements in which a value for the joint clearance (aperture) is given at which the contact pressure is zero. In addition, a value for the contact pressure is given at which the joint clearance is zero. Setting this contact pressure very high results in the joint never fully closing, such that fluid flow through the joint is still allowed. Also, the functional relationship in ABAQUS between the contact pressure and joint clearance or aperture is exponential. This relationship allows the model to simulate the nonlinear joint normal response observed in actual tests. Figure 2-17 shows such a nonlinear joint response as predicted by ABAQUS for the model shown in Figure 2-16 under increasing normal load.

The next step of the modeling will be to determine how ABAQUS can handle the nonlinear shear response along the joint. During the next reporting period, comparisons will be made between the ABAQUS results and those obtained from the experiment for both the mechanical response of the joint under normal and shear loading, as well as the hydrologic response assuming fully saturated joint conditions.

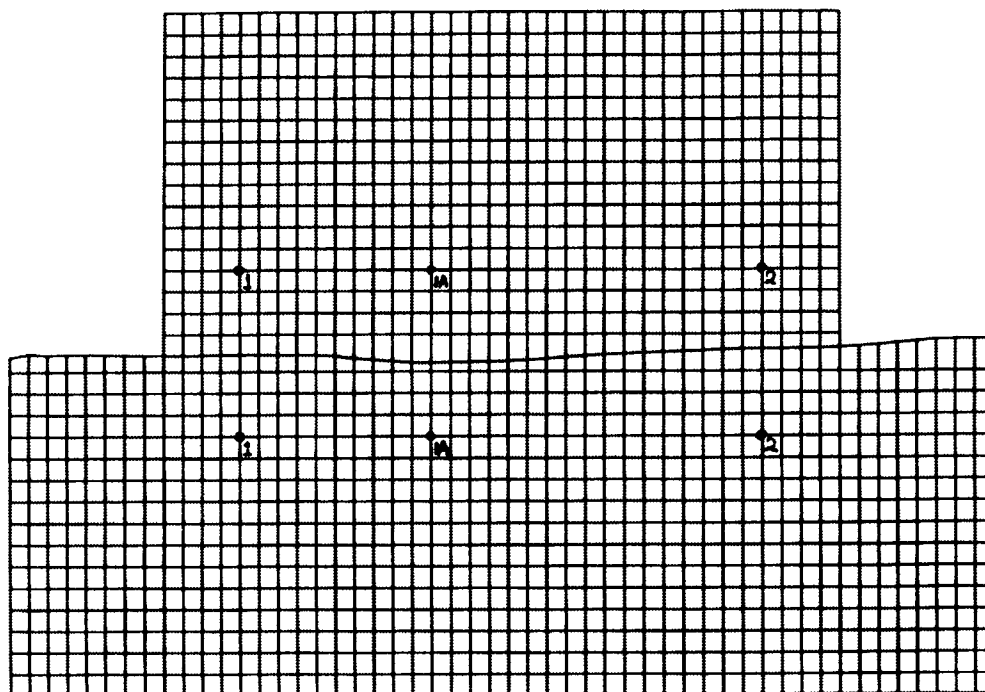


Figure 2-16. Initial ABAQUS model of TC5 experiment

2.3 ASSESSMENT OF PROGRESS TOWARD MEETING PROJECT OBJECTIVES

The primary objective of the Seismic Rock Mechanics Research Project is to identify seismic-related key technical issues that will affect repository design and performance and to develop techniques that could be used to predict the response of near-field jointed rock mass at the proposed HLW repository at YM, Nevada, when it is subjected to repetitive seismic (including earthquakes and nuclear testing at the Nevada Test Site) and thermal loads. This objective is being accomplished through laboratory and field experiments as well as computer modeling studies. Several seismic-related issues have been addressed. For instance, it has been determined through field experimental studies that repetitive, lower-magnitude seismic events can cause greater damage to underground tunnels than a single large-magnitude event, due to the cumulative effects of joint slip around the tunnels. Such cumulative effects will again be demonstrated through the small-scale experiments of a

rock mass. Most designs today consider only the maximum credible seismic event. The cumulative effect results have been presented to the Nuclear Waste Technical Review Board (NWTRB), and the NWTRB has incorporated these findings in its annual report as guidance for the U.S. Department of Energy (DOE) to consider in its ESF and repository design (Nuclear Waste Technical Review Board, 1992). The findings on the effect of repetitive seismic events have also directly supported the development of the Compliance Determination Method (CDM) for shafts and ramps design, specifically with regard to establishing review method steps for assessing protection against natural phenomena and environmental conditions [10 CFR 60.131(b)(1)]. These findings will be used further to support the development of the CDM for RRT 4.4 Assessment of Compliance with Design Criteria for Underground Facility; 5.3 Assessment of Compliance with the Design Criteria for the Postclosure Features of the Underground Facility; 5.4 Assessment of Compliance with the EBS Performance Objectives; and 6.1 Assessment of Compliance with the Requirement for Cumulative Releases of Radioactive Materials. Also,

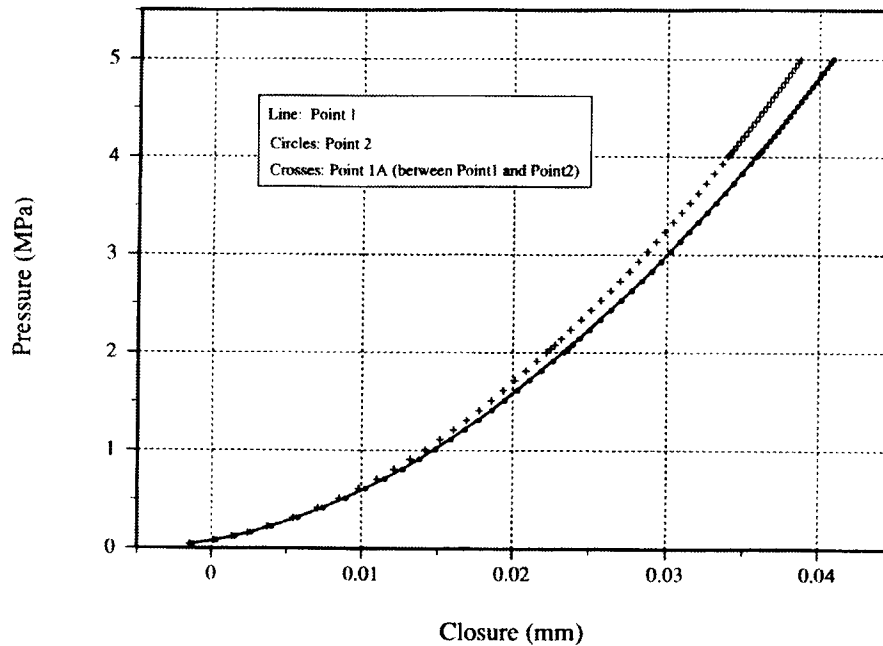


Figure 2-17. ABAQUS results for closure versus normal stress response between monitoring points

based on the field experiments performed at the Lucky Friday Mine, Mullan, Idaho (Task 5), both the magnitude and duration of water pressure changes due to seismic events were observed to be small (Hsiung et al., 1993f). These results would tend to indicate that significant changes in the water pressure below the proposed repository site due to seismic events of large magnitude may not be credible.

Through laboratory experiments and modeling studies, it has been found that the rock-joint models presently incorporated in the computer codes under consideration for use in seismic design in jointed rock masses do not correctly simulate anticipated cyclic pseudostatic and dynamic rock-joint behavior. Through identification of these problems and subsequent enhancement of the rock-joint models, the staff will be better able to review the DOE repository seismic design and to support the assessment of repository performance. In addition, several of the design-related CDMs have KTUs related to the impact of repetitive seismic motion on long-term performance of seals. Furthermore, observed deficiencies in the rock-joint model will be used as a basis for developing acceptance criteria in the CDMs relevant to design review of subsurface facilities. A verified code for seismic

analysis will increase the staff capabilities of performing independent detailed safety reviews regarding these issues.

The objective of DECOVALEX (Task 9) TMH modeling and coupled experiments is to address KTUs related to the impact of coupled TMH processes on repository design and performance. These activities are to evaluate methodologies including model validation and code verification for coupled TMH modeling of jointed rocks. The work being done in this task supports development by the technical assistance program of a compliance determination code for simulating coupled processes. This code will be used by the NRC and the CNWRA for determination of DOE compliance with NRC regulations on thermal and repetitive seismic loads. The results of seismic research have also been used for Site Characterization Plan reviews and are currently being used for ESF Title II Design reviews.

2.4 PLANS FOR NEXT REPORTING PERIOD

Dynamic scale model experiments on a jointed rock mass and the analysis of the results of these experiments will be performed during the next reporting

period. These experiments will provide a better understanding of jointed rock mass behavior subjected to repeated earthquake loads and will generate a complete data set for code verification. Work on DECOVALEX Phase III modeling and the MH experiments will continue. Other work will include preparation of the Report for Groundwater Hydrology Field Studies and the Final Project Report for the Seismic Rock Mechanics Research Project. These reports will document the results obtained from the Seismic Rock Mechanics Research Project and make recommendations on the use of these results.

2.5 REFERENCES

- Ahola, M.P., S.M. Hsiung, L.J. Lorig, and A.H. Chowdhury. 1992. *Thermo-Hydro-Mechanical-Coupled Modeling: Multiple Fracture Model BMT2, Coupled Stress-Flow Model TC1, DECOVALEX—Phase I*. CNWRA 92-005. San Antonio, TX: Center for Nuclear Waste Regulatory Analyses.
- Ahola, M.P., L.J. Lorig, A.H. Chowdhury, and S.M. Hsiung. 1993. *Thermo-Hydro-Mechanical Coupled Modeling: Near-Field Repository Model, BMT3, DECOVALEX—Phase II*. CNWRA 93-002. San Antonio, TX: Center for Nuclear Waste Regulatory Analyses.
- Brady, B.H.G., S.M. Hsiung, and A.H. Chowdhury. 1990. *Qualification Studies on the Distinct Element Code UDEC Against Some Benchmark Analytical Problems*. CNWRA 90-004. San Antonio, TX: Center for Nuclear Waste Regulatory Analyses.
- Brandshaug, T., B. Dasgupta, B.H.G. Brady, S.M. Hsiung, and A.H. Chowdhury. 1990. *Qualification Studies on the Finite Element Code HONDO II Against Some Benchmark Analytical Problems*. CNWRA 90-006. San Antonio, TX: Center for Nuclear Waste Regulatory Analyses.
- Fumagalli, E. 1968. *Model Simulation of Rock Mechanics Problems*. Rock Mechanics in Engineering Practice. K.G. Stagg and O.C. Zienkiewicz, eds. John Wiley & Sons. New York, NY: 353-384.
- Hsiung, S.M., and A.H. Chowdhury. 1991. *Report on Research Activities for Calendar Year 1990*. W.C. Patrick, ed. NUREG/CR-5817. Washington, DC: Nuclear Regulatory Commission.
- Hsiung, S.M., and A.H. Chowdhury. 1993. *NRC High-Level Radioactive Waste Research at CNWRA For Calendar Year 1991*. W.C. Patrick, ed. NUREG/CR-5817. Washington, DC: Nuclear Regulatory Commission.
- Hsiung, S.M., A.H. Chowdhury, W. Blake, M.P. Ahola, and A. Ghosh. 1992. *Field Site Investigation: Effect of Mine Seismicity on a Jointed Rock Mass*. CNWRA 92-012. San Antonio, TX: Center for Nuclear Waste Regulatory Analyses.
- Hsiung, S.M., M.P. Ahola, and A.H. Chowdhury. 1993a. *NRC High-Level Radioactive Waste Research at CNWRA January-June 1992*. W.C. Patrick, ed. NUREG/CR-5817. CNWRA 92-01S. Washington, DC: Nuclear Regulatory Commission.
- Hsiung, S.M., M.P. Ahola, A. Ghosh, and A.H. Chowdhury. 1993b. *NRC High-Level Radioactive Waste Research at CNWRA July-December 1992*. B. Sagar, ed. NUREG/CR-5817. CNWRA 92-02S. Washington, DC: Nuclear Regulatory Commission.
- Hsiung, S.M., M.P. Ahola, A. Ghosh, and A.H. Chowdhury. 1993c. *NRC High-Level Radioactive Waste Research at CNWRA January-June 1993*. B. Sagar, ed. CNWRA 93-01S. San Antonio, TX: Center for Nuclear Waste Regulatory Analyses.
- Hsiung, S.M., D.D. Kana, M.P. Ahola, A.H. Chowdhury, and A. Ghosh. 1993d. *Laboratory Characterization of Rock-Joints*. CNWRA 93-013. San Antonio, TX: Center for Nuclear Waste Regulatory Analyses.
- Hsiung, S.M., A. Ghosh, A.H. Chowdhury, and M.P. Ahola. 1993e. *Evaluation of Rock-Joint Models and Computer Code UDEC Against Experimental Results*. CNWRA 93-024. San Antonio, TX: Center for Nuclear Waste Regulatory Analyses.

- Hsiung, S.M., A.H. Chowdhury, W. Blake, and J. Philip. 1993f. Field investigation of mining-induced seismicity on local geohydrology. *Proceedings of the Fourth Annual International Conference on High-Level Radioactive Waste Management*. La Grange Park, IL: America Nuclear Society: 913-920.
- Hsiung, S.M., M.P. Ahola, A. Ghosh, and A.H. Chowdhury. 1994. *NRC High-Level Radioactive Research at CNWRA July-December 1993*. B. Sagar, Ed. CNWRA 93-02S. San Antonio, TX: Center for Nuclear Waste Regulatory Analyses.
- Kana, D.D., D.C. Scheidt, B.H.G. Brady, A.H. Chowdhury, S.M. Hsiung, and B.W. Vanzant. 1990. *Development of Rock-Joint Dynamic Shear Test Apparatus*. CNWRA 90-005. San Antonio, TX: Center for Nuclear Waste Regulatory Analyses.
- Kana, D.D., B.H.G. Brady, B.W. Vanzant, and P.K. Nair. 1991. *Critical Assessment of Seismic and Geomechanics Literature Related to a High-Level Nuclear Waste Underground Repository*. NUREG/CR-5440. Washington, DC: Nuclear Waste Regulatory Commission.
- Nuclear Waste Technical Review Board. 1992. *Fifth Report of the U.S. Congress and the U.S. Secretary of Energy*. Washington, DC: Nuclear Waste Regulatory Commission.
- Ofoegbu, G.I., S.M. Hsiung, A.H. Chowdhury, and J. Philip. 1994. *Field Site Investigation: Effect of Mine Seismicity on Groundwater Hydrology*. CNWRA 94-017. San Antonio, TX: Center for Nuclear Waste Regulatory Analyses.

3 INTEGRATED WASTE PACKAGE EXPERIMENTS

by Gustavo A. Cragnolino, Darrell S. Dunn, and Narasi Sridhar

Investigators: Gustavo A. Cragnolino, Darrell S. Dunn, and Narasi Sridhar (CNWRA)

NRC Project Officer: Michael B. McNeil

3.1 OVERALL TECHNICAL OBJECTIVES

The overall technical objectives of the Integrated Waste Package Experiments (IWPE) Project are to:

- (i) Conduct waste package experiments to scope and study the key parameters affecting long-term material performance
- (ii) Assess waste package materials and designs selected by the U.S. Department of Energy (DOE) and provide independent evaluation for reasonable assurance of long-term performance
- (iii) Support the Office of Nuclear Regulatory Research (RES) in addressing the needs of the Division of Waste Management (DWM)
- (ii) The prediction of environmental effects on the performance of waste packages and the EBS
- (iii) The prediction of release path parameters such as size, shape, and distribution of penetrations of waste packages due to thermomechanical, environmental, or criticality effects
- (iv) The prediction of thermomechanical effects on the performance of waste packages

To address these objectives, the IWPE program is divided into six tasks: Task 1—Corrosion; Task 2—Stress corrosion cracking (SCC); Task 3—Material stability; Task 4—Microbiologically influenced corrosion; Task 5—Other degradation modes; and Task 6—General reporting.

Several Key Technical Uncertainties (KTUs) developed as part of the compliance determination strategy (CDS) related to waste package performance and listed in the License Application Review Plan (LARP), Sections 5.2 Design Criteria for the Waste Package and its Components and 5.4 EBS Performance Objective (License Application Review Plan, 1992), are addressed in the IWPE program. These are:

- (i) The extrapolation of short-term laboratory and prototype test results to predict long-term performance of waste packages and engineered barrier systems (EBSs)

Results generated within the IWPE program are being used to provide input parameters to waste package performance assessment (PA) models (Cragnolino et al., 1994), as well as to verify the model assumptions and predictions. A key area of integration between the IWPE, thermohydrology, and geochemistry projects is in the prediction of environmental evolution very near the waste packages. The fundamental assumption in the waste package corrosion studies reported here is the presence of an aqueous environment, at least episodically. This is a conservative assumption, because the corrosion rate in a dry-steam or dry-air environment at anticipated repository temperatures is negligible (Farmer et al., 1991). However, the aqueous environment near the container can have a wide range of compositions. The experimental research and modeling efforts within the thermohydrology and geochemistry projects will assist evaluations of the presence and chemistry of aqueous

environments near the waste package. The results of the IWPE Project will identify the environmental factors of importance to waste package performance and, thus, guide the investigations of rock-water interactions in the geochemistry projects. Another aspect of the near-field environment is the effect of corrosion of containers/waste forms on the environment chemistry. This is especially important in occluded regions, such as crevices between the container and the rock.

3.2 SIGNIFICANT TECHNICAL ACCOMPLISHMENTS

3.2.1 Background

In the United States geologic disposal program, two types of waste package emplacement concepts are being considered: (i) vertical emplacement of a single-wall or double-wall container in a borehole with an air gap between the container and the borehole, and (ii) horizontal emplacement of a multiple-wall container surrounded by a suitable backfill in the drifts of the underground repository. The vertical emplacement of a thin (e.g., 12-mm thick), single-wall container made of an austenitic alloy was the reference design for the DOE site characterization plan (U.S. DOE, 1988). Over the last year or so, the horizontal drift emplacement of a double-wall container has received greater attention (Doering, 1993). A multipurpose canister (MPC) concept has evolved as the baseline design (Sridhar et al., 1994b) for handling spent fuel from a reactor site through intermediate storage and eventually to the disposal facility. The MPC is proposed to be contained in disposal overpacks. Because of the size of the proposed waste package design, drift emplacement is expected to be the preferred emplacement mode. It has also been proposed that high thermal loading via horizontal drift emplacement of large waste packages, containing up to 21 Pressurized Water Reactor (PWR) fuel assemblies, be used to create a dry-out zone around the EBS for thousands of years that will minimize corrosion and nongaseous radionuclide transport (Ruffner et al., 1993; Buscheck et al., 1993). The drying-out process may create deposition of solids rich in Ca and Si and solutions rich in Na or K. (Beavers et al., 1992; Murphy and Pabalan, 1994). In addition, backflow of the condensate through fractures may result

in an aqueous environment around the container, as indicated by the results of some field heater tests (Patrick, 1986; Zimmerman et al., 1986; Ramirez, 1991). The evaporation of water may cause the formation of solutions in the near-field that are rich in chloride and sulfate to the point of saturation (Abraham et al., 1986; Beavers et al., 1992; Walton, 1993). Hence, a conservative approach to container life prediction is to assume the presence of aqueous conditions surrounding the containers. The chemical composition of such an aqueous environment is not known, and a range of concentrations of various species has been investigated (Sridhar et al., 1993a). In the IWPE Project, solutions containing concentrations of chloride higher than 6 molal were included to confirm the concept of critical potentials for SCC.

The approach used in the example analysis of the substantially complete containment rule (Cragnolino et al., 1994) and in the Engineered Barrier System Performance Assessment Codes (EBSPAC) activities for the prediction of performance of container materials (Sridhar et al., 1993b) assumes that corrosion failure modes of importance to container life prediction are determined by the E_{corr} . The E_{corr} of the container material, which is a mixed potential dictated by the kinetics of the anodic and cathodic reactions at the surface exposed to the repository environment, changes with time in response to factors such as radiolysis, pH, temperature, and oxygen concentration (Macdonald and Urquidi-Macdonald, 1990). If the E_{corr} exceeds the pit initiation potential (E_p), pits initiate and propagate into the container wall. If the E_{corr} drops below E_p , pits already initiated continue to grow, but no new pits initiate. Finally, if the E_{corr} drops below the repassivation potential (E_{rp}), all pits repassivate and cease to grow. After repassivation, the corrosion of the container continues in a uniform manner at a low rate determined by the passive current density. This concept of critical potentials has been well established in the literature for pitting and crevice corrosion (e.g., Szklarska-Smialowska, 1986). Both E_p and E_{rp} are distributed values and depend on both material and environmental factors. Although two potentials, E_p and E_{rp} , are defined, in long-term prediction these two potentials may converge to one critical potential (Tsuji-kawa et al., 1987; Thompson and Syrett, 1992).

Additionally, while the method is illustrated for pitting, analogous parameters have been used to characterize the crevice-corrosion behavior of these alloys (Okayama et al., 1987). The concept of critical potential has been applied to SCC of many alloy-environment combinations (Cragolino and Sridhar, 1992a), but there are no data for the alloys and environments of interest to the proposed Yucca Mountain (YM) repository. Other environmental degradation phenomena, such as hydrogen embrittlement, also depend on the E_{corr} but do not exhibit a critical potential.

3.2.2 Previous Reports

The crucial questions in the measurement and use of E_{tp} are its dependence on the extent of prior pitting corrosion, measurement technique, environmental parameters, and microstructural characteristics. Previously reported results (Cragolino and Sridhar, 1992b; Sridhar and Cragolino, 1992a,b; Sridhar et al., 1993a,c; Sridhar et al., 1994c) have addressed some of these questions for pitting, while crevice corrosion was considered only in a preliminary fashion. For pitting, it was shown that the E_{tp} was independent of the extent of prior pitting and that it decreased logarithmically with an increase in chloride concentration. To a more limited extent, it was also shown that E_{tp} for alloy 825 was not dependent on the pH and concentration of species, such as sulfate, bicarbonate, and silica. Another important issue with respect to long-term prediction of container performance is the degree of conservatism entailed in the use of repassivation potentials irrespective of the variations in surface conditions. The effect of surface chromium depletion and surface roughness on localized corrosion of alloy 825 has been addressed in recently published papers (Dunn et al., 1993a,b). It has been shown that the E_{tp} measured on polished specimens is lower (more conservative) than the potentials required to grow pits on a Cr-depleted surface. The effect of external potential on the changes in the chemistry of crevice solutions was examined in a previous report (Sridhar et al., 1994a). This investigation indicated the importance of critical potential on changes in crevice

chemistry and provided a basis for future improvement in crevice corrosion modeling.

Studies on the effects of environmental factors and potential on the SCC of type 316L stainless steel (SS) were also reported previously (Sridhar et al., 1994a). The results were consistent with the assumption that E_{tp} formed a lower-bound value for the critical potential for SCC in chloride-containing environments. However, test technique was found to be important, with the U-bend, constant deflection test showing SCC over a greater range of chloride concentration than the slow strain rate tests.

3.2.3 Present Report

This report examines repassivation potential for crevice corrosion, E_{rcrev} , and the relationship between E_{tp} and E_{rcrev} . The applicability of these parameters, measured in relatively short-term tests (several hours to a few days), to long-term performance of materials (lasting several months to years) must be tested using appropriate experimental procedures. The results of ongoing, long-term, localized corrosion tests are reported. The results of further series of slow strain rate and constant deflection (U-bend) SCC tests on alloy 825 are also reported and compared with previous data for type 316L SS.

3.3 CREVICE CORROSION

3.3.1 Experimental Procedures

The specimens for the localized corrosion tests were machined from 12.5-mm-thick plate, the chemical composition of which has been reported before (Sridhar et al., 1993a). The specimen geometry used for the crevice repassivation tests is shown in Figure 3-1.

Crevices were created between the specimen surfaces and the teeth of polytetrafluoro ethylene (PTFE) serrated washers by bolting these washers on the specimens using an initial torque of 0.28 N•m (40 in.-oz). An alloy C-276 bolt and nut were used along with a PTFE bushing to prevent electrical contact with the specimen. The specimens were immersed partially such that the cylindrical post was outside the solution. The solution used was a 1,000 ppm chloride solution

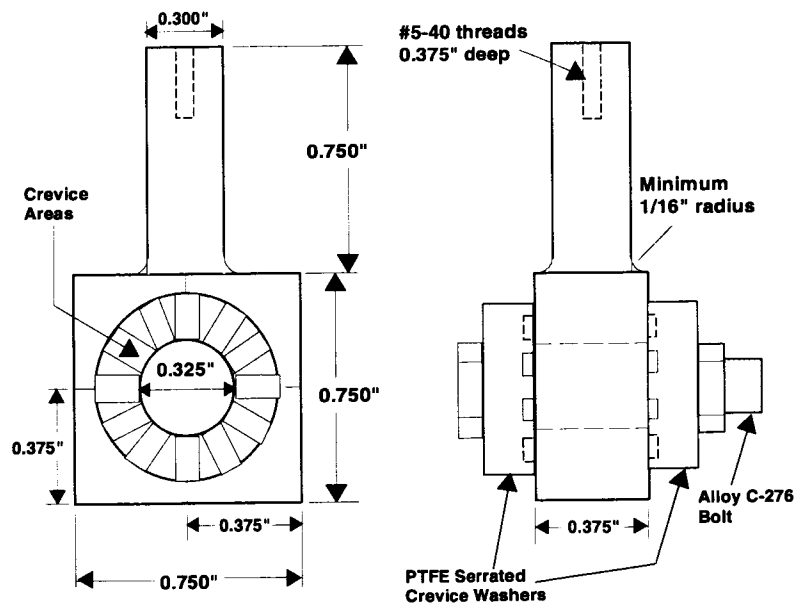


Figure 3-1. Schematic diagram of the crevice corrosion specimen and PTFE serrated washer. The shaded areas indicate the crevice areas. A Hastelloy alloy C-276 bolt and nut was used for tightening the crevice device.

containing 85 ppm HCO_3^- , 20 ppm SO_4^{2-} , 10 ppm NO_3^- , and 2 ppm F^- all as sodium salts. The characterization of this solution has been described previously (Sridhar et al., 1993a). The rest of the experimental apparatus and procedure has been described previously (Dunn et al., 1993a; Sridhar and Cragolino, 1993). The potential for initiating crevice corrosion was chosen so that pitting was largely avoided. The backward scan-rate for measuring repassivation potential was 5 mV/s. After the test, the crevice blocks were removed; the specimens were cleaned with water and acetone and examined under an optical microscope to measure depth of attack. The maximum depth of attack perpendicular to the crevice surfaces was measured by using the graduated fine focusing knob of the microscope, which was verified by using thickness gauges.

3.3.2 Results and Discussion

3.3.2.1 Repassivation

In Figure 3-2, the repassivation potential for crevice corrosion, E_{TCREV} , is compared to the

repassivation potential for pitting corrosion, E_{TP} , measured in a solution of identical composition using the same scan-rate. For charge densities in the range of 2 to 50 Coulombs/cm², the E_{TCREV} is 275 to 350 mV lower than E_{TP} , while for higher charge densities, E_{TCREV} is about 25 mV higher than E_{TP} . At present, the data are insufficient to determine whether the difference in the repassivation potentials at high charge density between pitting and crevice corrosion is statistically significant. Previously generated results, using a different scan-rate, have shown that the E_{TP} can vary by about 25 mV under the same environmental and material conditions (Sridhar et al., 1993a). However, the proximity of E_{TCREV} and E_{TP} values at higher charge densities supports the assumption of a single, lower-bound critical potential for both pitting and crevice corrosion in PA calculations (Cragolino et al., 1994).

3.3.2.2 Crevice Corrosion Propagation

The corrosion in the crevice areas was nonuniform and, in some specimens, pitting was observed outside the crevice areas. The maximum depth of corrosion in the crevice areas perpendicular to the

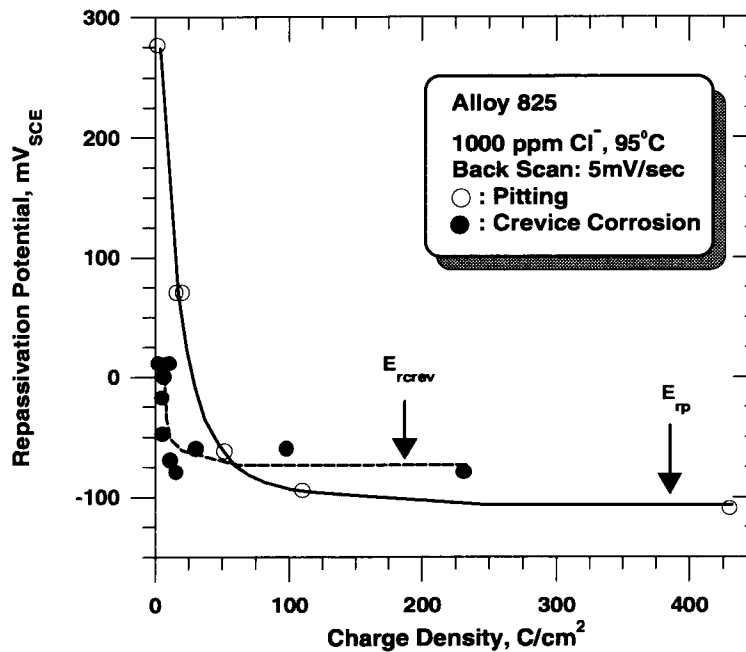


Figure 3-2. Repassivation potentials for crevice and pitting corrosion of alloy 825 in a 1,000 ppm chloride solution at 95 °C. The scan-rate was 5 mV/sec.

plane of the crevice is shown in Figure 3-3 as a function of charge density. The charge density discussed here is a nominal charge density derived from the measured total current and the nominal immersed area of the specimen without considering the actual area of the pit surface. The current density (C.D.) is also based on the nominal immersed area of the specimen.

The maximum crevice corrosion depth was roughly proportional to the square root of the charge density ($r^2 = 0.75$). A better fit was observed with a linear relationship ($r^2 = 0.84$), logarithmic ($r^2 = 0.89$), or even a second-order polynomial ($r^2 = 0.92$). If a Faradaic relationship is applied to a hemispherical pit, the pit depth should be proportional to $C^{0.33}$. In the case of a cylindrical pit where there is no radial growth, the pit depth should be linearly related to the charge density, provided the charge density is calculated based on nominal area rather than the changing area of the pit. The observed relationship is bounded by these two behaviors, indicating that the initial growth of the pit is

roughly hemispherical, followed by a deepening of the pit at the expense of the radius. The C.D. and potential are shown as functions of time in the inset of Figure 3-3. The nominal current density is essentially constant with time, and, hence, the relationship of maximum pit depth to charge density is essentially the same as that for maximum pit depth versus time. Thus, the true pit C.D. decreases roughly with $t^{-0.5}$, which is consistent with diffusion-controlled pit growth (Tester and Isaacs, 1975). For the same nominal charge density, the maximum depth of pitting corrosion observed earlier (Dunn et al., 1993a) was approximately the same as the maximum depth of crevice corrosion. In the waste package PA calculations (Cragnolino et al., 1994), a constant C.D. was assumed once the critical potential for initiation of localized corrosion was exceeded. The present results indicate that this is too conservative an assumption, and a lower rate of pit or crevice corrosion growth may be more realistic. However, further experiments are needed to confirm the above observations.

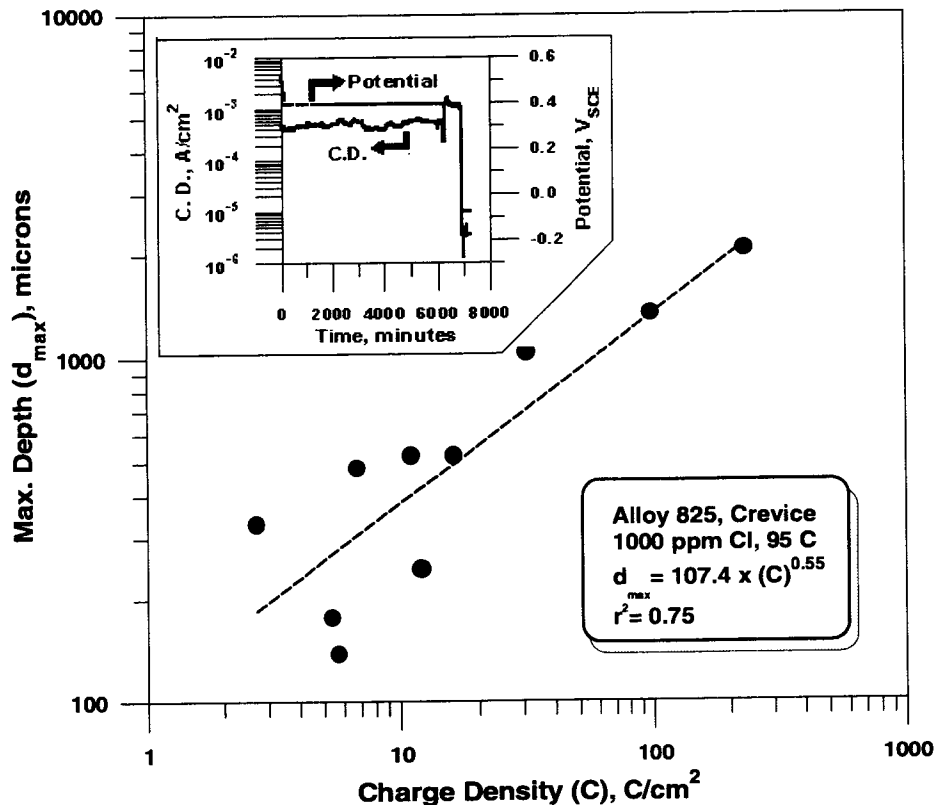


Figure 3-3. The maximum depth of crevice corrosion versus charge density for alloy 825 in 1,000 ppm chloride solution at 95 °C. The inset figure shows the current and potential versus time during one of the experiments.

3.3.2.3 Mechanism of Repassivation

During active pitting or crevice corrosion, rapid local dissolution of the alloy results in the generation of Fe^{2+} , Ni^{2+} , and Cr^{3+} ions. Hydrolysis of these cations results in the generation of H^+ and the concomitant migration of chloride ions to balance the charge. Migration of chloride into the pit or crevice area results in the formation of metal chloride complexes adjoining the metal and eventual precipitation of chloride salts such as $FeCl_2$, $NiCl_2$, and $CrCl_3$. The former has the lowest solubility and is expected to precipitate first. The formation of these salt layers on the walls of the pits or crevices has been predicted from electrochemical data (e.g., impedance measurements) and from visual observation of macroscopic pits with an optical microscope. The salt layer was thought to

stabilize the propagation of the localized corrosion front by providing a resistive drop in the potential at the deepest point in the pit such that the potential moves from the passive regime to the active regime (Beck, 1990). However, salt layer formation does not seem to be necessary for pit or crevice propagation. The polarization behavior of the metal in a simulated pit solution close to saturation with respect to metal chlorides has been examined by a number of investigators (Batista et al., 1988; Hakkarainen, 1983; Sridhar et al., 1993a). Active-passive peak is observed in some cases, although the passive current density in these cases is quite large. However, the active current density increases with the degree of saturation of the pit solution. Hence, the localized front can still be

stabilized if the concentration of chloride increases with depth.

The repassivation of pits or crevice corrosion has been hypothesized to be due to the decrease in chloride concentration in the localized area to a critical value (Hisamatsu, 1976; Gaudet et al., 1986; Steinsmo and Isaacs, 1993). It has been shown by a simplified transport model of a cylindrical pit (Gaudet et al., 1986; Steinsmo and Isaacs, 1993) that, as the external potential is reduced, the chloride concentration inside decreases due to lower generation of cations, and the pit repassivates once a critical chloride concentration (or a critical degree of saturation) is attained. The pit solution is generally assumed to be eventually saturated with respect to FeCl_2 , as this has lower solubility than NiCl_2 and CrCl_3 . Gaudet et al. (1986) predict that repassivation of type 304 SS occurs when the pit solution attains a saturation of about 40 percent. Hakkarainen (1983) measured the saturation at repassivation of type 304 SS to be about 80 percent. While these discrepancies need to be investigated further, the importance of this mechanism for the present experimental program is that, as long as the depth of localized corrosion is approximately the same, the repassivation potential would be expected to be similar. Gravano and Galvele (1984) used a different approach to calculate the changes in the concentration species inside the pit as a function of the product, $(x \cdot i)$, of pit depth (x) and pit current density (i) and found that both the H^+ and Cl^- concentrations change dramatically above a certain critical $x \cdot i$. This analysis would lead to a qualitatively similar conclusion regarding the similarity of the repassivation potentials for pitting and crevice corrosion.

A more fundamental model based on the nucleation of a monolayer of oxide in a chloride salt film has been proposed by Okada (1984); however, the parameters involved in this model have not been reported in the literature.

3.4 LONG-TERM LOCALIZED CORROSION TEST RESULTS

3.4.1 Experimental Procedure

The validity of using E_{tp} from short-term tests as a parameter for determining long-term performance was tested by potentiostatically polarizing specimens to potentials 100 mV above and 100 mV below the E_{tp} . Under these conditions, localized corrosion should not occur when the E_{corr} is less than E_{tp} . Long-term potentiostatic tests were conducted using alloy 825 specimens having both mill-finished, Cr-depleted surfaces and 600-grit finish polished surfaces. The characteristics of the Cr-depleted layer of this material have previously been reported (Sridhar et al., 1993a). The long-term test specimens were fully immersed in the solution, exposing the specimen-PTFE gasket interface to the solution. The specimen and solution were contained in a 2-L reaction vessel with 1,500 ml of solution. Test solutions were not deaerated but were not freely open to atmosphere. Under these conditions, the dissolved oxygen concentration is expected to be low. Since tests were conducted under potentiostatic conditions, this dissolved oxygen concentration is not expected to influence the results significantly. The test cells were equipped with a platinum counter electrode and a saturated calomel reference electrode. The sample was maintained at constant potentials above and below the predetermined repassivation potentials. Tests were conducted in 28-day intervals, at which time the solution was changed, and the sample was examined under a stereoscope at 70 X magnification and reweighed.

3.4.2 Results and Discussion

The results of a long-term potentiostatic test of alloy 825 in a 1,000-ppm Cl^- solution at 95 °C indicate that localized corrosion did not occur at a potential of 0 mV_{SCE} (100 mV less than the repassivation potential) over a cumulative test time of 9 months. The plot of current density versus time for this test (Figure 3-4) shows that brief current spikes occur immediately after the start of each test, but the current density rapidly decreases to a value of less than 1 $\mu\text{A}/\text{cm}^2$ for the remainder of the test segment. The weight of the sample

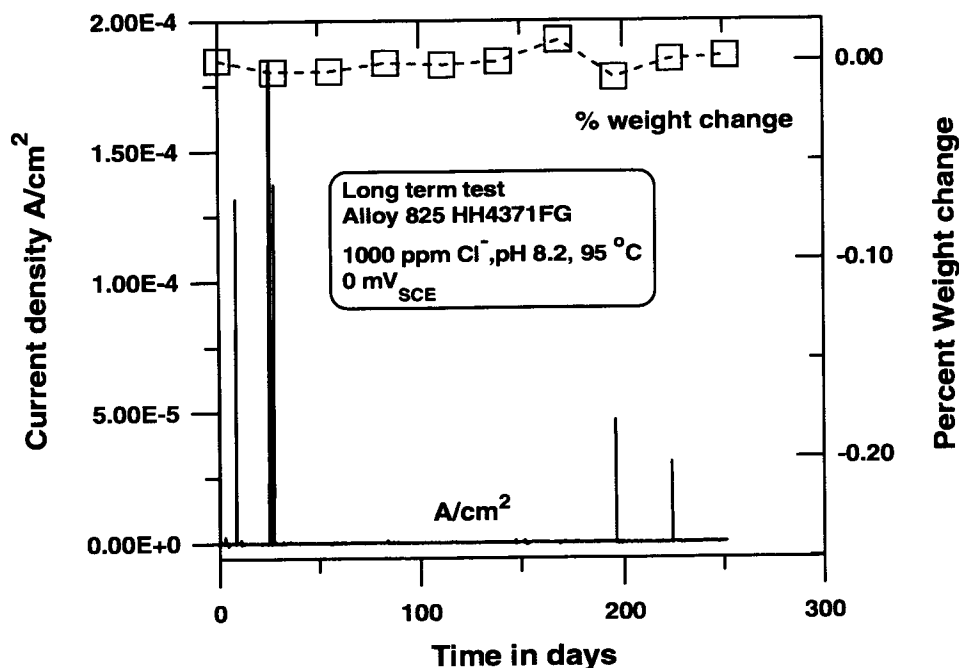


Figure 3-4. The current density and weight-loss versus time for a specimen of alloy 825 totally immersed in a 1,000 ppm chloride solution at 95 °C and potentiostatically held at 0 mV_{SCE} (about 100 mV below the repassivation potential).

during 9 months of testing has not significantly decreased, and there is no visible indication of localized corrosion. In contrast, crevice corrosion at the specimen-PTFE gasket interface was observed on the specimen held at 200 mV_{SCE} (100 mV above the repassivation potential) after 5 months of testing (Sridhar et al., 1994b). The onset of crevice corrosion after 139 days was indicated by a prolonged average current density greater than 10^{-5} A/cm², as shown in Figure 3-5.

However, because the crevice corrosion only occurred on an area of less than 0.3 cm², and the current density was calculated using the total specimen surface area of 15 cm², the actual crevice current density was in the range of 10^{-4} to 10^{-3} A/cm². The maximum depth of crevice corrosion in this region was measured to be about 700 μm. Significant weight loss was also observed at the conclusion of the last 28-day test segment, as shown in Figure 3-5. An additional

specimen that was potentiostatically held at 300 mV_{SCE} (300 mV below the repassivation potential) in a solution having a lower Cl⁻ but higher concentrations of SO₄²⁻ and NO₃⁻ did not undergo localized corrosion during the cumulative 3-month test period. The C.D. and percent weight-loss versus time data are plotted in Figure 3-6. The increase in current density observed in the last test segment was an artifact caused by an air bubble in the Luggin probe. No significant weight change or visible indications of localized corrosion were observed throughout the duration of the test.

Cyclic polarization tests have previously shown that the pit initiation potential, E_p , of alloy 825 in a 1,000-ppm Cl⁻ solution is greater than 600 mV_{SCE} (Sridhar et al., 1993b). The initiation of crevice corrosion has been observed to occur at slightly lower potentials, around 500 mV_{SCE}. In comparison, potentiostatic tests have shown that pits can be initiated and can penetrate through the Cr-depleted layer into the

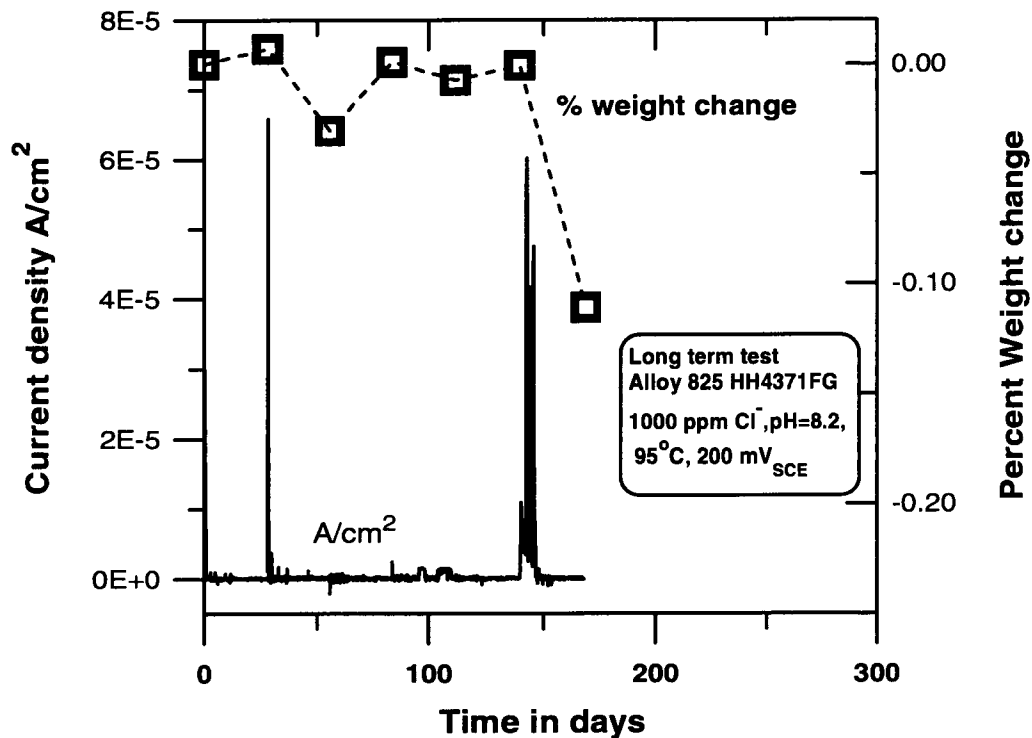


Figure 3-5. The current density and weight-loss versus time for a specimen of alloy 825 totally immersed in a 1,000 ppm chloride solution at 95 °C and potentiostatically held at 200 mV_{SCE} (about 100 mV above the repassivation potential).

bulk material at potentials of 300 mV_{SCE}. These potentials are higher than the repassivation potential for localized corrosion on alloy 825, which has been measured, using the cyclic polarization technique, to be in a range of 35 mV_{SCE} to 158 mV_{SCE}. The value of E_p has been reported to be scan-rate dependent, and consequently, time dependent. Decreasing the scan-rate decreases the value of E_p . A similar time dependence may be expected for the initiation potential for crevice corrosion. While E_{tp} has also been shown to be time dependent, decreasing the scan-rate results in higher values of E_{tp} . The present series of tests, conducted under potentiostatic conditions, can be viewed as having an extremely low scan-rate. During long-term testing, localized corrosion was observed at potentials of 200 V_{SCE}, which is approximately 100 mV above E_{tp} . No localized corrosion has been observed on the specimen maintained at a potential 100 mV below E_{tp} .

The geometry of the specimen allowed a comparison of pitting on polished and mill-finished surfaces, as well as crevice corrosion on polished surfaces. The polished surfaces were not observed to change throughout the course of the test. The mill-finished surfaces were observed to form corrosion product layers. These corrosion product layers were occasionally removed from the surfaces during the course of the test. The small fluctuations in weight observed in the test can be attributed to the process of corrosion product formation and removal. The crevice created by the PTFE gasket on the specimen surface proved to be the most critical region for localized corrosion. However, the most extreme case, a mill finished Cr-depleted surface under crevice conditions, has not been tested yet.

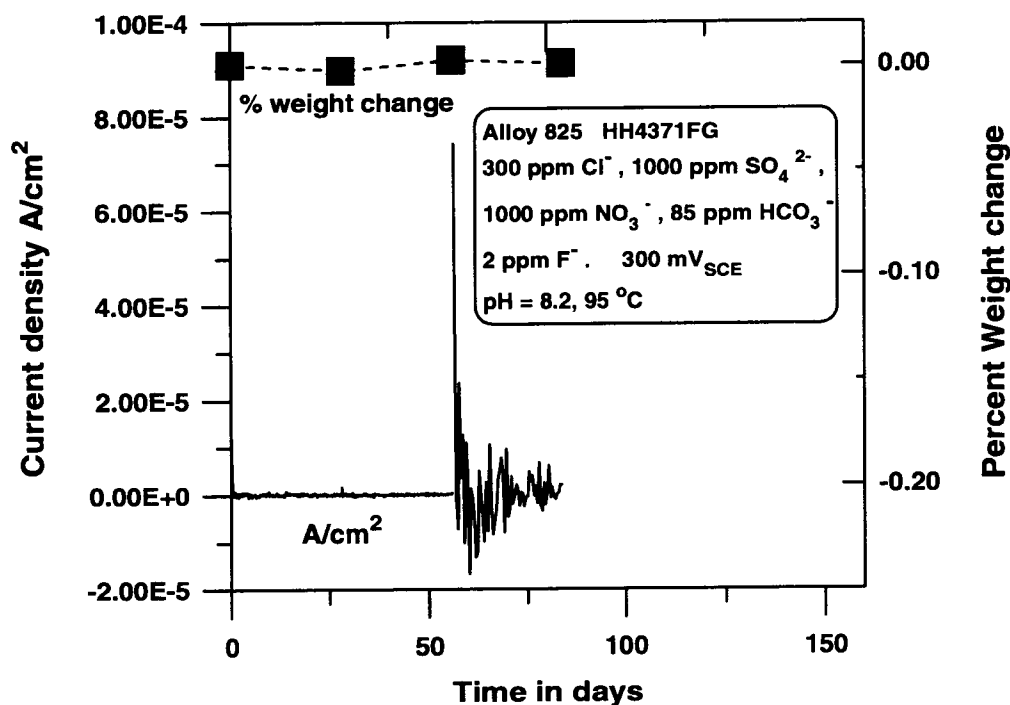


Figure 3-6. The current density and weight-loss versus time for a specimen of alloy 825 totally immersed in a 300 ppm chloride solution containing 1,000 ppm nitrate and 1,000 ppm sulfate at 95 °C and potentiostatically held at 300 mV_{SCE} (about 300 mV below the repassivation potential).

The absence of localized corrosion, as determined by both weight loss and visual inspection, on the specimen potentiostatically polarized to 300 mV_{SCE} in a 300 ppm Cl⁻, 1,000 ppm SO₄²⁻, 1,000 ppm NO₃⁻ solution is not surprising, since E_{rp} for alloy 825 in this solution is over 600 mV_{SCE}. The abrupt change in the pattern of current density spikes at the start of the third segment of the test (Figure 3-6) was attributed to the formation of an air bubble in the Luggin probe that caused poor contact between the reference electrode and the test solution.

3.5 STRESS CORROSION CRACKING STUDIES

3.5.1 Experimental Procedures

The chemical compositions of the two heats of alloy 825 used in this study were reported elsewhere

(Sridhar et al., 1994a). One of the heats, in the form of a hot-rolled and annealed plate, was adopted for the preparation of slow strain rate test specimens. Smooth tensile specimens, machined with the tensile axis perpendicular to the rolling direction, were used in most of the tests. In specific cases, circumferentially notched specimens were used. Experimental details on the slow strain rate tests, including characteristics and dimensions of the specimens, description of the experimental setup, and other relevant information, were previously reported (Sridhar et al., 1993c).

The slow strain rate tests were performed in concentrated chloride solutions prepared with salts of different cations (Mg²⁺, Li⁺, and Na⁺). Sodium thiosulfate was added to the NaCl solution to compare the behavior of alloy 825 with that previously reported for type 316L SS. In this case, the pH of the solution was adjusted to 4.0 by the addition of HCl. The

justification for the use of these solutions has been discussed previously (Sridhar et al., 1993c). An extension rate of 2.8×10^{-6} mm/s (1.1×10^{-7} in./s), which represents an initial strain rate of 2.2×10^{-7} s⁻¹, was used in these tests. All of the specimens were placed inside the electrochemical cell in such a way that the gauge length was completely immersed in the solution.

Another heat of alloy 825, in the form of cold-rolled and mill-annealed (MA) sheet, was used for the preparation of specimens for constant-deflection tests. U-bend specimens were machined from this sheet and stressed without any heat treatment. Specimen preparation and additional experimental details are reported elsewhere (Sridhar et al., 1994a).

The constant-deflection tests were conducted in solutions similar to those used in slow strain rate tests. Concentrated chloride solutions, prepared with either LiCl or NaCl reagents, were tested to compare the effects of both cations on the SCC behavior of alloy 825. These solutions were prepared using high-purity water with the pH adjusted to 4.0. Tests were conducted in successive periods of 28 days. At the end of each period, the specimens were optically examined at about 70 X magnification. If no signs of SCC or severe localized corrosion were detected, the same specimens were exposed, using freshly prepared solutions, to identical environmental conditions for an additional time interval.

3.5.2 Results

3.5.2.1 Slow Strain Rate Tests

The results of slow strain rate tests of alloy 825 in chloride solutions are summarized in Figure 3-7.

In this figure, E_p and E_{rp} for alloy 825 (Sridhar et al., 1993c) are plotted as a function of chloride concentration to indicate the location of the open-circuit or applied potentials used in the slow strain rate tests with respect to those potentials. It should be noted that E_{rp} deviates significantly from the linear dependence on the logarithm of chloride concentration observed at lower concentrations above 4 mol/kg water. As shown in Figure 3-7, SCC was observed, both at an anodic potential as well as at the E_{corr} , only in 40-percent

MgCl₂ solution (14.0 mol Cl⁻/kg water) at 120 °C. The elongation to failure was 44 percent at the E_{corr} (approximately -270 mV_{SCE}) and decreased to 36 percent at a slightly anodic potential (-260 mV_{SCE}), whereas the elongation to failure corresponding to a purely ductile fracture was approximately 60 percent. No SCC was observed in LiCl solutions at chloride concentrations of 9.1 mol/kg water at 110 °C under both open-circuit and anodic applied potentials. The addition of 0.01 mol/L of Na₂S₂O₃ to the NaCl solution containing 5.8 mol/kg water of chloride ions did not induce SCC, in contrast to the previously reported case (Sridhar et al., 1994a) of type 316L SS.

Also, SCC did not occur in another set of two tests in which circumferentially notched specimens were used and the strain rate was decreased five times with respect to that applied for smooth tensile specimens. One of these tests was conducted in 9.1 molal LiCl solution under open-circuit conditions (-290 mV_{SCE}) at 110 °C. The test was interrupted after 757 h of straining, corresponding to 1.96-mm extension. The other test was conducted in 5.8 molal NaCl solution containing 0.01 M Na₂S₂O₃. This test was initiated under open-circuit conditions, but a slight anodic potential was applied later in the course of the test, after 908 h of straining, in an attempt to promote crack initiation. Straining was interrupted after 1,104 h, corresponding to a nominal extension of 2.62 mm. In these two tests, the specimens were unloaded and removed from the electrochemical cell. No signs of SCC were detected in the notch area.

All observations were confirmed by a fractographic examination of the failed, smooth tensile specimens using the scanning electron microscope (SEM). Several thumbnail-shaped areas exhibiting transgranular quasi-cleavage features were observed along the periphery on the fracture surface of the specimens tested in MgCl₂ solution, both at the open-circuit as well as the anodic applied potential. One of these areas is shown at a high magnification in Figure 3-8, confirming the occurrence of SCC. The appearance of numerous secondary cracks on the side surface of these specimens is illustrated in Figure 3-9. The coalescence of deep, slightly branched cracks, growing in different planes, led to the generation of an extremely uneven fracture surface.

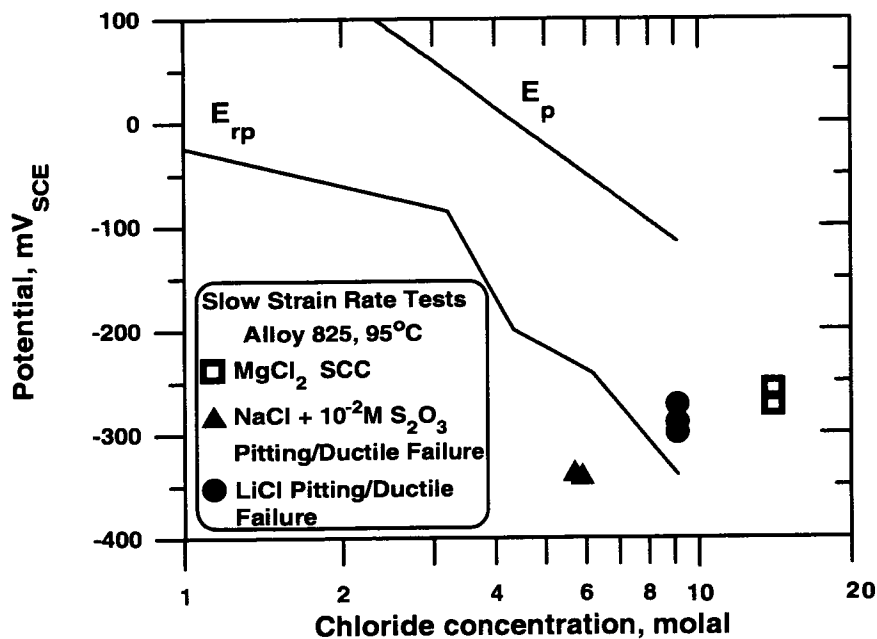


Figure 3-7. Result of slow strain rate tests of alloy 825 in concentrated chloride solutions of different cations ($MgCl_2$, $LiCl$, and $NaCl$) at temperatures ranging from 95 to 120 °C, with and without the addition of $Na_2S_2O_3$. Data points are shown in relation to the lowest values of pitting (E_p) and repassivation (E_{rp}) potentials, measured independently through cyclic polarization curves, as a function of chloride concentration.

Ductile failure promoted by coalescence of microvoids was observed in all the remaining tests. Signs of pitting corrosion were also detected on the fracture surface, although the dominant feature in the fractographs was the presence of dimples associated with ductile failure. Pits were also observed on the specimen surface, mainly at the vapor/solution interface.

No relevant slow strain rate test could be conducted under potentiostatic conditions at higher anodic potentials than those tested, because the occurrence of pitting corrosion became the dominant process accompanying the ductile failure. To avoid the occurrence of pitting corrosion, the potential was diminished by a few millivolts during the course of some tests in order to maintain the current well below 1 mA. Taking into consideration the resistance to SCC exhibited by alloy 825 in 5.8 molal $NaCl$, even in the

presence of sodium thiosulfate, no attempt was made to study the effect of lower chloride concentrations on the susceptibility to SCC.

3.5.2.2 Constant-Deflection Tests

Table 3-1 summarizes the results of constant-deflection tests using U-bend specimens of alloy 825 in concentrated chloride solutions (pH 4.0) at 95 °C, with chloride concentrations ranging from 5.8 to 9.0 mol/kg water. No SCC was observed in any of the 11 U-bend specimens tested, in some cases for a total testing time of 4,536 h (189 days). The time period interval for specimen examination was usually 672 h (28 days). Certain specimens were exposed to alternate cycles of full immersion in the concentrated solutions, followed by exposure to the vapor phase just above the solution/vapor interface. However, no SCC was

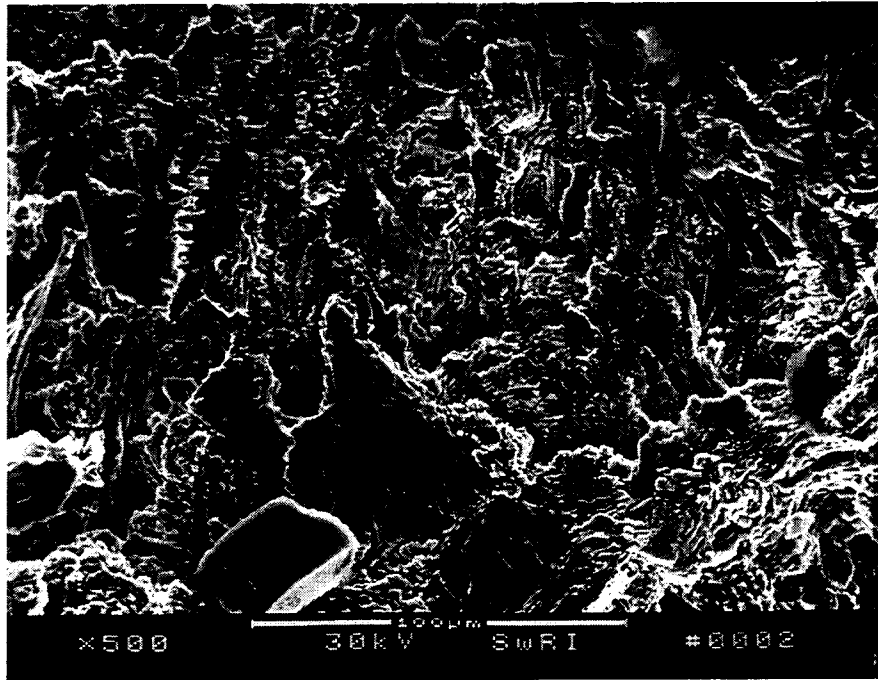


Figure 3-8. SEM fractograph showing the transgranular SCC area of the alloy 825 specimen fractured in a slow strain rate test at an applied potential of $-260 \text{ mV}_{\text{SCE}}$ in 40-percent MgCl_2 solution at 120°C

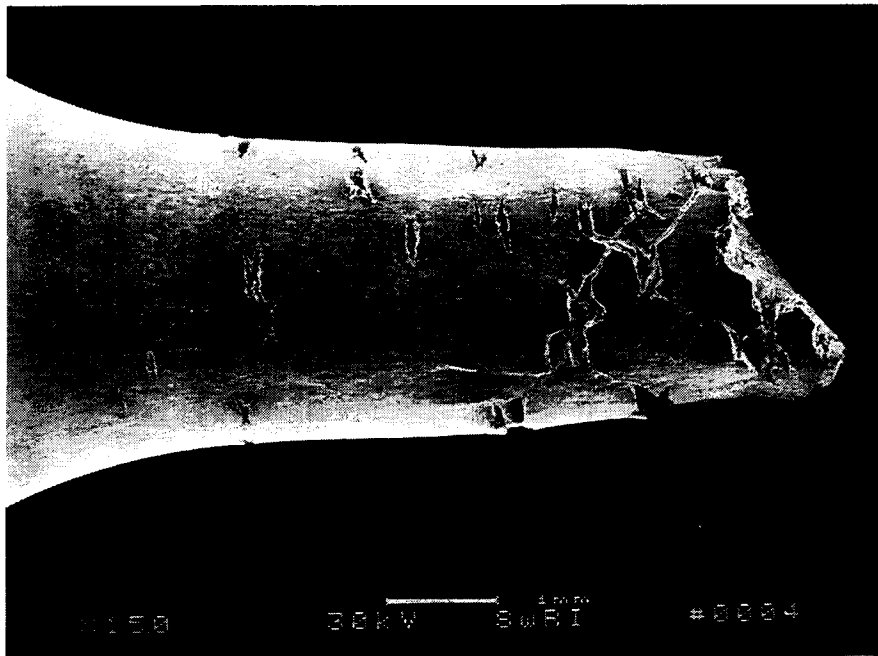


Figure 3-9. Side surface of alloy 825 specimen tested at $-260 \text{ mV}_{\text{SCE}}$ in 40-percent MgCl_2 solution at 120°C

Table 3-1. Summary of U-bend test results for alloy 825 in concentrated chloride solutions at 95 °C

Spec No.	Solution	E_{corr} (mV _{SCE})	E_{applied} (mV _{SCE})	Current (Amps)	Initial pH	Final pH	Test Time (hr)	Results
1	6.2 molal Cl ⁻ as NaCl	-170/-270	O.C.	—	4.2±0.5	6.3±0.3	4,536	No SCC
2	6.2 molal Cl ⁻ as NaCl	-160	-160	10 ⁻⁷ to 10 ⁻⁴	3.8	—	504	No SCC, large pit on specimen leg
3	5.8 molal Cl ⁻ as LiCl	-260	O.C.	—	4.5±0.6	6.3±0.2	4,536	No SCC
4	5.8 molal Cl ⁻ as LiCl	-220	-220	10 ⁻⁶ to 10 ⁻³	3.4	—	504	No SCC, large pit near apex of specimen
5	6.2 molal Cl ⁻ as NaCl	-270/-180	-260/-170	10 ⁻⁶ to 10 ⁻⁵	4.2±1.3	5.8	1,344	No SCC, localized corrosion
6	5.8 molal Cl ⁻ as LiCl	-260/-230	-250/-220	10 ⁻⁶ to 10 ⁻⁴	4.7±0.7	6.3±0.2	4,032	No SCC
7	9.0 molal Cl ⁻ as LiCl	-300/-260	-290/-260	-6×10 ⁻⁵ to 2×10 ⁻⁴	4.3±0.1	—	3,360	No SCC, pits above and below V/S interface
8	9.0 molal Cl ⁻ as LiCl	-300/-260	O.C.	—	4.3±0.1	—	3,360	No SCC, pits above and below V/S interface
9	6.2 molal Cl ⁻ as NaCl	-300/-280	-260/-330	10 ⁻⁵ to 4×10 ⁻⁴	4.1±0.6	6.5±0.2	2,688	No SCC
10	5.8 moles Cl ⁻ as LiCl	-310/-260	O.C.	—	4.9±0.4	6.0±0.2	2,688	No SCC
11	5.8 moles Cl ⁻ as LiCl	-310/-250	-300/-320	10 ⁻⁵ to 2×10 ⁻⁴	4.9±0.4	6.0±0.2	2,688	No SCC

O.C. — open circuit V/S — vapor/solution

detected under these conditions. For example, Specimens 1 and 3 were exposed for a total of seven 28-day periods. After an initial 28-day period in which Specimen 3 was immersed in the solution, it was exposed to the vapor phase for the remaining testing time. Specimen 1 was immersed in the solution in periods 1 and 6 and exposed to the vapor phase for the remaining times. Specimens tested under fully immersed conditions for 504 h (21 days) in both NaCl and LiCl solutions containing 6.0 mol Cl^- /kg water at potentials slightly anodic to the open-circuit potential exhibited localized corrosion, mostly in the form of small pits located mainly in the legs of the U-bends above the vapor/solution interface. In the most concentrated chloride solution tested (9.0 molal LiCl), small pits were noticeable in the area exposed to the liquid phase, as well as above the vapor/solution interface. However, these pits did not give rise to cracks upon further exposure.

The results of all the U-bend tests of alloy 825 are plotted in Figure 3-10 to indicate the location of the potentials used in the tests with respect to E_p and E_{rp} . It is seen that, within the range of chloride concentrations tested, no SCC occurred above or below E_{rp} .

3.5.3 Discussion

The results shown in Figure 3-7 clearly indicate that MA alloy 825 only failed by SCC in slow strain rate tests when exposed to MgCl_2 solutions at a chloride concentration of 14.0 mol/kg water and a temperature of 120 °C. On the other hand, SCC did not occur in LiCl and NaCl solutions in which the chloride concentration was equal to 9.3 mol/kg water or lower at temperatures below 110 °C. These results indicate that under the experimental conditions used in these tests, particularly in terms of temperature and strain rate, SCC cannot be promoted, regardless of the cation, at chloride concentrations less than or equal to 9.3 mol/kg water,

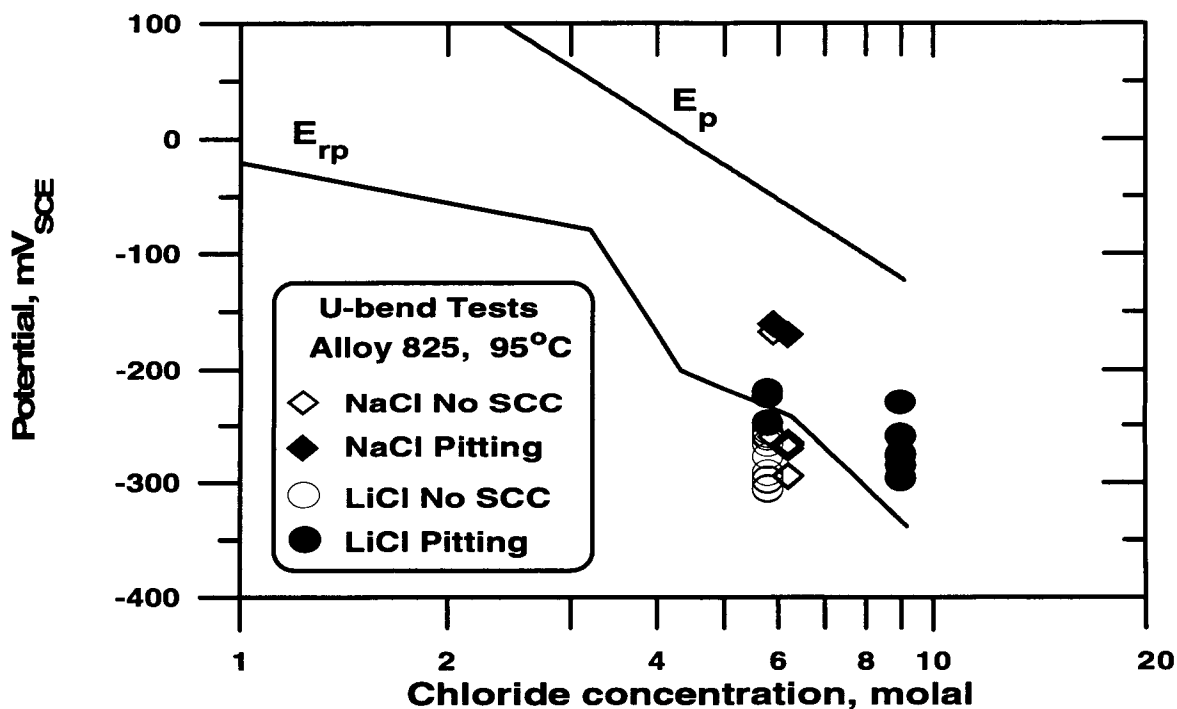


Figure 3-10. Results of constant-deflection tests of alloy 825 in concentrated chloride solutions of difference cations (LiCl and NaCl) at 95 °C. Data points are shown in relation to the lowest values of pitting (E_p) and repassivation (E_{rp}) potentials, measured independently through cyclic polarization curves, as a function of chloride concentration.

even at acidic pHs. Instead of SCC, the dominant failure mode was ductile failure accompanied by pitting corrosion. Under equivalent testing conditions, mill-annealed type 316L SS was found to be susceptible to cracking at chloride concentrations of 9.0 mol/kg water (Sridhar et al., 1993c; 1994a). In 40-percent $MgCl_2$ solution at 120 °C, the elongation to failure for type 316L SS was found to be 7.4 percent at the open circuit potential and 4.6 percent at a 20-mV anodic overpotential, whereas for alloy 825, the values were 44 and 36 percent respectively.

The addition of thiosulfate to a chloride solution containing 5.8 mol Cl^- /kg water promoted transgranular SCC of type 316L SS (Sridhar et al., 1994a). However, as shown in Figure 3-7, no SCC was observed on alloy 825 under the same testing conditions or under more severe conditions prompted by the use of a notched specimen tested at a lower extension rate for a very extended period (>1,000 h). Tsujikawa et al. (1993) have reported similar results for solution-annealed materials, indicating that 316L SS is susceptible to transgranular SCC in a 20-percent NaCl solution (4.3 molal) containing 0.001 to 0.1 M $Na_2S_2O_3$ (pH 4.0) in slow strain rate tests conducted at 80 °C, whereas alloy 825 was found to be fully resistant under equivalent testing conditions. As shown in Figure 3-7, pitting was observed in the thiosulfate-containing solution. The open-circuit potential and the anodic potential used for testing in this environment is well below the plotted values of E_{tp} . However, it should be noted that metastable sulfur oxyanions, such as $S_2O_3^{2-}$, induced a significant decrease in E_p when added to chloride solutions with respect to the plain chloride environment (Newman et al., 1982). A similar effect can be expected for E_{tp} , and this may explain the occurrence of pitting corrosion of alloy 825 at such low potentials.

The constant deflection tests confirmed the results of the slow strain rate tests in the case of alloy 825 in the sense that no SCC was found within the same range of chloride concentrations using both test methods. SCC was observed only in 40-percent $MgCl_2$ solution at 120 °C using slow strain rate tests. U-bend

testing will be conducted in the same solution to further compare both test measures. A large number of U-bend tests were conducted for extended periods in concentrated chloride solutions close to the solubility of NaCl at 95 °C, which is 6.66 mol/kg water (Linke, 1965), to confirm the superior resistance to SCC of alloy 825 compared to type 316L SS. Some of these observations have been reported previously (Sridhar, et al., 1994a), but the testing time in this reporting period has been extended significantly. On the other hand, SCC of type 316L SS was observed in constant deflection tests conducted in both LiCl and NaCl solutions at concentrations (5.8 mol/kg water) at which no cracking was detected in slow strain rate tests (Sridhar et al., 1994a). As discussed previously, this difference in the behavior of both alloys can be expected from their chemical composition (Cragolino and Sridhar, 1992a). The higher nickel content of alloy 825, combined with a higher level of chromium and molybdenum, makes this alloy far more resistant to SCC in chloride-containing environments than any of the austenitic SS. Contrary to the case of type 316L SS, in which a significant susceptibility to SCC in constant deflection tests was detected in the vapor phase under conditions leading to the formation of a liquid film on the surface, localized corrosion in the form of pitting was the dominant phenomenon for alloy 825. The constant deflection tests were extended for several months to determine if cracks could be initiated from pits. Apparently, this is not the case. However, the initiation of cracks could be promoted through the alteration of surface or near-surface conditions by the introduction of very localized plastic deformation via cold work or microchemical modifications through surface depletion of some alloying element or thickening of the passive film by oxidation in air (Dunn et al., 1993a,b). Additional experiments are needed to investigate these effects. In particular, constant deflection tests using double U-bend specimens in which the formation of a crevice environment in regions of highly localized tensile stress is promoted will be conducted under a variety of controlled potential and surface conditions to attain a better understanding of the events that may lead to crack initiation.

3.6 CONCLUSIONS AND RECOMMENDATIONS

3.6.1 Localized Corrosion

The similarities between repassivation potentials for crevice and pitting corrosion supports the use of a single, lower-bound critical potential for a given container material in PA calculations. The repassivation behavior can be modeled in terms of change in chloride concentration inside the crevice or pit, although changes in pH can also be considered in this model. The propagation of crevice corrosion occurs in a nonuniform manner, the maximum depth being slightly larger than pitting at equivalent charge density. The effect of microstructural changes on repassivation potential has not been investigated and may be important in future investigations.

The results from long-term potentiostatic tests indicate that the repassivation potential for localized corrosion is a conservative predictive tool for long-term performance. The pit and crevice corrosion-initiation potentials tend to decrease with time, making long-term predictions with these parameters difficult. The repassivation potential, on the other hand, tends to increase with time. This allows relatively short-term tests to yield values that can be used conservatively for long-term prediction. The fact that crevice corrosion was observed at a potential fully 300 mV below the crevice corrosion initiation potential points out the gross overprediction of material performance possible when the localized corrosion initiation potential is used as a parameter for estimating long-term behavior. The observation that localized corrosion occurred 100 mV above the repassivation potential indicates that the use of this parameter to predict long-term performance is not overly conservative.

3.6.2 Stress Corrosion Cracking

The applicability of critical potentials for localized corrosion for predicting SCC cracking is being studied using slow strain rate and constant-deflection tests on type 316L SS and alloy 825. The results generated thus far are consistent with the assumption that the repassivation potential for localized corrosion constitutes a lower bound for the critical potential for

SCC in the case of type 316L SS. However, the occurrence of SCC is apparently dependent on test technique. In slow strain rate tests, SCC of type 316L SS was promoted by concentrated chloride solutions (>9.1 mol/kg water) above 100 °C, and at lower chloride concentrations and temperatures, by the presence of thiosulfate. However, no SCC was observed with that technique at chloride concentrations lower than 6 mol/kg water, even in the presence of thiosulfate. On the other hand, SCC of type 316L SS was observed using U-bend specimens in constant-deflection tests conducted in concentrated chloride solutions or in more dilute solutions with and without the addition of thiosulfate. In dilute solutions, cracking was found to be confined to the region above the vapor/solution interface. In the case of alloy 825, no apparent discrepancies were observed by comparing the results of the slow strain rate tests with those of constant-deflection tests under environmental conditions similar to those used for testing type 316L SS. For alloy 825, SCC was only observed in slow strain rate tests at 120 °C in a highly concentrated chloride solution (40% Mg Cl₂). However, since alloy 825 is far more resistant to SCC than type 316L SS, additional studies are needed to reach a conclusion with respect to the effect of test technique. The need to study the effect of crevice conditions and concentration process at the vapor/solution interface on the initiation of cracks is emphasized to explore the full range of environmental conditions and electrochemical potentials that can cause cracking of these alloys in chloride-containing solutions at temperatures close to the boiling point.

3.7 ASSESSMENT OF PROGRESS TOWARDS MEETING PROJECT OBJECTIVES

The approach that is currently being used in waste package PA (Cragnolino et al., 1994) involves a single critical potential, the repassivation potential for deep pits, with an associated range for all three localized degradation modes: (i) pitting, (ii) crevice corrosion, and (iii) SCC. This approach, because it has been shown to be conservative and robust, would also reduce the KTUs related to the extrapolation of short-term tests to long-term prediction of waste package performance. The experimental results reported thus far indicate that,

at least for pitting and crevice corrosion, this approach is viable. In the case of SCC, the results are consistent with the assumption in modeling, but the sufficiency of specifying the same critical potential as that for the localized corrosion modes needs to be established. Further, the results of the SCC tests indicate the great importance of test technique. The constant-deflection tests produce cracking over a wider range of chloride concentration than the slow strain rate tests, for type 316L SS. For alloy 825, no SCC was observed in either test within the same range of chloride concentration.

Longer-term constant-deflection tests were used to confirm the superior resistance to SCC of alloy 825 compared to type 316L SS in solutions in which the NaCl concentration was close to saturation at 95 °C. Localized corrosion tends to prevail over SCC under such conditions.

3.8 PLANS FOR THE NEXT REPORTING PERIOD

Long-term tests under controlled potentials, anticipated to continue for time periods ranging from a few months to 5 yr, are necessary to verify several of the concepts discussed herein. These tests, which are continuing, will verify whether the E_{rp} for deep pits is a conservative parameter for predicting E_p and E_{rp} for all surface conditions. Tests with intentional crevices under potentiostatic control will also be started during the next reporting period to verify whether the E_{rp} for deep pits can be used to predict initiation and repassivation of crevice corrosion. In conjunction with these controlled potential tests, tests under naturally aerated conditions will also be conducted in which the E_{corr} will be monitored. Results of these ongoing tests will be reported in future semi-annual reports. A radially symmetrical crevice design would enable a better comparison of model and experiments. Additionally, the effect of solute transport on repassivation may become important for shallow crevices. Preliminary results (not reported in this semi-annual) indicate that this type of crevice device yields results that can be predicted by a model developed under the EBS program. This crevice device will be investigated further by varying the crevice depth. Finally, the changes in crevice chemistry under natural redox conditions need to be investigated.

Slow strain rate tests will continue with the aim of completing them during the next reporting period. Creviced specimens will be tested to evaluate the effect of crevice chemistry on the initiation of cracks. Double U-bend specimens will be used to develop crevice conditions in the region of highest tensile stress in constant-deflection tests to explore conditions that may lead to cracking in relatively dilute chloride solutions. Long-term SCC tests will be continued for periods extending from a few months to several years.

In order to evaluate the long-term behavior of container materials, their microstructural changes as a result of thermal exposure need to be understood. These studies are being performed for alloy 825 in Task 3. As part of this task, methods to quantify the grain boundary sensitization of alloy 825 are being developed. While such test techniques exist for SS, such as type 304L, no rapid and discriminatory method for estimating grain boundary sensitization of alloy 825 exists. The results from these studies will be presented in the next semi-annual report as a basis for further studies in this area and will be applied to the evaluation of the effect of thermal treatments on SCC.

3.9 REFERENCES

- Abraham, T., H. Jain, and P. Soo. 1986. *Stress Corrosion Cracking Tests on High-Level Waste Container Materials in Simulated Tuff Repository*. NUREG/CR-4619. Washington, DC: U.S. Nuclear Regulatory Commission.
- Batista, W., A.M.T. Louvisse, O.R. Mattos, and L. Sathler. 1988. The electrochemical behavior of Incoloy 800 and AISI 304 steel in solutions that are similar to those within occluded corrosion cells. *Corrosion Science* 28(8): 759-768.
- Beavers, J.A., N.G. Thompson, and C.L. Durr. 1992. *Pitting, Galvanic, and Long-Term Corrosion Studies on Candidate Container Alloys for the Tuff Repository*. NUREG/CR-5709. Washington, DC: U.S. Nuclear Regulatory Commission.
- Beck, T.R. 1990. Occurrence and properties of anodic salt films in pitting corrosion. *Advances in Localized Corrosion*. H. Isaacs, V. Bertocci, J.

- Kruger, and S. Smialowska, ed. Houston, TX: National Association of Corrosion Engineers: 85-91
- Buscheck, T.A., D.G. Wilder, and J.J. Nitao. 1993. Large-scale *in situ* heater tests for hydrothermal characterization at Yucca Mountain. *Proceedings of the Fourth Annual International High-Level Radioactive Waste Management Conference*. La Grange Park, IL: American Nuclear Society: 1854-1872.
- Cragnolino, G.A., and N. Sridhar. 1992a. *A Review of Stress Corrosion Cracking of High-Level Nuclear Waste Container Materials — I*. CNWRA 92-021. San Antonio, TX: Center for Nuclear Waste Regulatory Analyses.
- Cragnolino, G.A., and N. Sridhar. 1992b. *Integrated Waste Package Experiments. NRC High-Level Radioactive Waste Research at CNWRA, January 1 Through June 30, 1992*. W.C. Patrick, ed. CNWRA 92-01S. San Antonio, TX: Center for Nuclear Waste Regulatory Analyses.
- Cragnolino, G.A., N. Sridhar, J. Walton, R. Janetzke, J. Wu, and P. Nair. 1994. *Substantially Complete Containment — Example Analysis of a Reference Container*. CNWRA 94-003. San Antonio, TX: Center for Nuclear Waste Regulatory Analyses.
- Doering, T.W. 1993. Robust waste package concept (multibarrier). *Proceedings of the Fourth Annual International High-Level Radioactive Waste Management Conference*. La Grange Park, IL: American Nuclear Society: 551-557.
- Dunn, D.S., N. Sridhar, and G.A. Cragnolino. 1993a. The effect of surface conditions on the localized corrosion of a candidate high-level waste container material. *Corrosion Control for Low-Cost Reliability. Proceedings of the Twelfth International Corrosion Congress*. Houston, TX: NACE International: 5B: 4,021-4,030.
- Dunn, D.S., N. Sridhar, and G.A. Cragnolino. 1993b. Effects of surface conditions on the localized corrosion of alloy 825 high-level waste container material. Paper No. 94-138. *Corrosion '94*. Houston, TX: NACE International.
- Farmer, J.C., G.E. Gdowski, R.D. McCright, and H.S. Ahluwalia. 1991. Corrosion models for performance assessment of high-level radioactive waste containers. *Nuclear Engineering and Design* 129: 57-88.
- Gaudet, G.T., W.T. Mo, T.A. Hatton, J.W. Tester, J. Tilly, H.S. Isaacs, R.C. Newman. 1986. Mass transfer and electrochemical kinetic interactions in localized pitting corrosion. *AIChE Journal*. 32(6): 949-958.
- Gravano, S.M. and J.R. Galvele. 1984. Transport processes in passivity breakdown — III. Full hydrolysis plus ion migration plus buffers. *Corrosion Science* 24(6): 517-534.
- Hakkarainen, T. 1983. Repassivation of corrosion pits in stainless steel. *Passivity of Metals and Semiconductors*. M. Froment, ed. Elsevier Science Publishers B.V., Amsterdam, The Netherlands: 367.
- Hisamatsu, Y. 1976. Pitting corrosion of stainless steels in chloride solutions. *Passivity and Its Breakdown on Iron and Iron Base Alloys*. R.W. Staehle and H. Okada, (eds.) Houston, TX: NACE International Inc. 99-105.
- License Application Review Plan. 1992. *Draft License Application Review Plan for the Review of a License Application for a Geologic Repository for Spent Nuclear Fuel and High-Level Radioactive Waste, Yucca Mountain, Nevada*. NUREG-1323. Washington, DC: U.S. Nuclear Regulatory Commission: Office of Nuclear Material Safety and Safeguards.
- Linke, W.F. 1965. Solubilities: Inorganic and metal organic compounds. Washington, DC. American Chemical Society: 959.
- Macdonald, D.D., and M. Urquidi-Macdonald. 1990. Thin-layer mixed-potential model for corrosion of high-level nuclear waste canisters. *Corrosion* 46(5): 380-390.
- Murphy, W.M. and R.T. Pabalan. 1994. *Geochemical Investigations Related to the Yucca Mountain Environment and Potential Nuclear Waste*

- Repository. CNWRA 94-006. San Antonio, TX: Center for Nuclear Waste Regulatory Analyses.
- Newman, R.C., H.S. Isaacs, and B. Alman. 1982. Effects of sulfur compounds on the pitting behavior of type 304 stainless steel in near-neutral chloride solutions. *Corrosion* 38: 261–265.
- Okada, T. 1984. Considerations of the stability of pit repassivation during pitting corrosion of passive metals. *J. Electrochemical Society* 131(5): 1,026–1,032.
- Okayama, S., Y. Uesugi, and S. Tsujikawa. 1987. The effect of alloying elements on the repassivation potential for crevice corrosion of stainless steels in 3% NaCl solution. *Corrosion Engineering* 36: 157–168.
- Patrick, W.C. 1986. *Spent Fuel Test—Climax: An Evaluation of the Technical Feasibility of Geologic Storage of Spent Nuclear Fuel in Granite—Final Report*. UCRL-53702. Livermore, CA: Lawrence Livermore National Laboratory.
- Ramirez, A.L., ed. 1991. *Prototype Engineered Barrier System Field Test (PEBSFT) Final Report* UCRL-ID-106159. Livermore, CA: Lawrence Livermore National Laboratory.
- Ruffner, D.J., G.L. Johnson, E.A. Platt, J.A. Blink, and T.W. Doering. 1993. Drift emplaced waste package thermal response. *Proceedings of the Fourth Annual International High-Level Radioactive Waste Management Conference*. La Grange Park, IL: American Nuclear Society: 538–543.
- Sridhar, N., and G.A. Cragnolino. 1992a. Long-term life prediction of localized corrosion of Fe-Ni-Cr-Mo high-level nuclear waste container materials. *Corrosion '93*, Paper No. 93197. Houston, TX: National Association of Corrosion Engineers.
- Sridhar, N., and G.A. Cragnolino. 1992b. Integrated waste package experiments. *NRC High-Level Radioactive Waste Research at CNWRA, July–December 31, 1992*. B. Sagar, ed. NUREG/CR-5817. Washington, DC: Nuclear Regulatory Commission.
- Sridhar, N., and G.A. Cragnolino. 1993. Applicability of repassivation potential for long-term prediction of localized corrosion of alloy 825 and type 316L stainless steel. *Corrosion* 49(11): 885–894.
- Sridhar, N., G.A. Cragnolino, and D. Dunn. 1993a. *Experimental Investigations of Localized Corrosion of High-Level Waste Container Materials*. CNWRA 93-004. San Antonio, TX: Center for Nuclear Waste Regulatory Analyses.
- Sridhar, N., J.C. Walton, G.A. Cragnolino, and P.K. Nair. 1993b. *Engineered Barrier System Performance Assessment Codes (EBSPAC) Progress Report—October 1, 1992, through September 25, 1993*. CNWRA 93-021. San Antonio, TX: Center for Nuclear Waste Regulatory Analyses.
- Sridhar, N., G.A. Cragnolino, and D. Dunn. 1993c. Integrated Waste Package Experiments. *NRC High-Level Radioactive Waste Research at CNWRA January–June 1993*. B. Sagar, ed. CNWRA 93-01S. San Antonio, TX: Center for Nuclear Waste Regulatory Analyses.
- Sridhar, N., G.A. Cragnolino, and D. Dunn. 1994a. Integrated Waste Package Experiments. *NRC High-Level Radioactive Waste Research at CNWRA July–December 1993*. B. Sagar, ed. CNWRA 93-02S. San Antonio, TX: Center for Nuclear Waste Regulatory Analyses.
- Sridhar, N., G.A. Cragnolino, D.S. Dunn, and H.K. Manaktala. 1994b. *Review of Degradation Modes of Alternate Container Designs and Materials*. CNWRA 94-010. San Antonio, TX: Center for Nuclear Waste Regulatory Analyses.
- Sridhar, N., G.A. Cragnolino, J.C. Walton, and D. Dunn. 1994c. Prediction of crevice corrosion using modeling and experimental techniques. *Application of Accelerated Corrosion Tests to Service Life Prediction of Materials*. G.A.

- Cragnolino and N. Sridhar, eds. ASTM STP 1194. Philadelphia, PA: American Society for Testing and Materials.
- Steinsmo, U. and H.S. Isaacs. 1993. Dissolution and repassivation kinetics of Fe-Cr alloys in pit solutions. *J. Electrochemical Society* 140(3): 643-653.
- Szklarska-Smialowska, Z. 1986. *Pitting Corrosion of Metals*. Houston, TX: National Association of Corrosion Engineers: 201-236.
- Tester, J.W. and H.S. Isaacs. 1975. Diffusional effects in simulated localized corrosion. *J. Electrochemical Society* 122(11): 1438-1445.
- Thompson, N.G., and B.C. Syrett. 1992. Relationship between conventional pitting and protection potentials and a new, unique pitting potential. *Corrosion* 48(8): 649-659.
- Tsujikawa, S., Y. Soné, and Y. Hisamatsu. 1987. Analysis of mass transfer in a crevice region for a concept of the repassivation potential as a crevice corrosion characteristic. *Corrosion Chemistry within Pits, Crevices, and Cracks*. A. Turnbull, ed. London, U.K.: Her Majesty's Stationary Office: 171-186.
- Tsujikawa, S., A. Miyasaka, M. Ueda, S. Ando, T. Shibata, T. Haruna, M. Katahira, Y. Yamane, T. Aoki, and T. Yamada. 1993. Alternative for evaluating sour gas resistance of low-alloy steels and corrosion-resistant alloys. *Corrosion* 49(5): 409-419.
- U.S. Department of Energy. 1988. *Site Characterization Plan for the Yucca Mountain Site, Nevada Research and Development Area, Nevada*. DOE/RW-0199. Washington, DC: U.S. Department of Energy.
- Walton, J.C. 1993. Effects of evaporation and solute concentration on presence and composition of water in and around the waste package at Yucca Mountain. *Waste Management* 13: 293-301.
- Zimmerman, R.M., R.L. Schuch, D.S. Mason, M.L. Wilson, M.E. Hall, M.P. Board, R.P. Bellman, and M.P. Blanford. 1986. *Final Report: G-Tunnel Heated Block Experiment*. SAND84-2620. Albuquerque, NM: Sandia National Laboratories.

4 GEOCHEMICAL NATURAL ANALOG RESEARCH

by E. C. Pearcy

Investigators: English C. Pearcy, William M. Murphy, James D. Prikryl, and Ronald T. Green (CNWRA)

NRC Project Officer: Linda A. Kovach

4.1 TECHNICAL OBJECTIVES

The technical objective of the Geochemical Natural Analog Research Project is to provide field, laboratory, and theoretical analyses of natural systems that are analogous to some aspects of the proposed high-level waste (HLW) repository at Yucca Mountain (YM), Nevada. These analyses are designed to develop a better understanding of the utility and limitations of natural analog studies when employed to support a license application for a HLW repository and to provide fundamental data on the long-term behavior of HLW within a repository environment. Natural systems that have operated for periods comparable to that required for HLW disposal (i.e., 10^3 – 10^4 yr and greater) (U.S. Environmental Protection Agency, 1989) provide the only opportunity to obtain observational knowledge of the long-term behavior of HLW components. Such information is important for support of long-term predictive models of repository performance assessment (PA) (Nuclear Regulatory Commission, 1987). Many factors (e.g., identities, morphologies, and sequences of secondary phases and their ability to sequester radionuclides) affecting the long-term behavior and interaction of the waste form and engineered barrier system (EBS) with the geochemical environment of the proposed repository are poorly known. The absence of this basic information severely limits the confidence with which PA models may be evaluated.

The Geochemical Natural Analog Research Project will be important in addressing uncertainties raised in a number of Compliance Determination Strategies (CDSs). Specific Key Technical Uncertainties (KTUs) that will be supported include those in CDSs for groundwater travel time (3.3), hydrogeologic processes (3.2.2.1), hydrologic conditions (3.2.2.9), perched water (3.2.2.12), mineral assemblages (3.2.3.3), geochemical processes (3.2.3.5), EBS (3.2.3.5.4), cumulative release (6.1), and individual

protection (6.2). Data and interpretations developed within the Geochemical Natural Analog Research Project will assist resolution of KTU topics including: (i) equal or increased capacity of alteration mineral assemblages to inhibit radionuclide migration, (ii) uncertainty in identifying geochemical processes that reduce radionuclide retardation, (iii) uncertainty in determining the magnitude of the effect of the geochemical processes that reduce radionuclide "retardation," (iv) conceptual model representations of the natural and engineered systems, (v) uncertainty in extrapolation of short-term laboratory test results to predict long-term performance of waste packages and EBSs, and (vi) uncertainty in modeling groundwater flow through unsaturated fractured rock caused by the lack of codes tested against field and laboratory data. Information presented in this chapter relates primarily to KTU topics (iv) and (vi).

The Geochemical Natural Analog Research Project is required by its nature to be an integrated effort combining expertise in geochemistry, hydrology, and structural geology among others. This need for interdisciplinary input is reflected in a number of technical interfaces with other Nuclear Regulatory Commission (NRC) Office of Nuclear Regulatory Research (RES) projects. An active and ongoing connection has been established with the PA Research Project (Chapter 6 of this document). Within the Geochemical Natural Analog Research Project, the hydrologic properties of welded silicic tuff from the Nopal I analog site are being measured; these data are being analyzed within the PA Research Project to allow more complete interpretation of long-term transport of uranium (U) through tuff at the site. Observations and measurements from the Geochemical Natural Analog Research Project are also being used within the Sorption Research Project (Chapter 5 of this document) as a comparison to laboratory studies. Additionally, results from the Geochemical Natural Analog Research Project

are being used to guide and develop the anticipated Near-Field Environment Research Project. Specifically, at the Nopal I site, it has been observed that alteration phases formed after uraninite (a spent fuel analog material) are dominated by the minerals uranophane, soddyite, and wecksite. The Nopal I analog suggests that these phases are likely to be important to radionuclide transport in a YM repository; the Near-Field Environment Research Project may include experiments to determine thermodynamic properties of those minerals so that their behavior may be modeled.

The Geochemical Natural Analog Research Project addresses needs identified by the Office of Nuclear Material Safety and Safeguards (NMSS) concerning assessment of the degree to which data from analogous sites may be extrapolated to support modeling for a repository site and evaluation of means to derive reasonable assurance that PA models can be validated using data from natural analogs. Specific NRC research needs that will to some degree be met through this project include: (i) comparison of laboratory sorption, mineral stability, leaching and kinetic data with observations from natural systems; (ii) evaluation of radionuclide transport in unsaturated tuff; (iii) assessment of the effects of oxidation state on leaching and radionuclide release; and (iv) investigation of coupled interactions affecting radionuclide release and transport.

Research within the Geochemical Natural Analog Research Project includes work at two sites: the Nopal I U deposit in the Peña Blanca district, Chihuahua, Mexico (field work initiated February 1991), and the Akrotiri archaeological site on Thera (Santorini), Greece (field work initiated June 1992). Earlier reports in this series documenting progress to date include Pearcy et al. (1993a,b; 1994); Leslie et al. (1993b); Pearcy and Leslie (1993); and Pearcy and Murphy (1991a,b,c, 1992). This report describes recent results from the Nopal I site.

The general objective of this phase of study was to evaluate the Nopal I deposit for evidence of fracture transport of U away from the deposit. Specific objectives of this study were to: (i) determine the distribution of U within and around the deposit; (ii) map the locations, orientations, and forms of fractures within and around the deposit; and (iii) measure the concentrations of U within and around fractures that intersect the deposit. These data will provide constraints

on the transport of U away from a concentrated source, and retention under YM-comparable conditions. Differences in U transport through areas with distinct fracture characteristics will allow assessment of the importance of those characteristics for transport modeling. This characterization will also provide information necessary for design and implementation of field percolation tests. Such tests are under consideration to address the KTUs in modeling groundwater flow through unsaturated fractured rock caused by a lack of codes tested against field data. Study of contaminant transport in well constrained, YM-comparable systems, will allow testing of the ability of transport models to predict transport in real systems where the end state is observable.

4.2 SIGNIFICANT TECHNICAL ACCOMPLISHMENTS

One of the chief concerns in seeking to establish a geologic repository for HLW is the possibility that hazardous radionuclides could escape engineered barriers and be transported to the accessible environment. Movement along fractures in the host rock of a repository is one mechanism by which hazardous radionuclides can be transported to the accessible environment. NRC Iterative Performance Assessment (IPA) indicates that matrix transport is insignificant; all release is associated with fracture flow, and retardation associated with fracture flow is identified by IPA as a critical issue (Wescott et al., 1994). The possibility of fracture transport must be evaluated for the long time periods required for HLW isolation [e.g., 10^4 yr and greater (U.S. Environmental Protection Agency, 1989)]. One approach to this problem is to study fracture transport in natural systems that are analogous to the repository system and that have operated for long time periods.

The Nopal I deposit (defined as the volume of rock at Nopal I containing easily visible U mineralization) is roughly cylindrical in form with gross horizontal dimensions of about 18x30 m with a nominal ore zone extending some 100 m vertically. The upper portion of this well-defined body of U mineralization is hosted by heavily fractured, silicic tuffs (Nopal and Coloradas Formations), whereas the lowermost portion of the deposit occurs in a basal conglomerate (Pozos Formation). Mining during the late 1970s and early 1980s exposed the upper portion of the deposit on two broad horizontal surfaces with about a 10-m vertical

separation (Levels +00 and +10). Together, these surfaces completely span the outcrop of the deposit and expose much of the surrounding host rock, providing an opportunity to study transport of U from the deposit out into the host tuff.

4.2.1 Methods

Portions of Levels +10 and +00 of the Nopal I deposit were cleared of loose rock, soil, and debris; clearing began with picks and shovels and was completed with brooms. This effort provided a nearly continuous bedrock exposure across the outcrop of the deposit and the surrounding tuff (about 1,200 m² of the Level +10 surface and about 200 m² of Level +00). Spatial control was established using traditional plane table surveying techniques. A permanent 1×1-m grid with axes oriented NS and EW was constructed over the cleared areas using 6.4-cm P-K nails driven into the tuff to provide a location reference framework. This grid provides the location references in this report.

General U distributions within and around the deposit were mapped by gamma intensity. A contact gamma survey of the cleared bedrock areas was conducted with measurements taken at the intersections of the 1×1-m grid lines. Readings (mR/hr) were recorded on a survey meter (Ludlum model 3) equipped with a Geiger-Müller detector (Ludlum model 44-6).

Geologic features of the cleared areas of Levels +10 and +00 were mapped at the detailed scale of 1:25. Occurrence of U minerals, host rock type, and host rock alteration, as well as fracture locations and forms were mapped with reference to the 1-m grid. Fracture orientations were measured using standard Brunton transit techniques. Original field data were drafted on Mylar™ sheets from which they were digitized and compiled with ARC/INFO software for analysis and calculations. Analysis of fracture orientation data was accomplished using STEREO® software.

A 28-m length of a major EW fracture set located about 13.5 m N on the reference grid was sampled by collecting portions of fracture-filling minerals at approximately 1-m intervals. The 13.5-m N fracture set is a subplanar feature with a near-vertical dip; the trace of the set is approximately perpendicular to the W margin of the deposit. This fracture set was observed to be the longest and most continuous to intersect the deposit; fracture aperture varies from 2 to 7

mm. Sampling of the material filling the fracture was accomplished by scraping fracture-filling material from the rock surfaces using a steel pocket knife.

U contents of fracture-filling minerals and bulk rock samples were measured by gamma spectrometry using a Canberra system consisting of an intrinsic germanium detector (30-percent efficiency at 1.33 MeV for ⁶⁰Co), model 4610 multichannel analyzer board, and system 100 software for data acquisition and analysis. ²³⁴U/²³⁸U ratios were measured by alpha spectrometry with an EG&G ORTEC system including model 576A dual spectrometers with ion-implanted-silicon charged particle detectors, model 920-16 multichannel buffer, ALPHAMAT analysis software for acquisition control, and MAESTRO II multichannel analyzer emulation software for analysis of spectral data.

4.2.2 Results

Clearing and geologic mapping of the Level +10 and +00 surfaces showed that the area U mineralization is easily visible on the outcrop, is well-defined, is roughly elliptical in form, and has maximum horizontal dimensions of about 18×30 m. The host rock exposed in the cleared areas, Nopal Formation tuff, has been altered in the vicinity of the deposit. The main secondary minerals observed are kaolinite [Al₂Si₂O₅(OH)₄] and iron oxides (variably hematite [Fe₂O₃] and goethite [alpha-FeO•OH]). The abundance of kaolinite tends to increase close to the deposit. Iron oxides tend to be concentrated along fractures, though some highly fractured areas have generally abundant iron oxides.

Locations, lengths, and forms of 11,374 fractures were mapped. These fractures comprise the subset of those present that are resolvable at a scale of 1:25. Rock within the deposit area, and the surrounding tuff, is highly fractured (Figure 4-1). Most of the fractures are short (less than 1 m in length) and tend to occur as groups of subparallel breaks. More continuous fissures (i.e., those extending for tens of meters) are less common at Nopal I. In general, fractures close to the area of visible U mineralization tend to be more abundant and less continuous than those farther away.

Orientations (strike and dip) were measurable on 895 fractures within the cleared areas. These data show that the fractures may be grouped into six major sets. Most measurements have azimuths within about

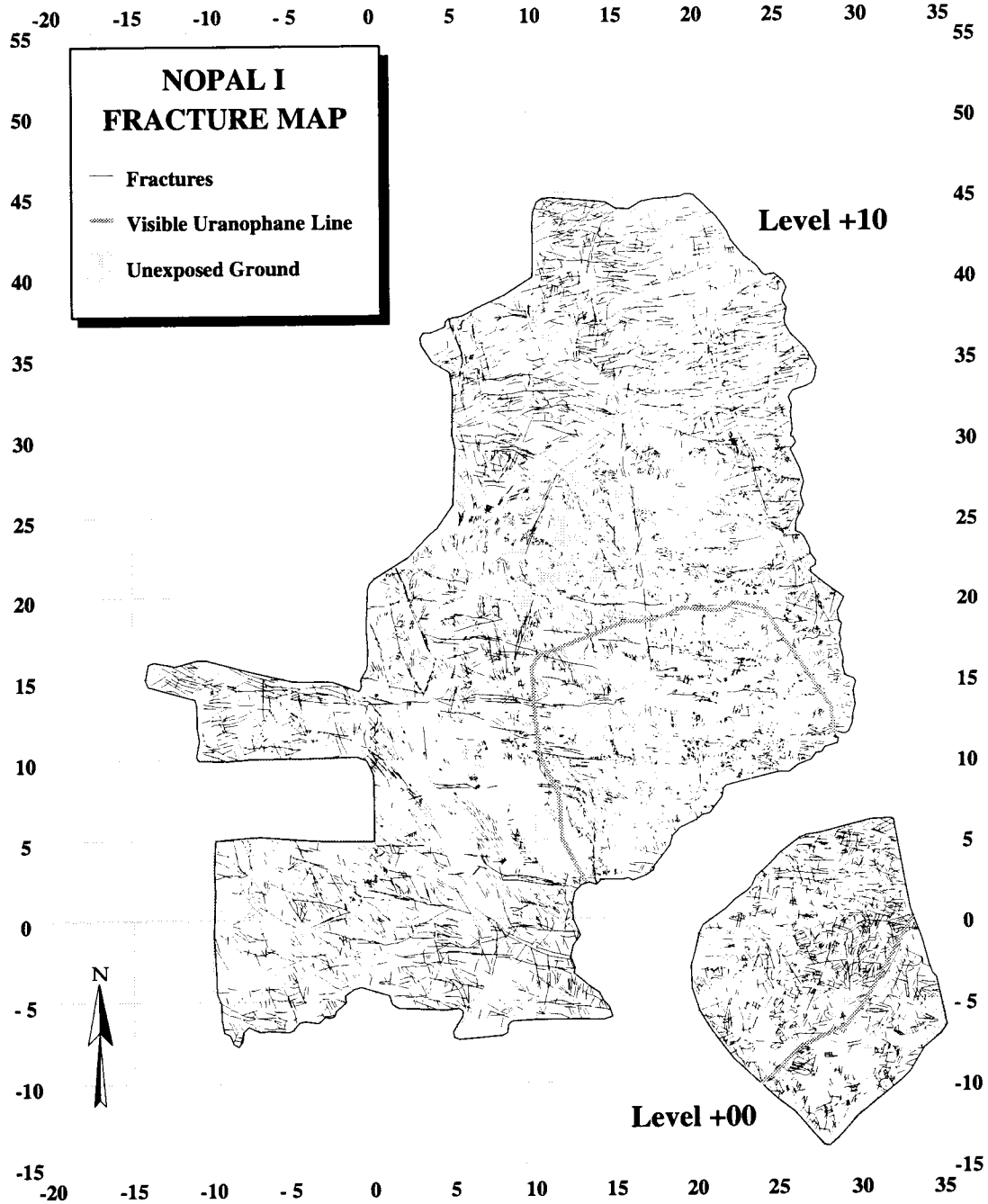


Figure 4-1. Fracture mapping of the Nopal I deposit was carried out at a scale of 1:25. Original field data were digitized and were manipulated using ARC/INFO software. This map includes 11,374 individual fractures. The visible uranophane line indicates the limit of visible U mineralization and marks the nominal edge of the deposit. Level +00 is 10 m lower in elevation than Level +10. The gap between the levels corresponds to the horizontal component of the slope of the face separating the levels and to large debris piles at the base of that face. Perimeter scales are in meters.

$\pm 30^\circ$ of EW; fractures with trends closer than 30° to NS are relatively rare at Nopal I. Fractures at Nopal I typically exhibit minor horizontal offsets (e.g., <5 cm). Cross-cutting relationships suggest a relative sequence of formation: (i) NE-trending fractures, (ii) NW-trending fractures, and (iii) EW-trending fractures. Within the mapped areas, N-dipping fractures are much more abundant than S-dipping fractures (70 percent N-dipping). Both N- and S-dipping fractures tend to have steep inclinations (average dip of 895 fractures is $63.0 \pm 18.5^\circ$ at 1 σ). The lack of low-angle fracture measurements partially represents sampling bias introduced by observations made on an artificially constructed surface that is nearly horizontal and which therefore intersects few fractures with shallow inclinations. Low-angle fractures are, nevertheless, significant features of the Nopal I deposit as evidenced by exposures of undulating, low-angle fissures in vertical faces nearby and some portions of the cleared areas of Levels +10 and +00 with well-developed slickensides. However, only limited observations of low-angle fractures are possible on the cleared areas examined in this study.

The major fracture set at 13.5 m N may be considered a mesofracture (i.e., aperture >1 mm and trace length >10 m). The concentration of U in the 13.5 m N fracture set varies systematically with distance from the deposit. U concentrations in fracture-filling material from the portion of the fracture located within the deposit are quite high (>7 wt% U), and there is a general decrease in the concentration of U in the fracture-filling material with distance from the western edge of the deposit. Close to the deposit (e.g., within 10 m), the concentration of U in the fracture-filling material is one to two orders of magnitude greater than U concentrations in the bulk tuff at comparable distances from the western boundary of the deposit.

A total of 1,489 contact gamma measurements was made. Contact gamma mapping of the cleared areas of Levels +10 and +00 showed the highest values to be 28 mR/hr and local background values to be about 0.05 mR/hr (Figure 4-2). The gamma survey readings are interpreted as proportional to the U concentration because gamma spectrometry of powdered bulk rock samples indicates: (i) thorium concentrations are approximately constant throughout the area (30–50 ppm), (ii) U concentrations vary from 20 to 23,000 ppm in the same area, and (iii) bulk solids are close to secular

equilibrium with respect to the ^{238}U and ^{232}Th decay series.

The results of the field gamma survey clearly demarcate the limits of the U mineralization on Levels +10 and +00. A field reading of 1.0 mR/hr corresponds approximately to a bulk rock U concentration of 500 ppm, which is also the apparent limiting value for the presence of U-bearing minerals. The Level +10 exposure of the deposit consists of an interior portion with low-gamma intensity (readings less than 1.0 mR/hr) without apparent U-bearing minerals [i.e., undetected in X-ray diffractometry (XRD) analysis or by binocular microscopy] and an outer ring 1 to 4 m wide of relatively high-gamma intensity (up to 28 mR/hr) containing abundant, but irregularly distributed, U minerals. Outside the deposit, on Level +10, the gamma intensity drops off quickly. This drop-off in gamma intensity is more abrupt on the western margin than on the northern margin of the deposit. North of the deposit, gamma intensities well above background (four to ten times background) extend continuously from the edge of the area of visible U mineralization for about 20 m. On Level +00, gamma intensity drops more slowly with distance from the deposit than on Level +10. This difference is particularly evident to the SE of the deposit on Level +00.

4.2.3 General Transport Through Fractured Tuff Surrounding the Deposit

Gamma intensity patterns, mineral distributions, and fracture patterns suggest that U has been remobilized from the area of the original deposit and transported away from the deposit along fracture paths. Geologic mapping of the Nopal I deposit shows that visible U mineralization is limited to a small well-defined area about 18×30 m. The roughly annular pattern of gamma intensities corresponds to variations in U and non-U mineral occurrence. The limits of the area of U mineralization correspond well to an abrupt decrease in gamma intensity on Level +10 (Figure 4-2), and the interior of the deposit has low-gamma intensity and no observable U minerals. Similarly, XRD analyses of bulk tuff samples from the interior portion of the deposit show abundant alunite [$\text{KAl}_3(\text{SO}_4)_2(\text{OH})_6$], which is not present in the outer high-gamma intensity ring (Leslie et al., 1993b). On Level +00, gamma intensities greater than 0.45 mR/hr extend well beyond the area of visible U mineralization (Figure 4-2). This

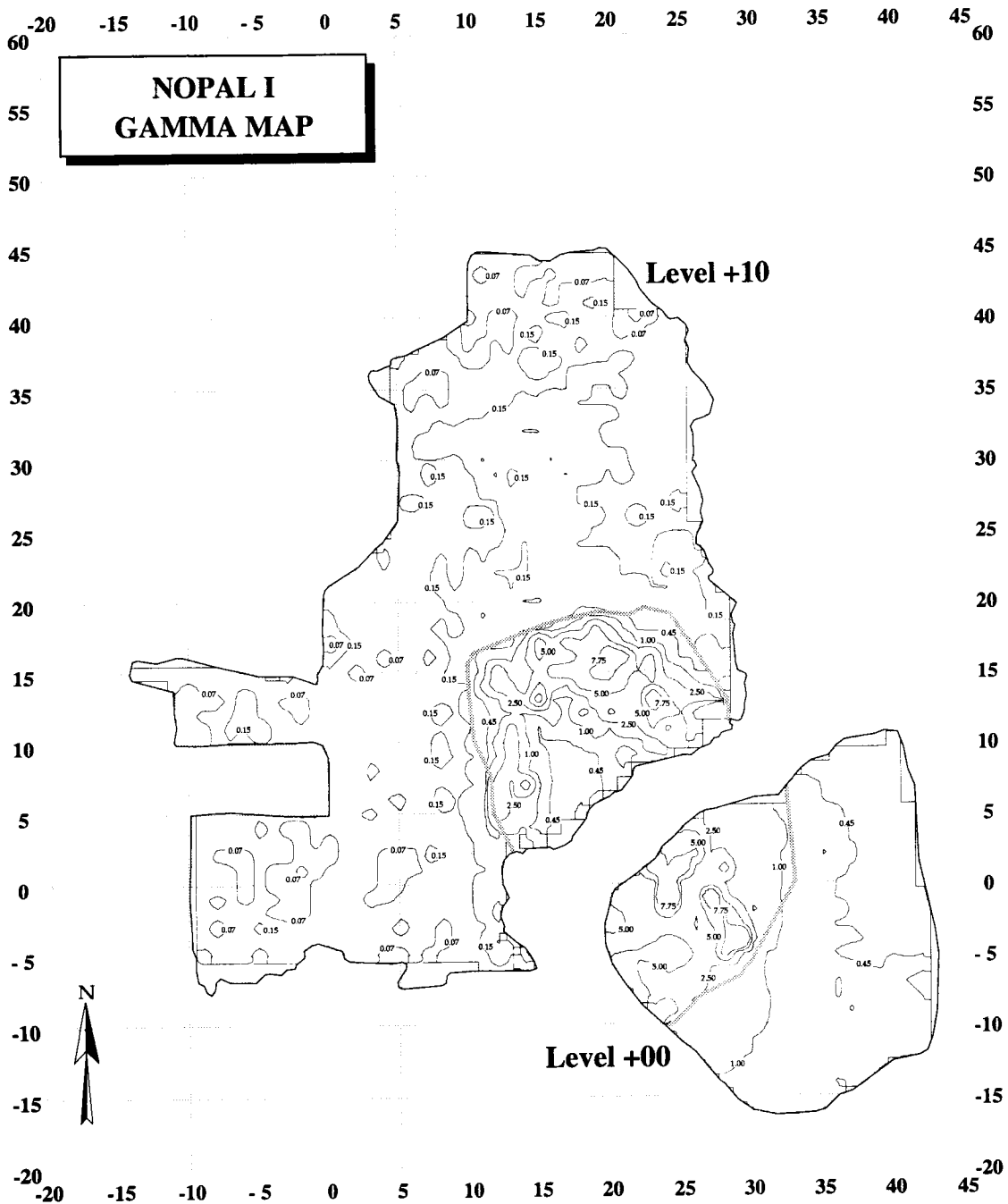


Figure 4-2. This map gives the results of a contact gamma survey conducted of the cleared areas of the Nopal I deposit with measurements made on a 1x1-m grid. The curved, shaded line indicates the limit of visible U mineralization and marks the nominal edge of the deposit. Contours have units of mR/hr. The areas of highest gamma intensity are well defined and, on Level +10, have a semiannular form. Anomalous gamma values are asymmetrically distributed around the deposit with a broader area of high-gamma values extending on Level +10 to the N than to the W and on Level +00 extending preferentially to the SE.

extension is most prominent along a SE-trend that corresponds to the downslope direction of the premining surface. Tuff in the area of this extension is heavily weathered to clay (mainly smectite with minor kaolinite). These observations suggest that the greater extent of high U concentrations away from the deposit on Level +00 reflects transport of U away from the deposit in the downslope direction during weathering of the deposit.

The primary ore mineral assemblage of the Nopal I deposit has been shown to be uraninite \pm kaolinite \pm pyrite \pm quartz (Pearcy et al., 1993b). Alteration of primary pyrite by interaction with oxidizing fluids is a likely mechanism leading to formation of the alunite and low pH solutions. Conditions under which alunite forms (oxidizing, low pH) are also conditions that tend to mobilize U. Mobilization of U associated with alunite formation is a probable explanation for the spatial correspondence among low-gamma intensities, the absence of U minerals, and the presence of alunite in the central portion of the deposit.

Contact gamma measurements indicate the presence of anomalous U (i.e., U concentrations above local background values) extending to the N of the deposit (i.e., outside the area of visible U mineralization) (Figure 4-2). This N-trending area of anomalous U may represent transport of U from the area of primary deposition. This interpretation is supported by U-series measurements (Leslie et al., 1993a), which have documented a significant U mobilization event at Nopal I at about 54 ka. If the area of visible U mineralization at Nopal I represents a source area (i.e., the distribution of U prior to subsequent transport), then the N-trending area of anomalous U may be interpreted as the horizontal transport vector along effective flow paths. Using the 0.15-mR/hr boundary (of the continuous area of anomalous U concentrations) as a basis for comparison of transport distances, there is evidence of relatively little transport from the area of visible U mineralization to the W (2 to 3 m maximum), whereas there is evidence of greater transport distance to the N (about 20 m).

There is a strong correspondence between the distribution of anomalous U concentrations to the N of the deposit and the locations of major fractures (i.e., fractures with traces extending more than 10 m). This correspondence suggests that individual major fractures

were more important to the long distance (e.g., tens of meters) transport of U away from the deposit than was the general fracture network comprising thousands of less continuous fractures.

The greater importance of individual major fractures for U transport compared to U transport through the general fracture network is supported by analyses of the general fracture density patterns. Fracture distribution within and around the Nopal I deposit is characterized in two ways (using a 1x1-m grid): (i) as the sum of fracture lengths per square meters, and (ii) as the number of fractures per square meters. Fracture density by length (i.e., m/m²) appears randomly distributed across the map area; there is no apparent correspondence to areas of U occurrence (Figure 4-3). This interpretation is confirmed by a lack of significant statistical correlation between gamma intensities and fracture density by length ($r^2 < 0.05$). Therefore, although individual major fractures appear to have been important to U transport, variations in fracture length density (which is insensitive to fracture continuity) do not appear to have been important for U transport. Fracture density calculated by frequency (i.e., number of fractures/m²) shows a general increase close to the deposit and somewhat higher values N of the deposit (Figure 4-4). This broad correspondence between fracture density by frequency and gamma intensity, which is apparent upon inspection of the maps, is not supported by a detailed comparison; there is no significant statistical correlation between fracture density by frequency and gamma intensity ($r^2 < 0.02$).

4.2.4 Transport Along a Major Fracture Set

The major EW fracture at 13.5 m N intersects the Nopal I deposit and extends across the Level +10 surface to the W. The general decrease in U concentration in the filling of the 13.5-m N fracture with increasing distance from the edge of the deposit suggests transport of U away from the deposit (Figure 4-5). This hypothesis is supported by several lines of evidence: (i) structural analysis of relative times of formation among Nopal I fracture sets, (ii) mineralogic gradients within the fracture-filling, and (iii) U-series isotopic measurements.

W-trending fractures at Nopal I, of which the fracture at 13.5 m N is one, are structurally the most recent among the various fracture sets at the site.

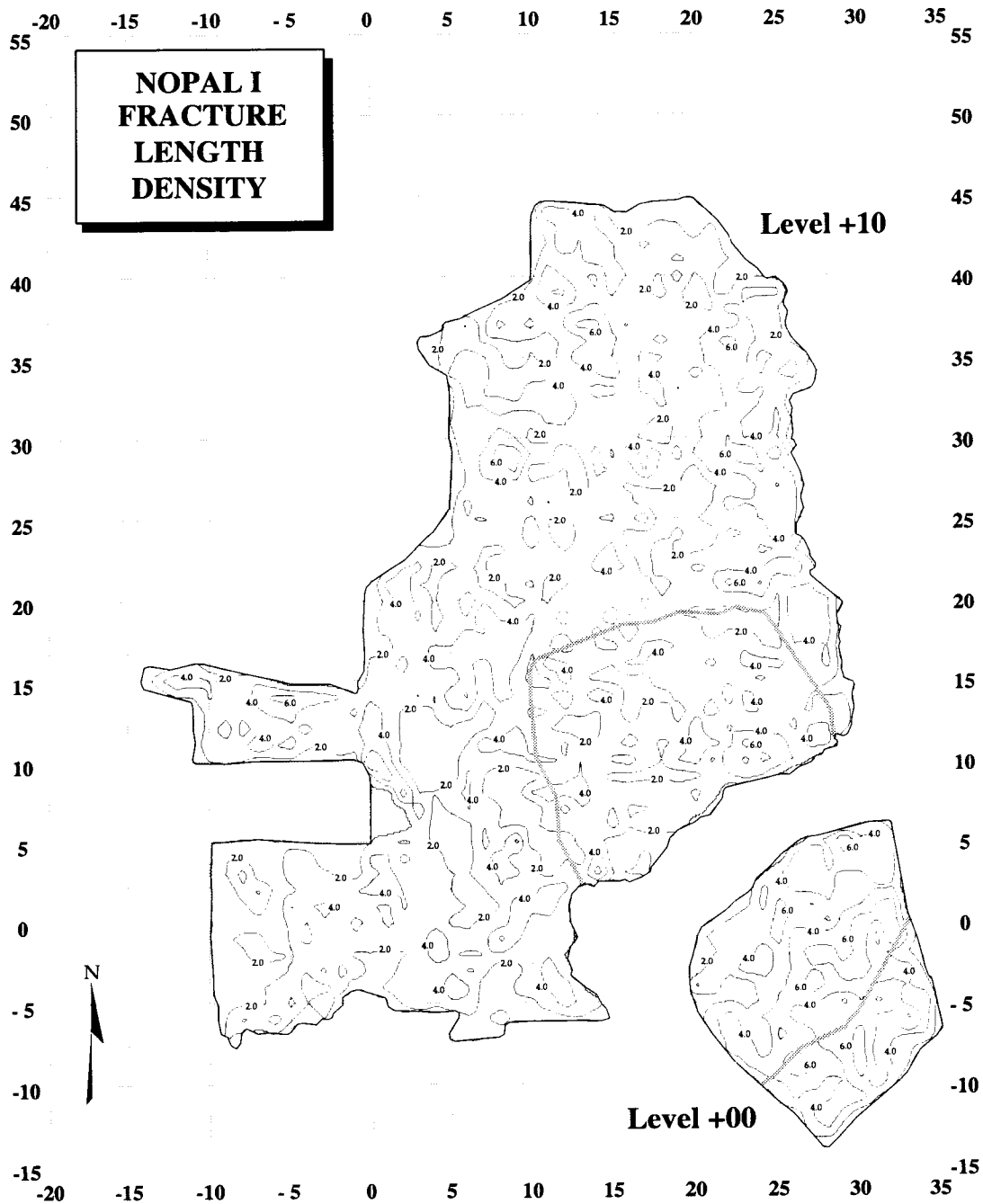


Figure 4-3. This map shows that fracture density calculated by length appears randomly distributed across the map area; there is no apparent correspondence to areas of U occurrence. The curved, shaded line indicates the limit of visible U mineralization and marks the nominal edge of the deposit. Contours have units of meters of fracture length per meters².

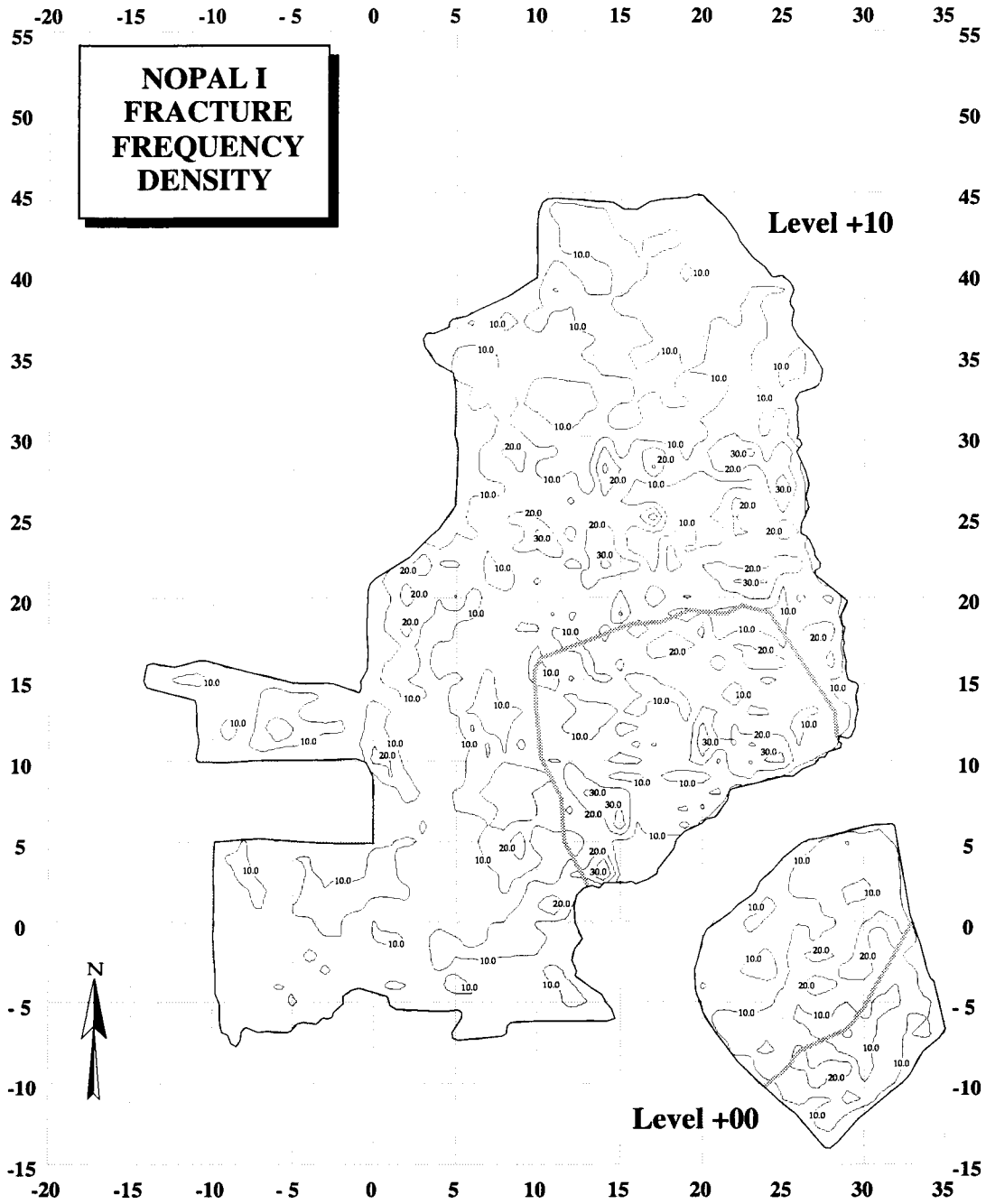


Figure 4-4. This map shows that there is a broad tendency for increased fracture frequency density in areas close to the Nopal I deposit as opposed to those areas farther away. This broad correspondence is not supported by a detailed comparison; there is no significant statistical correlation between fracture density by frequency and gamma intensity. The curved, shaded line indicates the limit of visible U mineralization and marks the nominal edge of the deposit. Contours have units of number of fractures per meters².

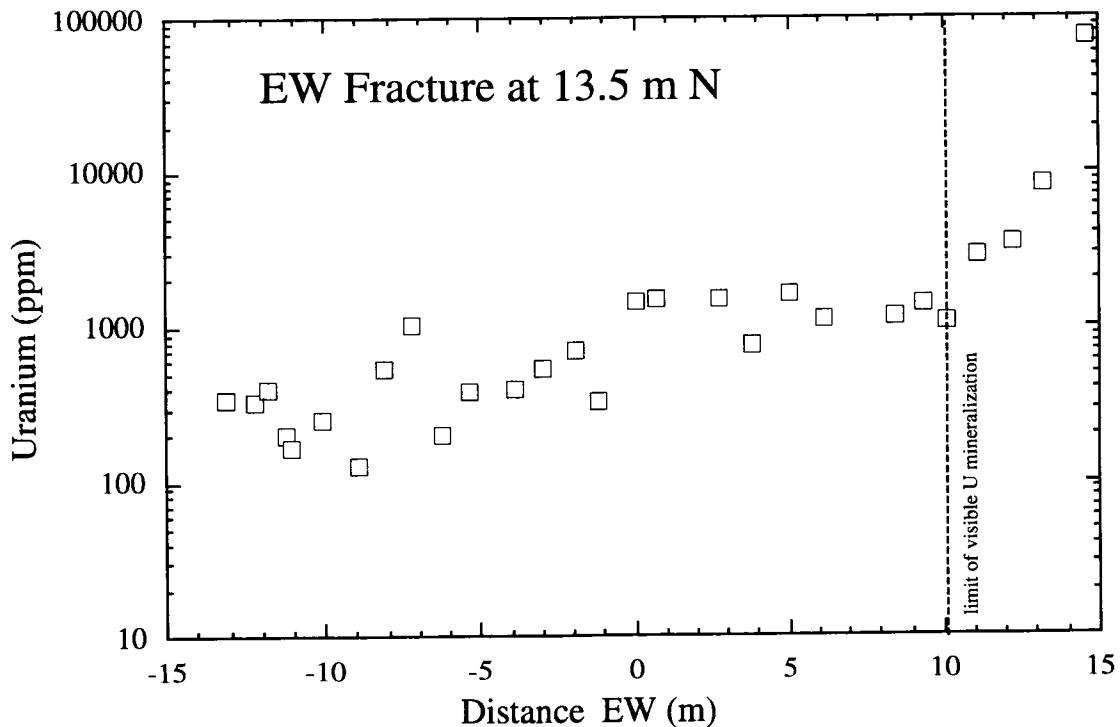


Figure 4-5. Concentration of U in the fracture-filling material along the major EW fracture at 13.5 m N. The vertical dashed line indicates the edge of the Nopal I deposit. Uncertainties in U concentration are much less than the plot symbol size.

Further, the 13.5-m N fracture is observed to crosscut the U deposit itself; that is, the 13.5-m N fracture forms a physical discontinuity within the deposit not offset by internal features of the deposit, indicating that the fracture is younger than the U deposit. Therefore, it is unlikely that U was transported along the 13.5-m N fracture toward the deposit during primary accumulation of U. Formation of the 13.5-m N fracture after accumulation of the U deposit presents a geometry in which the fracture extends from tuff outside the deposit where U concentrations are about 10 ppm to within the deposit where U concentrations average about 1,100 ppm (George-Aniel et al., 1991). This concentration gradient, present at the time of formation of the 13.5-m N fracture, is more likely to have resulted in movement of U away from the deposit than toward the deposit.

The mineralogical composition of the fracture-filling material offers additional constraints on the transport of U in the 13.5-m N fracture. Notably, XRD indicates that the amount of jarosite in the fracture-

filling diminishes with distance from the deposit. Jarosite occurs most commonly in acidic, sulfate-rich environments developed as a result of pyrite [FeS_2] oxidation during weathering (Nordstrom, 1982). The primary mineral assemblage of the Nopal I deposit has been established as uraninite \pm kaolinite \pm pyrite \pm quartz (Pearcy et al., 1993a). The occurrence of pyrite within the deposit and the absence of high concentrations of S or U in the host rocks outside the deposit (Pearcy et al., 1993a) suggest that the deposit itself was the source of both the S in the jarosite and the U in the fracture-filling. Although both the U content of the fracture-filling and the quantity of jarosite decrease with distance from the deposit, it is unlikely that jarosite is directly responsible for this U distribution because jarosite tends not to sequester U (or Th) during its formation (Dickson and Herczeg, 1992).

U-series isotopic measurements have documented significant U transport around the deposit during the last 1 Ma with a specific event dated at about 54 ka (Leslie et al., 1993a). Tuff samples collected in

generally fractured tuff along a 2-m transect across the western margin of the deposit show U-series disequilibria, indicating U transport outside the deposit during the last 1 Ma. This 2-m transect is approximately parallel to the 13.5-m N fracture and located about 4.4 m to the S. Paragenetically late, U-rich opal collected from the deposit about 5 m S of the 13.5-m N fracture has been dated by U-series techniques at 54.3 ± 2 ka. U-series dating of a U-enriched caliche collected from a remnant of the premining surface located about 30 m S of the 13.5-m N fracture also indicates significant U transport at 53.6 ± 8 ka. This evidence of relatively recent remobilization of U previously accumulated in the deposit is consistent with transport away from the deposit. Further, the discovery of a 54 Ka caliche adjacent to the deposit establishes the position of the deposit at the surface and hence subject to

hydrologically unsaturated, chemically oxidizing conditions for at least that period.

Anomalous U concentrations have been measured along the 13.5-m N fracture for a distance of 23.2 m outside the Nopal I deposit. A linear projection of the generally decreasing values outside the limit of the deposit predicts that background values would be reached at 26.3 m from the deposit edge (Figure 4-6). This distance is comparable to the maximum extent of anomalous U concentrations measured by contact gamma survey, which are also interpreted to be a result of U transport along major fracture paths. Maximum U transport distances away from the edge of the Nopal I deposit through tuff generally fractured at a centimeter scale are observed to be only about 0.5 to 1 m (Pearcy and Leslie, 1993). Transport distances along effective mesofracture paths are therefore at least 20 times greater

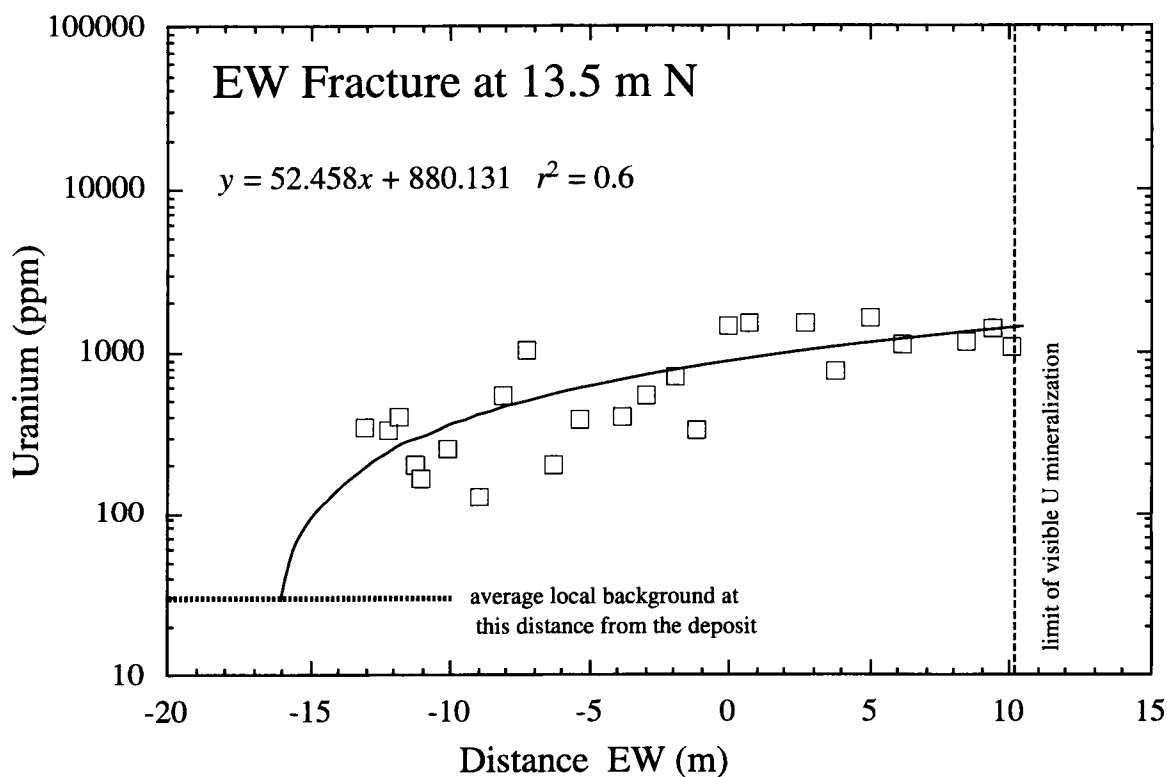


Figure 4-6. This plot shows the concentrations of U in the fracture-filling material along the major EW fracture at 13.5 m N outside the edge of the Nopal I deposit. A linear fit to these data predicts the concentration of U in the fracture-filling will reach local background levels (about 30 ppm) at 26.3 m from the edge of the deposit. Uncertainties in U concentration are much smaller than the plot symbol dimension.

than transport of U through tuff with a complex network of microfractures.

The decrease in U content along the 13.5-m N fracture away from the deposit could be due to chemical interaction (e.g., sorption), or chemical reaction (e.g., pH increase) of the U-transporting fluid with the wall rock, or differences in the nature of the interaction of the fluid with the wall rock due to varying composition/mineralogy of the bulk rock with distance from the deposit [e.g., George-Aniel et al. (1991); Ildefonse et al. (1990)]. As discussed earlier, alteration of the primary ore mineral assemblage appears likely to have produced an oxidizing, low pH solution capable of transporting U away from the area of original deposition and out along the 13.5-m N fracture. The decrease in U concentration in the fracture-filling material with distance may reflect reaction of such a fluid with the fracture wall rock.).

Earlier research (Pearcy and Leslie, 1993) demonstrated that a portion of the U transported away from the deposit along the 13.5-m N fracture moved out of the fracture and into tuff comprising a complex microfracture network (linear fracture densities >1 fracture cm) through which the 13.5-m N fracture forms a sub-planar discontinuity (Figures 4-7 and 4-8). Data for these perpendicular transect measurements are given in Table 4-1. U concentrations along each of the five perpendicular traverses drop off steeply and flatten with distance from the 13.5-m N fracture as the concentrations approach local background values.

It is interesting to note that the anomalous U within the 13.5-m N fracture is not reflected in the general gamma intensity map of Level +10 (Figure 4-2). This absence is because contact gamma measurements were made at the intersections of the 1x1-m sample location grid lines. Since the 13.5-m N fracture lies between the 13- and 14-m N lines, the fracture was missed in the gamma survey. Additionally, though the U concentrations in the 13.5-m N fracture-filling are anomalously high, for most of the fracture length the concentrations are close to or below the limits of detection of the field gamma meter used for the survey.

4.2.5 Relative Effectiveness of Mesofracture, Microfracture, Matrix Retardation and Retention of Uranium

Using the measurements discussed in preceding sections and data available from earlier research, it is possible to estimate the relative effectiveness of mesofracture, microfracture, and matrix retardation and retention for U transport at the Nopal I deposit. Consideration of the U contents retained in these three areas allows a qualitative ranking of effective retardation and retention. It is possible that additional U was transported along these paths and not retained (though there is no evidence for that). Nevertheless, U content estimates provide a basis for comparison among the three types of retardation and retention measured at the site.

The major fracture at 13.5 m N has a trace length greater than 10 m and an aperture of 2–7 mm and so may be referred to as a mesofracture. The original 2–7-mm opening has been essentially filled with mineral precipitates (e.g., iron oxides) that retain a portion of the U transported along this fracture. Measurements indicate that U was transported along the 13.5-m N fracture, away from the Nopal I deposit, for a distance of at least 23.2 m; projecting the U concentration trend to local background values suggests the likelihood of anomalous U transport to about 26.3 m W of the edge of the deposit. The average U concentration along that length (based on a linear fit to the concentrations outside the deposit) is 720 ppm U. Therefore:

$$\begin{aligned} \text{U content} &= (\text{length}) \times (\text{average aperture}) \\ &\times (\text{average U concentration}) = 91 \text{ ppm U m}^2 \end{aligned} \quad (4-1)$$

This value represents the two-dimensional (2D) U content of the portion of the 13.5-m N fracture outside the deposit. Regardless of the amount of U that may have been transported along this path, 91-ppm U m² is the amount that was retarded during mesofracture flow and retained to the present.

Similarly, the amount of U that was sequestered until present after transport out of the 13.5-m N fracture and into the enclosing microfracture network may be estimated by considering the portion of the system bounded to the E by the edge of the deposit, to the W by the projected limit of anomalous U

Major EW Fracture at 13.5 m N on Level +10 m

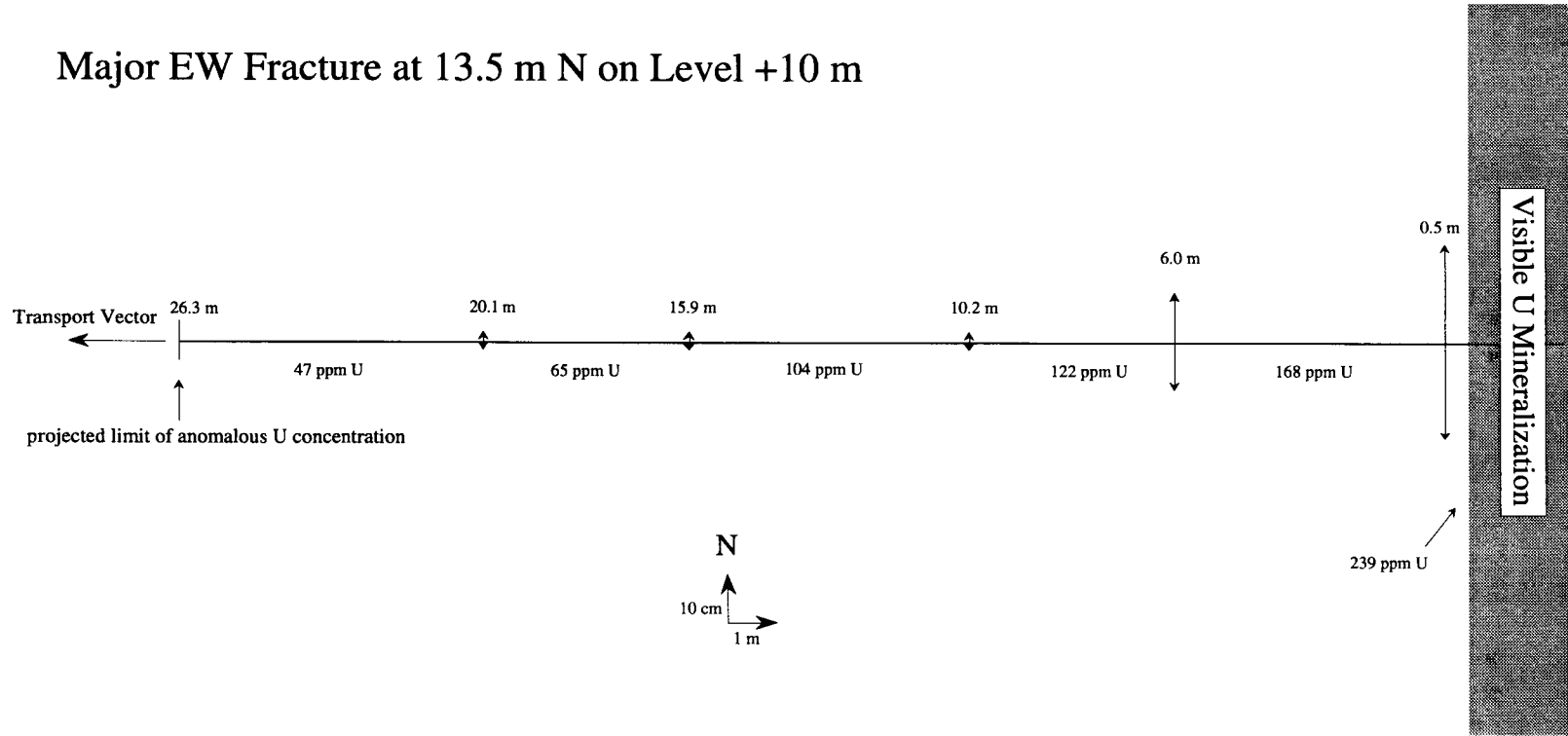


Figure 4-7. This drawing schematically illustrates the spatial relationships among the major EW fracture at 13.5 m N, the sample transects collected perpendicular to the fracture, and the edge of the Nopal I deposit. NS arrows give the distances of anomalous U concentrations from the major fracture; locations for each traverse are the distance from the edge of the deposit. U concentrations are given as the average for the microfractured areas N and S of the major fracture for each interval. Note that the drawing is scaled so that distances NS are expanded 10 times compared to distances. EW.

Model Uranium Concentrations Along a Major Fracture at 13.5 m N

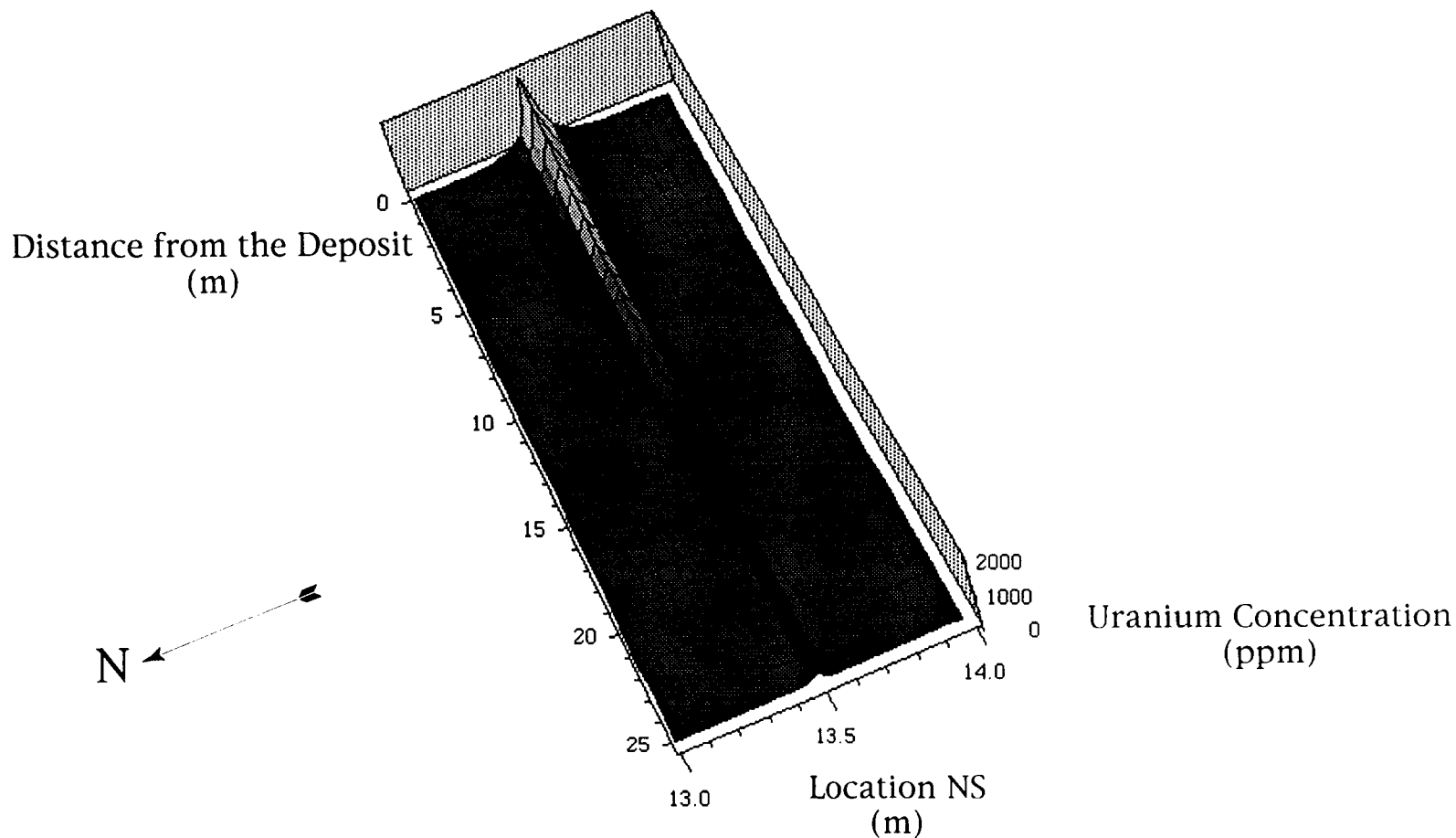


Figure 4-8. This model schematically illustrates variations in U concentrations along the major fracture at 13.5 m N and along transects perpendicular to the major fracture (i.e., Figure 4-7). Note that distances NS are expanded about 12 times compared to distances EW. Data which this surface approximates are given in Table 4.1.

Table 4-1. Uranium content of microfractured tuff measured along traverses perpendicular to the EW fracture at 13.5 m N

Traverse at 0.5 m from Deposit Edge ¹		Traverse at 6.0 m from Deposit Edge ¹		Traverse at 10.2 m from Deposit Edge ²		Traverse at 15.9 m from Deposit Edge ²		Traverse at 20.1 m From Deposit Edge ³	
Distance Interval from Fracture (cm)	Uranium Concentration (ppm)	Distance Interval from Fracture (cm)	Uranium Concentration (ppm)	Distance Interval from Fracture (cm)	Uranium Concentration (ppm)	Distance Interval from Fracture (cm)	Uranium Concentration (ppm)	Distance Interval from Fracture (cm)	Uranium Concentration (ppm)
0.00 to 3.00	898.70	0.00 to 3.00	205.90	0.05 to 0.53	177.40	0.25 to 0.61	110.60	0.00 to 0.84	67.90
0.00 to 3.00	315.10	0.00 to 3.00	150.70	0.73 to 0.85	109.30	0.81 to 0.99	43.50	1.04 to 1.21	72.70
3.00 to 6.00	213.10	3.00 to 6.00	48.43	1.05 to 1.31	87.95	1.19 to 1.35	36.50	1.41 to 1.62	62.50
3.50 to 7.50	175.90	3.50 to 7.50	77.76	1.52 to 1.72	102.70	1.55 to 1.75	32.20	1.82 to 2.02	52.60
7.50 to 13.50	146.10	6.00 to 9.00	38.57	1.92 to 2.12	104.00	1.95 to 2.51	35.62	2.22 to 2.41	46.64
9.00 to 12.00	158.00	10.50 to 14.50	64.32	2.32 to 2.48	126.70	—	—	—	—
13.50 to 19.50	84.84	10.00 to 13.00	38.40	2.67 to 2.91	128.50	—	—	—	—
12.00 to 15.00	130.40	14.50 to 18.50	70.48	3.11 to 3.19	112.50	—	—	—	—
28.50 to 31.50	91.65	—	—	—	—	—	—	—	—
37.00 to 33.00	134.85	—	—	—	—	—	—	—	—
46.50 to 53.50	53.36	—	—	—	—	—	—	—	—
46.50 to 53.50	124.69	—	—	—	—	—	—	—	—

¹Traverses at 0.5 and 6.0 m were collected both N (bold) and S of the EW fracture
²Traverses at 10.2 and 20.1 m were collected S of the EW fracture
³Traverse at 15.9 m was collected N of the EW fracture

concentration in the 13.5-m N fracture (26.3 m from the edge of the deposit), and bounded to the N and S by systematically variable distances corresponding to the limits of anomalous U concentration measured along the perpendicular traverses (Figure 4-7). The limit of likely influence of U transport from the major EW fracture into the microfractured tuff was chosen as the limit of continuous decrease in U concentration. Heterogeneities in these patterns make estimating the actual distances highly uncertain; this approach therefore gives a minimum estimate. Using the area limits illustrated in Figure 4-7, and linear interpolations of U concentration between adjacent traverses, the U content of the microfractured rock enclosing the 13.5-m N fracture is about 420 ppm U m².

Therefore, the dimensionless ratio:

$$\frac{(420 \text{ ppm U m}^2)}{(91 \text{ ppm U m}^2)} = 5 \quad (4-2)$$

describes the amount of U retained during transport into the microfracture network adjacent to the 13.5-m N fracture compared to the amount of U retained during transport within the 13.5-m N fracture. Because the lengths of the anomalous U paths into the microfracture network are minima, this ratio is also a minimum. Whatever the mechanisms for the U retardation (e.g., precipitation, sorption), it appears that much more U remains sequestered within the microfracture network than within the mesofracture along which the U was transported to the microfracture network.

For comparison with these fracture-controlled U inventories, the relative effectiveness of matrix retardation and retention of U at Nopal I may be estimated using measurements from microfracture autoradiography (Pearcy and Leslie, 1993). The microfractures are largely filled with uranophane [Ca(UO₂)₂Si₂O₇•6H₂O], which has a U concentration of 5.6×10⁵ ppm. The microfractures studied have apertures varying from 100 to 230 μm. Using 100 μm, the one-dimensional (1D) U content is 5.6×10⁴ ppm U mm. Autoradiographic measurements show transport of U out from the uranophane-bearing microfractures to a maximum distance of 0.28 mm (Pearcy and Leslie, 1993). Based on the specific activity of ²³⁸U, assuming secular equilibrium consistent with the location of the samples within the deposit and U-series measurements

on other samples from within the deposit and an alpha particle attenuation in tuff matrix of 4 μm, the average transported U content along these matrix paths is about 9,000 ppm U.

The 1D U content along the matrix diffusion path is:

$$(9,000 \text{ ppm U}) \times (0.28 \text{ mm}) = 2,520 \text{ ppm U mm} \quad (4-3)$$

and the ratio of the matrix U content to the microfracture U content is

$$\frac{(2,520 \text{ ppm U mm})}{(5.6 \times 10^4 \text{ ppm U mm})} = 0.05 \quad (4-4)$$

This analysis suggests that the amount of U retarded in the matrix (e.g., by sorption or other mechanisms) surrounding the microfractures and retained to the present is only 5 percent of the U retarded within the microfracture (e.g., by precipitation as uranophane) and retained. Further, 5 percent is a maximum value for the U inventory within the matrix because this estimate is based on the maximum matrix path length (0.28 mm) and a minimum fracture aperture (100 μm).

4.2.6 Conclusions

Data presented here document the distributions of U within and around the Nopal I deposit and the transport of U away from the deposit mainly along fracture paths. U-series isotopic measurements indicate mobilization of U from the deposit within the last 1 Ma. This observation is consistent with U-series dating of samples within and outside of the deposit showing significant U transport at about 54 ka. Discovery of a 54 ka caliche adjacent to the deposit establishes the position of the deposit at the surface and hence subject to hydrologically unsaturated, chemically oxidizing conditions for at least that period. Both the general U distribution within the deposit and the U concentrations within an individual major fracture appear to be related to secondary non-U mineral occurrence. These relationships suggest remobilization of U by oxidizing, low pH fluids, and transport away from the deposit. U-bearing fluids moving away from the deposit appear to have deposited U as the fluid interacted physically or chemically, or both, with the wall rocks of the fracture paths.

Greater transport distances were achieved along a few relatively continuous mesofractures (e.g., fractures with apertures >1 mm and traces extending more than 10 m) than through the general fracture network composed of thousands of less continuous microfractures (e.g., fractures with apertures <1 mm and traces on the order of cm) within and surrounding the deposit. U transport away from the deposit appears to be largely independent of the general fracture network pattern. Movement of U away from the Nopal I deposit, measured as net horizontal transport vectors along mesofracture paths, achieved maximum distances at least 20 times greater than transport of U through tuff with a complex network of microfractures. Transport of U away from individual microfractures into homogeneous, unfractured (at optical microscopy scales) tuff matrix appears limited to distances less than 1 mm.

Inventories of U retarded and retained (e.g., by sorption, precipitation, co-precipitation) along different types of transport paths vary greatly. U distribution patterns along and around a mesofracture at Nopal I indicate U transport along a two-stage path: (i) transport along the mesofracture, then (ii) transport out of the mesofracture into a complex network of microfractures (linear fracture densities >1 fracture/cm) through which the mesofracture passes. U distributions are interpreted as relative inventories of transported U within distinct portions of the transport system. The U content of a complex microfracture network is five times greater than the U content of the mesofracture through which U was introduced into the microfracture network. Data from individual microfractures with high U concentrations (e.g., 5.6×10^5 ppm) indicate that the amount of U transported out of a microfracture into the tuff matrix adjacent to the microfracture is only 5 percent of the U retained within a microfracture (mainly by precipitation as uranophane). This analysis suggests a relative ranking for transported U inventories: (i) microfracture network U content \gg mesofracture U content, and (ii) individual microfracture U content \gg adjacent matrix U content.

4.3 ASSESSMENT OF PROGRESS TOWARD MEETING PROJECT OBJECTIVES

The Geochemical Natural Analog Project is making good progress toward the objectives listed in Section 4.1. Research results presented in this report and

elsewhere (e.g., Pearcy et al., 1993b) have begun to provide a realistic understanding of the utility and limitations of natural analog studies when employed to support a license application for a HLW repository. Specifically, fundamental data have been gathered and interpreted on U mineral characteristics, stabilities, and alteration sequences in a geologic environment comparable to that anticipated for the proposed YM repository. This information is required for development and evaluation of reasonable PA models for radionuclide transport. For example, data being gathered within the Analog Research Project on the matrix hydraulic properties of silicic tuff is being used within the PA Research Project to support modeling efforts. Additionally, progress has been made in evaluation of the roles of fracture and matrix transport of U in a YM-like environment. This information has been used in the development of CDSs for mineral assemblages (3.2.3.3), geochemical processes (3.2.3.5), and EBS (5.4).

The detailed field and laboratory data in this report provide a more complete understanding of a system in which U has been available for transport under conditions comparable to those anticipated for YM. Specifically, IPA has identified substantial conceptual uncertainties regarding appropriate implementation of fracture transport and fracture retardation, and the relationship between fracture flow and matrix diffusion remains indeterminate in transport models.¹ Results reported here provide semi-quantitative constraints on U fracture transport distances and identify the portions of a complex fracture-matrix system that have retained (under YM-comparable conditions, for a period of at least 10^4 yr) the greatest proportion of transported U. These results will reduce conceptual uncertainties regarding U transport in future versions of PA models. For example, confirmation that model results for fracture-matrix partitioning and retention of U are scaled realistically can be derived from measurements of fracture and matrix U retention at Nopal I. Time scales of U transport out of a YM system can be evaluated against time scales of U retention at Nopal I. Fracture retardation remains a highly uncertain parameter in PA models; data reported here provide preliminary information that may allow constraint of fracture retardation. Additionally, the detailed characterization of the fracture network at Nopal I

1. T. McCartin and R. Codell, personal communications, June 1994.

described in this report provides information necessary for design and implementation of field-based hydraulic percolation tests. Such tests are under consideration to address the KTU identified in CDSs for hydrogeologic processes (3.2.2.1), hydrologic conditions (3.2.2.9), perched water (3.2.2.12) concerning groundwater flow codes not tested against field data. Study of contaminant transport in well-constrained, YM-comparable systems, will allow testing of the ability of transport models to predict transport in real systems where the end state is observable.

Progress to date at Akrotiri includes definition of specific areas for analog study, completion of initial observations confirming similarities to YM, completion of preliminary analyses of source term compositions, and constraints on conceptual models of hydraulic infiltration (e.g., Murphy et al., 1991; Percy et al., 1993; Percy et al., 1994). Specifically, samples collected in room Delta 3 may allow closely constrained (in time and space) study of elemental transport under conditions comparable to those anticipated at YM.

The U.S. Department of Energy (DOE) has initiated analog research related to the proposed YM repository. The DOE is studying water/rock interactions in hot springs in New Zealand in an attempt to validate the EQ3/6 computer code. In addition to these efforts, other DOE analog research is under consideration (e.g., Chapman et al., 1992). Center for Nuclear Waste Regulatory Analyses (CNWRA) work at Peña Blanca and Akrotiri provides a strong base of experience from which to evaluate DOE analog studies. Results from CNWRA analog research allows informed comment on selection of sites, site characterization techniques, applications of the analog data, and use of the analog data for assessment of aspects of a YM repository.

4.4 PLANS FOR NEXT REPORTING PERIOD

Field research anticipated during the next report period (July 1, 1994 to December 31, 1994) comprises work at both the Peña Blanca site and the Akrotiri site. At Peña Blanca, electromagnetic measurements will be conducted over the entire Nopal cuesta. These measurements will allow assessment of perched water zones (or other conductors) at depths of up to 150–200 m. Seasonal variations in perched water zones are postulated to be an important part of recent interaction of water with the Nopal I U deposit. Field

research at Akrotiri is anticipated to include sampling of Minoan tuff beneath a bronze artifact discovered during 1993 excavations and measurement of hydraulic properties (e.g., saturated conductivity, unsaturated conductivity, sorptivity, moisture content, and suction potential) of the Cape Riva and Minoan tuffs.

Laboratory research during the next period is planned to include U content and rare earth content measurements on samples from Peña Blanca. Optical microscopy, scanning electron microscopy, energy-dispersive x-ray analyses, and powder diffraction x-ray analyses are planned for both Peña Blanca samples and Akrotiri samples. Measurement of the matrix hydraulic properties of the Nopal tuff will continue. Selective leachate analyses for transported trace elements are anticipated to be completed on tuff samples collected as vertical profiles beneath the discovery location of the Delta 3 bronzes.

Modeling and data interpretation activities planned during the next report period include attempts to extend infiltration calculations for the Peña Blanca site and use of an abstracted Kd for fracture transport of uranium at Peña Blanca to place realistic constraints on retardation factors for fracture transport of uranium. Interpretations of the hydrologic data from the Akrotiri site will continue to allow assessment of the effects of intermittent water infiltration over the 3,600-yr burial period. Using data from the Akrotiri site and numerical flow and transport modeling of the same general character as that which will be available for PA for YM, model results will be compared to the record of contaminant transport over a period of 3,600 yr in unsaturated, oxidizing, silicic tuff. The exercise is initially being conducted as a blind exercise, without knowledge of the extent of the contaminant plume. Results of this exercise will be analyzed to evaluate the manner in which models for radionuclide transport over long time periods can be supported by natural analog studies as specified in 10 CFR Part 60.

4.5 REFERENCES

- Chapman, N., P.L. Cloke, J.-C. Petit, J.A.T. Smellie, and A.E.J. van Luik. 1992. *Applications of Natural Analogue Studies to Yucca Mountain as a Potential High-Level Radioactive Waste Repository*. Las Vegas: Office of Civilian Radioactive Waste Management, U.S. Department of Energy.

- Dickson, B.L., and A.L. Herczeg. 1992. Deposition of trace elements and radionuclides in the spring zone, Lake Tyrrell, Victoria, Australia. *Chemical Geology* 96: 151–166.
- George-Aniel, B., J.L. Leroy, and B. Poty. 1991. Volcanogenic U mineralization in the Sierra Peña Blanca District, Chihuahua, Mexico: Three genetic models. *Economic Geology* 86: 233–248.
- Ildefonse, P., J.-P. Muller, and G. Calas. 1990. Assessment of radionuclide migration in natural analogues by radiation-induced centers in kaolinites. *Symposium Proceedings of the Scientific Basis for Nuclear Waste Management XIV*. T.A. Abrajano, Jr. and L.H. Johnson, eds. Boston, MA: Materials Research Society 212: 474.
- Leslie, B.W., E.C. Pearcy, W.M. Murphy, and J.D. Prikryl. 1993a. Fracture and matrix controlled U migration at the Peña Blanca natural analog site. *Fourth International Conference on the Chemistry and Migration Behavior of the Actinides and Fission Products in the Geosphere*. Charleston, SC: University of Georgia. 110.
- Leslie, B.W., E.C. Pearcy, and J.D. Prikryl. 1993b. Geochemical natural analogs. *NRC High-Level Radioactive Waste Research at CNWRA January–June 1992*. W.C. Patrick, ed. NUREG/CR-5817. Washington, DC: Nuclear Regulatory Commission: 3(1).
- Nordstrom, D.K. 1982. *Aqueous Pyrite Oxidation and the Consequent Formation of Secondary Iron Minerals*. Acid Sulfate Weathering. Soil Science Society of America. Special Publication Number 10: 37–56.
- Nuclear Regulatory Commission. 1987. *Disposal of High-Level Radioactive Wastes in Geologic Repositories*. Title 10, Energy, Part 60. Washington, DC: U.S. Government Printing Office.
- Pearcy, E.C., and W.M. Murphy. 1991a. Geochemical natural analogs. *Report on Research Activities for the Quarter January 1 through March 31, 1991*. W.C. Patrick, ed. CNWRA 91-01Q. San Antonio, TX: Center for Nuclear Waste Regulatory Analyses: 7-1 to 7-7.
- Pearcy, E.C., and W.M. Murphy. 1991b. Geochemical natural analogs. *Report on Research Activities for the Quarter April 1 through June 30, 1991*. W.C. Patrick, ed. CNWRA 91-02Q. San Antonio, TX: Center for Nuclear Waste Regulatory Analyses: 7-1 to 7-7.
- Pearcy, E.C., and W.M. Murphy. 1991c. Geochemical natural analogs. *Report on Research Activities for the Quarter July 1 through September 30, 1991*. W.C. Patrick, ed. CNWRA 91-03Q. San Antonio, TX: Center for Nuclear Waste Regulatory Analyses: 7-1 to 7-9.
- Pearcy, E.C., and W.M. Murphy. 1992. *Site Selection and Workplan Report for the Geochemical Natural Analog Research Project*. CNWRA 92-014. San Antonio, TX: Center for Nuclear Waste Regulatory Analyses.
- Pearcy, E.C., and B.W. Leslie. 1993. Geochemical natural analogs. *NRC High-Level Radioactive Waste Research at CNWRA January 1 through June 30, 1993*. W.C. Patrick, ed. CNWRA 93-01S. San Antonio, TX: Center for Nuclear Waste Regulatory Analyses: 7-1 to 7-20.
- Pearcy, E.C., W.M. Murphy, R.T. Green, B.W. Leslie, and J.D. Prikryl. 1993a. Geochemical natural analogs. *NRC High-Level Radioactive Waste Research at CNWRA Calendar Year 1991*. W.C. Patrick, ed. NUREG/CR-5817. Washington, DC: Nuclear Regulatory Commission: 7-1 to 7-32.
- Pearcy, E.C., J.D. Prikryl, W.M. Murphy, and B.W. Leslie. 1993b. *U Mineralogy of the Nopal I Natural Analog Site, Chihuahua, Mexico*. CNWRA 93-012. San Antonio, TX: Center for Nuclear Waste Regulatory Analyses.
- Pearcy, E.C., R.T. Green, and W.M. Murphy. 1994. Geochemical natural analogs. *NRC High-Level Radioactive Waste Research at CNWRA July 1 through December 31, 1993*. W.C.

Patrick, ed. CNWRA 93-02S. San Antonio, TX: Center for Nuclear Waste Regulatory Analyses: 5-1 to 5-16.

U.S. Environmental Protection Agency. 1989. *Environmental Radiation Protection Standards for Management and Disposal of Spent Nuclear Fuel, High-Level and Transuranic Radioactive Wastes*. Title 40, Protection of the Environment, Part 191 (40 CFR 191.13). Washington, DC: U.S. Government Printing Office.

Wescott, R.G., M.P. Lee, N.A. Eisenberg, and T.J. McCartin, eds. 1994. *Phase 2 Demonstration of the NRC's Capability to Conduct a Performance Assessment for a High-Level Waste Repository*. NUREG-1464. Washington, DC: U.S. Nuclear Regulatory Commission. In preparation.

5 SORPTION MODELING FOR HLW PERFORMANCE ASSESSMENT

by Roberto T. Pabalan, David R. Turner, and F. Paul Bertetti (CNWRA)

Investigators: Roberto Pabalan, David Turner, F. Paul Bertetti, Todd Dietrich, James Prikryl, and Paula Muller

NRC Project Officer: George F. Birchard

5.1 TECHNICAL OBJECTIVES

A fundamental concern in evaluating the suitability of Yucca Mountain (YM), Nevada as a repository for high-level nuclear wastes (HLW) is the possibility of radionuclide migration from the repository to the accessible environment as dissolved constituents in groundwaters. An important mechanism for attenuating radionuclide migration is sorption of radionuclides on minerals encountered along the flow paths. Sorption is specifically referred to in 10 CFR 60.122(b) as a favorable geochemical condition that will tend to inhibit radionuclide migration and "favorably affect the ability of the geologic repository to isolate the waste." Conversely, geochemical processes that "would reduce sorption of radionuclides" are listed [10 CFR 60.122(c)(8)] as a potentially adverse condition that could reduce the effectiveness of the natural barrier system.

To support the Nuclear Regulatory Commission (NRC) HLW program, the Center for Nuclear Waste Regulatory Analyses (CNWRA) is conducting research activities under the Sorption Modeling for HLW Performance Assessment Research Project. The broad objective is to develop sufficient understanding of radionuclide transport issues so that timely preclicensing guidance can be provided to the U.S. Department of Energy (DOE) and a sound basis is available for evaluating the DOE license application. The results will be used to support the NRC License Application Review Plan (LARP), particularly Sections 3.2.3.2, 3.2.3.3, and 3.2.3.5, pertaining to favorable and potentially adverse geochemical conditions and processes at a potential repository site, and Section 3.4, which addresses the effectiveness of natural barriers against the release of radioactive material to the environment. Laboratory (Task 3) and modeling (Task 2) studies of radionuclide sorption, retardation, and transport, which are central to the Sorption Research Project, will provide independent bases for addressing

Key Technical Uncertainties (KTUs) including: (i) identity and magnitude of the effects of geochemical processes that reduce radionuclide retardation, (ii) parametric representation of retardation processes, (iii) capacity of alteration mineral assemblages to inhibit radionuclide migration, and (iv) effect of degree of saturation on radionuclide sorption and transport. In addition, development of Compliance Determination Methods (CDMs) for determining compliance with the regulatory requirements will utilize data and models generated from this research project.

Results arising from this project will be integrated with those from other CNWRA activities. For example, data on uranium sorption will be used in interpreting data on U distribution and migration at the Peña Blanca field site of the Geochemical Natural Analog Research Project (Chapter 4), as well as in developing conceptual models for radionuclide transport/retardation in near- and far-field environments related to the Performance Assessment Research Project (Chapter 6) and the Iterative Performance Assessment (IPA) Phase 3. Results of activities undertaken during the first half of 1994 are discussed below.

5.2 SORPTION EXPERIMENTS

To develop an understanding of radionuclide sorption processes and the important physical and chemical parameters that affect sorption behavior in the YM environment, experiments are being conducted to investigate the sorption behavior of U and other actinides on geologic media. During the first half of 1994, experiments were completed to determine the possible effects of pH and solid-mass to solution-volume (M/V) ratio on the sorption of U(6+) on montmorillonite, which is an important alteration mineral occurring underneath YM, Nevada. The experimental data were interpreted using a surface-complexation model (SCM), which permitted predictions to be made regarding U sorption on

montmorillonite at other physicochemical conditions. Methods and results of experiments concerning U sorption on montmorillonite are discussed in Section 5.2.1, and modeling results are given in Section 5.3.

Because of the low U concentrations used in these experiments, the potential sorption of U by the container walls was a major concern. Losses of U and other actinides from solution to container walls have been reported in the literature (e.g., Tripathi, 1984; Rogers and Meijer, 1993). Likewise, experience at the CNWRA has shown that container sorption losses are significant, repeatable, and dependent on U concentration and pH (Pabalan and Turner, 1994). Moreover, it is known that sorption to container walls is reversible and exhibits kinetics similar to sorption onto geologic substrates (Pabalan and Turner, 1994). In order to better understand the requirements for correcting experimental data for container sorption, studies were conducted to determine: (i) the dependence of container sorption on the type of container used, and (ii) the impact of sorption competition between container walls and an introduced sorbent. These experiments are discussed in Section 5.2.2.

5.2.1 Uranium Sorption on Montmorillonite

5.2.1.1 Preparation of Na-montmorillonite

The Na-montmorillonite used in the sorption experiments was prepared from powdered clay material (SAZ-1; "Cheto" Ca-form montmorillonite, Apache County, Arizona) obtained from the Source Clay Minerals Repository. The <2- μm fraction that was used in the experiments was separated based on the procedure described in Jackson (1956) by placing 0.6 g of clay powder in a 50-mL polypropylene (PP) centrifuge tube containing 25 mL of deionized water. The clay was then suspended using a vortex mixer; some of the clay immediately settled to the bottom of the tube and was later discarded. The remaining clay suspension was transferred into a second tube and centrifuged for 4 min at 1,000 rpm. The supernatant was then poured into a third tube and centrifuged for 8 min at 10,000 rpm. Most of the supernatant was discarded, and the remainder was vortexed; subsequently the suspension, which contained the <2- μm clay particles, was transferred into a beaker. The procedure was repeated until several grams of <2- μm clay fraction

were retrieved. Scanning electron microscopy was done which verified that most of the clay particles are <2 μm .

To convert the original Ca-montmorillonite into Na-form, the <2- μm clay fraction was reacted with 2-M NaCl solution in a beaker using a stirplate to keep the clay in suspension (the NaCl solution causes the clay to flocculate and sink unless the solution is stirred). Every 1 or 2 days the beaker was taken off the stirplate, the clay allowed to settle, and the solution replaced with fresh NaCl solution. After about 10 days, the clay was rinsed repeatedly with deionized water until the water no longer gave a positive Cl^- test with 0.1-M AgNO_3 . Subsequently, the clay material was freeze-dried.

5.2.1.2 Experimental Procedure

The sorption experiments were conducted by reacting weighed amounts of Na-montmorillonite with 40 mL of U solutions in Teflon-FEP (fluorinated ethylene propylene) centrifuge bottles. The aqueous solutions had initial U concentrations of approximately 50 ppb (mostly as ^{233}U) and were prepared using a radiochemically pure ^{233}U solution standard issued by the U.S. Department of Energy New Brunswick Laboratory as Certified Reference Material (CRM) 111-A. The ionic strength of the solutions was kept close to 0.1 molal using a NaNO_3 matrix. To evaluate the effect of M/V ratio on U sorption on montmorillonite, one set of experiments used 0.1 g of solid (M/V=2.5 g/L) and another set used 0.01 g of Na-montmorillonite (M/V=0.25 g/L).

Prior to addition of the solid phase, the initial pH of each solution was adjusted to a value in the range of 2.0 to 9.0 at approximately 0.25-pH intervals by addition of HNO_3 or NaHCO_3 . The amount of reagent needed to achieve the desired initial pH of the U solutions was estimated using the EQ3NR geochemical code (version 3245.R124) with database Data0.com.R12. The solutions, which were kept open to atmospheric $\text{CO}_2(\text{g})$ throughout the experiment, were agitated using gyratory shakers. For U solutions with added NaHCO_3 , it took at least 10 days to equilibrate with atmospheric $\text{CO}_2(\text{g})$ and reach a constant pH.

After all solutions had attained a constant pH, 500- μL samples were taken from each using Eppendorf micropipets for analysis of initial U concentrations. Na-montmorillonite was then added to each solution, and the mixtures were allowed to equilibrate. The mass of the solutions was monitored through the duration of the

experiment to allow corrections to be made for any increase in U concentration due to evaporation. After equilibrium was reached (approximately 10 days), samples were taken from each solution to determine the final U concentration. The equilibrium pH of each solution was also measured. Reverse experiments were subsequently initiated for mixtures with M/V equal to 2.5 g/L by adjusting the pH of the experimental solutions to lower or higher pH by addition of HNO₃ or NaHCO₃, respectively. After an additional period of about 10 days, the pH of the solutions was measured and aqueous samples were taken for analysis of U concentrations. U analyses were done using a Packard Model 1900 TR Liquid Scintillation Analyzer, and pH measurements were made using a Ross combination pH electrode and an Orion 920A pH meter.

5.2.1.3 Experimental Results and Discussion

Experimental results on U sorption on Na-montmorillonite are shown in Figures 5-1 and 5-2, which are plots of measured U solution concentration versus equilibrium pH for mixtures with M/V equal to 2.5 and 0.25 g/L, respectively. The diamond symbols in the two figures represent U concentrations of solutions without a mineral phase present. The decrease in U concentration towards near-neutral pH indicates that significant amounts of U were lost from solution due to sorption on the container walls. Container sorption is strongly dependent on solution pH and reaches a maximum at pH ≈ 6. The circles in Figures 5-1 and 5-2 represent U concentrations of the experimental mixtures at the end of the forward or reverse experiment. These data show that the amount of U remaining in solution decreased substantially after addition of Na-montmorillonite and depended strongly on the equilibrium pH and on M/V.

The relative amounts of U sorbed on Na-montmorillonite (%U sorbed) were calculated from the equation:

$$\%U \text{ sorbed} = \frac{(U_i - U_f)}{U_i} \times 100\% \quad (5-1)$$

where U_i is the initial U concentration of the experimental mixture (prior to addition of the mineral phase) and U_f is the U concentration at the end of the forward or reverse experiment. Because container sorption, and hence U_i , are pH-dependent and because the initial pH of experimental mixtures is generally

different from the final pH, the hypothetical value of U_i at the specific pH of the corresponding U_f data point had to be calculated. To allow this calculation to be done, equations that best fit the container sorption versus pH data for the two sets of experiments were derived by nonlinear regression. These equations are represented as solid curves in Figures 5-1 and 5-2. This method of calculating U_i assumes that the amount of U sorbed on the container is the same whether the mineral phase is present or not. Additional experiments are currently under way to determine if this is true. There is also an observed difference in container sorption between the two sets of experiments. The reason for this difference is not clear at present, but it is possible that different commercial batches of containers may have different sorption properties. Additional experiments are needed to investigate this possibility.

Figure 5-3 shows the calculated percent of U sorbed on Na-montmorillonite as a function of pH. It is evident from this figure that U sorption on Na-montmorillonite is strongly dependent on pH and on the M/V ratio. At an M/V equal to 2.5 g/L, the amount of U sorbed increases sharply at pH values above about 3.0 (adsorption edge) and decreases sharply at pH values above about 8.0 (desorption edge). The amount of U sorbed reaches a maximum value of about 99 percent at pH ~ 6.3. At lower M/V (0.25 g/L), the sorption envelope collapses, that is, the adsorption edge shifts to higher pH, the desorption edge moves to lower pH, and the sorption maximum decreases. However, the solution pH at which sorption maximum occurs remains about the same (~ 6.3). Also shown in Figures 5-1 and 5-3 are the reverse data for experiments at M/V=2.5 g/L, which generally plot along the same sorption and desorption trends as the forward data points. This correspondence between forward and reverse data indicates that U sorption on montmorillonite is reversible, which was also observed for U sorption on clinoptilolite and α -alumina (Pabalan et al., 1993; Pabalan and Turner, 1994; Prikryl et al., 1994).

The experimental data discussed above were evaluated using surface-complexation models as part of the activities in Task 2 of this research project. The results of the modeling effort are given in Section 5.3.

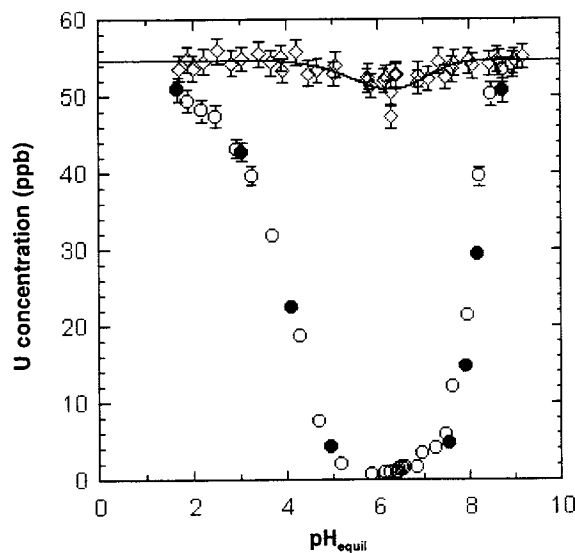


Figure 5-1. U solution concentration versus equilibrium pH for U sorption experiments at an M/V ratio equal to 2.5 g/L. The diamond symbols represent measured values for solutions without montmorillonite. The curve represents an equation which was best fit to these data and was used to calculate the initial U concentrations, U_i , of experimental solutions. Open and closed circles represent data at the termination of forward and reverse experiments, respectively. Error bars were calculated based on 2% 2σ counting errors in liquid scintillation analysis.

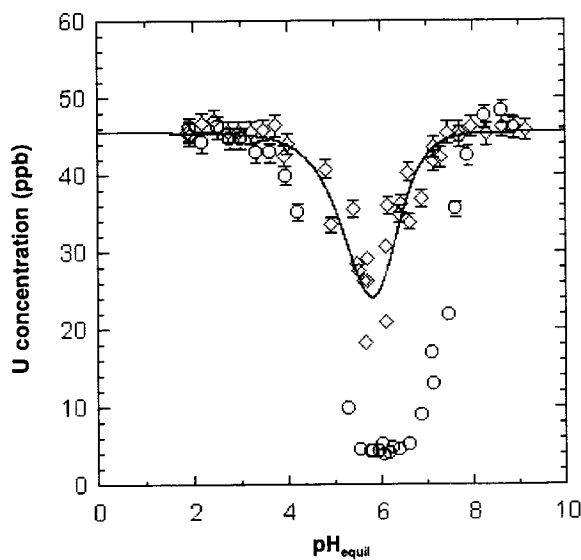


Figure 5-2. U solution concentration versus equilibrium pH for U sorption experiments at an M/V ratio equal to 0.25 g/L. The diamond symbols represent measured values for solutions without montmorillonite. The curve represents an equation which was best fit to these data and was used to calculate the initial U concentrations, U_i , of experimental solutions. Circles represent data at the termination of forward experiments. Error bars were calculated based on 2% 2σ counting errors in liquid scintillation analysis.

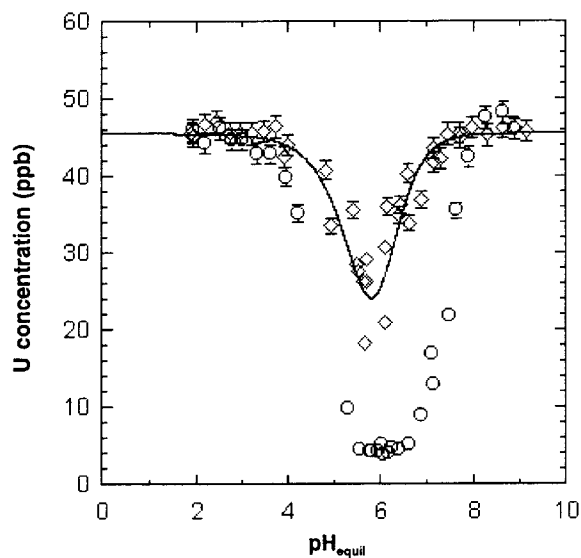


Figure 5-3. U solution concentration versus equilibrium pH for U sorption experiments at an M/V ratio equal to 0.25 g/L. The diamond symbols represent measured values for solutions without montmorillonite. The curve represents an equation which was best fit to these data and was used to calculate the initial U concentrations, U_i , of experimental solutions. Circles represent data at the termination of forward experiments. Error bars were calculated based on 2% 2σ counting errors in liquid scintillation analysis.

5.2.2 Uranium Sorption on Containers

5.2.2.1 Experimental Procedure

The relative sorption of U from solution to container walls was evaluated for containers composed of PP, Teflon-FEP, and polycarbonate (PC). Initially, sorption of U on PP and Teflon-FEP was compared. Solutions with an initial U concentration of approximately 5- and 50-ppb were transferred to both types of containers and reacted at room temperature, open to atmospheric $\text{CO}_2(\text{g})$, for a period of about 3 weeks; pH was fixed at 6.8 and 6.5 for the 5- and 50-ppb solutions, respectively, by the addition of NaHCO_3 . Throughout the experiment, a gyratory shaker was used to agitate the solutions (~ 120 rpm). Solutions were sampled by taking 500 μL aliquots at intervals of about 1 week (three samples) and analyzed for U concentration using a Packard Model 1900TR Liquid Scintillation Analyzer. A second experiment was conducted using Teflon-FEP and PC containers. Experimental conditions were similar except that pH was fixed at 6.6 and 6.0 for the 5- and 50-ppb solutions, respectively.

The effect of competitive sorption was investigated using PC containers and SpectraPor-4 cellulose dialysis membranes. Dialysis membranes were used because they are capable of sorbing heavy metals from solution and because they can be easily separated from the solution prior to the desorption step. Solutions with an initial U concentration of approximately 5- and 50-ppb and pH of 6.2 and 5.0, respectively, were added to 50-mL PC containers. After equilibration with atmospheric $\text{CO}_2(\text{g})$, sample aliquots of 500 μL were withdrawn from each 50-mL PC container for analysis of U. Subsequently, a weighed quantity of dialysis membrane was added to each 50-mL PC container. The membranes remained in contact with PC container solutions for 1 week, after which sample aliquots were again withdrawn from each container for analysis of U. The dialysis membranes were then removed and transferred to 125-mL polyethylene bottles, each of which contained a known quantity of 0.1-N HNO_3 . Following transfer of the dialysis membranes, solutions within each 50-mL PC container were also acidified with 0.1-N HNO_3 . The addition of acid shifted the solution pH to less than 3, effecting desorption of U from both the membranes and container walls. After desorbing the U for 1 week, samples were withdrawn

for analysis of U from both the 50-mL PC container solutions and membrane desorption solutions (125-mL polyethylene bottles). A comparison was made between the amount of total U initially sorbed onto the container walls and the amount of U remaining on the container walls following equilibration with the dialysis membrane. The initial percent U sorbed to container walls was calculated using the equation:

$$\text{Initial \%U sorbed} = \frac{U_{I\text{-Container}}}{U_{\text{Total}}} \times 100 = \quad (5-2)$$

$$\frac{(U_{\text{Total}} - U_{I\text{-Solution}})}{U_{\text{Total}}}$$

where U_{Total} is the total amount U, in grams, introduced into the system, based on analysis of the solutions added to the 50-mL PC containers, $U_{I\text{-Container}}$ is the amount U sorbed to the container walls after equilibration with atmospheric $\text{CO}_2(\text{g})$, and $U_{I\text{-Solution}}$ is the amount U remaining in the 50-mL PC container solution, based on analysis of solutions prior to addition of the membrane. The final percent U sorbed on the container walls was calculated using the equation:

$$\text{Final U\% sorbed} = \frac{U_{F\text{-Container}}}{U_{\text{Total}}} \times 100 = \quad (5-3)$$

$$\frac{(U_{\text{Total}} - U_{F\text{-Solution}} - U_{\text{Membrane}})}{U_{\text{Total}}} \times 100$$

where U_{Membrane} is the amount U sorbed on dialysis membrane, based on analysis of the membrane desorption solutions, $U_{F\text{-Container}}$ is the amount U sorbed on the 50-mL PC container walls following equilibration with the dialysis membrane, and $U_{F\text{-Solution}}$ is the amount U remaining in the PC container solutions, based on analysis of the PC container solutions after addition of acid. The amount of U throughout the experiment was accounted for by mass balance using the equation:

$$U_{\text{Total}} = U_{\text{Memsoln}} + U_{\text{Containsoln}} \quad (5-4)$$

where U_{Memsoln} is the amount U contained in the acidified membrane desorption solution and $U_{\text{Containsoln}}$ is the amount U contained in the acidified PC container desorption solution.

5.2.2.2 Container Sorption Results and Discussion

Measurements of U sorption on PP and Teflon-FEP showed that at both the 5- and 50-ppb concentrations, losses to the PP containers were greater than losses to the Teflon-FEP containers (Figure 5-4). Both containers, however, sorbed significant amounts of U from solution. Results of the experiment comparing Teflon-FEP and PC sorption are given in Figure 5-5, which shows that losses of U from solution are somewhat less in the PC containers compared to Teflon-FEP at both the 5- and 50-ppb U concentrations. Unfortunately, the 50-ppb PC container solutions equilibrated at a significantly lower pH (5.7) than the 50-ppb Teflon-FEP container solutions (pH~6.0). Because of the dependence of container sorption on pH, it is difficult to determine if the lower sorption onto the PC containers is due to differences in pH or due to differences in the sorption property of the two container types. This difficulty is highlighted by comparing the percent U sorbed by Teflon-FEP in the PP and PC container experiments. In this case, a small shift in pH (~ 0.3 - 0.4) toward the pH of maximum sorption has resulted in a significant difference in percent U sorbed. Further comparison between sorption on PC and on Teflon-FEP containers is illustrated in Figure 5-6, which shows the initial percent U lost from solution to the container walls over a broad pH range. A Mann-Whitney rank sum test comparing the amount of U lost (PC exp #2 and FEP exp #1) between pH 4.5 and 7 indicates that there is no statistically significant difference in the sorption characteristics of PC and Teflon-FEP over this pH range. Conclusions that can be made from these experimental data are: (i) a significant loss of U in solution to container walls occurs no matter what the container type, and (ii) the relative affinity of container material for U is $\text{PP} \gg \text{Teflon-FEP} \geq \text{PC}$.

While others have neglected the effects of container sorption (Tripathi, 1984; Rogers and Meijer, 1993), previous experimental data generated in this project have been corrected based on values for sorption losses in control solution containers (e.g., Pabalan and Turner, 1994; Prikryl et al., 1994). Results of the competitive sorption experiment between PC container walls and cellulose dialysis membranes show that U sorbed on container walls is desorbed as a result of competition from the membrane (Figures 5-7 and 5-8). Not all of the sorbed U is released; about 40 and 50 percent of the amount of U originally sorbed to PC

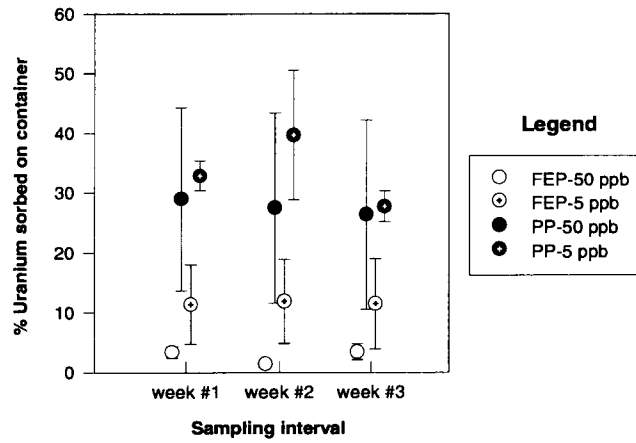


Figure 5-4. Percent U sorbed by Teflon-FEP and polypropylene containers at uranium concentrations of approximately 5 and 50 ppb. Data points represent average values from three experimental solutions for each container type. Error bars represent 1σ variation between experimental solutions.

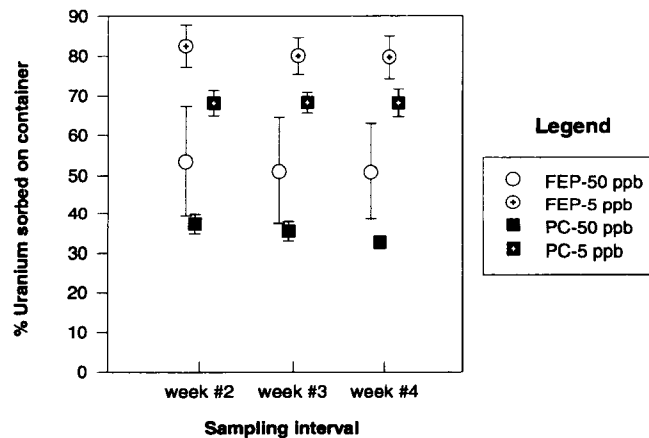


Figure 5-5. Percent U sorbed by Teflon-FEP and polycarbonate containers at uranium concentrations of approximately 5 and 50 ppb. Data points represent average values from four experimental solutions for each container type. Error bars represent 1σ variation between experimental solutions.

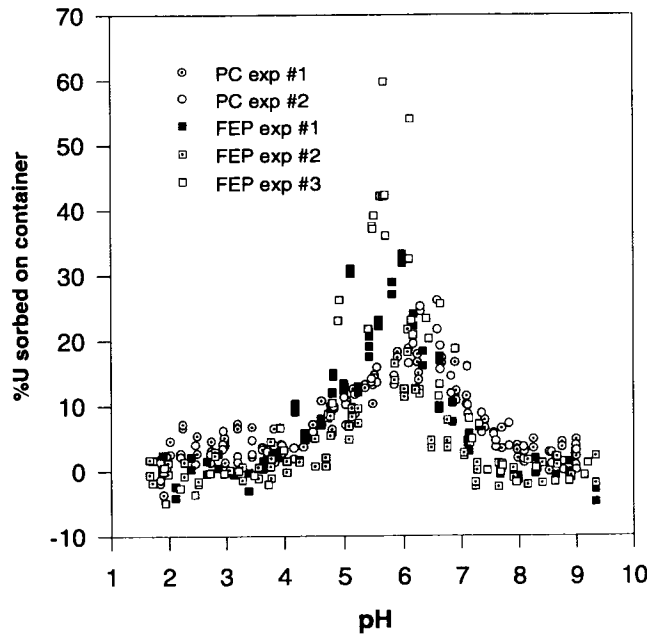


Figure 5-6. Comparison of percent U lost from solution in Teflon-FEP and polycarbonate (PC) containers at an initial U concentration of approximately 50 ppb. A Mann-Whitney rank sum test shows no significant difference in the sorption peaks of Teflon-FEP and PC containers (PC exp #2 and FEP exp #1) between pH 4.5 and 7.

container walls of the 5- and 50-ppb U solutions, respectively, remains after introduction of the dialysis membrane. The magnitude of U sorption by the dialysis membrane is similar to the magnitude of U sorption by geologic substrates in previous experiments at similar U concentrations (Pabalan and Turner, 1994). Mass balance of the experimental system showed that all U was recovered within experimental uncertainty (<10 percent). Possible reasons for the lack of complete desorption of U from PC walls include: (i) a failure to allow enough time for the kinetics of the sorption process (usually about 2 weeks versus the 1 week time frame used in this experiment), (ii) the maximum sorption capability of the dialysis membrane was reached during the experiment and prevented further desorption from the walls, or (iii) the equilibrium of the

membrane-PC wall system was achieved and the partitioning of U as shown by the data is correct. The results of this competitive sorption experiment indicate that desorption of U from an experimental container wall due to the introduction of a competitive substrate is likely. The differences in the sorption characteristics of cellulose membranes and geologic substrates used in previous experiments do not allow for direct correlation of the competitive sorption data presented here. Additional experiments must be undertaken to assess the nature of sorption competition between containers and clinoptilolite, montmorillonite, quartz, etc. Corrections made to experimental data for sorption onto container walls must take into account the desorption process.

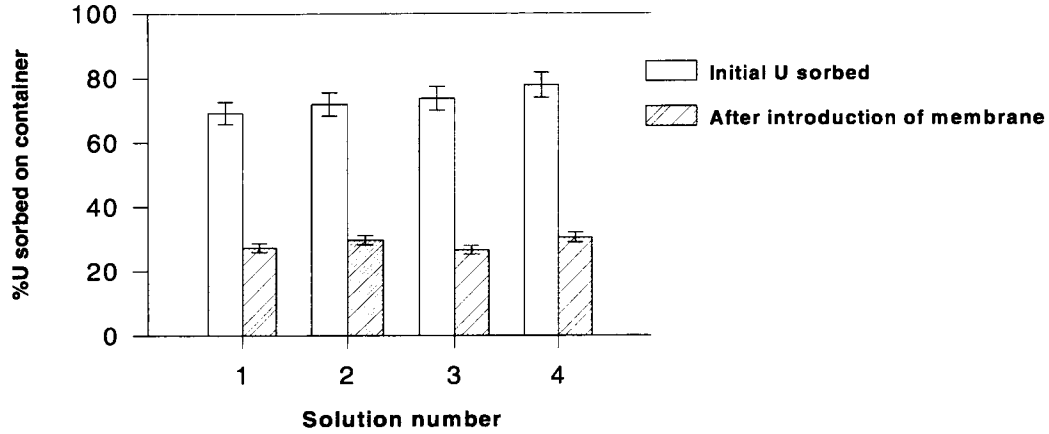


Figure 5-7. Comparison of percent U initially sorbed and percent U desorbed due to competitive sorption at a uranium concentration of approximately 5 ppb for polycarbonate containers. Error bars represent 2σ error for replicate samples.

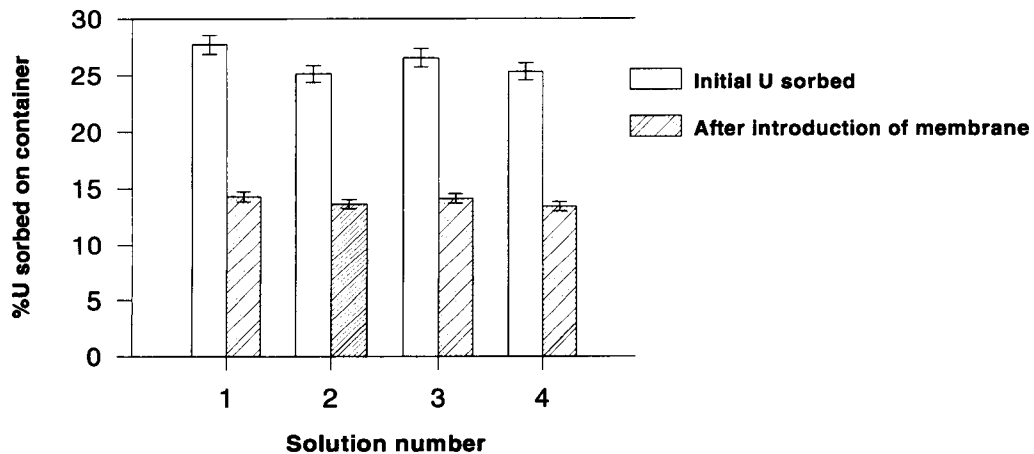


Figure 5-8. Comparison of percent U initially sorbed and percent U desorbed due to competitive sorption at a uranium concentration of approximately 50 ppb for polycarbonate containers. Error bars represent 2σ error for replicate samples.

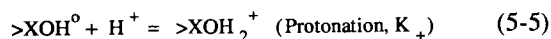
5.3 SORPTION MODELING

One of the goals of conducting sorption experiments is to provide data that will help in the development and calibration of more mechanistic geochemical models that are capable of simulating the influence of changing chemical conditions on radionuclide sorption behavior. SCMs are a class of models that have been developed and used with success in sorption modeling. These models are based on the assumption of analogous behavior between the complexation of radionuclides with aqueous ligands in the bulk solution and the formation of radionuclide complexes with functional binding sites at the mineral-water interface. In SCMs, the surface sites are treated as another ligand competing for the radionuclide. Additional terms account for the effects of electrostatic interactions at the mineral surface on the system chemistry.

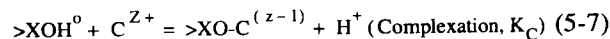
5.3.1 Model Description

Recent efforts in surface complexation theory have developed a uniform Diffuse-Layer Model (DLM) for application to the sorption of heavy metals (Dzombak and Morel, 1990). The model has also been applied with good success to simulate the sorption behavior of actinides such as U and neptunium (Bradbury and Baeyens, 1993; Turner, 1993; Pabalan and Turner, 1994). The DLM is perhaps the simplest of the SCMs, using a one-layer representation of the mineral-water interface. Although ionic strength effects on the electrostatic interactions are included in the DLM, supporting electrolytes such as Na^+ , K^+ , and NO_3^- are assumed not to interact with the surface and sorption reactions for these ions are not included in the geochemical model. The details of the DLM are described in detail elsewhere (Dzombak and Morel, 1990; Davis and Kent, 1990; Turner, 1993) and only a brief overview will be presented here.

Neutral amphoteric surface sites ($>\text{XOH}^0$) are assumed to develop charge through adding a proton (protonation) or removing a proton (deprotonation) to form charged surface sites represented as $>\text{XOH}_2^+$ and $>\text{XO}^-$, respectively. These reactions are written in the form



where K_+ and K_- are referred to as the surface acidity constants. Sorption is represented by postulating the formation of one or more complexes at the mineral-water interface between these sites and the cations and anions in solution. For the DLM, sorption is assumed to take place directly on the mineral surface, forming what are called inner-sphere complexes. For example, for the cation C^{z+}



where the constant K_C is often referred to as the binding constant.

The acidity constants K_+ and K_- are determined by analysis of potentiometric titration data for the mineral of interest (Turner, 1993). The values are model specific, but once they are defined, the acid-base behavior of the surface is characterized, and these values become fixed in the geochemical model. For the DLM, the remaining adjustable parameter is the binding constant.

SCMs such as the DLM are designed to reproduce macroscopic behavior in solid-gas-water systems. For example, since H^+ is the potential determining ion, the protonation/deprotonation of the surface sites and the formation of surface complexes vary as a function of pH; this feature enables the DLM to simulate pH-dependent sorption behavior observed for many toxic elements including the actinides. Although the models define one or more surface reactions, there is typically a lack of independent analytical data supporting the formation of a particular surface complex. In the absence of this data, the exact form of the surface reaction is generally selected by the modeler based on the analogous reactions in aqueous speciation.

5.3.2 Geochemical Modeling of Uranium (6+)-Montmorillonite Sorption

As discussed above in Section 5.2, the sorption of U(6+) on montmorillonite was investigated as a function of solution pH and M/V. One test of the adequacy of the DLM would be to develop a simple conceptual model that is capable of reproducing the observed sorption behavior. This test is especially

Table 5-1. DLM parameters used to model Uranium (6+) sorption on Montmorillonite

Mineral Properties and Experimental Conditions	
Specific Surface Area (A_{SP}) ^(a)	78 m ² /g
Surface Site Density (N_S) ^(b)	2.3 sites/nm ²
Solid Concentration (M/V)	0.25 g/L: 2.5 g/L
Si: Al ratio	3.0:1.0
Total Uranium (6+)	50 ppb (2.1×10^{-7} M)
p(CO ₂)	$10^{-3.5}$ atm
Surface Reactions	Log K
$>SiOH^0 = >SiO^- + H^+$ ^(c)	-7.20
$>AlOH^0 = >AlO^- + H^+$ ^(c)	-9.73
$>AlOH^0 + H^+ = >AlOH_2^+$ ^(c)	8.33
$>SiOH^0 + UO_2^{2+} = >SiO-UO_2^+ + H^+$ ^(d)	1.40
$>AlOH^0 + UO_2^{2+} + H_2O = >AlO-UO_2OH^0 + 2H^+$ ^(d)	-4.84
(a) Assumed value (Triay et al., 1993)	
(b) From Dzombak and Morel (1990).	
(c) From Turner (1993).	
(d) Determined for M/V = 0.25 g/L.	

challenging given that the DLM was developed principally to model sorption on simple (hydr)oxides such as goethite and Al₂O₃ instead of a complex multioxide such as montmorillonite.

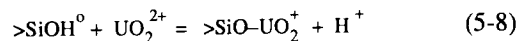
Previous studies have established that it is possible to model the sorption behavior of aluminosilicates such as montmorillonite by considering the surface to be comprised of stoichiometric proportions of silanol (>SiOH⁰) and aluminol (>AlOH⁰) sites (Riese, 1982; Rai et al., 1988; Pabalan and Turner, 1994). Model parameters are given in Table 5-1. For the Na-montmorillonite used in the experiments, the Si:Al ratio is approximately 3:1. Because specific area measurements (A_{SP}) are not yet available, a specific surface area of 78 m²/g (Triay et al., 1993) was

assumed, together with a site density of 2.3 sites/nm² (Dzombak and Morel, 1990), to calculate the total number of available sites. The acidity constants for the >SiOH⁰ and >AlOH⁰ sites were derived based on interpreting potentiometric titration data for SiO₂ and α -Al₂O₃, as described in Turner (1993). Only one type of silanol and aluminol site was assumed.

To determine the binding constants for the U(6+) sorption reactions, the nonlinear parameter optimization code FITEQL was used (Westall, 1982). As input, the user specifies a chemical equilibrium model for the system of interest and assumes a surface complexation reaction of the general form used in Eq. (5-3). The input file also includes the pH-dependent sorption data. Using mass balance and mass action

constraints, FITEQL iteratively adjusts the binding constant for the postulated sorption reaction until the difference between the calculated results and the experimental data is minimized.

In the current study, the equilibrium constants for the $UO_2-H_2O-CO_2$ system were selected from the CNWRA MINTEQA2 database (Turner, 1993), which is based on the Nuclear Energy Agency (NEA) Thermodynamic Database for U (Grenthe et al., 1992). With the purpose of maintaining the simplest model, the following two inner-sphere reactions proved to be most capable of reproducing the observed data at $M/V=0.25$ g/L



The binding constants determined for these reactions using FITEQL are listed in Table 5-1.

These values were then used with the geochemical sorption/speciation code MINTEQA2 (Allison et al., 1991) to predict $U(6+)$ sorption on montmorillonite. The model predictions are compared to the experimental results in Figure 5-9. In general, the model predictions reproduce the observed sorption

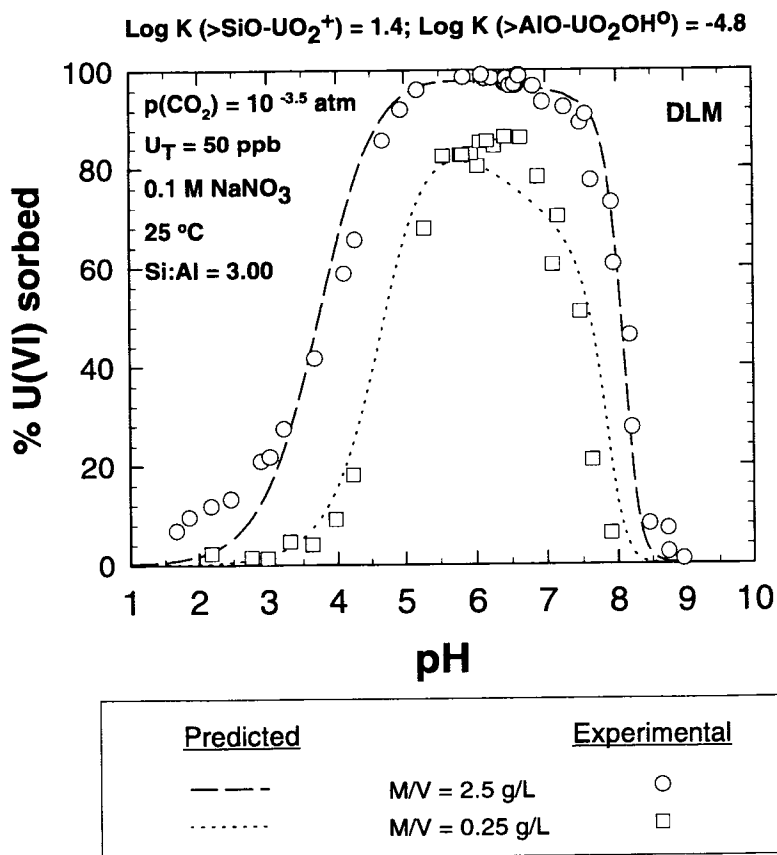


Figure 5-9. Diffuse-Layer Model (DLM) model results for Uranium(6+)-Montmorillonite sorption. The model parameters and experimental conditions are given in Table 5-1. The binding constants were determined using FITEQL to interpret the sorption data for $M/V=0.25$ g/L

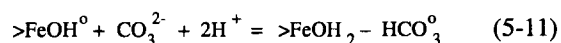
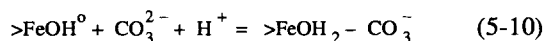
behavior quite well. There is a slight underprediction of sorption at $\text{pH} < 3$, and a slight underprediction of the sorption maximum for the lower M/V ratio.

5.3.3 Geochemical Modeling of Carbon Sorption on Fe-(hydr)oxides

Several studies have demonstrated that a desorption edge develops at high pH in an actinide- $\text{H}_2\text{O}-\text{CO}_2$ system (Tripathi, 1984; Hsi and Langmuir, 1985). One possible explanation for this behavior is the competition for available surface sites by carbon species such as CO_3^{2-} and HCO_3^- (LaFlamme and Murray, 1987; Zachara et al., 1987; Bruno et al., 1992; van Geen et al., 1994). In addition to its effect on sorption of actinides, the sorption of carbon species may contribute to the retardation of ^{14}C transport (Meijer, 1993). SCMs could provide a means of quantitatively accounting for the magnitude of these effects.

To date, quantitative information on carbon sorption is available for only a few minerals. Recent studies (Zachara et al., 1987; van Geen et al., 1994) have reported carbon sorption results for Fe-(hydr)oxides such as ferrihydrite and goethite. These data offer an opportunity to test the applicability of the uniform surface complexation approach for modeling carbon sorption. The data of Zachara et al. (1987) for carbon-ferrihydrite sorption at M/V ratios of 0.77 and 0.077 g/L are used in the following discussion.

Most of the experimental data of Zachara et al. (1987) are at pH values below the zero point of charge (pH_{ZPC}) of ferrihydrite ($\text{pH}_{\text{ZPC}} = 8.0$). Below the pH_{ZPC} , the positively charged surface sites ($>\text{FeOH}_2^+$) are predominant, the surface exhibits a net positive charge and adsorption of negatively charged species such as CO_3^{2-} and HCO_3^- will be electrostatically favored. It is also important to note that the DLM treats like charged surface complexes such as $>\text{FeOH}_2-\text{HCO}_3^0$ and $>\text{FeOH}-\text{H}_2\text{CO}_3^0$ as effectively equivalent, and only one has been considered here. The inner-sphere surface reactions selected for the conceptual model are



The experimental conditions and the mineral properties used in the modeling exercise are listed in Table 5-2 and the modeling results are shown in Figure 5-10. As with the U(6+)-montmorillonite model, FITEQL was used initially to determine binding constants for these reactions by considering each reaction separately. As a further test of the model, the binding constants determined from the 0.77 g/L data (Zachara et al., 1987) were used to predict sorption for a M/V ratio of 0.077 g/L. Despite differences in mineral properties and the surface acidity constants (K_+ and K_-) used in the models of carbon sorption on ferrihydrite, the binding constants determined for $>\text{FeOH}_2-\text{CO}_3^-$ or $>\text{FeOH}_2-\text{HCO}_3^0$ (Table 5-2) agree very closely with the values determined for carbon sorption on goethite by [Log $K=12.71$ and 20.78 , respectively; van Geen et al. (1994)]. This close agreement suggests that carbon binding may be similar for both goethite and ferrihydrite, and it may be possible to model sorption for these iron (hydr)oxides using a single set of sorption parameters.

It is also possible that more than one carbon surface complex is formed over the pH range of the experiment. To examine this, both reactions given in Eqs. (5-6) and (5-7) were included in a FITEQL run with both binding constants optimized simultaneously. The resultant binding constants differed slightly from those determined by considering each reaction separately (Table 5-2). The model prediction is included in Figure 5-10 for comparison.

5.3.4 Model Results and Discussion

One test of the flexibility of the model is the ability to predict the changes in sorption behavior induced by changes in geochemical conditions. For U(6+) sorption on montmorillonite, the model developed to interpret the data at $M/V=0.25$ g/L reproduces the observed data very well as a function of pH. To predict the effect of changing M/V ratio, the binding constants determined for Eqs. (5-4) and (5-5) from $M/V=0.25$ g/L data were kept constant while varying only M/V (and the resultant total site concentration). Applying the model with parameters developed from data at $M/V=0.25$ g/L predicted the experimental results at $M/V=2.5$ g/L very well, although there is a slight underprediction of sorption at $\text{pH} < 3$. This underprediction is possibly due to the effects of ion exchange in the clay structure, although this awaits independent confirmation.

Table 5-2. DLM parameters used to model carbon sorption on ferrihydrite

Mineral Properties and Experimental Conditions – Montmorillonite	
Specific Surface Area (A_{SP}) _(a)	600 m ² /g
Surface Site Density (N_S) _(a)	2.3 sites/nm ²
Solid Concentration (M/V) _(b)	0.077 g/L:0.77 g/L
Total Carbon _(b)	4.6 × 10 ⁻⁶ M
Surface Reactions	Log K
$>FeOH^0 = >FeO^- + H^+$ _(a)	-8.93
$>FeOH^0 + H^+ = >FeOH_2^+$ _(a)	7.29
$>FeOH^0 + CO_3^{2-} + H^+ = >FeOH_2-CO_3^-$ _(c)	13.06
$>FeOH^0 + CO_3^{2-} + 2H^+ = >FeOH_2-HCO_3^0$ _(c)	20.75
Both reactions simultaneously: $>FeOH^0 + CO_3^{2-} + H^+ = >FeOH_2-CO_3^-$ _(c) $>FeOH^0 + CO_3^{2-} + 2H^+ = >FeOH_2-HCO_3^0$ _(c)	12.96 19.80
(a) From Dzombak and Morel (1990).	
(b) From Zachara et al. (1987).	
(c) Determined for M/V = 0.77 g/L.	

In general, the DLM results on carbon sorption on ferrihydrite indicate that either surface complex can reproduce the observed desorption edge at higher pH (Figure 5-10). The surface complex $>FeOH_2-HCO_3^0$ provides a slightly better simulation of the desorption edge and is better able to reproduce the sorption maximum at the two M/V ratios. However, the sorption edge at lower pH is slightly overpredicted. Assuming formation of only $>FeOH_2-CO_3^-$ does a slightly better job in predicting sorption behavior at pH<5, but slightly overpredicts sorption at higher pH values. Assuming both species exist simultaneously results in prediction curves similar to those for $>FeOH_2-CO_3^-$, with a slight improvement at the pH extremes. Since one goal of performance assessment is to use simplified approaches, it may be preferable to invoke conceptual models that require only a single surface complex. Nevertheless, the uniform DLM approach advocated in several recent studies (Dzombak and Morel, 1990; Davis and Kent,

1990; Bradbury and Baeyens, 1993) is able to reproduce the general sorption data reasonably well given the scatter in the data. As data become available for carbon sorption on different mineral surfaces, it should be relatively straightforward to include the effects of carbon competition for surface sites in subsequent models.

Meijer (1993) pointed out that carbon sorption is likely to be low for minerals where the pH_{ZPC} is lower than expected pH conditions in the groundwater. These minerals include those such as quartz, feldspar, and some clays. Under these conditions, $>XO^-$ is the dominant surface site relative to $>XOH_2^+$ and sorption of negatively charged CO_3^{2-} and HCO_3^- is electrostatically inhibited. At the low carbon concentrations used in experiments with relatively sorptive minerals with high pH_{ZPC} such as goethite and ferrihydrite, the amount of aqueous carbon sorbed is typically less than 100 percent. This behavior is true for

[Data from Zachara et al. (1987); T=25 °C; $C_T=4.6 \times 10^{-6}$ M]

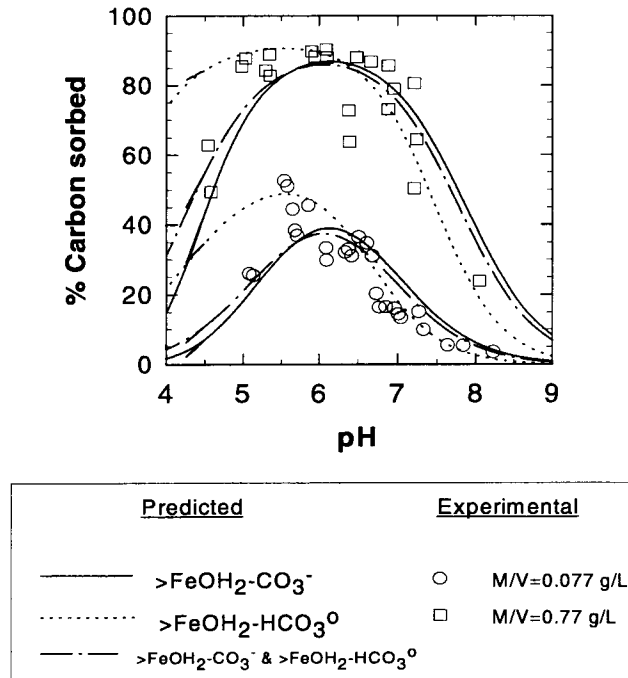


Figure 5-10. DLM model results for carbon-ferrihydrate sorption. The model parameters and experimental conditions are given in Table 5-2. The binding constants were determined using FITEQL to interpret the sorption data for M/V=0.77 g/L (data from Zachara et al., 1987)

experiments using M/V ratios up to 10 g/L for goethite (van Geen et al., 1994) and 0.77 g/L for ferrihydrate (Zachara et al., 1987), and sorption is reduced even more at pH greater than about 7 and less than about 5. This behavior suggests that the contribution of sorption of aqueous carbon species to ^{14}C retardation may be minor, especially relative to the effect of aqueous carbonate species (or even calcite precipitation) on the retardation of gaseous transport of CO_2 (Codell and Murphy, 1992). Studies have shown that CO_2 may sorb on minerals directly from the gas phase (Russell et al., 1975), although this has not yet been quantitatively addressed in geochemical models.

The conceptual model developed for U(6+) sorption on montmorillonite does not explicitly invoke the formation of either U-carbonate surface species such

as $>SiOH_2-UO_2(CO_3)_2^-$ or the competition for sites by carbon species (e.g., $>AlOH_2-CO_3^-$). At relatively low carbon concentrations, this assumption may be reasonable. At higher carbon concentrations, however, the coverage of surface sites by carbonate may become significant, leading to a reduction in sorption of radionuclides if they are more weakly sorbed than carbonate (van Geen et al., 1994). At present, there is insufficient data to characterize the sorption of carbon on montmorillonite in the manner discussed above for ferrihydrate. Instead, in the model developed here, the desorption edge at higher pH is produced by increased carbon concentration and the more effective competition of carbonate ligand for the available U relative to the surface sites. While this representation may not be strictly accurate for the reactions occurring at the mineral-water interface, in the absence of definitive data

on the surface complexes being formed, it was decided to use the simplest model capable of reproducing the observed sorption behavior.

The success of the DLM in predicting these experimental results suggests that it may be possible to use simple conceptual models of the type developed here to extrapolate to a variety of chemical conditions from a relatively limited data set. This ability to extrapolate is in contrast to typical empirical approaches, in which the lack of a strong theoretical basis makes extrapolation beyond experimental conditions uncertain. For these models, addressing the full range in expected chemical conditions may quickly lead to a considerable experimental burden. The mechanistic approach developed here also has the advantage of identifying critical chemical conditions that have the most effect on radionuclide sorption, and establishing those conditions where sorption is most limited.

Figure 5-11 represents the type of extrapolation that may be possible using the DLM developed from the U(6+)-montmorillonite sorption data. The vertical (z) axis represents the percent sorbed, while the x- and y-axes represent sorption as a function of M/V (g/L) and pH, respectively. The sorption envelope defined by the sorption and desorption edges is relatively constant. Due to the increase in the total number of available sites, sorption increases with increasing M/V, and the sorption behavior seems relatively constant for M/V greater than about 1 g/L. The sorption maximum predicted by the model does not quite reach 100 percent, even at higher M/V ratios. Based on the conceptual chemical model, similar behavior would be predicted by increasing the other parameters used to calculate the total number of sites (specific surface area, site density). These values are generally measured, however, and are better constrained in natural systems (within a factor of four or five) than the effective M/V.

Current performance assessment efforts rely on empirical sorption models such as the K_d approach. Ideally, sorption models such as SCMs should be directly incorporated into reactive transport codes, but this comes at the expense of increased computational burden. This limitation is even more important for stochastic approaches that rely on sampling techniques and many realizations to generate population statistics. For the purposes of performance assessment, it may be possible to use the DLM to assess the effect of critical parameters such as total carbon (C_T) and M/V ratio for

conditions beyond the ranges used in sorption experiments. The calculated sorbed and aqueous concentrations can be used to develop a look-up table of K_d values predicted as a function of these variables. One of the most difficult aspects of this type of approach, however, is in determining the appropriate values for these parameters in a groundwater system. While geochemical models can be used to limit likely pH and $p(\text{CO}_2)$ conditions, determining the effective solid concentration that is "seen" by groundwater containing dissolved radionuclides is particularly difficult. For the purposes of performance assessment calculations, the variables could be sampled over likely ranges, and the associated K_d used in transport calculations. While this approach is not an explicit incorporation of geochemistry in the transport calculations, it does provide a step toward a more theoretical basis for sorption modeling in performance assessment.

5.4 ASSESSMENT OF PROGRESS TOWARD MEETING PROJECT OBJECTIVES

The broad objective of this project is to develop sufficient understanding of issues relevant to radionuclide transport. An important mechanism for attenuating radionuclide transport is sorption of radionuclides on minerals encountered along the flow paths. Results of laboratory experiments on U sorption combined with modeling efforts using surface-complexation models are providing us with an understanding of the important parameters that control the sorption behavior of an actinide element. For example, the experimental results reported here and in previous CNWRA reports (e.g., Pabalan and Turner, 1994) demonstrate that U sorption on montmorillonite, clinoptilolite, and α -alumina, which are sorbents of very distinct mineralogic and surface properties, is strong at near-neutral pH (~6.3). In all those cases, the amount of U sorbed is strongly dependent on pH and decreases steeply away from near-neutral pH. The M/V ratio (or analogously, surface-area to solution-volume ratio) also influences sorption, that is, as the ratio increases, the relative amount of U sorbed on the solid also increases. Because of the strong dependence on pH and M/V ratio, modeling of sorption processes will likely require that changes in groundwater chemistry and in rock/fluid ratio be properly accounted for in performance assessment calculations if retardation by sorption processes is included. However, the success of the surface-complexation model in describing and

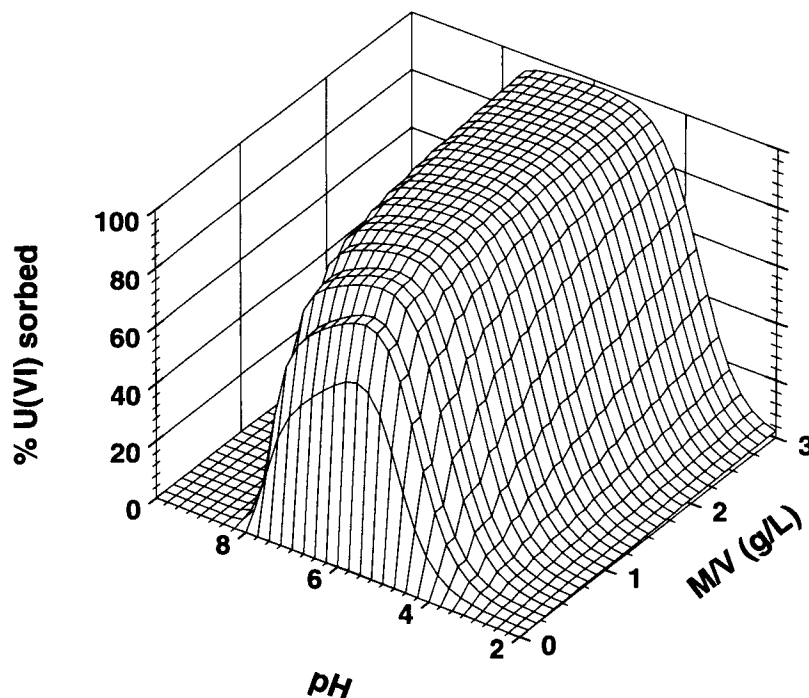


Figure 5-11. Diffuse-Layer Model (DLM) model results for uranium(6+)-montmorillonite sorption as a function of M/V and pH. Total uranium = 50 ppb. The model parameters and experimental conditions are given in Table 5-1.

predicting U sorption on montmorillonite and other minerals suggests that SCMs offer a scientifically defensible approach that may be useful for performance assessment calculations.

The similarity in the pH-dependence of U sorption on montmorillonite, clinoptilolite, and α -alumina is important. It may help identify simplified approaches to modeling sorption and thus help in the development of CDMs relevant to the KTUs identified in Section 5.1 and in developing conceptual models related to the Performance Assessment Research Project and the Iterative Performance Assessment Phase 3. The information derived from the laboratory experiments may also help interpret data on U distribution and migration at the Peña Blanca field site of the Geochemical Natural Analog Research Project.

5.5 PLANS FOR NEXT REPORT PERIOD

Additional experiments studying U sorption on montmorillonite will be conducted at an M/V of 0.025 g/L to further test the predictive capability of the surface-complexation model. Experiments with different initial U concentrations will also be conducted to determine the dependence of U sorption on radionuclide concentration. In addition, experiments to study the possible effect of $p\text{CO}_2$ on the sorption equilibrium will be done using clinoptilolite as the sorbent phase. These experiments will be conducted in a controlled-atmosphere glove box. Preliminary experiments will also be initiated using ^{237}Np and ^{239}Pu as the sorbing radionuclides. The data generated from all these experiments will continue to be utilized in the

modeling activities being conducted in this project and extended to radionuclide transport models used in Iterative Performance Assessment. To better quantify the sorption competition between container walls and mineral sorbents, additional steps will be included in the sorption experiments to desorb the radionuclide off the containers and minerals and measure their concentration.

Modeling efforts will continue to focus on developing the necessary binding constants for surface complexation modeling of actinide sorption. These efforts will include models of experimental data developed in this project. Of particular interest will be the new experiments involving Np and Pu as sorbates. To develop a more complete understanding of other radionuclides, preliminary modeling efforts will also continue to address sorption data available from other experiments. U sorption models developed for iron (hydr)oxides will be used to calculate effective K_d values and investigate their variations as a function of pH, M/V, and total carbonate concentration. This work may provide insight onto reasonable ranges to be included in transport models used in performance assessment and with U transport at the Peña Blanca Natural Analog Site.

5.6 REFERENCES

- Allison, J.D., D.S. Brown, and K.J. Novo-Gradac. 1991. MINTEQA2/PRODEFA2, *A Geochemical Assessment Model For Environmental Systems: Version 3.0 User's Manual*. EPA/600/3-91/021. U.S. Environmental Protection Agency, Athens, GA.
- Bradbury, M.H., and B. Baeyens. 1993. A general application of surface complexation to modeling radionuclide sorption in natural systems. *Journal of Colloid and Interface Science* 158: 364–371.
- Bruno, J., W. Stumm, P. Wersin, and F. Brandberg. 1992. On the influence of carbonate in mineral dissolution: I. The thermodynamic and kinetics of hematite dissolution in bicarbonate solutions at $T = 25^\circ\text{C}$. *Geochimica et Cosmochimica Acta* 56: 1,139–1,147.
- Codell, R.B., and W.M. Murphy. 1992. Geochemical model for ^{14}C transport in unsaturated rock. *Proceedings of the Third International Conference on High-Level Radioactive Waste Management 2*. La Grange Park, IL: American Nuclear Society: 1,959–1,965.
- Davis, J.A., and D.B. Kent. 1990. Surface complexation modeling in aqueous geochemistry. M.F. Hochella, Jr., and A.F. White, eds. *Reviews in Mineralogy: Volume 23*. Mineral-Water Interface Geochemistry. Washington, DC: Mineralogical Society of America: 177–260.
- Dzombak, D.A., and F.M.M. Morel. 1990. *Surface Complexation Modeling: Hydrous Ferric Oxide*. New York, NY: John Wiley and Sons.
- Grenthe, I., J. Fuger, R.J. Lemire, A.B. Muller, C. Nguyen-Trung, and H. Wanner. 1992. *Chemical Thermodynamics Series, Volume 1: Chemical Thermodynamics of Uranium*. Nuclear Energy Agency. New York, NY: Elsevier.
- Hsi, C.-K.D., and D. Langmuir. 1985. Adsorption of uranyl onto ferric oxyhydroxides: Application of the surface complexation site-binding model. *Geochimica et Cosmochimica Acta* 49: 1,931–1,941.
- Jackson, M.L. 1956. Soil Chemical Analysis – Advanced Course. Madison, WI: Department of Soil Science, University of Wisconsin.
- LaFlamme, B.D., and J.W. Murray. 1987. Solid/Solution Interaction: The effect of carbonate alkalinity on adsorbed thorium. *Geochimica et Cosmochimica Acta* 51: 243–250.
- Meijer, A. 1993. Far-field transport of carbon dioxide: Retardation mechanisms and possible validation experiments. *Conference Proceedings FOCUS '93: Site Characterization and Model Validation*. La Grange Park, IL: American Nuclear Society: 110–112.

- Pabalan, R.T., J.D. Prikryl, P.M. Muller, and T.B. Dietrich. 1993. Experimental study of U(6+) sorption on the zeolite mineral clinoptilolite. C.G. Interrante and R.T. Pabalan, eds. *Scientific Basis for Nuclear Waste Management XVI*. MRS Symposium Proceedings 294, Pittsburgh, PA: Materials Research Society: 777-782.
- Pabalan, R.T., and D.R. Turner. 1994. *Sorption Modeling for HLW Performance Assessment. NRC High-Level Radioactive Waste Research at CNWRA July - December, 1993*. B. Sagar, ed. CNWRA 93-02S. San Antonio, TX: Center for Nuclear Waste Regulatory Analyses: 6-1 to 8-23.
- Prikryl, J.D., R.T. Pabalan, D.R. Turner, and B.W. Leslie. 1994. Uranium sorption on α -alumina: Effects of pH and surface-area/solution-volume ratio. *Radiochimica Acta*, (in press).
- Rai, D., J.M. Zachara, L.E. Eary, C.C. Ainsworth, J.E. Amonette, C.E. Cowan, R.W. Szelmeczka, C.R. Resch, R.L. Schmidt, D.C. Girvin, and S.C. Smith. 1988. *Chromium Reactions in Geologic Materials*. EPRI-EA-5741. Palo Alto, CA: Electric Power Research Institute.
- Riese, A.C. 1982. *Adsorption of Radium and Thorium onto Quartz and Kaolinite: A Comparison of Solution/Surface Equilibria Models*. Unpublished. Ph.D. Dissertation. Golden, CO.
- Rogers, P.S.Z., and A. Meijer. 1993. Dependence of radionuclide sorption on sample grinding, surface area, and water composition. *Proceedings of the Fourth International Conference on High Level Radioactive Waste Management*. La Grange Park, IL: American Nuclear Society: 1,509-1,516.
- Russell, J.D., E. Patterson, A.R. Fraser, and V.C. Farmer. 1975. Adsorption of carbon dioxide on goethite (α -FeOOH) surfaces, and its implications for anion adsorption. *Journal of the Chemical Society of London, Faraday Transactions I* 71: 1,623-1,630.
- Triay, I.R., B.A. Robinson, R.M. Lopez, A.J. Mitchell, and C.M. Overly. 1993. Neptunium retardation with tuffs and groundwaters from Yucca Mountain. *Proceedings of the Fourth International Conference on High Level Radioactive Waste Management*. La Grange Park, IL: American Nuclear Society: 1,504-1,508.
- Tripathi, V.S. 1984. *U(VI) Transport Modeling: Geochemical Data and Submodels*. Unpub. Ph.D. Dissertation. Stanford, CA: Stanford University.
- Turner, D.R. 1993. *Mechanistic Approaches to Radionuclide Sorption Modeling*. CNWRA 93-019. San Antonio, TX: Center for Nuclear Waste Regulatory Analyses.
- van Geen, A., A.P. Robertson, and J.O. Leckie. 1994. Complexation of carbonate species at the goethite surface: Implications for adsorption of metal ions in natural waters. *Geochimica et Cosmochimica Acta* 58: 2,073-2,086.
- Westall, J.C. 1982. *FITEQL: A Computer Program for Determination of Chemical Equilibrium Constants From Experimental Data, Version 2.0*. Report 82-02. Corvallis, OR: Oregon State University, Department of Chemistry.
- Zachara, J.M., D.C. Girvin, R.L. Schmidt, and C.T. Resch. 1987. Chromate adsorption on amorphous iron oxyhydroxide in the presence of major groundwater ions. *Environmental Science and Technology* 21: 589-594.

6 PERFORMANCE ASSESSMENT RESEARCH

by Robert G. Baca, Ronald T. Green, Peter C. Lichtner, and Stuart A. Stothoff

Investigators: Robert G. Baca, Ronald T. Green, Sitakanta Mohanty, Stuart A. Stothoff, and Gordon W. Wittmeyer (CNWRA); Christopher J. Freitas (SwRI); Evaristo J. Bonano and Mohan Seth (Consultants)

NRC Project Officer: John D. Randall

6.1 TECHNICAL OBJECTIVES

Postclosure Performance Assessment (PA), as a scientific evaluation process, will provide the quantitative basis for judging the acceptability of the proposed repository system at Yucca Mountain (YM). In conducting a PA, the Nuclear Regulatory Commission (NRC) will utilize a hierarchy of models and codes. The top level or total-system PA (TSPA) code, which is being developed under the NRC Nuclear Material Safety and Safeguards (NMSS) Iterative Performance Assessment (IPA) activity, models a wide variety of processes, phenomenological interactions, and future system states, but in a necessarily simplified manner. In contrast, the lower-level codes in this hierarchy are very sophisticated, but model only a few processes in a very detailed manner. Quite interestingly, both types of codes typically exceed the computational limits of conventional computers and push the capability of the most advanced, high-performance supercomputers. The technical objectives of the PA Research Project are to develop PA modeling technology appropriate for NRC's compliance determination in three specific areas: (i) alternate conceptual models of key phenomena and future system states (i.e., disruptive scenarios), (ii) efficient and robust computational and computer techniques for solving the model equations, and (iii) formalized approaches for testing and evaluating (i.e., validating) computer models.

One of the primary programmatic objectives of the PA Research Project is to provide modeling technology that will benefit the ongoing NRC IPAs. Another, and equally important, programmatic objective is to provide the knowledge base necessary for supporting: (i) revision of the postclosure PA

Compliance Determination Strategies (CDSs) (i.e., CDS 6.1, 6.2, and 6.3), and (ii) development of postclosure performance Compliance Determination Methods (CDMs) that will be incorporated into appropriate sections of the License Application Review Plan (LARP). Specifically, this research project is contributing to the knowledge base for addressing Key Technical Uncertainties (KTUs) associated with:

- (i) Conceptual models
- (ii) Mathematical models
- (iii) Model parameters
- (iv) Future system states
- (v) Model validation

At present, the KTU related to the first three items resulted in the associated CDS being classified as Review Level 4, while the CDS associated with the fourth item is classified Review Level 5; these KTUs are broadly addressed in Tasks 1 and 2 of this research project. The last KTU requires a type Level 5 Review of CDS 6.1,—Assessment of Compliance with the Requirement for Cumulative Releases of Radioactive Materials, and is being addressed in a focused effort under Task 3 of this research project. In addition, the practical experience and expertise gained from this research project will place the NRC and the Center for Nuclear Waste Regulatory Analyses (CNWRA) in a position to thoroughly and independently evaluate the U.S. Department of Energy (DOE) PA models and codes.

Because of its multidisciplinary nature, the PA Research Project is an integrated programmatic effort drawing on expertise from such technical areas as

hydrology, geochemistry, structural geology, volcanology, seismology, climatology, computational fluid dynamics, and computer science. At present, the PA Research Project is programmatically integrated with the NMSS IPA activity and three other Office of Nuclear Regulatory Research (RES) projects: (i) the Geochemical Analog of Contaminant Transport in Unsaturated Rock Research Project, (ii) the Sorption Modeling for High-Level Waste Performance Assessment Research Project, and (iii) the Stochastic Unsaturated Flow and Transport Research Project. In relation to the Geochemical Analog of Contaminant Transport in Unsaturated Rock Research Project, data from rock cores obtained from the Peña Blanca field site are being analyzed to improve conceptual and mathematical models of: (i) variably saturated flow in the fractured-porous tuff, and (ii) radionuclide transport in discrete fractures and diffusion into and out of the rock matrix. In addition, data on diffusion and sorption coefficients, compiled under the Sorption Modeling for High-Level Waste Performance Assessment Research Project, are contributing to conceptual/mathematical model development of radionuclide transport phenomena. Simulation studies conducted under the Stochastic Unsaturated Flow and Transport Research Project have identified a number of computational aspects that currently limit the practical application of detailed hydrologic codes (e.g., BIGFLOW) to the YM site. Work conducted under Task 2 of the PA Research Project is being focused to reduce or remove these computational limitations.

The PA Research Project is designed to address a number of user needs identified by the NMSS for postclosure PA. Specific research needs include: (i) selection of means to identify and screen scenarios, (ii) efficient integration of mathematical models into high-level waste (HLW) PA methodology, (iii) validation of mathematical models, (iv) evaluation of mathematical models, (v) evaluation of mathematical flow and transport models applicable to unsaturated fractured rock and application to a range of scales and heterogeneities, and (vi) appraisal of the applicability of existing mathematical models of hydrologically and chemically coupled flow and transport.

Research conducted under the PA Research Project is divided among three major tasks. The first task, Conceptual Model Development, focuses on developing conceptual/mathematical models in two areas: (i) flow and transport phenomena, and (ii) disruptive event scenarios. In the second task, Computational Model Development, research is directed toward the development of advanced numerical methods necessary to implement PA conceptual and mathematical models. Under the third task, Model Evaluation, a general model validation strategy is being developed based on the experience gained from the INTRAVAL project test cases. Work completed on these tasks has been reported in previous semi-annual research reports. This section describes the results of the PA Research Project for the first half of 1994.

6.2 SIGNIFICANT TECHNICAL ACCOMPLISHMENTS

In this reporting period, research emphasis was placed on the technical objectives of the first task of the PA Research Project, which deals with two major topics: (i) disruptive event scenarios, and (ii) flow and transport phenomena. On the first topic, a comprehensive review was performed on scenario selection methodologies (Bonano and Baca, 1994). The review included scenario approaches used in repository programs in the United States [e.g., NRC, DOE, Electric Power Research Institute (EPRI)], and in other countries (Canada, Sweden, United Kingdom, and France). Regarding the second topic, a modeling study was completed on analysis of fracture flow at the Peña Blanca Natural Analog Site. The study examines the rates of water movement for two conceptual models of fracture flow in the fractured-porous tuff geology. The study provided insights important to a proposed infiltration experiment at the Peña Blanca site. Significant findings and results of these two activities are summarized in the following subsections.

6.2.1 Review of Scenario Selection Methodologies

In the United States and many other countries, scenario methodologies have been widely used in TSPAs to account for the uncertainty in future system

states. Each scenario, representing a plausible realization of the future state of the disposal system, is comprised of events and processes (EPs¹) that can affect the long-term performance. Associated with each scenario is a probability of occurrence expressing the likelihood that the scenario will occur within the regulatory period. In principle, the probability of occurrence of a given scenario is estimated from the probability of occurrence of the EPs that form the scenario. The wide acceptance of the scenario approach notwithstanding, difficulties are associated with its implementation. Among these difficulties are: (i) the lack of uniqueness in the definition of the term "scenario," even extending to the use of other terminology, (ii) the lack of uniqueness in the scenario selection approach (not only in the methodology used, but also in the general types of EPs that are considered),

1. The term events and processes (EPs) will be used throughout this report for the purpose of consistency. Different groups used terms other than EPs; some examples are features, events, and processes (FEPs) and factors.

(iii) the considerable reliance on subjective judgments, (iv) the multiple interpretations for the treatment of human intrusion, and (v) the difficulty of estimating the probability of occurrence of the EPs and of the scenarios.

As a first step towards the identification of possible ways to resolve these difficulties, a review of the current state-of-the-art in scenario selection methodologies and approaches was conducted, the findings of which were published as a formal CNWRA report (Bonano and Baca, 1994). The review focused on scenario selection approaches being used by the major radioactive waste management programs in the United States and in several member countries of the Organization of Economic Cooperation and Development (see Table 6-1). In addition, the review highlighted similarities and differences between the different methodologies and, where possible, explained the nature and source of the differences. The review also included an examination of the Environmental Simulation Approach (ESA) with the objective of determining: (i) whether the ESA is truly an alternative

Table 6-1. Scenario selection methodologies reviewed

Country	Organization
United States	Nuclear Regulatory Commission Sandia National Laboratories Department of Energy/Yucca Mountain Project Department of Energy/Waste Isolation Pilot Plant Electric Power Research Institute
Canada	Atomic Energy of Canada Limited
Sweden	Swedish Nuclear Waste Management Company/Swedish Nuclear Power Inspectorate
United Kingdom	United Kingdom Nirex Ltd., Department of Environment, Her Majesty's Inspectorate of Pollution* * (This is not considered a scenario approach, but because it was reviewed, for completeness purposes, it is included in this list.)
France	National Agency for Radioactive Waste Management

to the scenario approach, and if so, (ii) what advantages it may offer over the latter. The review concluded with an examination of key issues related to scenario development and selection that still remain open and for which resolution is necessary. A brief summary of Bonano and Baca (1994) is provided below.

6.2.1.1 Nuclear Regulatory Commission/Sandia National Laboratories Scenario Methodology

The seminal work on scenario selection methods for the deep geologic disposal of HLW was performed for the NRC by Sandia National Laboratories (SNL). A scenario selection methodology (Cranwell et al., 1990) was originally developed in the late 1970s and early 1980s for an HLW repository in bedded salt. The methodology was later applied to an HLW repository in basalt and in tuff. That methodology was the focal point of the Nuclear Energy Agency (NEA) Scenario Working Group (Nuclear Energy Agency, 1992), which coined the name "NRC/SNL scenario methodology." The methodology consists of five major steps:

- (i) Identification of EPs that could adversely impact the performance of the repository
- (ii) Classification of the EPs to assist in arguments of completeness
- (iii) Screening of the initial list of EPs
- (iv) Screening of scenarios
- (v) Selection of a final set of scenarios for the PA

The use of expert judgments permeates every step of this methodology. Deficiencies of the methodology include: (i) potential generation of an inordinately large number of scenarios; (ii) inability to account for the time-dependent onset, evolution, or interaction of the EPs in a given scenario; (iii) mutual exclusivity of scenarios (i.e., independence in the probability sense); and (iv) potential to lead to an underestimation of risk. These deficiencies notwithstanding, scenario selection approaches adopted by many other repository programs both in the United

States and other countries are based, by and large, on the NRC/SNL scenario methodology.

In the NRC IPA exercises (Phases 1 and 2), a scenario selection approach has been used that differs from the original NRC/SNL methodology in two basic aspects: (i) the nature of the EPs that can be considered, and (ii) the use of scenario classes. While the NRC/SNL scenario methodology, in principle, considers initiating EPs that are natural-, repository-, or human-induced in the IPA exercises, the NRC considers only EPs with sources outside the accessible environment. For example, repository-induced EPs are not considered in scenario construction; instead, they are incorporated into the models and database used to simulate the repository system. Uncertainty in repository-induced EPs is represented through uncertainty in the models and data used in the PA.

The NRC is currently using the term "scenario class" to represent a given grouping of EPs and, in that context, it is equivalent to the term "scenario" originally used by Cranwell et al. (1990). For each scenario class, several scenarios can be generated from different sequences of the EPs in the class. The probability of the scenario class is the product of the probability of each of the individual EPs, assuming the EPs are independent. Each of the scenarios within a class is, in turn, assigned a probability by allocating the class probability evenly among the scenarios.

6.2.1.2 Department of Energy Yucca Mountain Project

The Yucca Mountain Site Characterization Plan (YMSCP) outlined the approach that the DOE intends to follow in developing and selecting scenarios for PA. This approach consists of five basic steps:

- (i) Identification of release phenomena
- (ii) Identification of potentially significant EPs
- (iii) Identification of release scenarios
- (iv) Grouping of release scenarios into scenario classes

- (v) Screening of scenarios and scenario classes

This approach was applied in the YMSCP to expand the list of scenarios originally developed by Ross (1987).

More recently, Barr et al. (1993) proposed an approach based on a "generalized event tree," as an extension of the NRC/SNL scenario methodology. The structure of the generalized event tree centers on five basic pieces of information: (i) the identification of an EP, (ii) the impact of the EP on the groundwater flow system, (iii) the impact of the EP on the waste, (iv) the release of waste from the engineered-barrier system (EBS) due to the occurrence of one or more EPs, and (v) the transport of radionuclides to the accessible environment due to the occurrence of one or more EPs. Using this information, a scenario class can be constructed by starting with an initiating EP and following a path that connects physically plausible EPs leading to a release of radionuclides to the accessible environment. Each path, or scenario class, is accompanied by one or more schematic drawings of possible conceptual models for each EP in the scenario class; thus, a scenario is the combination of a scenario class and a given set of conceptual models.

6.2.1.3 Waste Isolation Pilot Plant

Since the early 1970s, there have been several studies aimed at the identification of scenarios for deep geologic disposal in bedded-salt formations in the southwestern United States; some of these have been specific to the Waste Isolation Pilot Plant (WIPP). However, a systematic scenario approach only recently has been implemented. Guzowski (1990) applied the NRC/SNL scenario methodology and concluded that, due to the geological stability of the region where the WIPP is located, EPs due to natural processes have negligible probability of occurrence; consequently, WIPP PA calculations are currently considering only scenarios due to human intrusion. The majority of WIPP scenario activities have centered on using expert judgments in the estimation of the modes of human intrusion and the associated probability of occurrence (Hora et al., 1991).

6.2.1.4 Scenario Analysis in Electric Power Research Institute Studies for Yucca Mountain

EPRI developed and applied a risk-based methodology to examine the performance of a hypothetical HLW repository at YM (McGuire, 1990; 1992). The application of the methodology included the identification of scenarios. A multidisciplinary group of experts was assembled to provide judgments reflecting uncertainties in scientific techniques, assumptions, and data and parameters needed for the calculations. Logic trees were also used to organize and aggregate the judgments. The logic trees were used to track the effects of external EPs on the behavior of the repository. These effects were represented by values of specific parameters (e.g., the effects of climate change were represented by the value of the net infiltration) and the expert judgments were estimates of the probability for different values of the parameters.

In some respects, the EPRI approach is similar to that proposed by Barr and Dunn (1993) for YM in that both approaches allowed for multiple conceptual interpretations. Like many scenario approaches, the EPRI approach relies heavily on the use of expert judgments, and its major difficulty is the estimation of the conditional probabilities for each branch of tree in a manner such that they capture complex interactions and dependencies between the effects of the different EPs represented in the tree.

6.2.1.5 Atomic Energy of Canada Laboratory Scenario Selection Approach

Atomic Energy of Canada Laboratory (AECL) adopted the NRC/SNL scenario methodology and customized it to render it applicable to the disposal of radioactive wastes generated from Canadian Deuterium Uranium (CANDU) reactors in plutonic rocks of the Precambrian Shield (Stephens and Goodwin, 1990). A group of experts was assembled to execute the steps in the methodology; however, before engaging in the application of the methodology, they agreed on definitions of key terms such as "scenario." They generated a list of 270 EPs that could influence the performance of any of the various components of the

disposal facility. Of these, 145 were judged to need qualitative treatment only, while 125 required quantitative evaluation. The latter were used to construct scenarios. Rather than use the event-tree approach in the NRC/SNL scenario methodology, the group of experts constructed a "central scenario" that included as many EPs as possible. An EP was excluded from the central scenario if: (i) it was deemed to be important only under rare or unusual circumstances, (ii) its presence was incompatible with the presence of another more important EP already in the central scenario, and/or (iii) its exclusion resulted in a simplification of the PA. A total of 117 EPs were included in the central scenario. The remaining eight EPs were used to construct alternative scenarios. However, 255 alternative scenarios were generated, and this number was deemed to be too high. Therefore, the number of remaining EPs was reduced to two, leading to three alternative scenarios. The group of experts assigned a probability of occurrence to the central scenario and the three alternative scenarios.

6.2.1.6 Swedish Scenario Selection Approach

The Swedish Nuclear Waste Management Company (SKB) and the Swedish Nuclear Power Inspectorate (SKI) conducted a joint scenario selection project for a hypothetical spent fuel and HLW repository in crystalline rock (Andersson et al., 1989; Andersson and Eng, 1990). The objective of the project, however, was primarily to examine scenario selection approaches rather than to develop scenarios for PA calculations. The starting point of the project was the NRC/SNL scenario methodology, and the first three steps in that methodology were exercised. One important deviation was the introduction of the "process system" as a means to implement different treatments for EPs with different origins. The process system is to include all EPs that are either active continuously or that are in standby mode and will be activated by the occurrence of other externally driven EPs. These latter EPs are then used to develop alternative scenarios. The SKB/SKI team used a group of experts to identify, screen, and classify EPs. After EPs were identified, they were sorted into one of four classes. One class consisted of those EPs to be included in the process system; another, naturally occurring external EPs that should be

considered to form alternative scenarios; a third, humanly induced EPs that should be considered in the formulation of alternative scenarios, and finally, those EPs considered to be insignificant and not to be considered further. In general terms, the process system is similar to the central scenario in the AECL approach.

6.2.1.7 United Kingdom Nirex Ltd. Scenario Selection Approach

The use of the NRC/SNL scenario methodology, whether as originally developed or modified in some fashion, relies on a bottom-up approach, by generating as comprehensive a list of EPs as possible and using these to construct scenarios. An alternative approach, used by UK Nirex Ltd., starts by postulating unacceptable consequences of deep geologic disposal of radioactive wastes and seeks to identify the causes that can lead to those consequences using a fault-tree, in a top-down approach (Billington et al., 1990; Nuclear Energy Agency, 1992). The UK Nirex Ltd scenario approach consists of six basic steps:

- (i) Division of the disposal system into a set of different "scenario elements"
- (ii) Construction of an influence diagram describing the interdependence between the scenario elements
- (iii) Postulation of alternative states that each scenario element can attain as it evolves in time
- (iv) Generation of combinations of alternative states, with each combination representing a potential scenario
- (v) Screening of scenarios
- (vi) Estimation of probability of occurrence for each of the surviving scenarios

A major drawback of this approach is that there is no universally established method to decompose the disposal system into scenario elements. For example, scenario elements can be identified based on different criteria, such as cause (natural phenomena, human actions, etc.), disposal system component (repository, geologic setting, biosphere), etc. One of the major

limitations of the UK Nirex Ltd approach is that use of different criteria to identify the scenario elements can have significant influence on the scenarios developed. One of the results of applying a top-down approach is the generation of a considerably smaller number of scenarios when compared to bottom-up approaches.

6.2.1.8 French Scenario Selection Approach

The French radioactive waste disposal regulation, Fundamental Safety Regulation No. III-2-f (RFS), promulgated by the Central Agency for the Safety of Nuclear Facilities in 1991, is very prescriptive with respect to the conduct of PA for a waste disposal facility and, within the context of that PA, to the selection of scenarios. The RFS states that PA will be a deterministic evaluation of the possible radiological impacts from two types of situations: (i) a reference (or base case) situation which represents the occurrence of certain or highly probable EPs, and (ii) hypothetical situations representing the occurrence of low-probability EPs that can lead to adverse consequences. The RFS further specifies that the PA must focus on the evaluation of a limited number of representative situations (or scenarios) from different families of scenarios, such that those selected have the highest possible consequences.

France's National Agency for Radioactive Waste Management (ANDRA) has developed a scenario approach (Raimbault et al., 1992) based on these guidelines that consists of four steps: (i) identification of a comprehensive set of initiating EPs; (ii) ranking of the EPs based on probability (expressed qualitatively; e.g., more likely or less likely), consequence, or relevance to a given disposal site; (iii) identification of secondary EPs caused by the initiating EPs; and (iv) grouping of the EPs into families of scenarios and selection of the scenario from each family with the highest potential consequence. This high-consequence scenario is called the "envelope scenario" and is the one to be used in PA calculations. The concept of a base-case scenario (situation) and alternative scenarios (situations) is very similar to the approaches used by AECL and SKB/SKI. One key point is that the RFS eliminates the need to quantitatively estimate the probability of occurrence of scenarios.

6.2.1.9 British Environmental Simulation Approach

The UK Department of Environment, Her Majesty's Inspectorate of Pollution (HMIP), undertook a research program to integrate the ESA into PA, and it was the centerpiece of the Dry Run 3 exercise (Sumerling, 1992). HMIP proposed the ESA as an alternative that would overcome limitations of the scenario approach. The HMIP ESA consists of two basic steps: (i) generation of possible future evolutions of the natural environment due to climate change, and (ii) the estimation of the effects of those evolutions on repository performance.

The fundamental premise of the HMIP approach is that possible future climate changes can be forecast from the reconstruction of the dominant amplitudes and frequencies of global climate changes over the past 3 m.y. The results of the Dry Run 3 exercise support the conclusion that the ESA can indeed yield different estimates of repository performance when compared to the scenario approach. However, earlier assertions by HMIP that the ESA will overcome the scenario-approach limitations do not seem to be supported by the exercise results (Zimmerman et al., 1992). In particular, the conclusion that the ESA is more conservative (i.e., yields higher risk estimates) than the scenario approach was not supported. Finally, the identification and construction of possible future climate sequences from past data relies heavily on expert judgments.

Methodological comparisons between the ESA and the scenario approach were extensively discussed by the NEA Scenario Working Group. This group concluded that: (i) there are more similarities than differences between the two approaches, and (ii) the two approaches should not be viewed as being mutually exclusive, rather they should be considered complementary to each other. The scenario approach is likely to benefit greatly from modeling advances developed under the ESA while the former provides a framework for the systematic identification and selection of EPs to include in the ESA. One key conclusion of the NEA Scenario Working Group was that, to date, the ESA has only been able to consider

climate changes, and that other EPs that could affect repository performance still need to be dealt with using some form of conventional scenario approach.

6.2.1.10 Open Issues In Scenario Selection

Although many scenario studies have been conducted to-date, a number of critical issues still remain unresolved. Among these issues are: (i) the lack of uniqueness in scenario-selection approaches, (ii) the almost exclusive reliance on subjective expert judgments, (iii) the alternative interpretations of the interactions among the EPs comprising each scenario, (iv) the treatment of human intrusion, and (v) the estimation of the probability of occurrence of EPs and of scenarios. Each of these issues impacts the selection of scenarios that, in turn, affect PA results. Therefore, studies aimed at the resolution of these issues are warranted.

The lack of uniqueness in the scenario-selection approach will make it difficult to resolve the problem of completeness and to reconcile potentially different sets of scenarios developed by different groups (e.g., regulators and proponents of a disposal facility). Alternative interpretations will most likely lead to different scenarios because these interpretations will influence the retention or elimination of given EPs, and because of the level of complexity with which the EPs are modeled.

While there is consensus within the international waste management community on the need to consider the impact of human actions on repository performance, there is much disagreement on how EPs arising from these actions should be handled. There are various sources for this disagreement: among these are philosophical ones (e.g., advertent versus inadvertent intrusion), technical ones (e.g., the estimation of the probability of human intrusion), and regulatory ones (e.g., the consideration of human intrusion in the same context as other EPs and scenarios in a PA). International activities, such as the NEA Human Intrusion Workshop and the Human Intrusion Working Group, have not produced definitive resolutions to this disagreement. Preliminary PA calculations by various groups both within and outside the United States

indicate that human intrusion can lead to high and early releases of radionuclides to the accessible environment and, consequently, treatment of human intrusion can considerably impact PA results.

The use of expert judgments in scenario selection ranges from very formal methods (e.g., those used in the WIPP and the CNWRA studies on the estimation of modes and probability of occurrence for human intrusion and climate change, respectively) to semiformal methods (e.g., those used in the AECL and SKB/SKI projects) to informal methods [e.g., those used to generate the first list of scenarios for YM by Ross (1987)]. Because a uniform methodology or framework with a specified level of formality and rigor has not been adopted to elicit this type of judgments, it would be difficult to scrutinize the judgments and the information basis, assumptions, and logic used by experts to arrive at the judgments. Furthermore, because scenario selection is viewed by many outside the waste management community as a highly speculative exercise, the multiplicity of approaches used to elicit the judgments could undermine the credibility of scenario selection. A related issue is the estimation of the probability of occurrence of EPs and of scenarios, which will also rely on expert judgments. The lack of a uniform systematic approach for the elicitation of expert judgments on the probability of EPs and of scenarios is likely to be detrimental to the credibility of the estimate of the probabilities as well as to the reconciliation of difference in estimates used by different groups.

6.2.2 Percolation Simulation Evaluation

Analyses of water percolating through partially-saturated, fractured tuff have been conducted as part of the Analysis of the Hydraulic Characteristics of Hydrothermally Altered Tuff (IM 5704-191-094-004). These analyses are part of an integrated effort with the Natural Analog Research Project to investigate flow and transport through fractured porous media. In further support of this integrated effort, a percolation experiment at the Peña Blanca Natural Analog Site has been identified as part of a newly proposed hydrogeology research project at CNWRA. Information gained from the proposed percolation experiment will assist in evaluating conceptual and mathematical

models for flow and transport through partially saturated, fractured tuff and support analyses conducted by the Natural Analog Research Project. Percolation at the Peña Blanca site has been simulated to assess the feasibility of proposed field experiments. The fortuitous geometric and physical attributes of the Peña Blanca Natural Analog qualify the site for such an experiment. These attributes include an extensive area of exposed rock (identified as the +10 level), a series of existing 2-in. diameter boreholes, and 80 m of adit associated with previous mining activities (Pearcy et al., 1993). The proposed field-scale percolation test entails infiltrating water from the +10 level and monitoring the arrival of the water in the adit located at a depth of 8–10 m. This field test provides the opportunity to observe the arrival of water with conservative or nonconservative tracers after moving through 8–15 m of partially saturated, fractured tuff. In addition, the location of a brecciated ore zone at the analog site provides a system with a range of physical and hydraulic properties (i.e., porosity, hydraulic conductivity, unsaturated flow parameters, and fracture characteristics), that permit the examination of flow and transport through a variety of physical systems relevant to and expected to be present at YM.

The proposed field experiment is designed to test conceptual and mathematical models of percolation processes expected below the horizon where infiltration is significant. Models for near-surface infiltration will not be tested because the analog site at Peña Blanca has been altered (i.e., surface sediments, vegetation, and weathered rock have been removed) to reduce most of the near-surface processes that affect infiltrating water. The conceptual model of the proposed field-scale percolation test specifies that water is introduced into the subsurface along a 3-m wide zone directly over the long dimension of the adit. Two conceptual models of the fractured tuff at the Peña Blanca Natural Analog Site are assessed in this analysis, the first characterizing the medium as a uniform, homogeneous porous medium, and the second characterizing the medium as a homogeneous composite of fractures and rock matrix (Wang and Narasimhan, 1986; Klavetter and Peters, 1986; Nitao, 1988a). Flow of groundwater for the two conceptual models is simulated with the numerical code VTOUGH (Pruess, 1987 and Nitao, 1988b) and the results are compared.

6.2.2.1 Model Development

A vertical two-dimensional (2D) numerical flow model is assembled to replicate the subsurface at the Peña Blanca Analog Site. A 2D characterization is assumed adequate, particularly during the preliminary phases of these analyses, as water can be infiltrated along a line source directly overlying the adit. The model assumes symmetry through the vertical axis of the adit and extends from the surface to a depth of 12 m in the z-direction and from the vertical axis of the 3-m wide adit to a distance of 12 m in the x-direction (Figure 6-1). Infiltration of water through the modeled medium is simulated by establishing the hydraulic head at atmospheric pressure over a 1.5-m wide section (equal to a 3-m wide section for the entire adit) along the upper boundary directly over the adit. The model contains 40 equally spaced rectilinear elements in both the vertical and horizontal coordinate directions. The vertical and top boundaries are no-flow boundaries. The bottom boundary is established at a constant saturation of 0.5, the same as the initial saturation of the interior nodes, where the constant-saturation condition is considered adequate for early time simulations and loses validity as the wetting front nears the bottom of the domain.

The adit has a height and total width of 3 m and is established as an extremely low-permeability zone as a preliminary characterization of a seepage face. This coarse characterization of the adit boundary is equivalent to a no-flow boundary at the adit wall. Adit and lower boundary treatments are considered adequate at this time as the results of interest are the liquid flow regime through the sub-surface above the adit and the approximate arrival time of the infiltration front at the adit boundary, and as quantification of water seeping into the adit is not assessed at this time.

The permeability and retention curve parameters assigned to the matrix in the simulations were determined from property values measured in the laboratory on rock sampled from the Nopal Formation at Peña Blanca as part of the Natural Analog Research Project and evaluated as part of the PA Research Project. Measurement of the hydraulic properties of the Nopal Formation provides information required for resolution of flow and transport rates of water and

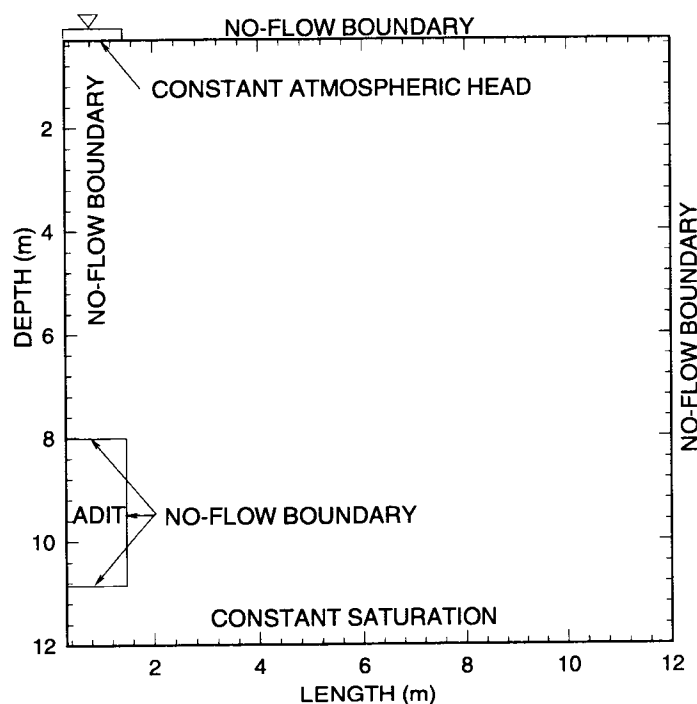


Figure 6-1. Model dimensions and boundary conditions

uranium (U) through the analog site. The hydraulic property parameters for the fractures were taken from values published for tuff samples at YM (Klavetter and Peters, 1986).

Nopal Formation media properties measured during this effort include porosity, bulk density, permeability, and the retention curve. A total of five (5- to 8-kg) rock samples from the Nopal Formation of the Peña Blanca site (labeled nrg1-5) representing various degrees of hydrothermal alteration associated with the Nopal U ore body were collected and analyzed to determine their hydraulic properties. Preliminary results from these measurements indicate that processes associated with hydrothermal activities have significantly changed the hydraulic properties for the variably altered rock samples. For example, the porosity of rock sampled from an area not visibly altered by the hydrothermal activities is measured at 5 to 8 percent compared to porosities of rock immediately adjacent to the ore body at 25 to 30 percent. Similarly, permeabilities of the host rock are approximately

$1.0 \times 10^{-14} \text{ m}^2$ as compared to altered rock with permeabilities as high as $1.0 \times 10^{-12} \text{ m}^2$.

Properties assigned to the modeled medium were taken from nrg5, a sample representative of rock exhibiting an intermediate level of hydrothermal alteration at Peña Blanca. Accordingly, intermediate values of 10 percent for porosity and $1.0 \times 10^{-13} \text{ m}^2$ for permeability have been assigned to the model medium. The retention curve for the rock sample was determined using a combination of measurement methods: a pressure plate extractor (PPE) was used to measure saturation for suction pressures less than 10 bar and a chilled mirror psychrometer (CMP) was used for higher suction pressures. The preliminary measured retention curve data for nrg5 are illustrated in Figure 6-2. Refinement of the measurement methods and the measured values is ongoing.

A van Genuchten-type curve was fitted to the measured retention data using RETC, an inverse program for quantifying the hydraulic functions of unsaturated media (van Genuchten et al., 1991). The

RETENTION CURVE - nrg5

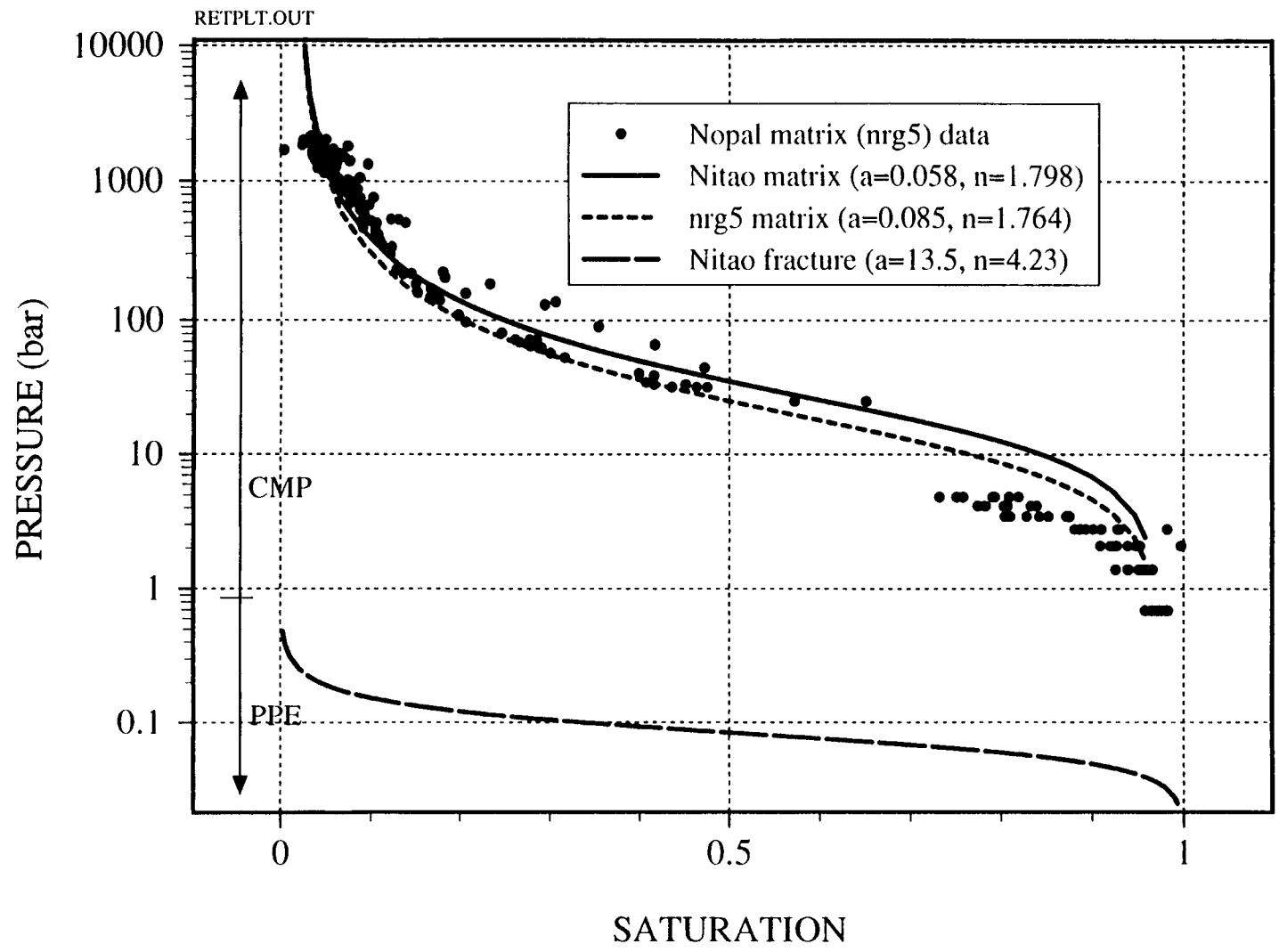


Figure 6-2. Retention data and calculated retention curves for nrg5, a generic tuff sample (Nitao, 1988b), and a fracture (Klavetter and Peters, 1986).

retention function relating suction pressure and saturation is expressed in RETC as (van Genuchten, 1980)

$$S = \frac{1}{[1 + (\alpha h)^n]^m} \quad (6-1)$$

where S is moisture content, h is the pressure head, α is a fitting parameter associated with the air-entry value, and n and m are two general fitting parameters. Equation (6-1) and the fitting parameters are commonly referred to as the van Genuchten retention equation and the van Genuchten parameters, respectively. The number of fitting parameters can be reduced to two by assuming $m=1-1/n$, a relationship frequently invoked with many classes of geologic material especially when the amount of retention data is limited (van Genuchten et al., 1991).

A two-parameter van Genuchten curve was fit to the nrg5 retention data; parameter values for this curve are presented with the comparable values for the matrix of typical YM tuff (Nitao, 1988a) in Table 6-2 for comparison. In Table 6-2, the columns with S_r and S_s refer to the residual and saturated moisture contents, respectively. Although the van Genuchten parameter values are similar, values for permeability for the two tuff matrices differ by five orders of magnitude. The hydraulic property parameters assigned to the fractures were taken from values published for tuff samples at YM (Klavetter and Peters, 1986). The retention curves for the two matrices and the fracture using the van Genuchten parameters presented in Table 6-2 are illustrated in Figure 6-2.

The liquid relative permeability, k_{rl} , can be expressed in terms of pressure head and the three fitting parameters (Nitao, 1988b)

$$k_{rl} = \frac{\{1 - (\alpha h)^{n-1} [1 + (\alpha h)^n]^{-m}\}^2}{[1 + (\alpha h)^n]^{m/2}} \quad (6-2)$$

The relative permeability for the equivalent continuum model can be expressed as a volume average of the fracture and matrix relative permeabilities (Wang and

Narasimhan, 1986; Klavetter and Peters, 1986; Nitao, 1988b)

$$k_{rl}^b = \frac{[K_f k_{rl}^f \phi_f + K_m k_{rl}^m (1 - \phi_f)]}{K_b} \quad (6-3)$$

where b , f , and m refer to the bulk, fracture, and matrix, respectively, ϕ is porosity, and the saturated bulk liquid hydraulic conductivity, K_b , is defined by

$$K_b = K_f \phi_f + K_m (1 - \phi_f) \quad (6-4)$$

A plot of the bulk equivalent medium permeability versus bulk gas saturation, calculated by multiplying k_{re} , [Eq. (6-3)], by K_b , [Eq. (6-4)], is shown in Figure 6-3 for the Peña Blanca composite model with a matrix permeability of $1.0 \times 10^{-13} \text{ m}^2$ and fracture permeabilities of $1.0 \times 10^{-11} \text{ m}^2$ and $1.0 \times 10^{-9} \text{ m}^2$, and for the homogeneous matrix-only model. The composite models correspond to bulk permeabilities of $1.78 \times 10^{-13} \text{ m}^2$ and $1.9 \times 10^{-12} \text{ m}^2$, respectively. There is no significant difference between the matrix and composite permeabilities for the model with the lower fracture permeability. For the higher fracture permeability model, there exists a distinct difference between the matrix and composite permeabilities at high liquid saturations.

6.2.2.2 Simulation Results

Contours of liquid saturation at selected times (i.e., 0.5, 1.0, and 2.0 d) after the initiation of infiltration are presented in Figures 6-4 through 6-6 for two cases with the same matrix permeability ($1.0 \times 10^{-13} \text{ m}^2$). Liquid saturation for a case with fracture permeability of $1.0 \times 10^{-11} \text{ m}^2$ is illustrated in part (a), and for a case with fracture permeability of $1.0 \times 10^{-9} \text{ m}^2$ in part (b), of Figures 6-4 through 6-6. Saturation contour plots for a matrix-only model with a matrix permeability of $1.0 \times 10^{-13} \text{ m}^2$ (not shown) yield an infiltration profile that is essentially the same as that for the composite-medium case with fracture permeability of $1.0 \times 10^{-11} \text{ m}^2$. This similarity is consistent with the composite permeability/saturation curve (Figure 6-3) for a composite medium with a matrix permeability of $1.0 \times 10^{-13} \text{ m}^2$ and a fracture permeability of $1.0 \times 10^{-11} \text{ m}^2$, which is almost identical to the

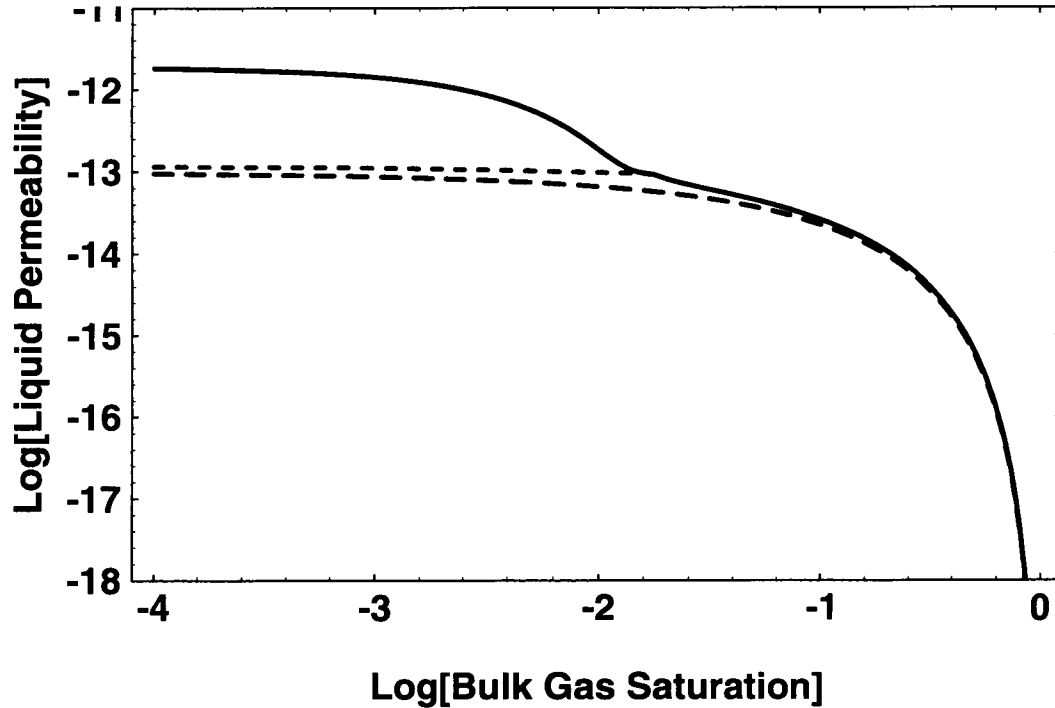


Figure 6-3. Permeability versus bulk gas saturation for the composite model with a matrix permeability of $1.0 \times 10^{-13} \text{ m}^2$ and fracture permeabilities of $1.0 \times 10^{-9} \text{ m}^2$ (solid curve), and $1.0 \times 10^{-11} \text{ m}^2$ (dotted curve), and homogeneous matrix-only model with the same matrix permeability (dashed curve). The dotted curve with the lower fracture permeability gives effectively the same permeability as the matrix alone.

permeability/saturation curve for a matrix-only model with a permeability of $1.0 \times 10^{-13} \text{ m}^2$.

As illustrated in the contour plots, the advancing infiltration front for the two models reflects the change in fracture permeability. The saturation fronts for both cases are similarly diffuse with no indication of a distinct infiltration front as would be implied by a steep gradient in saturation. As the rate of infiltration in the matrix-only medium model is similar to that of a composite model with a fracture permeability only two orders of magnitude greater than the matrix, but less than that of a composite model where the fracture permeability exceeds that of the matrix by at least four orders of magnitude, it would appear that fractures must be significantly greater than two orders of magnitude more permeable than the matrix to have a significant influence. These preliminary results illustrate relatively similar infiltration profiles

predicted using two characterizations of the medium. Additional simulations based on other, less similar, models could provide less similar infiltration front predictions. In particular, a modeled medium exhibiting a discrete fracture network would not be expected to predict either similar arrival times or similar infiltration profiles.

Based on these preliminary simulations, it appears that infiltration tests can be conducted at Peña Blanca with arrival times predicted to be on the order of a few days. Earlier or later arrival times are possible through selection of a location at the Peña Blanca Natural Analog Site, that exhibits higher or lower matrix and fracture permeabilities. The presence of infiltrating water monitored in the matrix at the adit walls and the saturation profile monitored using a neutron probe in a properly constructed borehole through the water pond down into the adit would provide supporting evidence

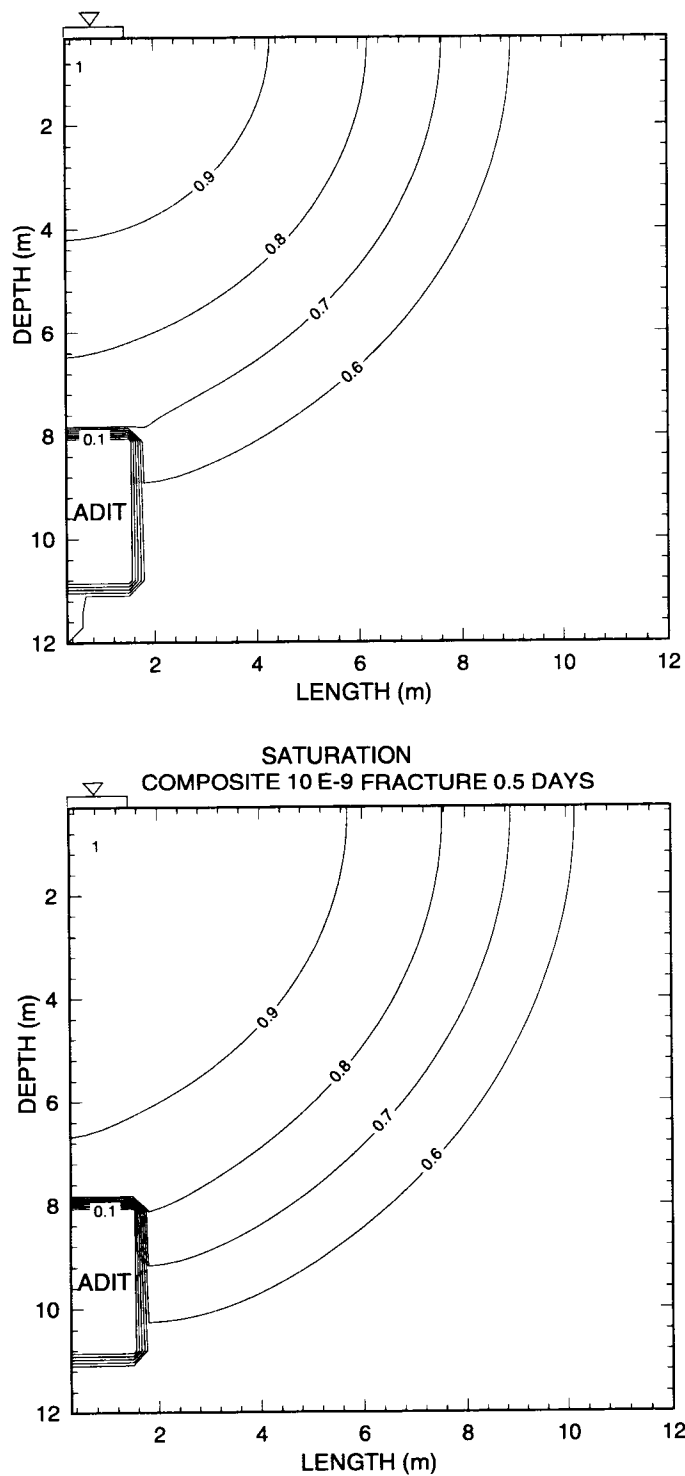


Figure 6-4. Liquid saturation contours for a simulation time of 0.5 days of infiltration for a matrix/fracture composite medium with a matrix permeability of $1.0 \times 10^{-11} \text{ m}^2$ and (a) a fracture permeability of $1.0 \times 10^{-11} \text{ m}^2$, and (b) a fracture permeability of $1.0 \times 10^{-9} \text{ m}^2$

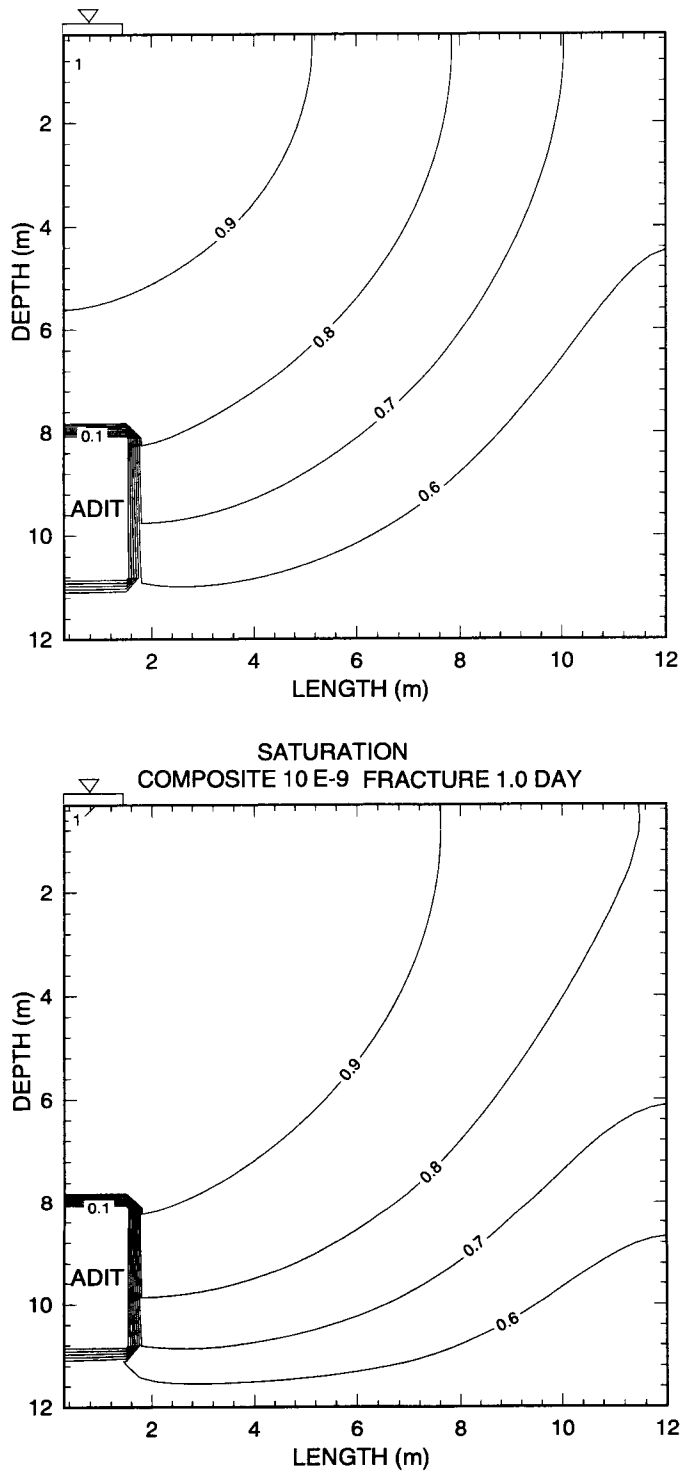


Figure 6-5. Liquid saturation contours for a simulation time of 1.0 day of infiltration for a matrix/fracture composite medium with a matrix permeability of $1.0 \times 10^{-11} \text{ m}^2$ and (a) a fracture permeability of $1.0 \times 10^{-11} \text{ m}^2$, and (b) a fracture permeability of $1.0 \times 10^{-9} \text{ m}^2$.

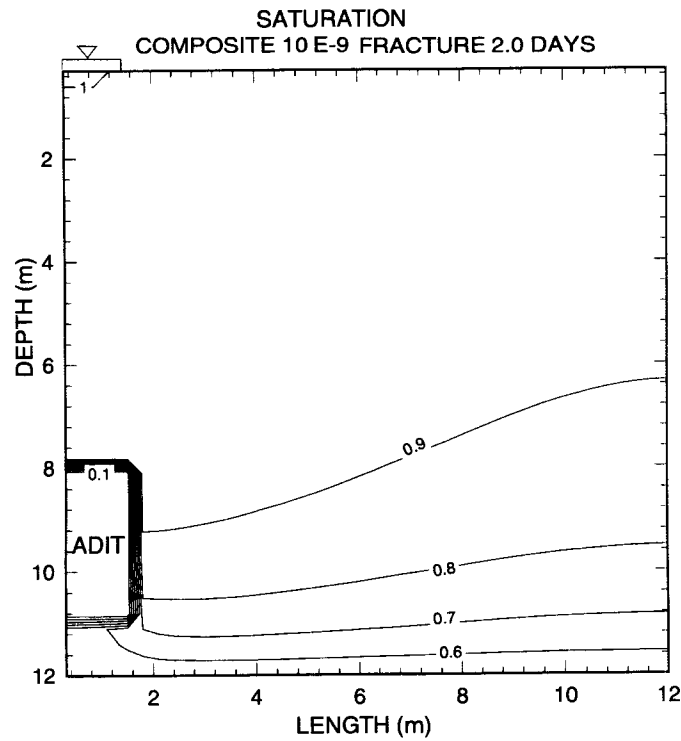
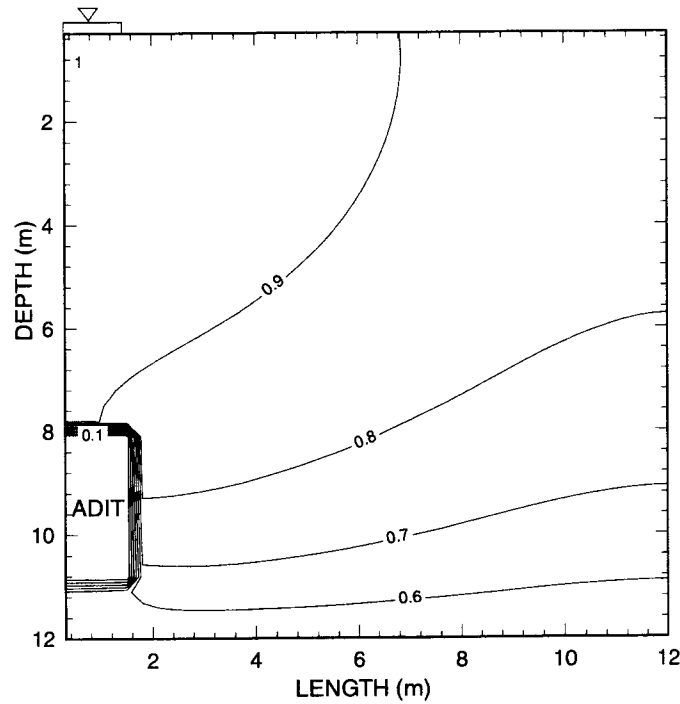


Figure 6-6. Liquid saturation contours for a simulation time of 2.0 days of infiltration for a matrix/fracture composite medium with a matrix permeability of $1.0 \times 10^{-11} \text{ m}^2$ and (a) a fracture permeability of $1.0 \times 10^{-11} \text{ m}^2$, and (b) a fracture permeability of $1.0 \times 10^{-9} \text{ m}^2$.

as to the presence of matrix/fracture or fracture-only infiltration. Incorporated in the observed infiltration rate of water are the combined effects of matrix/fracture interactions (i.e., fracture coatings, relative permeabilities, channel versus sheet flow, time for matrix/fracture interaction, and magnitude of the matrix/fracture transfer term). The arrival time of the infiltrating water will indicate the value of the bulk permeability of the medium, a medium characteristic that is not easily predicted or determined in the laboratory.

6.3 ASSESSMENT OF PROGRESS

As in the previous reporting period, high priority was given to the technical scope of Task 1—Conceptual Model Development, which currently includes research on hydrologic conceptual models and disruptive event scenarios. Strong emphasis was placed on development of conceptual and mathematical models of infiltration and fracture flow phenomena because the NRC, DOE and EPRI IPA studies have consistently shown these processes to be the “most significant” determinants of the total-system performance of the proposed repository at YM. Activities within the technical scope of Task 2—Computational Model Development and Task 3—Model Evaluation were reduced in accordance with technical direction from the NRC project officer.

A new model was developed for the purpose of predicting time-dependent infiltration phenomena at the YM site. The new model is designed to calculate the infiltration rate as function of the meteorologic

conditions (e.g., precipitation, cloud cover, air temperature, short wave radiation) and the hydraulic properties of the rock strata. Both liquid and vapor flow are computed as a function of gravity, capillary pressure, and temperature gradients. The new infiltration model is currently being used in an IPA Phase 3 auxiliary analysis to: (i) gain insight regarding the factors controlling infiltration phenomena at YM and (ii) develop a physically based probability density function for infiltration rate. The latter will be used as input to the Total Performance Assessment (TPA) code. This new model is expected to be a key IPA auxiliary analysis code and, therefore, an important CDM tool. Documentation of this new model is incomplete at this time. Therefore, the model is not presented here in depth.

New conceptual and mathematical models were developed to describe time-dependent fracture flow. The new models, which are based on fundamental principles of classical fluid dynamics (as opposed to porous media theory), are intended to provide a technical basis for evaluating model uncertainties (Conceptual and Mathematical Model KTUs) associated with both the NRC and DOE flow models that employ Equivalent Porous Media (EPM), Dual Continuum (DC), or Dual Permeability (DP) assumptions. The new models will permit: (i) greater understanding of matrix-fracture interactions and (ii) direct evaluation of the possible nonconservatism associated with EPM, DC, and DP flow model formulations. The knowledge gained from these two items will directly benefit the development of CDMs for the License Application Review Plan (LARP) as well as position the staff to

Table 6-2. Hydraulic properties of a rock sample nrg5 from Peña Blanca compared to a YM tuff and fracture samples (Nitao, 1988a; Klavetter and Peters, 1986)

Medium	n	$m=1-1/n$	α (1/Pa)	k (m ²)	S_r	S_s	Porosity
YM matrix	1.798	0.4438	5.8×10^{-7}	1.9×10^{-18}	0.001	0.11	0.11
nrg5 matrix	1.764	0.4331	8.5×10^{-7}	1.0×10^{-13}	0.002	0.097	0.1
YM fracture	4.23	0.7636	1.315×10^{-4}	1.0×10^{-11}	0.001	0.0018	0.0018

better review DOE activities. Although not reported in this chapter, details on these new models may be found in "Water Film Flow in a Fracture in Unsaturated Porous Medium," CNWRA 94-009. In addition, key aspects of this work are summarized in a paper entitled "Penetration Length of Viscous Flow in Fractures in Unsaturated Porous Medium," which was recently submitted to Water Resources Research.

Disruptive event scenarios are a basic component of TSPA calculations. The NRC and DOE IPA studies currently suggest that the climate scenario is, by a large margin, more important to post-closure performance than volcanism, seismo-mechanical, or human intrusion. However, other scenario categories such as faulting (a site-induced disruptive event) and water refluxing (a repository-induced disruptive event) may also be very important to total-system performance. As presented earlier, the NRC/SNL scenario-selection methodology appears to be a widely accepted approach for identifying applicable disruptive event scenarios. This view is supported by the findings of the state-of-the-art review documented in the report "Review of Scenario Selection Approaches for Performance Assessment of High-Level Waste Repositories and Related Issues," CNWRA 94-002. This document, which is relevant to the Future System States KTU, was revised to accommodate NRC staff comments and submitted for publication as a NUREG/CR report.

Although only limited research was performed on computational model development, the results of that work have helped eliminate limitations of existing PA codes. For example, computational problems were initially encountered in performing the CTOUGH flow simulations (documented in this chapter) for the Peña Blanca site. These problems were associated with the large memory requirements and relatively long run times. To overcome these problems, a new matrix solver routine, which uses a band scheme with D-4 ordering, was developed and implemented in the CTOUGH code. The new solver routine is more than twice as fast as the original band solver and requires less than a third of the computer memory. A related activity involved a technology transfer for the PORFLOW code; a 2-day seminar was organized and presented to the NRC staff at their offices in Rockville.

With the agreement of the NRC project officer, a new activity was initiated as part of the model evaluation task. The activity entails a study of data filtering and its impact on model predictions. Hydrologic data for the Las Cruces trench is being used to evaluate unsaturated flow model predictions. The study is expected to yield insights regarding the degree to which predictive reliability is dependent on the amount of available data. This study addresses the Model Validation KTU. Detailed discussion of progress on this study will be included in the next reporting period.

6.4 PLANS FOR NEXT REPORTING PERIOD

In the next reporting period, emphasis will be placed on research activities that: (i) directly support PA methodology and technology needs of IPA and (ii) contribute to the technical integration of other research projects (e.g., Volcanic Systems, Geochemical Natural Analogs, and Subregional Hydrology) and production of CDM tools. Concurrent with research on the various topics outlined below, technical reports produced in the current and next reporting period will be subjected to external peer reviews. A series of NUREG/CR reports will be produced subsequent to the peer reviews.

Under Task 1, research effort will be devoted to three specific topics that represent high priority needs of IPA, namely: (i) refinement and applications of models to quantitatively evaluate the "extended dry concept" associated with the DOE Multi-Purpose Container concept, (ii) quantitative analyses of fracture flow and matrix-fracture interactions, and (iii) implementation of new approaches to model disruptive scenarios. In addition, the conceptual models, knowledge base, and data generated by other research projects will be integrated to produce improved consequence modules for the TSPA computer code. The products of this task will be aimed at making direct contributions to the NRC IPA Phase 3 exercise.

As part of Task 2, research studies will be conducted on two specific topics: (i) evaluation of new high-performance computing technology and (ii) acquisition and testing of DOE PA numerical models.

With regards to the first topic, the Parallel Virtual Machine (PVM) technology will be evaluated by direct application to the TPA code. The PVM system, which utilizes a series of workstations to parallelize computations, may provide a more efficient and cost-effective alternative to executing the TPA code on a Cray supercomputer. With respect to the second topic, a number of the PA codes and modules utilized by DOE contractors (e.g., SNL, Los Alamos National Laboratory, and Lawrence Berkeley Laboratory) to assess the isolation performance of YM will be acquired and tested. Testing of these codes and modules will consist of running a series of benchmark test cases and comparing the numerical results against those obtained with comparable CNWRA/NRC codes and modules. This work is expected to directly benefit the IPA activity as well as position the CNWRA staff to thoroughly review the DOE TSPAs for the YM site.

Within Task 3, model evaluation studies will primarily focus on a collaborative effort with the University of Arizona on testing flow and transport models using field data from the Apache Leap Test Site and the Queen Creek-Never Sweat Tunnel site. These modeling studies are expected to be conducted in two parts: (i) model applications to aid in the design of the actual field experiments and (ii) model applications for the purpose of making direct comparisons with field data. This work will be closely coordinated with that of the Subregional Hydrology Project and the NRC/SKI effort on regulatory perspectives on model validation. Findings and developments of this task are expected to provide support to NRC technical positions and guidance on model validation.

6.5 REFERENCES

- Andersson, J., and T. Eng. 1990. The joint SKI/SKB scenario development project. *Safety Assessment of Radioactive Waste Repositories*. Paris, France: Nuclear Energy Agency: Organization for Economic Cooperation and Development: 397-404.
- Andersson, J., T. Carlsson, T. Eng, F. Kautsky, E. Soderman, and S. Wingefors. 1989. *The Joint SKI/SKB Scenario Development Project*. SKI Technical Report 89:14. Stockholm, Sweden: Swedish Nuclear Power Inspectorate.
- Barr, G.E., and E. Dunn. 1993. A working definition of scenario and a method of scenario construction. *Proceedings of the Fourth Annual International Conference on High-Level Radioactive Waste Management*. La Grange Park, IL: American Nuclear Society: 1,093-1,098.
- Barr, G.E., E. Dunn, H. Dockery, R. Barnard, G. Valentine, and B. Crowe. 1993. *Scenarios Constructed for Basaltic Igneous Activity at Yucca Mountain and Vicinity*. SAND91-1653. Albuquerque, NM: Sandia National Laboratories.
- Billington, D.E., D.A. Lever, and S.J. Wisbey. 1990. Radiological assessment of deep geological disposal: Work for UK Nirex Ltd. *Safety Assessment of Radioactive Waste Repositories*. Paris, France: Nuclear Energy Agency: Organization for Economic Cooperation and Development: 271-282.
- Bonano, E.J., and R.G. Baca. 1994. *Review of Scenario Selection Approaches for Performance Assessment of High-Level Waste Repositories and Related Issues*. CNWRA 94-002. San Antonio, TX: Center for Nuclear Waste Regulatory Analyses.
- Cranwell, R.M., R.V. Guzowski, J.E. Campbell, and N.R. Ortiz. 1990. *Risk Methodology for Geologic Disposal of Radioactive Waste: Scenario Selection Procedure*. NUREG/CR-1667, SAND80-1429. Washington, DC: Nuclear Regulatory Commission.
- Guzowski, R.V. 1990. *Preliminary Identification of Scenarios that May Affect the Escape and Transport of Radionuclides from the Waste Isolation Pilot Plant, Southeastern New Mexico*. SAND89-7149. Albuquerque, NM: Sandia National Laboratories.
- Hora, S.C., D. von Winterfeldt, and K.M. Trauth. 1991. *Expert Judgment on Inadvertent Human Intrusion into the Waste Isolation Pilot Plant*. SAND 90-3063. Albuquerque, NM: Sandia National Laboratories.

- Klavetter, E.A., and R.R. Peters. 1986. *Estimation of Hydrologic Properties of an Unsaturated, Fractured Rock Mass*. SAND84-2642. Albuquerque, NM: Sandia National Laboratories.
- McGuire, R.K., ed. 1990. *Demonstration of Risk-Based Approach to High-Level Waste Repository Evaluation*. EPRI NP-7057. Palo Alto, CA: Electric Power Research Institute.
- McGuire, R.K., ed. 1992. *Demonstration of Risk-Based Approach to High-Level Waste Repository Evaluation: Phase 2*. EPRI TR-100384. Palo Alto, CA: Electric Power Research Institute.
- Nitao, J.J. 1988a. *Numerical Modeling of the Thermal and Hydrological Environment around a Nuclear Waste Package using the Equivalent Continuum Approximation: Horizontal Emplacement*. UCID-21444. Livermore, CA: Lawrence Livermore National Laboratory.
- Nitao, J.J. 1988b. *V-TOUGH. An Enhanced Version of the TOUGH Code for the Thermal and Hydrologic Simulation of Large-Scale Problems in Nuclear Waste Isolation*. UCID- 21954. Livermore, CA: Lawrence Livermore National Laboratory.
- Nuclear Energy Agency. 1992. *Systematic Approaches to Scenario Development*. Paris, France: Nuclear Energy Agency: Organization for Economic Cooperation and Development.
- Pearcy, E.C., J.D. Prikryl, W.M. Murphy, and B.W. Leslie. 1993. *Uranium Mineralogy of the Nopal I Natural Analog Site, Chihuahua, Mexico*. CNWRA 93-012. San Antonio, TX: Center for Nuclear Waste Regulatory Analyses.
- Pruess, K. 1987. *TOUGH: User's Guide*. NUREG/CR-4645. Washington, DC: Nuclear Regulatory Commission.
- Raimbault, P., C. Izabel, and J.M. Peres. 1992. Methodology developed by the French National Nuclear Waste Management Agency (ANDRA) for the performance assessment of a deep geological repository. *Proceedings of the Third International Conference on High Level Radioactive Waste Management*. La Grange Park, IL: American Nuclear Society: 510-516.
- Ross, B. 1987. *A First Survey of Disruption Scenarios for a High-Level Waste Repository at Yucca Mountain, Nevada*. SAND85-7117. Albuquerque, NM: Sandia National Laboratories.
- Stephens, M.E., and B.W. Goodwin. 1990. Scenario analysis for the postclosure assessment of the Canadian concept for nuclear fuel waste disposal. *Proceedings of the Safety Assessment of Radioactive Waste Repositories*. Paris, France: Nuclear Energy Agency: Organization for Economic Cooperation and Development: 405-416.
- Sumerling, T. J., ed. 1992. *Dry Run 3: A Trial Assessment of Underground Disposal of Radioactive Wastes Based on Probabilistic Risk Analysis: Overview*. DoE/HMIP/RR/92.039. London, England: UK Department of the Environment, Her Majesty's Inspectorate of Pollution.
- van Genuchten, M.Th. 1980. A closed-form equation for predicting the hydraulic conductivity of unsaturated soils. *Soil Science Society of America Journal* 44: 892-898.
- van Genuchten, M.Th., F.J. Leij, and S.R. Yates. 1991. *The RETC Code for Quantifying the Hydraulic Functions of Unsaturated Soils*. EPA/600/2-91/065. Riverside, CA: U.S. Salinity Laboratory: U.S. Department of Agriculture: Agricultural Research Service.
- Wang, J.S.Y., and T.N. Narasimhan. 1986. *Hydrologic Mechanisms Governing Fluid Flow in Partially Saturated Fractured, Porous Tuff at Yucca Mountain*. SAND84-7202. Albuquerque, NM: Sandia National Laboratories.
- Zimmerman, D.A., E.J. Bonano, P.A. Davis, C.P. Harlan, and M.S.Y. Chu. 1992. *Peer Review of the U.K. DoE Dry Run 3 Exercise (A Trial Probabilistic Risk Assessment of a Hypothetical Nuclear Waste Repository at Harwell, Oxfordshire)*. SAND92-1945. Albuquerque, NM: Sandia National Laboratories.

7 VOLCANISM RESEARCH

by Brittain E. Hill, Gerry L. Stirewalt, and Charles B. Connor

Investigators: Charles B. Connor, Brittain E. Hill, Gerry L. Stirewalt, Kathy H. Spivey, and Peggy Hunka (CNWRA)

NRC Project Officer: L.A. Kovach

7.1 TECHNICAL OBJECTIVES

Characterization of the frequency and nature of past volcanic events in the Yucca Mountain region (YMR) and assessment of the probability and consequences of future volcanism are critical aspects of precicensing scientific investigation. The technical objectives of the Volcanic Systems of the Basin and Range Research Project are to: (i) assess the probability of continued magmatic activity in the YMR; (ii) evaluate the quality, quantity, and uncertainties associated with volcanological data in the YMR and nearby volcanic fields; and (iii) develop models that better predict the interaction between crustal tectonics and volcanism in the western Great Basin (WGB). Effective review of the U.S. Department of Energy (DOE) license application will require insight into volcanic processes operating in the YMR on several scales. These processes include assessment of WGB tectonic and structural controls on volcanism on local scales (10^2 to 10^3 km²), the longevity of vent complexes and individual volcanoes in the WGB, and the relationship between specific mappable faults, joints and fractures, and volcanic conduits such as dikes and dike swarms. The WGB has been the site of recurring small-volume basaltic volcanism throughout the Quaternary. Modern analogs and theoretical studies have demonstrated convincingly that this activity encompasses a variety of eruption styles, from the gentle effusion of lavas to sub-Plinian and Plinian-style activity that has produced large and highly dispersive ash columns (e.g., Williams, 1950; McGetchin et al., 1974; Wilson et al., 1978; Wilson, 1980; Amos et al., 1983; Head and Wilson, 1989). The Volcanic Systems of the Basin and Range research project has been designed to assess the probability of future volcanism in the YMR, taking into account the range of activity and the structural controls on activity that are an inherent part of WGB volcanism.

Insight gained through the Volcanic Systems of the Basin and Range research project will support the following sections of the License Application Review Plan (LARP): (i) evidence of igneous activity as a potentially adverse condition, Section 3.2.1.9; (ii) impact of volcanism on groundwater movement, Section 3.2.2.7; and (iii) assessment of compliance with the requirement for cumulative releases of radioactive materials, Section 6.1. Research is necessary to develop these three sections of the LARP for the purpose of providing the Nuclear Regulatory Commission (NRC) with the methodology and acceptance criteria to determine DOE compliance with 10 CFR Part 60 requirements. Compliance Determination Strategies (CDSs) and Compliance Determination Methods (CDMs) for LARP sections associated with evidence of Quaternary volcanism include Key Technical Uncertainties (KTUs) of Type 5, indicating that independent research by the NRC may be required to evaluate volcanism, and that volcanism poses a high risk of the NRC reaching unwarranted conclusions regarding compliance with 40 CFR Part 191 and 10 CFR 60.122(c)(15).

To date, eight KTUs related to igneous activity have been identified as part of the CDSs concerned with evidence of Quaternary igneous activity. These KTUs are:

- Low resolution of exploration techniques to detect and evaluate igneous features
- Inability to sample igneous features
- Development and use of conceptual tectonic models as related to igneous activity
- Development of a conceptual groundwater flow model

- Prediction of future changes in the hydrologic system (due to tectonism)
- Conceptual model representation of the natural and engineered systems
- Variability in the model parametric values
- Prediction of future system states (disruptive scenarios)

Evaluation of these KTUs will require detailed safety review supported by analyses (Type 4), and detailed safety review supported by independent tests, analyses, and other investigations (Type 5).

Specific tasks within the Volcanic Systems of the Basin and Range project address the KTUs. For example, development of the Volcanism Geographic Information System (GIS) directly addresses KTUs related to the inability to sample igneous features, development and use of conceptual tectonic models as related to igneous activity, assessing variability in the model parametric values, and disruptive scenarios. The KTUs arise largely because volcanic systems of the WGB are complex and seemingly disparate. The petrogenesis of these volcanic fields, their relationship to regional tectonic setting and local structures, and geochronological investigations of the patterns of volcanism in these fields are active topics of research directly focused on resolution of KTUs.

In addition to evaluation of these KTUs, independent NRC research in volcanism is needed to provide a basis for reviewing DOE's assessment of the potential consequences of igneous activity on repository performance. Research in the Volcanic Systems of the Basin and Range project also will provide confirmatory data for addressing issues related to waste isolation.

Successful completion of the Volcanic Systems of the Basin and Range project and efficient integration with the LARP will require interaction with the Field Volcanism research project, an NRC research project that concentrates on eruption energetics, degassing, and controls on magma movement at shallow levels (Figure 7-1). The Tectonic Setting of the Central Basin and Range research project; and Geologic Setting Element Task 3 (Division of Waste Management) on faulting and dike interaction, also will provide direct input into the Volcanic Systems of the Basin and Range project. The Volcanic Systems of the Basin and Range project, together with these associated investigations,

will form the basis of volcanism models in Iterative Performance Assessment (IPA) (Figure 7-1). The link between volcanism studies and IPA has been established, with preliminary probability models serving as the basis for IPA phase 2 scenarios for volcanism. Results from the data limitations and uncertainty analysis (Task 3) in the Volcanic Systems of the Basin and Range project likely will be incorporated into volcanism scenarios for IPA phase 3. Volcanism research also provides support of NRC reactive work during the prelicensing stage (Figure 7-1). Results of the Volcanic Systems of the Basin and Range research project also are utilized in reactive work, including NRC-DOE Technical Exchanges and in the review of Topical Reports, Study Plans, and related reports.

Research efforts in the Volcanic Systems of the Basin and Range project initially have been directed toward the development of probability models of potential volcanic events in the YMR, based on geologic insight into tectonic processes operating in the WGB and geologic controls on areal basaltic volcanism in general. These models are summarized in Connor and Hill (1993a,b). Review of the regional tectonic setting of basaltic volcanism in the Great Basin, Task 1 of this project, is provided by Stirewalt et al. (1992). A review and analysis of dating techniques for volcanic rocks (Hill et al., 1993) was completed as the first part of Task 3 in this project. Ongoing research includes an analysis of the limitations and uncertainties associated with volcanologic data in the WGB (Task 3), development of probability models (Task 4), and development of integrated magmo-tectonic models for the YMR (Task 4). This current report describes research activities since January 1994.

7.2 SIGNIFICANT TECHNICAL ACCOMPLISHMENTS

Work during this reporting period has concentrated on completion of the major stage of development in the Volcanism GIS (Task 2). Geological, geochemical, and geochronological data have been compiled for the Cima Volcanic Field, California; the Coso Volcanic Field, California; the Lunar Crater-Pancake Range Volcanic Field, Nevada; and the Big Pine Volcanic Field, California. This activity resulted in Major Milestone 122-030, "The CNWRA Volcanism Geographic Information System Database" (Connor and Hill, 1994a), and supported presentations at the 61st Advisory Committee on

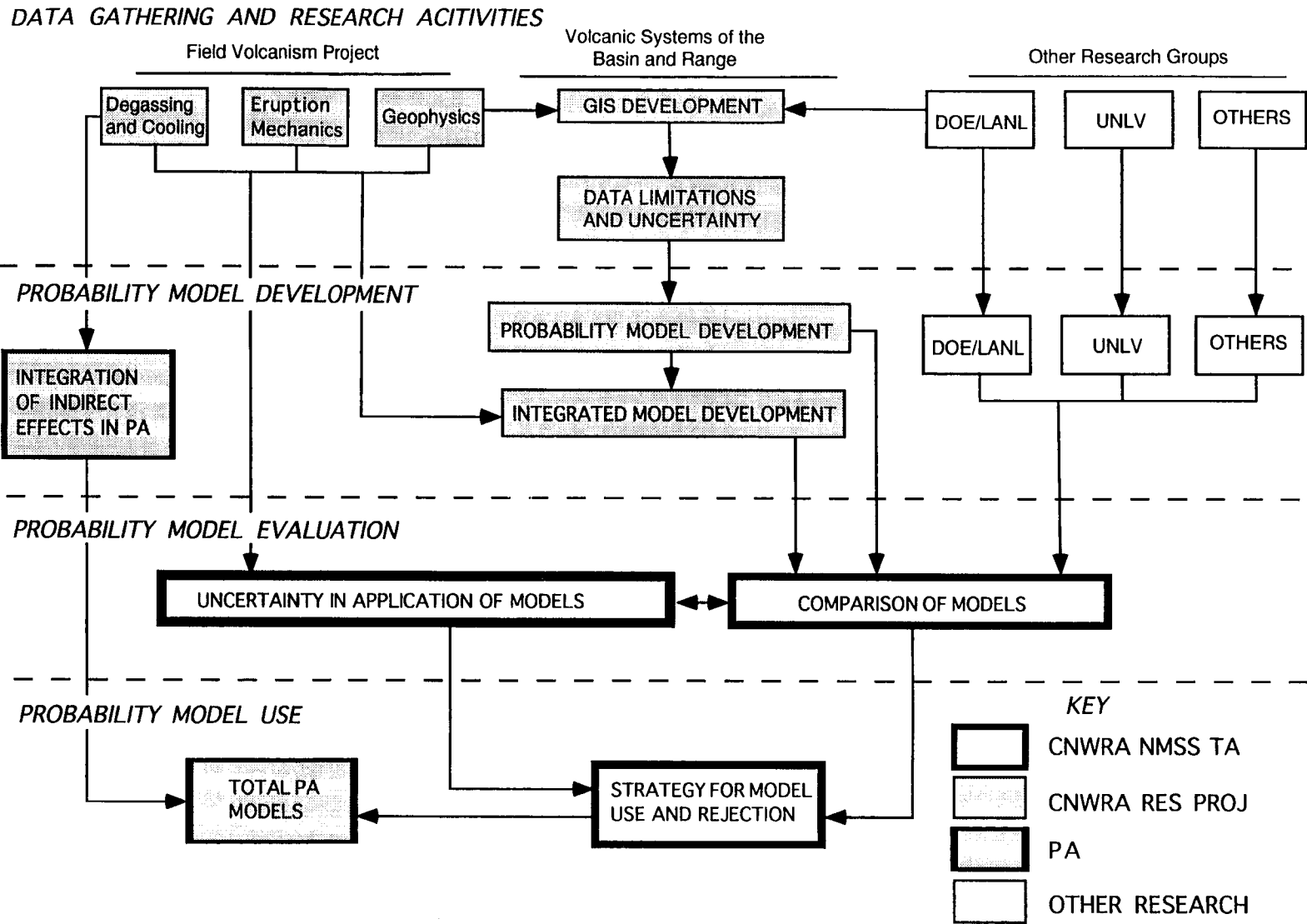


Figure 7-1. Overview of the relationship between the Volcanic Systems of the Basin and Range research project and other research and technical assistance activities. Projection is Universal Transverse Mercator, Zone 11.

Nuclear Waste (ACNW) meeting. A peer-review of both the Volcanic Systems of the Basin and Range and Field Volcanism research programs was initiated as part of Task 3 review activities. Work also began on developing a strategy for the critical review of volcanic and tectonic data compiled in the Volcanism GIS and an assessment of conceptual magmo-tectonic models for the WGB (Task 3). Probability models developed as part of Task 4 supported presentations at the 61st ACNW meeting and the March 1994 Nuclear Waste Technical Review Board meeting on probabilistic volcanic hazards assessment. In addition, a more detailed examination of the spatially nonhomogeneous Poisson probability models for volcanic eruption presented in Connor and Hill (1993a) was accepted for review by the *Journal of Geophysical Research*.

7.2.1 Volcanism Geographic Information System

The Volcanism GIS has been developed primarily as a tool for the analysis of natural analogs in the Basin and Range and nearby regions. Data have been compiled for five volcanic fields in the western United States. These fields include the YMR, and Cima, Coso, Lunar Crater, and Big Pine Volcanic Fields. The fields are summarized in the following sections. Two large Colorado Plateau-margin volcanic fields, the Springerville Volcanic Field and the San Francisco Volcanic Field, also may be useful in developing and testing volcanism probability models. Volcano locations and ages for these two volcanic fields also have been incorporated into the database.

Most of the data compiled in the Volcanism GIS originate in the published literature and include maps, data tables, digitized images, and binary geophysical data. In addition to model development, this GIS will be useful in evaluating the completeness and adequacy of the DOE volcanism database used to demonstrate compliance with 10 CFR Part 60 requirements relating to igneous activity. The Volcanism GIS will contain confirmatory data for addressing issues related to waste isolation and provide data that may be required to explore alternate hypotheses. The Volcanism GIS database currently contains the following data types: vent locations and lava flow outlines, age determinations, fault traces, geochemical analyses, geologic contacts, and topographic data. (Numerical parameters may include \pm ranges to quantify the uncertainties in these data. For

descriptive data, use of standard approaches for mapping and data acquisition generally ensures information acquired will be suitable for use.) These data are useful for description and investigation of the tectonic settings, physical volcanology, and petrogenesis of WGB volcanic fields. The Volcanism GIS will provide a substantial data set with which to test and develop probability models of potential volcanic disruption of the candidate repository. Using these data, it will be possible to evaluate probability models more fully, by viewing probability estimates together with structural and related geological data.

A computerized GIS provides the means necessary to construct models relating quantitative physical data to spatial data. Development of the GIS, as opposed to simple computer spreadsheets and maps, is necessary in order to fully assess volcanic activity in the WGB because:

- A tremendous range of information on volcanism is found in a broad variety of sources in the geologic literature; these data must be tabulated and evaluated in a consistent manner in order to quantify the range of WGB volcanic activity.
- It is important to be able to compare easily a large amount of complex data, such as geochemical data, from different volcanic fields.
- There is a need for simple and complex hypothesis testing using a variety of spatial and temporal data.
- It is important to understand the extent and limits of volcanological data in order to guide the license application review in an effective and timely manner.

The Volcanism GIS utilizes data from other Center for Nuclear Waste Regulatory Analyses (CNWRA) research projects, primarily from the Tectonic Processes in the Basin and Range project. The Tectonics project is constructing a GIS at two geographic scales, each with available digital elevation model (DEM) data. The regional scale encompasses much of the southwestern United States, including the YMR, WGB, and the Mojave provinces. Faults and cinder cone fields are represented at a scale of 1:2,500,000 in this database, and topography is digitized at a 3-arc-second resolution (Young et al., 1994). The

Yucca Mountain regional database covers an area immediately around the candidate repository site, and includes nine 7.5-minute quadrangles. The digital terrain data for this area consists of elevation data collected at 30-m intervals. Additional geologic data, including faults, photo-lineaments, bore-hole locations, and volcano locations are digitized from large-scale maps of this area. Other data in the Tectonics GIS include regional Quaternary fault traces, and earthquake hypocenter locations, magnitudes, and times. Earthquake data are from the National Earthquake Information Center PDE catalog. The Tectonics GIS database also includes strain data, and regional aeromagnetic and gravity data sets for North America from the Decade of North American Geology Geophysical Database. In addition, the tectonics database contains the outlines of Plio-Quaternary volcanic fields in the southwestern United States. These volcanic fields are classified on the basis of the ages of most recent activity (Smith and Luedke, 1984).

7.2.1.1 Coso Volcanic Field

The Coso Volcanic Field (CoVF) is a bimodal volcanic field that erupted both primitive basalts and high SiO₂ rhyolites, often penecontemporaneously (Figure 7-2). Pleistocene eruptions in the CoVF are represented by 38 high-silica rhyolite domes and flows and 14 basaltic centers, which range in age from 1.1 to 0.04 Ma (Duffield et al., 1980). About 30 Pliocene basaltic eruptions between 4 and 2.5 Ma form a broad southeast- to north- and west-trending arc (Figure 7-2). Volcanism generally has migrated to the south since the Miocene (Figure 7-2), although this progression has been fairly irregular. Current activity in the CoVF is limited to geothermal resources found in this area and fumaroles that occur at the surface along faults cutting younger dacite-to-rhyolite domes. Because of these geothermal resources, the CoVF has been the site of numerous geophysical investigations, largely in an effort to characterize the structure of the field and to image shallow crustal magma bodies in the region using seismic tomographic and related techniques.

The CoVF lies in a tectonically complex area due to the transition in this region from dominantly E-W extension associated with the Basin and Range, to strike-slip and oblique-slip deformation west of the CoVF (Roquemore, 1980). Evidence of Holocene deformation and active faulting is abundant in the region and includes dramatic offsets of Pliocene and, in

some cases, Pleistocene lava flows, and historical seismicity within the boundaries of the CoVF (Duffield et al., 1980). Duffield and Roquemore (1988) noted that, unlike other ranges in the region, the Coso Range has a nearly equant shape, indicating it is the product of perhaps more complex tectonic processes than has led to the formation of the N-S fault blocks of the Inyo Mountains and other ranges in the vicinity.

Bacon (1982) found that both basalts and rhyolites of the CoVF apparently follow a time-volume predictable pattern [since about 0.4 Ma]. Basalts have erupted at a rate of 2.8 km³/m.y. since about 0.4 Ma and rhyolites at a rate of 5.4 km³/m.y. since about 0.25 Ma. Bacon (1982) developed this volume-time relationship using a regression fit on the timing of eruptions and the cumulative volume just prior to eruptions. Extrapolating this regression, a basaltic eruption would be expected in the CoVF sometime in the next 55,000 yr, and a rhyolite eruption would be expected in 60,000 ± 33,000 yr. Bacon (1982) relates his time-predictable pattern to similar patterns in seismology, suggesting that it results from the increase of some parameter at a constant rate until it reaches a critical point, at which time volcanic eruptions occur. Two parameters that may lead to this type of behavior are pressure in the magma reservoir and extensional strain in the overlying rocks (Bacon, 1982). Bacon (1982) favors a relationship to extensional strain, largely because the CoVF is in an area of active extension. In his model, stress in the crust is accommodated by intruding dikes. The greater the volume of intrusions associated with a given eruptive sequence, the more strain is accommodated. As tectonic strain builds at a constant rate, a longer period of quiescence occurs between successive larger eruptions.

Because of bimodal volcanism, the CoVF is not directly analogous to the YMR. However, the region has been the focus of numerous detailed petrologic, tectonic, and geophysical investigations. Many of the patterns discerned through these studies may provide a basis for interpretation of similar trends, or simply suggest lines of inquiry for the study of the YMR and more analogous regions located elsewhere in the WGB.

7.2.1.2 Cima Volcanic Field

The Cima Volcanic Field (CVF) is located in the northeastern Mojave desert, approximately 150 km SSE of Yucca Mountain and 120 km SW of Las Vegas. The field is comprised of approximately 40 cinder cones, 60 lava flows, and several maar volcanoes,

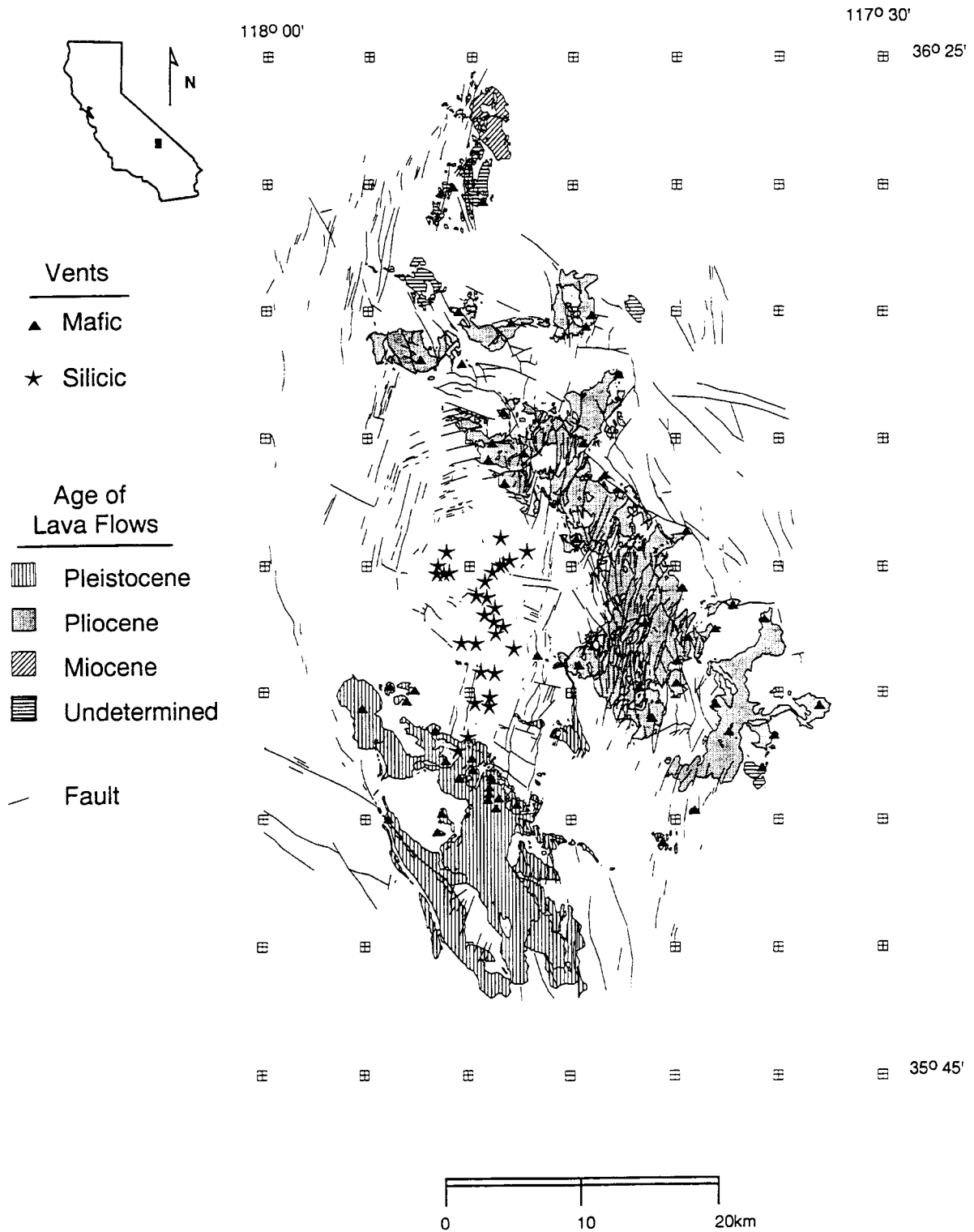


Figure 7-2. Distribution of basaltic vents, lava flows, and faults in and around the Coso Volcanic Field. Epoch age is based on K/Ar dates and stratigraphic relationships. Data sources are summarized in Connor and Hill (1994a). Projection is Universal Transverse Mercator, Zone 11.

distributed over an area of approximately 150 km² (Figure 7-3) (Dohrenwend et al., 1984; 1986). These features define an episode of volcanic activity that began approximately at 10 Ma and has continued through the latest Pleistocene (Turrin et al., 1985). The CVF is one of the most studied volcanic fields in the entire WGB. Mapping by Hewitt (1956) and Barca (1965) is supplemented by detailed volcanological studies (Dohrenwend et al., 1984; Wells et al., 1985). Geochemical and petrologic studies of the field include investigations by Katz (1981), Wilshire (1986), and Farmer et al. (1991). The CVF has been the site of intensive geomorphic studies, calibrated by numerous radiometric age determinations (Dohrenwend et al., 1984, 1986; Turrin et al., 1985; Wells et al., 1985). Primarily the abundance of volcanoes and the relatively large number of dates make the CVF an excellent area for testing probability model accuracy and investigations on the relationship between local geologic conditions and volcano locations.

Turrin et al. (1985) report 53 high-precision K/Ar dates for the lava flows of the CVF. These data, together with paleomagnetic data collected as part of the same study, provide a reasonably complete record of the timing of basaltic volcanism in this field. Based on these data, Dohrenwend et al. (1984) identified three periods of activity in the field, each lasting approximately 1 m.y. These periods are 7.6 to 6.5 Ma, 4.5 to 3.6 Ma, and 1 Ma to the present. The initial period of activity is only represented by a small volume, highly dissected flow and vent complex located on the southeastern margin of the field (Figure 7-3). Eruptions during 4.5 to 3.6 Ma occurred in the northern half of the field and were the most voluminous. Quaternary eruptions occurred in the southern half of the field (Figure 7-3) and can be further subdivided based on paleomagnetic epochs and the degree of soil development on lava flows from this period (Wells et al., 1985). The CVF currently is being used by DOE researchers as an analog site for the YMR (e.g., Wells et al., 1990). In addition, several calibrated Quaternary dating techniques, such as cinder cone erosion and soil development, are being developed at the CVF (Hill et al., 1993).

7.2.1.3 Big Pine Volcanic Field

The Big Pine Volcanic Field (BPVF) is located in Owen's Valley, a deep NNW-trending alluvial basin between the east flank of the Sierra Nevada on the west and the west flank of the White-Inyo Mountains on the

east (Figure 7-4). More than 25 basaltic cinder cones of alkaline and subalkaline composition (Ormerod, 1988), and one small-volume rhyolite dome, comprise the BPVF. These cones are scattered over an area of approximately 400 km² and all erupted during the Pleistocene. The Owen's Valley fault extends the length of the Owen's Valley near its topographic center. Several cones lie along the trace of this fault or along nearby fault segments in the BPVF, but most cones are located at higher topographic levels, close to inferred range-bounding faults (Figure 7-4).

The BPVF is moderately well mapped and studied. Regional mapping by Moore (1963) has been further refined and modified by Darrow (1972) and Ormerod (1988), both of whom studied the petrogenesis of BPVF basalts. Martel et al. (1987) mapped a small area around the Fish Springs cinder cone, located in the northern part of the field along the Owen's Valley fault, in detail. Most flows in the BPVF have been dated by K/Ar or ⁴⁰Ar/³⁹Ar methods. These dates are summarized in Bierman et al. (1991). The oldest centers in the field are on the east side of Owen's Valley (1.05±0.08 Ma) and in Oak Creek Canyon in the southern part of the field (1.18±0.05 Ma). Ormerod (1988) suggested there was a shift in the locus of effusive activity from north to south through time in the BPVF, excluding the Oak Creek basalts. Based on the compilation of Bierman et al. (1991), it is clear that most activity in the field occurred between 1.0 and 0.3 Ma.

The BPVF offers a remarkable opportunity to study the relationship between basaltic volcanism and extensional tectonism. The field straddles the active Owen's Valley Fault Zone, and several cones in the field are cut by, or overlie, individual fault segments. In particular, the Fish Springs cinder cone has been offset by 78 m as a result of slip since the cone formed 0.314 ± 0.036 Ma (Martel et al., 1987). The Fish Springs fault dips at between 90° and 60°. The Red Mountain Cone (Figure 7-4) directly overlies a prominent NNW-trending fault that is also part of the Owen's Valley fault system. Even the earliest workers in the BPVF (e.g., Moore, 1963) reported the dramatic relationship between fault traces and cinder cone alignments in the field, particularly high above the valley floor on the west side of the field (Figure 7-4).

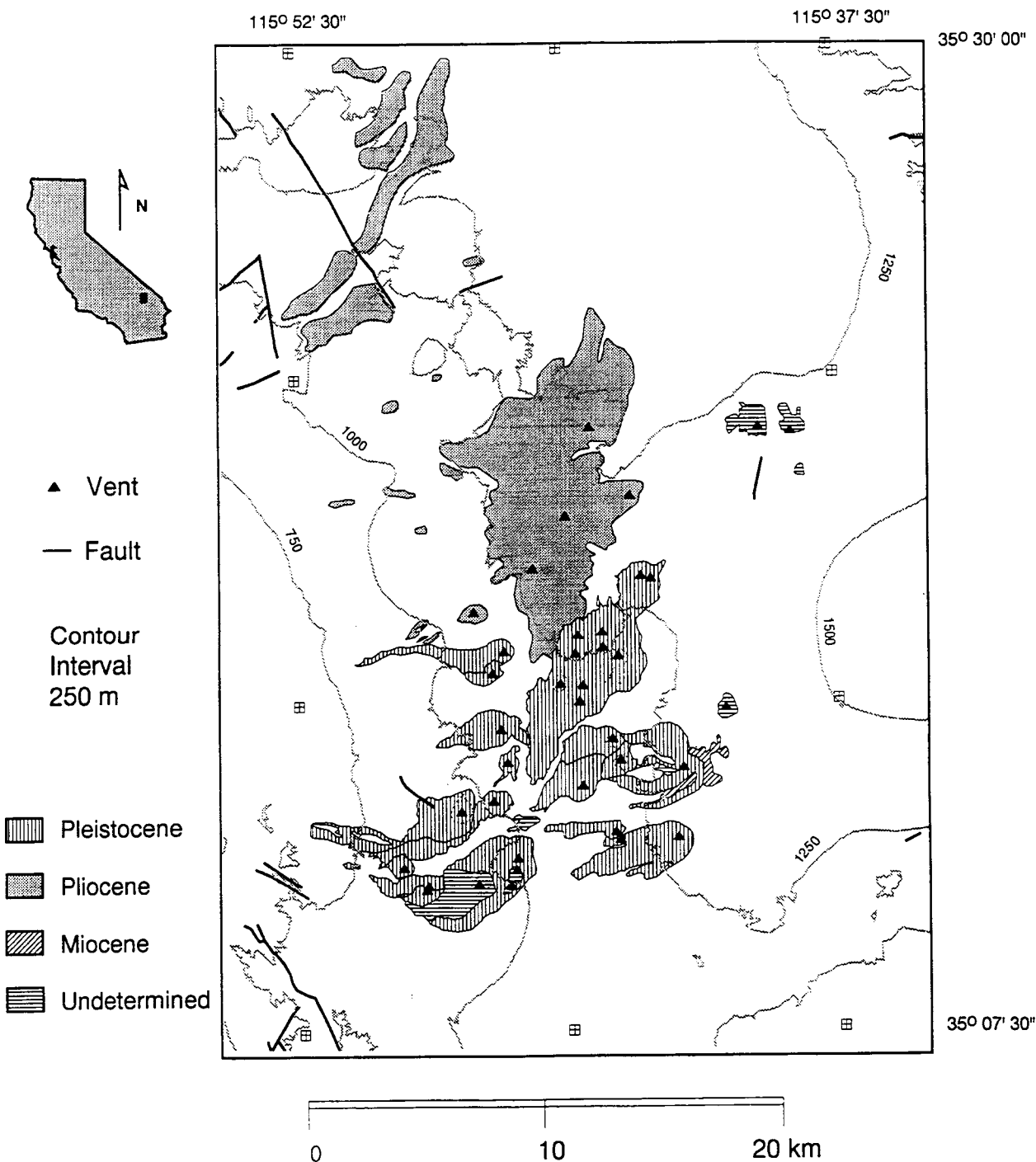


Figure 7-3. Distribution of basaltic vents, lava flows, and faults in and around the Cima Volcanic Field. Epoch age is based on K/Ar dates and stratigraphic relationships. Data sources are summarized in Connor and Hill (1994a). Note that Quaternary volcanoes erupted on a topographic highland and that the volcanoes are distributed over 450 m of vertical relief. Projection is Universal Transverse Mercator, Zone 11.

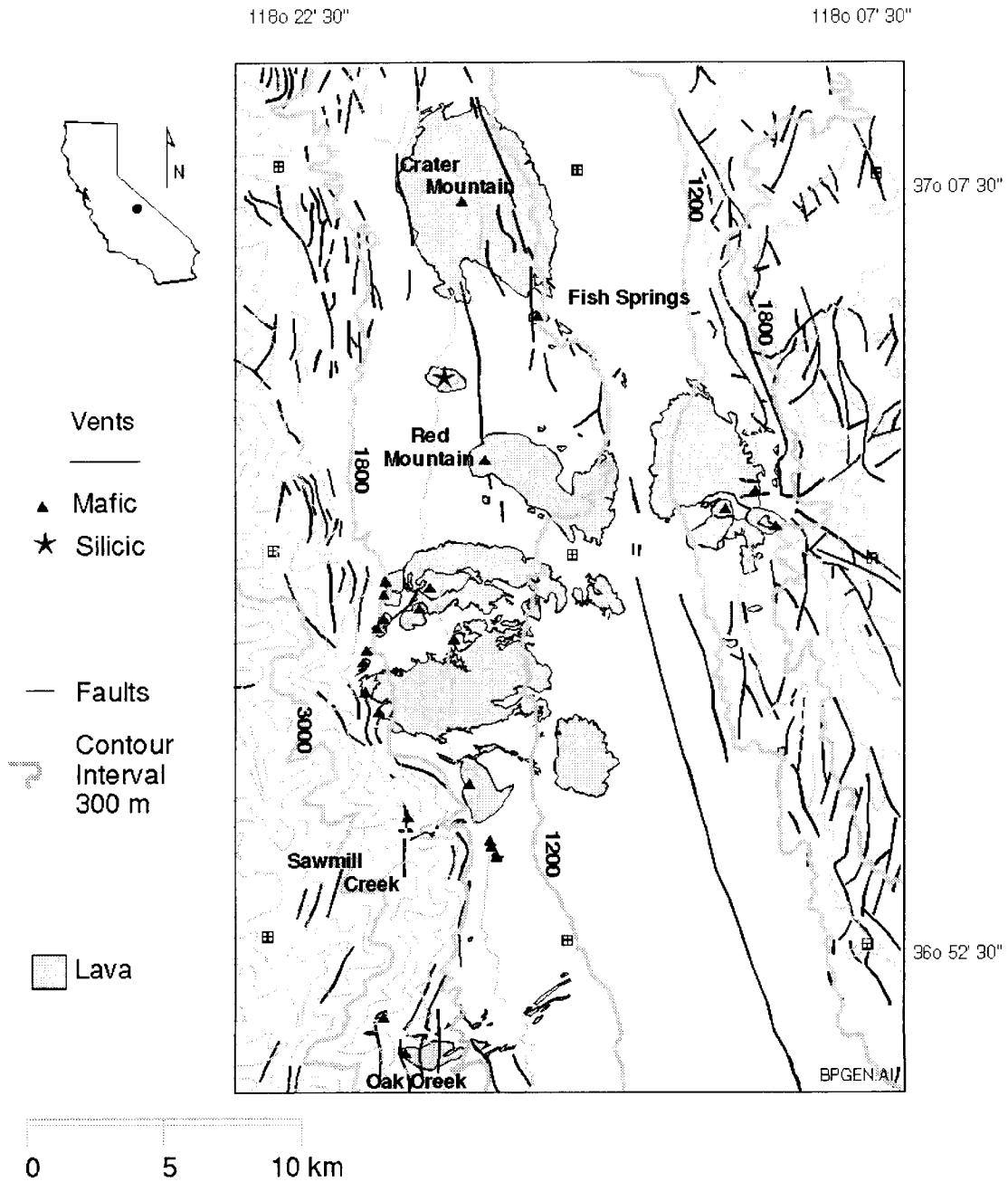


Figure 7-4. Distribution of basaltic vents, lava flows, and faults in and around the Big Pine Volcanic Field. Data sources are summarized in Connor and Hill (1994a). Note that Quaternary volcanoes erupted from about 1,200 m elevation on the Owen's Valley floor to 2,000 m on the eastern slopes of the Sierra Nevada Mountains. Projection is Universal Transverse Mercator, Zone 11.

7.2.1.4 Lunar Crater Volcanic Field

The Lunar Crater Volcanic Field (LCVF) includes alkalic basaltic volcanoes distributed throughout the Pancake and Reveille ranges, roughly 120 km NNE of Yucca Mountain (Figure 7-5). The LCVF is comprised of approximately 75 cinder and

spatter cones and three maars, distributed over an elongate NNE-trending zone measuring 100x25 km in area (Foland and Bergman, 1992). Basic mapping in the area was done by Scott and Trask (1971). The focus of studies in the LCVF has been the development of temporal and spatial patterns of volcanism, primarily because of the distinctive migration of vents from

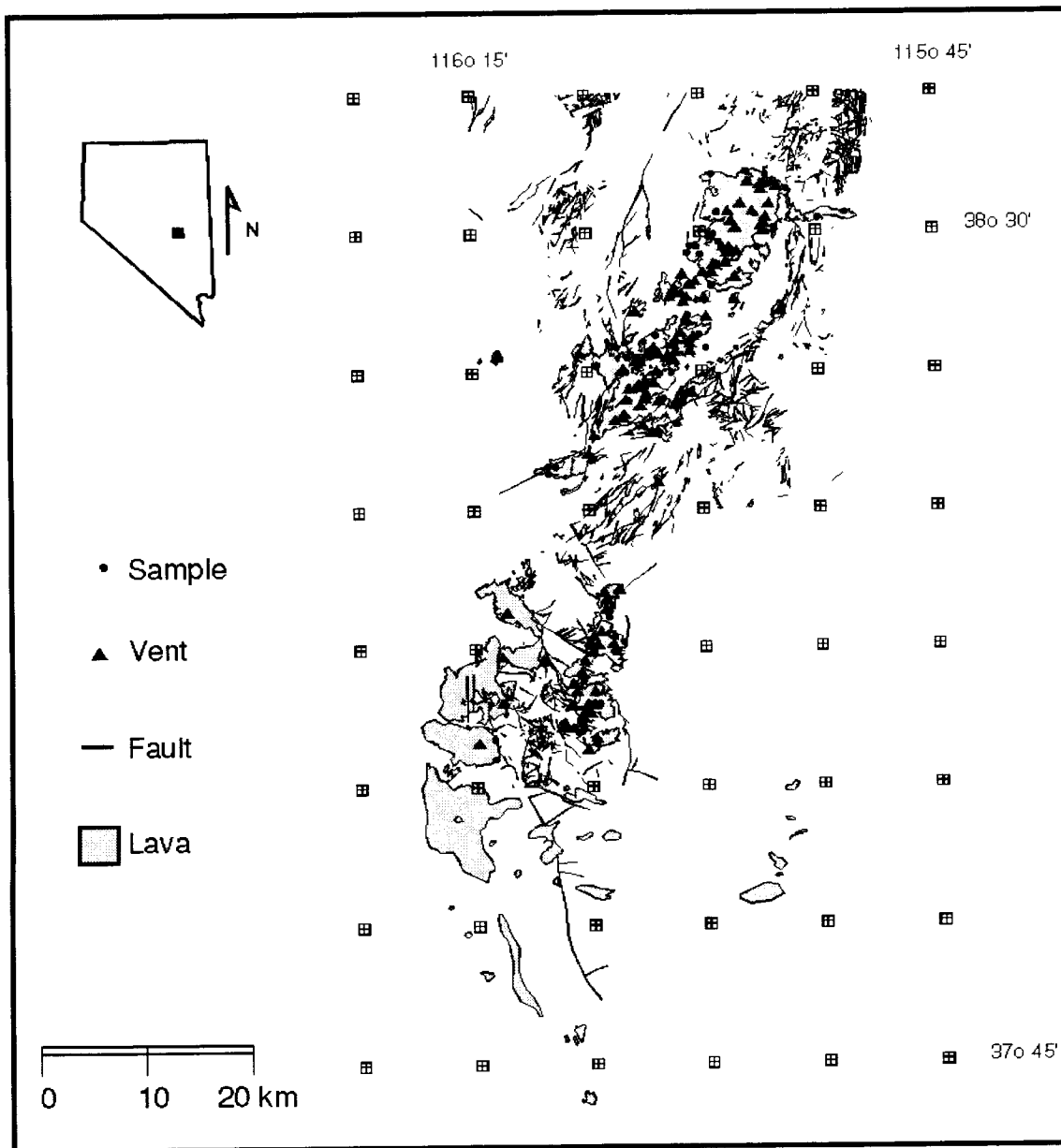


Figure 7-5. Distribution of basaltic vents, lava flows, and faults in and around the Lunar Crater Volcanic Field. Data sources are summarized in Connor and Hill (1994a). Projection is Universal Transverse Mercator, Zone 11.

southwest to northeast through time in this field, parallel to both regional tectonic and structural patterns.

Alkalic basaltic volcanism in the LCVF has occurred in this area since about 9 Ma, with most activity between 6 and 0.3 Ma (Foland and Bergman, 1992). This period of activity is a long one compared with WGB volcanic fields, and is comparable to the period of activity in the YMR. Most volcanic activity in the southern part of the LCVF, in the Reveille Range, took place between 4 to 6 Ma. In contrast, activity occurred between 4 and 0.3 Ma in the Pancake Range (Naumann et al., 1991; Foland and Bergman, 1992). However, it is clear this is only a general trend, more pronounced than, but similar to, those observed on smaller scales in the YMR, CoVF, and CVF. Volcanism may occur at given locations within the LCVF over periods of 3–4 m.y. and, at a given time, volcanism may occur over areas of several hundred square kilometers (Foland and Bergman, 1992).

The LCVF is both geochemically and structurally part of the Basin and Range province, rather than the WGB (e.g., Farmer et al., 1989). However, the long durations of volcanic activity and discernible spatial and temporal trends to volcanism make the LCVF a good analog for the YMR. The LCVF overlies Paleozoic sediments and Tertiary volcanic rocks that have been deformed by NE-trending normal faults. Scott and Trask (1971), Naumann et al. (1991), and Foland and Bergman (1992) have noted that the overall trend of the volcanic field is coincident with both regional tectonic patterns of deformation and local fault zones. Quaternary lavas in the southern part of the Pancake range are occasionally offset by faults (Figure 7-5).

7.2.2 Critical Review of Compiled Volcanic and Tectonic Data

A critical review of data compiled in the CNWRA Volcanism GIS database is part of Task 3 of the Volcanic Systems of the Basin and Range research project. The purposes of this review are to (i) assess the accuracy and completeness of volcanic and tectonic data in the GIS; (ii) evaluate uncertainties related to collection of the data, including analytical methods; and (iii) examine the assumptions made in existing models of Basin and Range magmatism and tectonism. Assessment of uncertainties in the database is important for being able to use these data in development of independent alternative conceptual models that

realistically represent the volcano-tectonic framework of the Basin and Range and the YMR. In addition, the limitation of these data and models must be understood clearly before the GIS can be used as an effective tool in preclicensing and licensing activities.

Several projects related to a critical review of Basin and Range data have been completed. Existing models of Basin and Range regional volcanism and tectonism were reviewed by Stirewalt et al. (1992). In summary, Cenozoic magmatic activity in the Basin and Range can be broadly correlated with extensional strain in both space and time. However, no single magmo-tectonic model currently exists to quantify this general correlation or apply this empirical relationship to the next 10,000 yr in the YMR. Limitations of current geochronological techniques and dating studies in the YMR were assessed by Hill et al. (1993). This review focused on evaluation of the uncertainties associated with dates of basaltic volcanoes and volcanic rocks younger than about 10 Ma in the YMR. Difficulties in dating paleoseismic events and faulting were discussed by Young and Stirewalt (1994). In addition to these projects, a strategy for assessing the effects of uncertainty in volcanism probability models currently is under development as an NRC technical assistance task.

Initial work in the critical review task has focused on developing a strategy to evaluate uncertainties associated with data and models used in volcanism research. This strategy emphasizes (i) assessment of the completeness and accuracy of data in the Volcanism GIS, (ii) quantification and analysis of uncertainties associated with volcanism data, and (iii) evaluation of the accuracy in volcano-tectonic models to depict volcanological processes.

7.2.2.1 Assessment of Accuracy and Completeness

The accuracy of data contained in the Volcanism GIS is dependent upon the accuracy associated with collection of geologic field data or samples for analysis, as well as with the methods used to analyze the samples. Completeness of data simply relates to the thoroughness of data coverage at both regional scales and at the scales of individual volcanic fields. Both of these data uncertainties are relatively easy to evaluate and quantify.

The first measure of accuracy for data in the Volcanism GIS is consideration of the data source. Data

must originate from individuals or groups that are technically adept, and the data must have undergone a measure of peer review. This qualification does not limit data sources to articles from peer-reviewed journals or published documents. Articles produced as Open-File Reports (e.g., U.S. Geological Survey and State Geological Surveys) or contractor reports (e.g., CNWRA, Los Alamos, and Sandia National Laboratories) normally undergo internal, and sometimes external, peer review. Student theses are extensively reviewed by the university faculty before acceptance, and may undergo a level of review exceeding that for journal reviews. In addition, data from most research programs associated with the Yucca Mountain project (e.g., CNWRA, Los Alamos, and Sandia National Laboratories) are produced under rigorous Quality Assurance (QA) procedures.

Inaccuracies will occur even in the most extensively reviewed report. Many geologic parameters are difficult to measure in the field, and errors in the collection of these data often will be transparent to a reviewer. Potential sources of error may be related to, for example, inaccurate location of volcanic features and data collection points on maps, or incorrect measurement of fault displacement. In addition, there are possibilities of human error in the transfer of data drawn from other sources, for example, errors in digitizing field maps. Some errors in data accuracy are immediately apparent, such a lava flow dated at 1 Ma but which stratigraphically overlies a well-dated 0.1-Ma lava. However, most volcanic fields do not have a level of study that is sufficient to resolve potential data inaccuracies. For example, a stratigraphically isolated volcano may have a 2-Ma date yet be surrounded by 0.2-Ma volcanoes. The accuracy of the 2-Ma date cannot be rigorously evaluated without confirmatory testing, although relatively subjective criteria such as cone morphology can aid in this assessment.

Evaluating the completeness of the data coverage in the Volcanism GIS requires analysis at several different scales. For individual volcanic fields, this evaluation consists of a thorough search to acquire all of the data available for the field. Careful searches of journal indices, such as the GEOREF index published by the American Geological Institute, yield publications with the appropriate volcanic field name in either the title or in associated keywords. The references contained in these publications can then be checked to ensure that no relevant article has been overlooked.

Finally, communication with active researchers in these volcanic fields will usually ensure that all relevant sources of information are contained in the database. Appropriate checks will be implemented as review of the database proceeds.

Many volcanic fields in the WGB, such as the Death Valley, Darwin Plateau, Saline Range, and Reville Range/Lunar Crater Volcanic Fields, lack sufficient published information to be robust analogs for the YMR (Stirewalt et al., 1992; Connor and Hill, 1994b). Published studies for each of these volcanic fields indicate that these fields may be analogous to some aspects of YMR basaltic volcanism. However, the ages and locations of many vents in these fields are unknown, mapping is often at a reconnaissance scale, and few volcanological studies have been conducted. An evaluation of data completeness thus consists of ensuring that all available data have been compiled, and that sufficient data exist to use the volcanic field as an analog for the YMR.

7.2.2.2 Assessment of Data Uncertainties

All geologic data, such as volcano age or fault slip-rate, are associated with some level of error or uncertainty. Although data uncertainty can be minimized, it cannot be eliminated entirely. The critical process is to accurately quantify the uncertainty associated with the data. For example, every geochemical analysis has errors in precision (i.e., how exactly an element can be measured) and in accuracy (i.e., how well the measured value represents the actual elemental abundance in the sample). The uncertainties in some measurements can exceed 25 percent. This uncertainty should not be ignored and should be estimated when it is not reported in the original reference. In addition, this uncertainty must be propagated through subsequent calculations, so that an appropriate uncertainty can be assigned to the results of the calculations. Three types of uncertainty are associated with data and models in the Volcanism GIS:

- Basic data or parameter uncertainty, generally related to the precision and accuracy of analyses or direct measurements
- Uncertainty associated with subjective data, such as volcano location or fault displacement

- Uncertainties associated with conceptual models, primarily related to the accuracy of these models in representing geological processes

Some work on the analysis of data uncertainty has been undertaken as a technical assistance task for the Engineering and Geosciences Branch of the NRC Office of Nuclear Materials Safety and Safeguards. As reported by Connor and Hill (1994b), data uncertainty can be propagated using simple arithmetic operations (e.g., Wang et al., 1975). For measured values A and B that have uncertainties of ±a and ±b, respectively:

$$A \pm a + B \pm b = A + B \pm (a^2 + b^2)^{0.5} \quad (7-1)$$

$$A \pm a - B \pm b = A - B \pm (a^2 + b^2)^{0.5} \quad (7-2)$$

$$A \pm a \times B \pm b = A \times B \pm A \times B \times \left[\left(\frac{a}{A}\right)^2 + \left(\frac{b}{B}\right)^2 \right]^{0.5} \quad (7-3)$$

$$\frac{A \pm a}{B \pm b} = \frac{A}{B} \pm \frac{A}{B} \left[\left(\frac{a}{A}\right)^2 + \left(\frac{b}{B}\right)^2 \right]^{0.5} \quad (7-4)$$

In addition, if an exponent *d* is well known:

$$(A \pm a)^d = A^d \pm (d \times a \times A^{d-1}) \quad (7-5)$$

As a practical example, the uncertainty associated with an average age of a volcano can generally be represented by one standard deviation of the data set if the uncertainty associated with the dates is small. However, if the uncertainties are large, then these uncertainties should be propagated through the statistical calculations. Using the above relationships and the dates ($X_i \pm x_i$) in Table 7-1:

$$\text{Average} = X \pm \bar{x} = \frac{\sum X_i}{n} \pm \frac{(\sum x_i^2)^{0.5}}{n} \quad (7-6)$$

$$\text{Standard Deviation} = \left[\frac{\sum (X_i \pm x_i - \bar{X} \pm \bar{x})^2}{n-1} \right]^{0.5} \quad (7-7)$$

In this example, ignoring the uncertainty associated with these dates gives an average date of 0.26 Ma, with a one-standard deviation uncertainty estimate of only 0.04 Ma (Table 7-1). Note, however, that the error associated with the five individual dates ranges

from 38 to 92 percent and averages 57 percent, but the calculated uncertainty on the average date is only 15 percent. This low level of uncertainty does not accurately represent the uncertainty associated with the individual dates, because it only provides the uncertainty in the average. Propagating the uncertainty associated with the individual dates through the calculations results in a standard deviation of 0.05±0.05 Ma. Combining these individual uncertainty terms with the average uncertainty of 0.07 Ma (Table 2-1) yields a combined uncertainty of 0.17 Ma. This value more accurately represents the 57-percent error associated with the individual dates. Reducing the average date to an appropriate number of significant figures yields an age estimate of 0.3±0.2 Ma, which correctly represents the precision and accuracy associated with the data. The Little Black Peak dating example clearly demonstrates why basic data, as opposed to simple averages, need to be reported in order to accurately assess data uncertainties. By ignoring the uncertainty associated with these dates, the simple average and one standard deviation (i.e., 0.26±0.04 Ma) yield a false measure of how well the age of Little Black Peak is known. Without a careful accounting of such uncertainties, application of a probability model would indicate that Little Black Peak was temporally, as well as spatially, distinct from the 0.1±0.05-Ma Lathrop Wells eruption (Crowe and Perry, 1991). However, propagation of the data uncertainty as explained above yields an average age of 0.3±0.2 Ma, which indicates that Little Black Peak may be contemporaneous with Lathrop Wells (Hill et al., 1993).

Models for YMR volcanism thus can and need to be carefully assessed by reasonably propagating data uncertainties through calculations. Calculated results will then have an associated uncertainty that appropriately reflects the uncertainty in the model parameters. Rather than evaluations of differences in volcanism model results that are qualitative and highly subjective, quantified uncertainties can be used to evaluate whether results from different models are statistically distinct for given levels of confidence.

Although the age of a volcano is a relatively straightforward example of data uncertainty analysis, many types of geological data cannot be measured accurately because the data are relatively subjective. For example, determining the volume of an eruption is critical for many probability models. The ash associated with the eruption can be comparable to the volume of

Table 7-1. Compilation of published dates for Little Bear Peak, Nevada

Data Source	Date (Ma)	$\pm 1\sigma$ (Ma)	Error (1%)
Crowe et al. (1982)	0.29	0.11	38
Crowe et al. (1982)	0.32	0.15	47
Crowe et al. (1982)	0.24	0.22	92
Crowe and Perry (1991)	0.21	0.13	64
Crowe and Perry (1991)	0.22	0.10	45
Average $\pm 1\sigma$	0.26 \pm 0.04		57
Average with Uncertainty [Eq. (7-6)]	0.26 \pm 0.07		
Standard Deviation with Uncertainty [Eq. (7-7)]		0.05 \pm 0.05	
Age Estimate with Uncertainty	0.26 \pm 0.17 (i.e., 0.3 \pm 0.2)		

the cinder cone and associated lava flows (e.g., Budinkov et al., 1983). However, this ash rarely is preserved and the volume of ash must be estimated using field relationships and models from the literature. The uncertainties associated with this estimate are highly subjective, because the areal extent and thickness of the ash must be determined with few measurements. Other types of subjective data include vent locations in older volcanic fields, fault displacement and direction, vent alignments, and estimates of intrusion to extrusion volumes. Uncertainties are difficult to estimate for these data and are rarely reported. However, such estimates are critical because the uncertainties may be greater than the actual datum.

7.2.2.3 Assessment of Model Uncertainties

Although conceptual models are not directly contained within the Volcanism GIS, many of the fundamental assumptions in these models can be evaluated with the GIS data. For example, some probability models assume that volcanoes are randomly distributed in an area (e.g., Crowe et al., 1982). If, however, volcanoes are not randomly distributed, then geological processes must control their location. Numerous hypotheses on volcano distribution can be tested with the Volcanism GIS, including controls by:

- Elevation. If magma behaves as a hydrostatic fluid, then lower elevations

should favor volcano emplacement. Evaluating the elevation differences in and between volcanic fields can be accomplished in the Volcanism GIS.

- Proximity to basin-bounding faults. For example, if large normal faults localize magma ascent, then normal faults at basin margins may localize volcanism. Distances from volcanoes to presumed marginal faults can be analyzed from the data in the GIS.
- Bedrock geology. Different types of country rock may have density contrasts or fracture characteristics that enhance volcano or dike emplacement (e.g., Spence and Turcotte, 1990; Rubin, 1993). If map coverage is sufficient, this possible relationship can be tested in the GIS.
- Proximity to older volcanoes. Previous ascent of magma may provide thermal or mechanical pathways for subsequent magmas (e.g., Marsh, 1984). Spatial or temporal clustering of volcanoes might support this hypothesis, and can be determined with the GIS.

- Faults. Pre-existing high-angle faults in the country rock may localize magma ascent (e.g., Nakamura, 1977; Delaney et al., 1986). The GIS can determine volcano proximity to faults with specific ages, displacement directions, or orientations.

The results of these tests can be used to quantify the accuracy of the assumptions used in models of volcano location. Although this process will not result in a numerical uncertainty being attached to the model, it will provide a relatively objective basis for excluding specific assumptions or models from consideration in the DOE license application review.

In addition to determining model accuracy, the Volcanism GIS can bound the accuracy of some models. For example, a commonly held paradigm is that crustal extension enhances and localizes basaltic magmatism in western North America (e.g., Christiansen and Lipman, 1972; Smith and Luedke, 1984; Armstrong and Ward, 1991). Although this relationship is accurate at regional scales and geologic intervals of time (e.g., Gans et al., 1989), it has not been rigorously tested at Quaternary volcanic fields. Decompression melting associated with extension may occur on time scales as short as 1 m.y. (e.g., Pedersen and Ro, 1992) and on the scales of individual volcanic fields (e.g., McKenzie and Bickle, 1988). However, these temporal and spatial intervals have not been tested in the WGB. If limits on fault age and displacement can be combined with volcano age and location in the GIS, then this general hypothesis can be tested for the WGB and other continental volcanic fields. Ultimately, this magmo-tectonic model would have to have a precision that is applicable to areas as small as the YMR and for 10,000-yr intervals of time.

7.2.3 Peer Review of CNWRA Volcanism Research

A peer review of CNWRA volcanism research is being conducted as part of Task 3 activities in the Volcanic Systems of the Basin and Range research project. This review will be used to:

- Validate the objectives and approaches of CNWRA volcanism research and its application to licensing issues at the proposed Yucca Mountain High-Level Nuclear Waste (HLW) repository site

- Improve research scope and methodologies, and investigate new issues that may not be part of the original research plans
- Evaluate interpretations of the available CNWRA data, and explore alternative hypotheses for these data

This review was initiated as part of the overall goal of having eventual peer review of all research projects at the CNWRA. The volcanism research projects are in a stage of development in which suggestions for improvement from peer-review panel members can be incorporated effectively into the overall research plans.

The basic outline and milestone dates for the peer review include:

- Develop the objectives of the review in detail (May 19, 1994)
- Recruit panel members (June 27, 1994)
- Provide relevant literature to panel members (August 17, 1994)
- Convene review panel in San Antonio for 2-day meeting (either September or October 1994)
- Conduct 2-day field trip to the Crater Flat area of Nevada immediately after meeting
- Panel members prepare individual recommendations in a 10-page report (November 1994)
- Synthesize recommendations into formal report to NRC-RES (February 1995)

Work during this reporting period has focused on the elicitation of panel membership from the volcanological community. A relatively rigorous process has been undertaken in order to convene a panel that is truly independent from the CNWRA, NRC, and DOE. In addition, the elicitation is planned to be as objective as possible to avoid skewing panel membership to experts who may have predetermined opinions of CNWRA volcanism research activities. By this constraint, previous or active CNWRA volcanism consultants, employees of the DOE and its subcontractors, and employees funded by the State or

Counties of Nevada, are ineligible for panel membership.

A panel of five members with backgrounds in basaltic volcanism, Basin and Range geology, numerical and empirical modeling of magma ascent and eruption processes, probability modeling, and heat and mass transfer processes, will cover the major topics of CNWRA volcanism research. An initial list of 72 potential panel members was developed based on publications in the appropriate fields of volcanology and familiarity to CNWRA staff. These people were solicited for their opinions on who they would select as experts in the appropriate fields of volcanology, and if they were possibly interested in panel membership. A second list of potential panel members was created from responses to the initial solicitation. In all, 150 letters have been sent to solicit panel nominations. As of June 17, 1994, 65 responses have been received recommending a total of 185 panel members. A histogram of the number of votes per nominee is shown in Figure 7-6. For all candidates, 24 have at least 6 votes, 13 have at least 8 votes, and 6 have at least 10. Of the 65 responses, 31 people have indicated that they definitely would be interested in participating on the review panel. For these 31 people, 3 have at least 10 votes, 5 have at least 8 votes, and 12 have at least 6 votes (Figure 7-6). The leading candidates adequately represent the appropriate volcanological subdisciplines.

A formal invitation for panel membership was sent to the five leading candidates on June 24, 1994. The principal problem will be in scheduling the review panel meeting around the availability of the candidates. In case it becomes impossible to get a mutually agreeable schedule for all the leading candidates, other candidates may have to be considered. Once the panel membership and meeting dates are arranged, background information will be sent to the panel members. This information will include project plans, all deliverables associated with the projects, background information on the regulatory framework for research in the YMR, other publications produced as part of these projects, and a brief synopsis of ongoing work. The 2-day meeting in San Antonio will consist of presentations by CNWRA staff and discussions led by the panel members. The meeting will then move to the Crater Flat area, Nevada, for evaluation of the field characteristics of basaltic volcanism in the YMR. Participants will return to their home institutions and prepare a roughly 10-page report with overall comments on the general

scope and focus of CNWRA volcanism research and recommendations for specific improvements to this research. Panel members also will be asked to include some of their observations on the YMR volcanism. These reports will be compiled by CNWRA staff and specific recommendations made for changes in the volcanism research projects.

7.3 ASSESSMENT OF PROGRESS

During the last 6 mo, significant progress has been made in the development of a Volcanism GIS for fields in the WGB. This GIS is being used to develop and test models for the geologic controls on volcano distributions, such as elevation or proximity to surface faults. In addition, the Volcanism GIS is being used to compile a large amount of data from a wide range of sources into a usable format. The Volcanism GIS thus will be useful for reviewing the scope and completeness of the DOE license application, and in testing volcanism models for the YMR and analogous volcanic fields. Major Milestone 122-030 (Connor and Hill, 1994a) described the Volcanism GIS and was delivered on schedule.

An analysis of volcanism data and model uncertainties also is progressing. A critical review and analysis of geochronological techniques (Hill et al., 1993) was completed last period as part of Task 3 uncertainty analyses. Work continues in developing a robust strategy for the assessment of uncertainties in Volcanism GIS data and models. Results of this work will demonstrate the completeness and accuracy of data used in the Volcanism GIS and independently assess the uncertainties associated with published volcanological data. In addition, the precision and accuracy of proposed magma-tectonic models are being reviewed as part of this task. Quantification of uncertainty associated with data and models is crucial to the evaluation of models proposed for YMR volcanism. In addition, these uncertainties will be critical to evaluating KTUs related to the development and use of conceptual tectonic models that relate to igneous activity, conceptual model representations of the natural system, and variability in model parametric values.

The peer review of CNWRA volcanism research will provide an objective evaluation of ongoing and proposed investigations and improve planned research activities. The member elicitation process is being conducted as objectively as possible, and will result in an independent review panel that lacks a vested

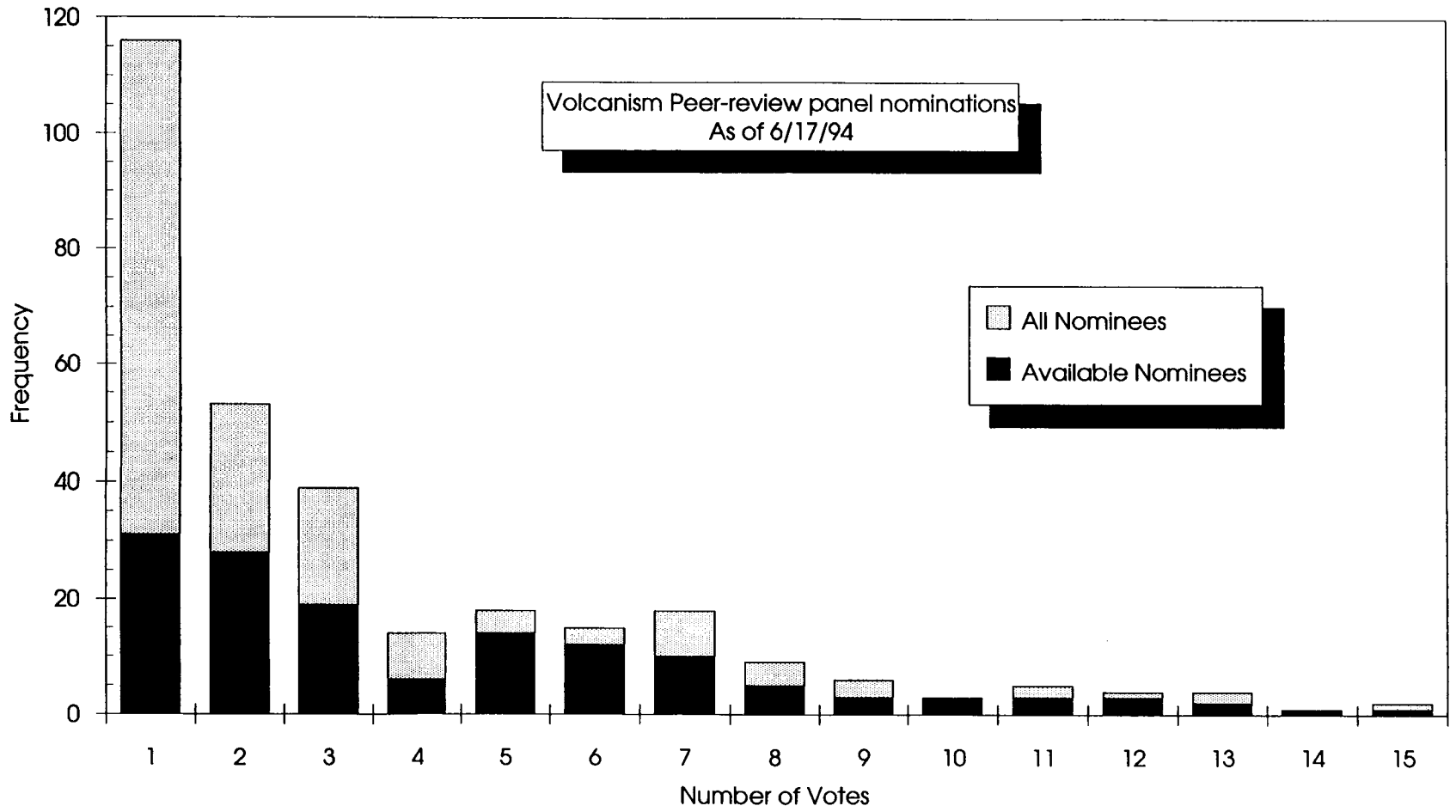


Figure 7-6. Histogram of the number of votes received by all peer-review panel nominees and those nominees who have expressed direct interest and availability for panel participation

interest in its recommendations. Although this review was not part of the original project plan, CNWRA and NRC management consider independent peer review crucial for all CNWRA research programs.

The nonhomogeneous Poisson probability model of Connor and Hill (1993a,b) has been expanded to include a test of model performance through time in the YMR and greater explanation of underlying principles and data. A manuscript currently is in review for the *Journal of Geophysical Research*. Probability models are being developed as part of the analysis of database and model development task (Task 4) for the Volcanic Systems of the Basin and Range project.

7.4 PLANS FOR NEXT REPORTING PERIOD

Work during the next 6 mo will focus on the peer review of CNWRA volcanism research. Although the exact dates are not yet known, the review panel will meet during September or October 1994.

The critical review of compiled volcanic and tectonic data will continue during the next 6 mo, with a major milestone detailing the results of this review planned for January, 1995. This review will evaluate the completeness of the data used in the Volcanism GIS and assess the uncertainties associated with these data. This report also will address assumptions made in existing volcano-tectonic models for the WGB.

Data compilation and analysis will continue in the Volcanism GIS. Information for the Death Valley and Pisgah-Amboy-Dish Hill Volcanic Fields will be entered into the GIS. In addition, aeromagnetic and gravity data from published sources will be integrated into existing coverages.

7.5 REFERENCES

- Amos, R.C., S. Self, and B. Crowe. 1983. Pyroclastic activity at Sunset Crater: Evidence of a large magnitude, high dispersal strombolian eruption. *EOS, Transactions of the American Geophysical Union* 62: 1,085.
- Armstrong, R.L., and P. Ward. 1991. Evolving geographic patterns of Cenozoic magmatism in the North American Cordillera: The temporal and spatial association of magmatism and metamorphic core complexes. *Journal of Geophysical Research* 96: 13,201–13,224.
- Bacon, C.R. 1982. Time-predictable bimodal volcanism in the Coso Range, California. *Geology* 10: 65–69.
- Barca, R.A. 1965. *Geologic Map and Sections of the Northern Portion of the Old Dad Mountain Quadrangle, San Bernardino County, California*. California Division of Mines and Geology Map Sheet 7. Sacramento, CA: California Division of Mines and Geology.
- Bierman, P., A. Gillespie, K. Whipple, and D. Clark. 1991. *Quaternary Geomorphology and Geochronology of Owen's Valley, California*. Geological Society of America field trip: Geological excursions in southern California and Mexico. W.J. Walawender and B.B. Hanan, eds. Guidebook for the 1991 Annual Meeting of the Geological Society of America. San Diego, CA: 199–223.
- Budinkov, V.A., Y.K. Markhinin, and A.A. Ovsyannikov. 1983. The quantity, distribution and petrochemical features of pyroclastics of the great Tolbachik fissure eruption. S.A. Fedotov and Y.K. Markhinin, eds. *The Great Tolbachik Fissure Eruption*. New York, NY: Cambridge University Press: 41–56.
- Christiansen, R.L., and P. Lipman. 1972. Cenozoic volcanism and plate tectonic evolution of the western United States: II, Late Cenozoic. *Philosophical Transactions of the Royal Society of London A-271*: 249–284.
- Connor, C.B., and B.E. Hill. 1993a. Estimating the probability of volcanic disruption of the candidate Yucca Mountain repository using spatially and temporally nonhomogeneous Poisson models. *Proceedings, American Nuclear Society Focus '93 Meeting*. La Grange Park, IL: American Nuclear Society.
- Connor, C.B., and B.E. Hill. 1993b. Volcanism research. *NRC High-Level Radioactive Waste Research at CNWRA, January 1 Through June*

- 30, 1993. CNWRA 93-01S. San Antonio, TX: Center for Nuclear Waste Regulatory Analyses.
- Connor, C.B., and B.E. Hill. 1994a. *The CNWRA Volcanism Geographic Information System Database*. CNWRA 94-004. San Antonio, TX: Center for Nuclear Waste Regulatory Analyses.
- Connor, C.B., and B.E. Hill. 1994b. *Strategy for the Evaluation and Use of Probability Models for Volcanic Disruption Scenarios*. CNWRA 94-015. San Antonio, TX: Center for Nuclear Waste Regulatory Analyses.
- Crowe, B., and F.V. Perry. 1991. *Preliminary Geologic Map of the Sleeping Butte Volcanic Centers*. Report LA-12101-MS. Los Alamos, NM: Los Alamos National Laboratory.
- Crowe, B.M., M.E. Johnson, and R.J. Beckman. 1982. Calculation of the probability of volcanic disruption of a high-level nuclear waste repository within southern Nevada, USA. *Radioactive Waste Management and the Nuclear Fuel Cycle* 3: 167–190.
- Darrow, A.C. 1972. *Origin of the Basalts of the Big Pine Volcanic Field, California*. M.S. Thesis. Santa Barbara, CA: University of California Santa Barbara.
- Delaney, P.T., D.D. Pollard, J.I. Ziony, and E.H. McKee. 1986. Field relations between dikes and joints: Emplacement processes and paleostress analysis. *Journal of Geophysical Research* 91(B5): 4,920–4,938.
- Dohrenwend, J.C., L.D. McFadden, B.D. Turrin, and S.G. Wells. 1984. K-Ar dating of the Cima Volcanic Field, eastern Mojave Desert, California: Late Cenozoic volcanic history and landscape evolution. *Geology* 12: 163–167.
- Dohrenwend, J.C., S.G. Wells, and B.D. Turrin. 1986. Degradation of Quaternary cinder cones in the Cima Volcanic Field, Mojave Desert, California. *Geological Society of America Bulletin* 97: 421–427.
- Duffield, W.A., C.R. Bacon, and G.B. Dalrymple. 1980. Late Cenozoic volcanism, geochronology, and structure of the Coso Range, Inyo County, California. *Journal of Geophysical Research* 85(B5): 2,381–2,404.
- Duffield, W.A., and G.R. Roquemore. 1988. Late Cenozoic volcanism and tectonism in the Coso Range area, California. *This Extended Land: Geological Journeys in the Southern Basin and Range*. D.L. Weide and M.L. Farber, eds. Geological Society of America, Cordilleran Section Field Trip Guidebook. Las Vegas, NV: University of Nevada: 159–176.
- Farmer, G.L., F.V. Perry, S. Semken, B. Crowe, D. Curtis, and D.J. DePaolo. 1989. Isotopic evidence on the structure and origin of subcontinental lithospheric mantle in southern Nevada. *Journal of Geophysical Research* 94(B6): 7,885–7,898.
- Farmer, G.L., H.G. Wilshire, J.L. Wooden, A.F. Glazner, and M. Katz. 1991. Temporal variations in the sources of alkali basalts at the Cima volcanic field, SE California. *Geological Society of America Abstracts with Programs* 23(2): 23.
- Foland, K.A., and S.C. Bergman. 1992. Temporal and spatial distribution of basaltic volcanism in the Pancake and Reveille Ranges north of Yucca Mountain. *Proceedings of the Third International High-Level Radioactive Waste Management Conference*. La Grange Park, IL: American Nuclear Society: 2,366–2,371.
- Gans, P.B., G.A. Mahood, and E. Schermer. 1989. *Synextensional Magmatism in the Basin and Range Province: A Case Study from the Eastern Great Basin*. Geological Society of America Special Paper 233. Denver, CO: Geological Society of America.
- Head, J.W., III, and L. Wilson. 1989. Basaltic pyroclastic eruptions: Influence of gas-release patterns and volume fluxes on fountain structure, and the formation of cinder cones, spatter cones, rootless flows, lava ponds and lava flows. *Journal of Volcanology and Geothermal Research* 37: 261–271.

- Hewitt, D.G. 1956. *Geology and Mineral Resources of the Ivanpah Quadrangle, California and Nevada*. U.S. Geological Survey Professional Paper 275. Washington, DC: U.S. Government Printing Office.
- Hill, B.E., B.W. Leslie, and C.B. Connor. 1993. *A Review and Analysis of Dating Techniques for Neogene and Quaternary Volcanic Rocks*. CNWRA 93-018. San Antonio, TX: Center for Nuclear Waste Regulatory Analyses.
- Katz, M.M. 1981. *Geology and Geochemistry of the Southern Part of the Cima Volcanic Field*. M.S. Thesis. Los Angeles, CA: University of California.
- Marsh, B.D. 1984. Mechanics and energetics of magma formation and ascension. *Explosive Volcanism: Inception, Evolution, and Hazards*. National Research Council/Geophysics Study Committee, eds. Studies in Geophysics. Washington, DC: National Academy Press: 67–83.
- Martel, S.J., T.M. Harrison, and A.R. Gillespie. 1987. Late Quaternary vertical displacement rate across the Fish Springs fault, Owen's Valley, California. *Quaternary Research* 27: 113–129.
- McGetchin, T.R., M. Settle, and B.A. Chouet. 1974. Cinder cone growth modeled after Northeast Crater, Mount Edna, Sicily. *Journal of Geophysical Research* 79(B4): 3,257–3,272.
- McKenzie, D., and M.J. Bickle. 1988. The volume and composition of melt generated by extension of the lithosphere. *Journal of Petrology* 29: 625–679.
- Moore, J.G. 1963. *Geology of the Mount Pinchot Quadrangle, Southern Sierra Nevada, California*. U.S. Geological Survey Bulletin 1130. Washington, DC: U.S. Government Printing Office.
- Nakamura, K., 1977. Volcanoes as possible indicators of tectonic stress orientation—Principles and proposal. *Journal of Volcanology and Geothermal Research* 2: 1–16.
- Naumann, T.R., E.I. Smith, M. Shafiqullah, and P.E. Damon. 1991. New K/Ar ages for Pliocene mafic to intermediate volcanic rocks in the Reveille Range, Nevada. *Isochron/West* 57: 12–16.
- Ormerod, D.S. 1988. *Late-Subduction to Post-Subduction Magmatic Transitions in the Western Great Basin, USA*. Ph.D. Thesis. United Kingdom: Open University.
- Pedersen, T., and H.E. Ro. 1992. Finite duration extension and decompression melting. *Earth and Planetary Science Letters* 113: 15–22.
- Roquemore, G. 1980. Structure, tectonics, and stress field of the Coso Range, Inyo County, California. *Journal of Geophysical Research* 85(B5): 2,434–2,440.
- Rubin, A.M. 1993. Dikes versus diapirs in viscoelastic rock. *Earth and Planetary Science Letters* 117: 653–670.
- Scott, D.H., and N.J. Trask. 1971. *Geology of the Lunar Crater Volcanic Field, Nye County, Nevada*. U.S. Geological Survey Professional Paper 599-I. Washington, DC: U.S. Government Printing Office.
- Smith, R.L., and R.G. Luedke. 1984. Potentially active volcanic lineaments and loci in western conterminous United States. *Explosive Volcanism: Inception, Evolution, and Hazards*. National Research Council/Geophysics Study Committee, eds. Studies in Geophysics. Washington, DC: National Academy Press: 47–66.
- Spence, D.A., and D.L. Turcotte. 1990. Buoyancy-driven magma fracture: A mechanism for ascent through the lithosphere and the emplacement of diamonds. *Journal of Geophysical Research* 95(B4): 5,133–5,139.
- Stirewalt, G.L., S.R. Young, and K.D. Mahrer. 1992. *A Review of Pertinent Literature on Volcanic-magmatic and Tectonic History of the Basin and Range*. CNWRA 92-025. San Antonio, TX: Center for Nuclear Waste Regulatory Analyses.

- Turrin, B.D., J.C. Dohrenwend, R.E. Drake, and G.H. Curtis. 1985. K/Ar ages from the Cima Volcanic Field, eastern Mojave Desert, California. *Isochron/West* 44: 9–16.
- Wang, C.H., D.L. Willis, and W.D. Loveland. 1975. *Radiotracer Methodology in the Biological, Environmental, and Physical Sciences*. Englewood Cliffs, NJ: Prentice-Hall, Inc.
- Wells, S.G., J.C. Dohrenwend, L.D. McFadden, B.D. Turrin, and K.D. Mahrer. 1985. Late Cenozoic landscape evolution on lava flow surfaces of the Cima volcanic field, Mojave Desert, California. *Geological Society of America Bulletin* 96: 1,518–1,529.
- Wells, S.G., L.D. McFadden, C.E. Renault, and B.M. Crowe. 1990. Geomorphic assessment of late Quaternary volcanism in the Yucca Mountain area, southern Nevada: Implications for the proposed high-level radioactive waste repository. *Geology* 18: 549–553.
- Williams, H. 1950. *Volcanoes of the Parícutin region*. U.S. Geological Survey Bulletin 965B: 165–275. Washington, DC: U.S. Government Printing Office.
- Wilson, L., R.S.J. Sparks, T.C. Huang, and N.D. Watkins. 1978. The control of volcanic column heights by eruption energetics and dynamics. *Journal of Geophysical Research* 83(B4): 1,829.
- Wilson, L. 1980. Relationships between pressure, volatile content, and ejecta velocity in three types of volcanic explosion. *Journal of Volcanology and Geothermal Research* 8: 297–313.
- Wilshire, H.G. 1986. Xenoliths of the Cima volcanic field, California. *Geological Society of America Abstracts with Programs* 18(2): 199.
- Young, S.R., and G.L. Stirewalt. 1993. Tectonics Research. *NRC High-Level Radioactive Waste Research at CNWRA, July 1 Through December 31, 1993*. CNWRA 93-02S. San Antonio, TX: Center for Nuclear Waste Regulatory Analyses.
- Young, S.R., R.H. Martin, and B. Henderson. 1993. Tectonic Processes of the Central Basin and Range. *NRC High-Level Radioactive Waste Research at CNWRA, January 1 Through June 30, 1993*. CNWRA 93-02S. San Antonio, TX: Center for Nuclear Waste Regulatory Analyses.

8 TECTONIC PROCESSES IN THE CENTRAL BASIN AND RANGE REGION

by David A. Ferrill, Stephen R. Young, Gerry L. Stirewalt, Alan P. Morris, and D. Brent Henderson

Investigators: David A. Ferrill, Stephen R. Young, Gerry L. Stirewalt, Ronald H. Martin, Alan P. Morris, Richard Klar, and Kathy Spivey (CNWRA); and D. Brent Henderson (SwRI)

NRC Project Officer: George F. Birchard

8.1 TECHNICAL OBJECTIVES

The principal objectives of the Tectonics Research Project are to: (i) compile and integrate tectonic data for the central Basin and Range and Yucca Mountain (YM) regions, and (ii) develop and assess models of tectonic processes in those regions. Of particular concern is the adequacy of existing and anticipated data for determining compliance with performance objectives. A Geographic Information System (GIS) is being used to compile data from various sources into a common framework for data management, review, and analyses. Significant technical accomplishments to date consist of: (i) development of digital terrain models of the YM and central Basin and Range regions; (ii) production of integrated maps that include Quaternary faults, Quaternary basaltic volcanic fields, historic earthquake seismicity, and *in situ* stress data; (iii) compilation of an initial database of geodetically measured regional strain and geologically determined slip rates for individual fault systems; and (iv) an initial evaluation of historic earthquakes.

Information on patterns and rates of historic and prehistoric faulting and seismicity will be necessary to assess compliance with specific regulatory requirements in License Application Review Plan (LARP) Sections 3.2.1.5 through 3.2.1.8. Structural deformation such as uplift, subsidence, folding, and faulting during the Quaternary Period, if characteristic of the controlled area or if capable of affecting isolation within the controlled area, is specifically included as a potentially adverse condition in 10 CFR 60.122(c)(11) [LARP 3.2.1.5]. Key technical uncertainties (KTUs) addressed by this project include: (i) poor resolution of critical exploration methods and uncertainty in interpretation and modeling techniques available to detect and investigate structural geologic features in the subsurface, and (ii) description and abstraction of fault segmentation, distributive faulting, alternative fault

shapes, and associated earthquake seismicity in alternative conceptual tectonic models. Likewise, in 10 CFR 60.122(c)(4) [LARP 3.2.2.8], structural deformation, such as uplift, subsidence, folding, or faulting that may adversely affect the regional groundwater flow system is considered to be a potentially adverse condition. Historic earthquakes, which, if repeated, could affect the site significantly [10 CFR 60.122(c)(12)]; and indications, based on correlation of earthquakes with tectonic processes, that either the frequency or magnitude of earthquakes may increase [10 CFR 60.122(c)(13)] require assessment as potentially adverse conditions [LARP 3.2.1.6 and 3.2.1.7]. Earthquake activity that may occur more frequently, or with higher magnitude than is typical of the geologic setting [10 CFR 60.122(c)(14)], would require assessment as a potentially adverse condition [LARP 3.2.1.8]. KTUs for these sections are due to poor correlation of earthquakes with surface expression of tectonic features, and uncertainties in earthquake predictions because of spatial and temporal migration of seismicity from one fault system to another in the Basin and Range region. Tectonics Research will integrate existing regional data on Quaternary fault segmentation, distributive faulting, historic seismicity, and paleoseismicity for assessment of estimates of fault slip, ground rupture, and earthquake seismicity at YM. Thus, for instance, estimates of earthquake magnitudes based on fault characteristics (e.g., trace length, average slip rate) may be tested against fault systems elsewhere within the geologic setting.

Important goals of this project include development and analyses of alternative tectonic models, evaluation of potential hazards due to fault displacement and seismic shaking, and initiation of field studies to address tectonic issues. Field studies will focus on the following topics: (i) development of structural/tectonic analogs for YM, (ii) development and assessment of alternative structural/tectonic models, (iii) interaction of faulting and igneous activity

(collaboration with Volcanology Research), and (iv) formation of structural/tectonic controls on regional groundwater flow (collaboration with Regional Hydrology Research).

Key elements of the Tectonic Processes of the Central Basin and Range Research Project (Young et al., 1994) are:

- Task 1: Review of literature on Late Neogene and Quaternary tectonism in the central Basin and Range Region
- Task 2: Compilation of tectonic data
- Task 3: Critical review of compiled tectonic data
- Task 4: Completion of field investigations to assess estimates of Late Neogene and Quaternary strain and to support development and assessment of tectonic models
- Task 5: Assessment of geochronological methods for dating and characterizing fault slip and seismic events
- Task 6: Analyses of database and modeling of tectonic processes and geologic deformation
- Task 7: Preparation of semi-annual research reports

Tasks 1 and 5 of the project have been completed. Tasks 2, 3, and 4 are scheduled to end during FY95. Tasks 6 and 7 are planned to continue through FY96. Research efforts in tectonics during the reporting period have focused on Tasks 2, 3, and 4 of the Tectonics Research Project, and, in collaboration with Regional Hydrology Research, on regional groundwater flow in the Death Valley region.

8.2 SIGNIFICANT TECHNICAL ACCOMPLISHMENTS

Significant accomplishments since the last report include: (i) evaluation of the National Earthquake Information Center (NEIC) hypocenter database, with emphasis on the temporal and spatial clustering of earthquakes, relationships between earthquakes and mapped faults, and the 3-dimensional (3-D) distribution of earthquakes through time in the sequence of

earthquakes associated with the 1992 Ms7.6 Landers earthquake, (ii) reconnaissance field work in the Black Mountains, (iii) analysis of fault slip in 3-D stress fields, and (iv) collaborative research, with the Regional Hydrology Research, on the geometry of the regional carbonate aquifer system and the effects of *in situ* stress on transmissivity and regional groundwater flow.

8.2.1 Earthquake Distribution in Southern Nevada and Southern California

Historic earthquake data from the NEIC Preliminary Determination of Epicenters (PDE) database through February 11, 1992, are included in the Tectonics Research GIS (compiled in ARC/INFO Version 6.1) and have been studied to evaluate relationships between earthquakes and mapped faults, temporal and spatial clustering, and 3-D distribution of earthquake hypocenters through time, with emphasis on the Landers earthquake sequence. The data set does not include all recorded earthquakes for the studied region in that it lacks most earthquakes smaller than M=3. The data set should in general include all recorded earthquakes of M=3 and larger for which epicenter locations have been determined. The data presented in Figure 8-1 include all earthquakes in the database. Therefore, earthquakes with man-made sources (i.e., nuclear testing at the Nevada Test Site) have not been excluded. The hypocenters (3-D positions of the earthquake foci) have considerably better accuracy for the map view position than the vertical positions. The horizontal positions are provided in the PDE database to the nearest 0.001 arc degree, which corresponds to a N-S distance on the ground of about 110 m, and, at the latitudes under consideration, an east-west distance in the range of 85–95 m. The vertical positions (depths) are reported in whole kilometers. As indicated by the difference in reporting resolution between the horizontal and vertical positions, the vertical positions have about an order of magnitude lower reported resolution than the horizontal positions. Inaccuracy in earthquake hypocenter depths is significantly greater for earthquakes recorded prior to the mid-1960s.

The distribution of earthquake hypocenters in southern Nevada and southern California (Figure 8-1) illustrates a dramatic increase in the number of recorded earthquakes over the last 50 yr and the clustering of earthquakes along the San Andreas Fault system, western Mojave Desert, southern Sierra Nevada Range, Owen's Valley, Long Valley Caldera, Walker Lane

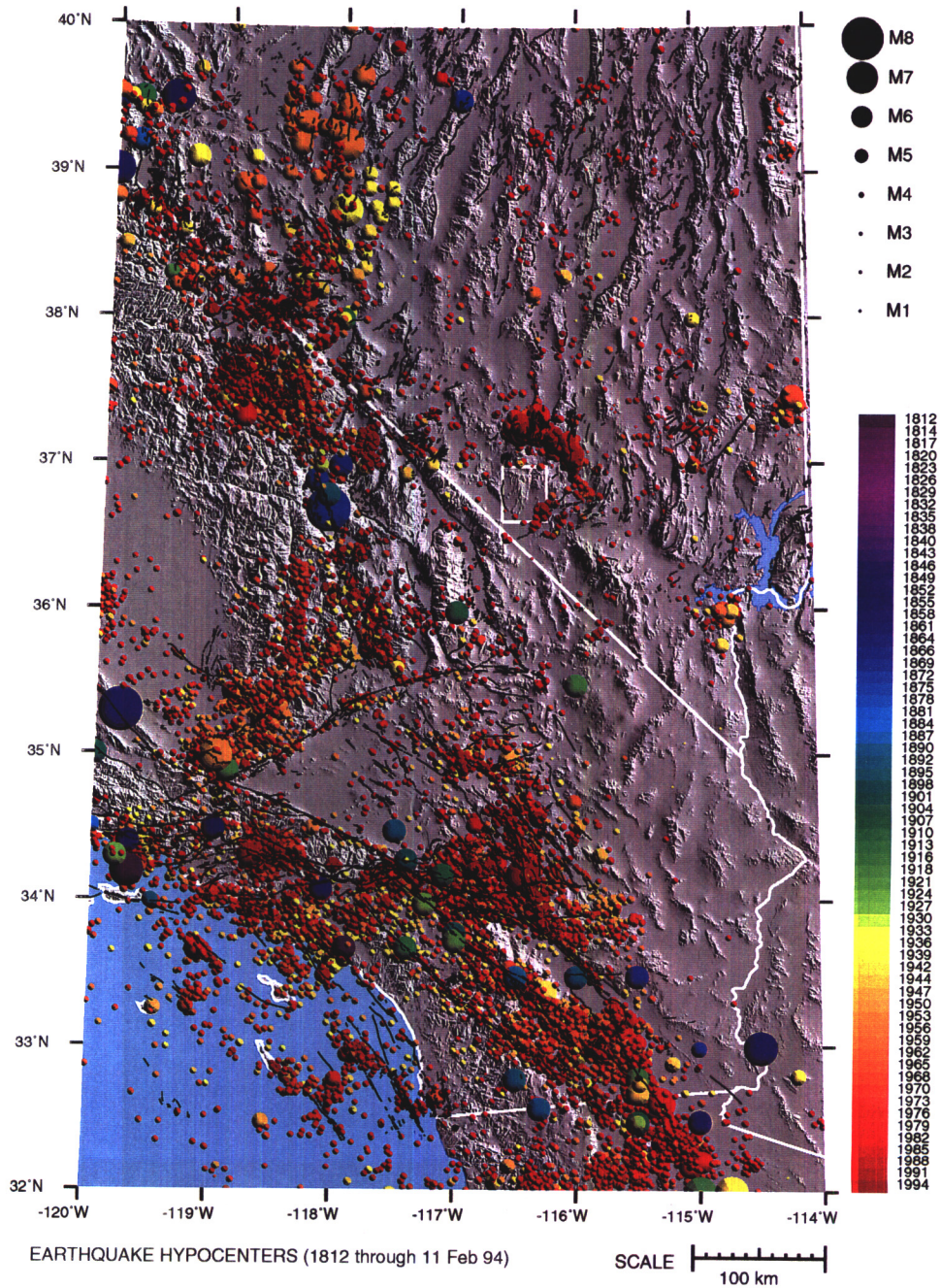


Figure 8-1. Earthquake hypocenters in southern California, southern Nevada, and western Arizona are colored by date, sized by magnitude, and stacked by depth. Earthquake data are from PDE Catalog/National Earthquake Information Center. Magnitudes are assigned a value from one of the following fields in order of preference: *M_s* (average surface-wave magnitude), *m_b* (average body-wave magnitude), contributed magnitude 1, or contributed magnitude 2. Fault traces are from Jennings (1991) in California; and Dohrenwend (1982), Dohrenwend and Moring (1991 a,b,c), Dohrenwend et al. (1991 a-f, 1992 a,b), and Nakata et al. (1982) in Nevada. The white rectangle indicates the boundary of the nine 7.5 minute USGS topographic quadrangles that comprise the Yucca Mountain area.

Seismic Belt, Central Nevada Seismic Belt, and the Intermountain Seismic Belt (Figure 8-2) (Rogers et al., 1991; Smith and Arabasz, 1991; Oldow, 1992). Most of these seismically active areas show abundant recent activity as indicated by the red spheres, which represent earthquakes that occurred from the 1960s through February 1994 (Figure 8-1). The northwestern corner of the map contains a concentration of large yellow and orange spheres, indicating two clusters of earthquakes; one that occurred in the early 1930s (yellow spheres) and the other in the mid-1950s (orange spheres). The concentration of earthquakes in the 1930s includes the 1932 Cedar Mountain earthquakes (M7.2 and M6.2) and the 1934 Excelsior Mountain earthquake (M6.3), which produced significant normal-displacement surface rupture (Rogers et al., 1991). The cluster of earthquakes in the 1950s includes the 1954 earthquakes at Rainbow Mountain (M6.8 and M6.8), Fairview Peak (M7.3), and Dixie Valley (M6.9), each of which caused normal-displacement surface rupture (Slemmons, 1957; Doser, 1986; Zhang et al., 1991; Rogers et al., 1991). No similar sequences of earthquakes had been recorded in those areas prior to the relatively intense activity in the 1930s and 1950s, nor have major earthquakes been recorded in those areas since that time (Figure 8-1).

The earthquake record for the western Great Basin extends for less than 200 yr. Networks of seismographs have existed in the region for less than 100 yr. The historic earthquake record is too brief to accurately assess earthquake risk. As an example, the Death Valley-Furnace Creek (DVFC) fault system appears from the earthquake data to be relatively quiet seismically (Figure 8-2). In contrast, Reheis (1994) has, based on trenching studies and ^{14}C dating in the northern Furnace Creek fault system (Fish Lake Valley), interpreted a minimum of seven ground-rupturing events over the past 5,000 yr, a recurrence interval of 500–1,000 yr, and an average right-lateral displacement rate of 4–7 to 12 mm/yr. The time interval since the last ground-rupturing earthquake in the northern Furnace Creek fault system is thought to equal or exceed the recurrence interval (Reheis, 1994). Based on the temporal and spatial clustering of earthquakes observed regionally and the geological interpretations of slip along the DVFC fault system, modern aseismicity is not an indication that the system is incapable of supporting large earthquakes. Rather, the DVFC-Fish Lake Valley fault system is arguably the most active fault system in the western Great Basin, and, as such, may be capable of

supporting very large ($>M7.5$) earthquakes (Reheis 1994).

8.2.2 Landers Earthquake Sequence

The Ms7.6 Landers earthquake that occurred on June 28, 1992, near Landers, California and the sequence of aftershocks is particularly important for understanding the seismic risk for YM because the Landers sequence is similar to the type and magnitude of a large earthquake that would potentially occur along the DVFC fault system. The Landers rupture and the DVFC fault system are similar in that both are steeply dipping right-lateral strike slip faults, and the Landers surface rupture and aftershock sequence has a bend at its northern end that is similar to the bend of about 20° at the point along the DVFC fault system nearest YM. The DVFC fault system is, at its closest, 50 km southwest of YM and may be the most active fault in the western Great Basin. As such, the DVFC fault system may be considered to be the most proximal potential source (with respect to YM) of a large magnitude mainshock (e.g., M7). A large earthquake of M7 or greater along the DVFC fault system could directly influence faulting at YM and produce local aftershocks and more distant remotely triggered earthquakes that could also have a significant impact on YM. The Landers earthquake sequence is important to understanding earthquake potential and tectonics of the Central Basin and Range for several reasons: (i) large magnitude, (ii) major surface rupture, (iii) remote triggering of other earthquakes, including Little Skull Mountain earthquake, (iv) pattern of slip and distribution of aftershocks comprise one model for major earthquakes along the DVFC fault system, and (v) surface rupture caused on several mapped faults and a previously unmapped linking fault.

The Landers earthquake sequence (Figures 8-3 and 8-4), as it is referred to here, began with the April 22, 1992, Joshua Tree (Ms6.3) earthquake with an epicenter located between the Pinto Mountain Fault and the Mission Creek Fault (segment of the San Andreas fault system). The Landers mainshock occurred about 2 mo later, on June 28, 1992, approximately 30 km north-northwest of the Joshua Tree epicenter and about 7 km north of the Pinto Mountain Fault. The Landers mainshock was followed 3 hr later by the Ms6.7 Big Bear Lake earthquake, 35 km to the west. The following day (June 29, 1992), an earthquake (Ms5.4) occurred in Nevada near Little Skull Mountain about 15 km

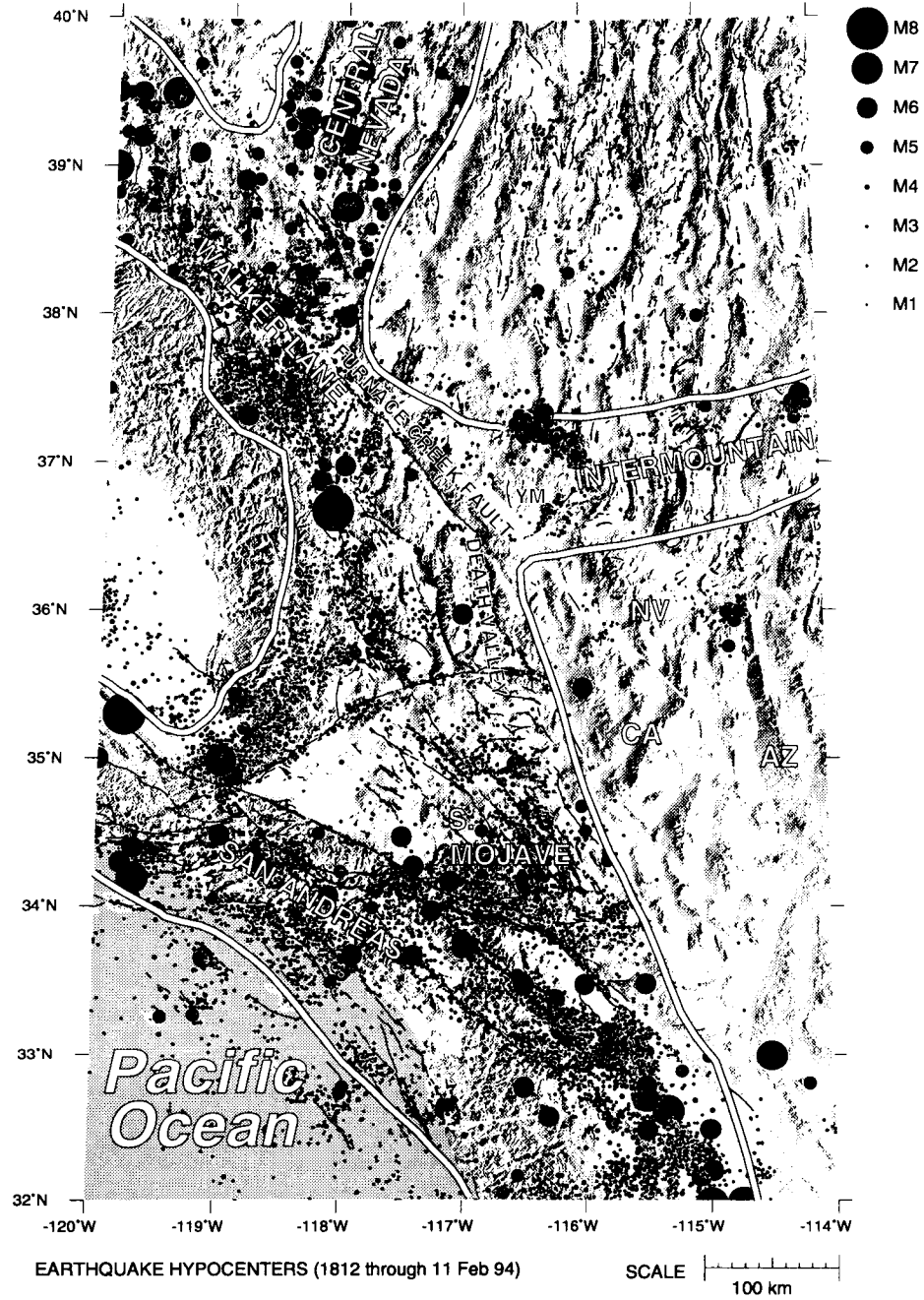


Figure 8-2. Earthquake activity belts of southern California and southern Nevada.

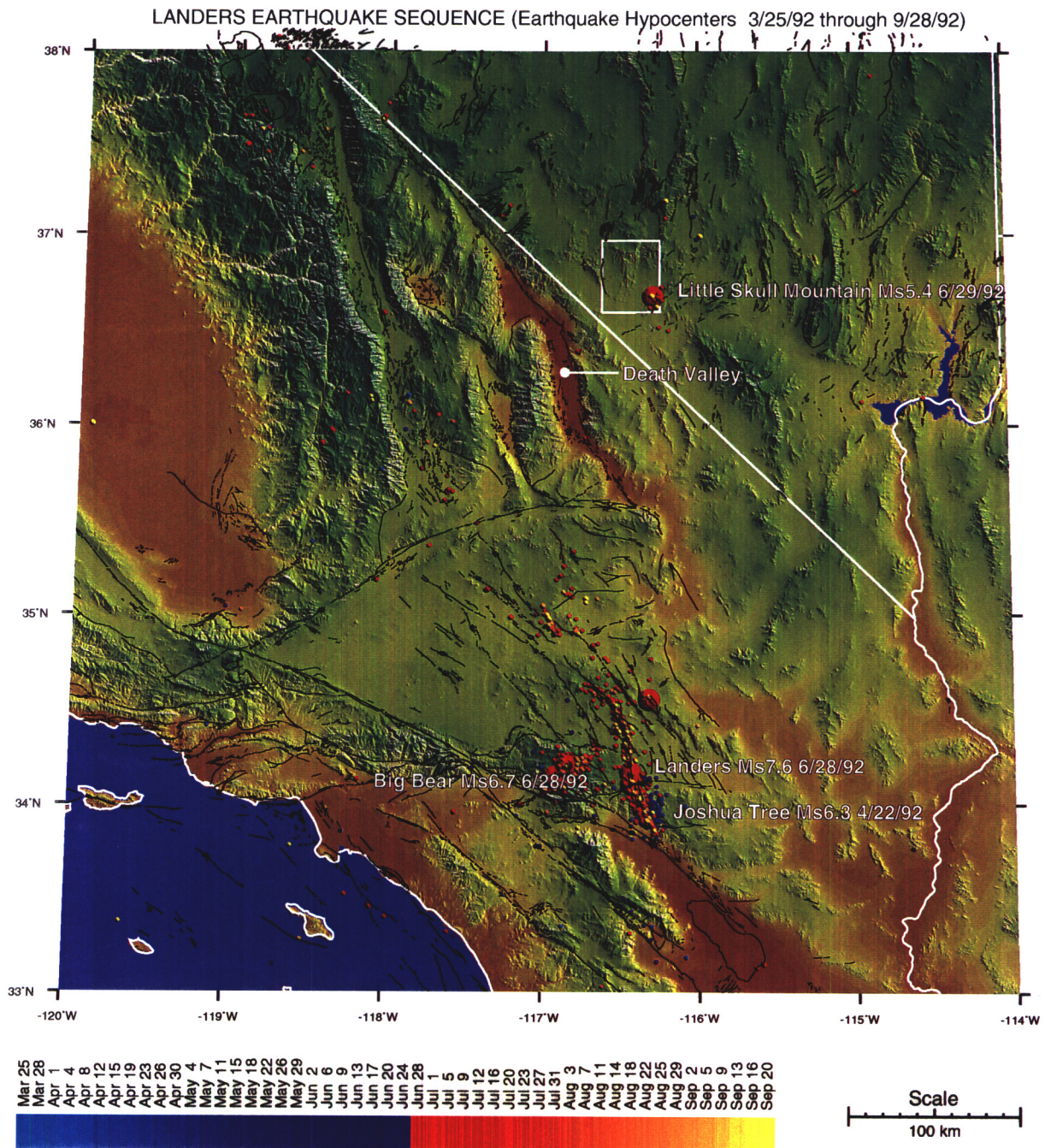


Figure 8-3. Landers earthquake sequence in plan view. Earthquake hypocenters are colored by date, sized by magnitude, and stacked by depth. Earthquake data are from PDE Catalog/National Earthquake Information Center. Magnitudes are assigned a value from one of the following fields in order of preference: Ms (average surface-wave magnitude), mb (average body-wave magnitude), contributed magnitude 1, or contributed magnitude 2. Fault traces are from Jennings (1992) in California; and Dohrenwend (1982), Dohrenwend and Moring (1991 a,b,c), Dohrenwend et al. (1991 a-f, 1992 a,b), and Nakata et al. (1982) in Nevada. The white rectangle indicates the boundary of the nine 7.5-minute USGS topographic quadrangles that comprise the Yucca Mountain area.

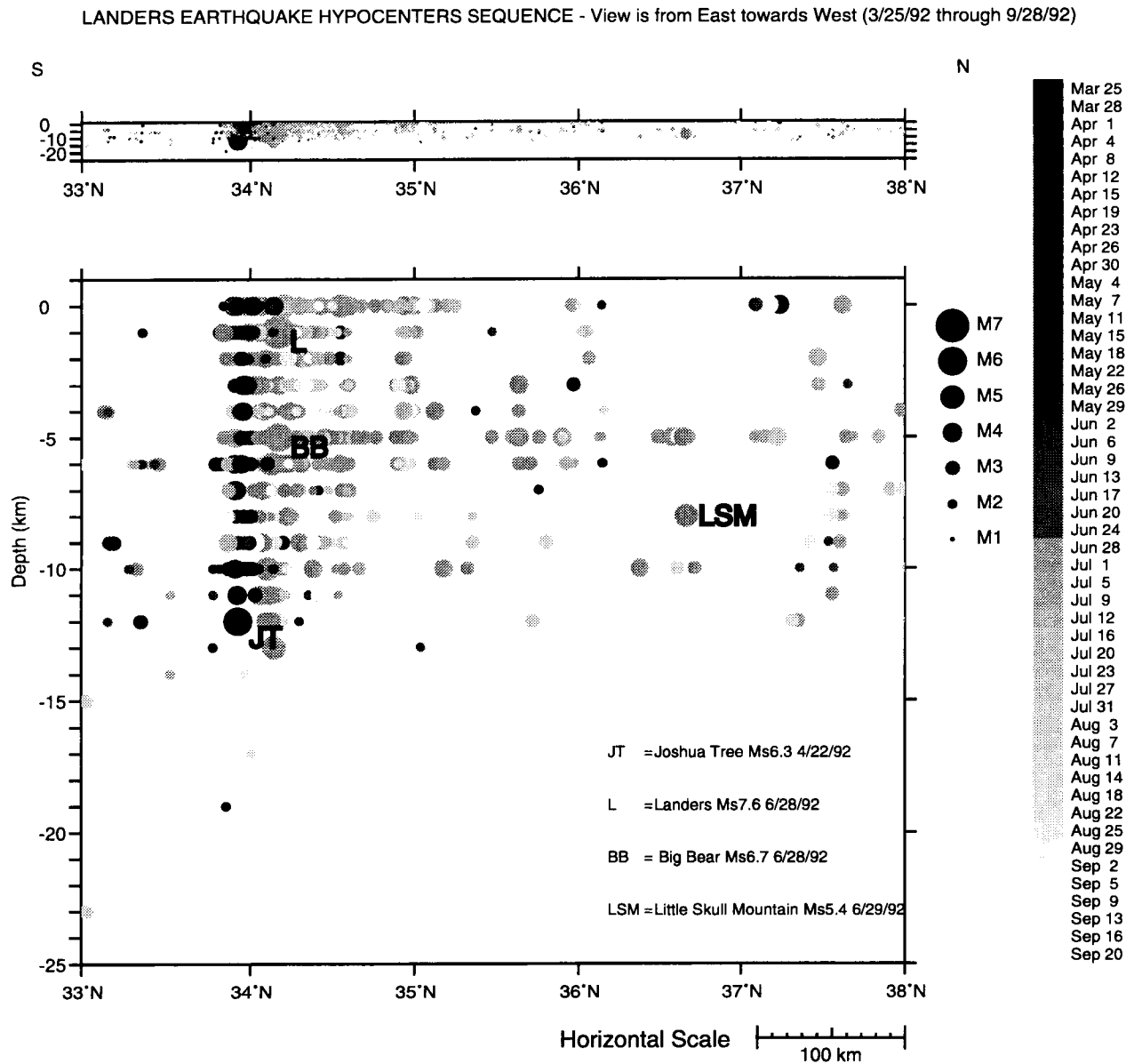


Figure 8-4. Landers sequence in profile view. Earthquake hypocenters are shaded by date and sized by magnitude. Earthquake data are from PE Catalog/National Earthquake Information Center. Magnitudes are assigned a value from one of the following fields in order of preference: Ms (average surface-wave magnitude), mb (average body-wave magnitude), contributed magnitude 1, or contributed magnitude 2.

southeast of YM. The Landers earthquake sequence ended a period of relative seismic quiescence in the immediate area of the Landers–Big Bear earthquake sequence that had lasted for over 4 yr (Wiemer and Wyss, 1994).

Surface rupture associated with the Landers earthquake extends from a few km south of the Landers epicenter to about 70 km north of the epicenter, and is characterized by right-lateral strike slip or right-lateral-dominated oblique slip (Kanamori et al., 1992; Sieh et al., 1993; Hudnut et al., 1994). Nearly continuous surface rupture associated with the Landers earthquake occurred along portions of several previously mapped faults (from south to north, the Johnson Valley Fault, Homestead Valley Fault, Emerson Fault, and Camp Rock Faults) and the previously unmapped Kickapoo Fault, linking the Johnson Valley and Homestead Valley Faults (Hart et al., 1993; Sieh et al., 1993; Sowers et al., 1994). Measured slip varies along the trace of the rupture. Based on mapped displacements, slip maxima occur along two distinct segments: one located about 15 km north of the Landers mainshock epicenter and the other 40 km north of the Landers epicenter (Kanamori et al., 1992; Hudnut et al., 1994). The total-slip maximum of 7 m occurred on the segment 40 km north of the mainshock epicenter along the Emerson Fault (Galway Lake Road site) (Irvine and Hill, 1993; Hart et al., 1993; Reynolds, 1993; Arrowsmith and Rhodes, 1994) (Figure 8-5). The variations in the amount of slip along the fault are interpreted to suggest that the Landers rupture event was composed of two subevents marked by the surface slip maxima along the trace of the surface rupture (Kanamori et al., 1992; Topozada, 1993; Dreger, 1994; Hudnut, et al., 1994).

The aftershock pattern and surface rupture for the Landers sequence define an arcuate, vertical surface that extends for 95 km. This surface has a strike of N10° W in the south and curves into a trend of N30° W in the north (Figure 8-3) (Sieh, et al., 1993). Viewing the earthquake sequence in three dimensions illustrates some important points regarding the aftershock patterns with respect to the mainshocks (Figures 8-3 and 8-4). The hypocenter for the Joshua Tree mainshock is reported at a depth of 12 km. Hypocenters for the subsequent aftershocks of the Joshua Tree earthquake were virtually all shallower (Figure 8-4). The pattern for the Landers earthquake and aftershocks is dramatically different. The hypocenter for the Landers mainshock is reported to be at a depth of 1 km. The bulk of aftershock

hypocenters occurred deeper and to the north of the Landers mainshock (Figure 8-4).

The Landers earthquake, based on cumulative numbers of earthquakes, cumulative seismic moment, and statistical analyses, triggered a dramatic increase in earthquake activity throughout much of the western United States (Hill et al., 1993). Some noteworthy characteristics of the triggered earthquake activity are that: (i) all the recognized triggered earthquake activity occurred north of the Landers mainshock; (ii) much of the triggered activity occurred in areas of geothermal or relatively recent volcanic activity; (iii) triggered activity occurred up to 1,250 km from the Landers mainshock; (iv) all sites of triggered activity show strike-slip to normal displacements, suggesting that regionally σ_3 , the least principal stress, is horizontal (Hill et al., 1993). Remotely triggered earthquakes associated with the Landers mainshock have been interpreted for the following sites, with distances in kilometers from the Landers mainshock shown in parentheses: Coso–Indian Wells (165–205), Little Skull Mountain, Nevada (280), White Mountains, California (380–420), Long Valley (415), Mono Basin (450), Cedar City, Utah (490), western Nevada (450–650), Lassen (840), Burney (900), Cascade, Idaho (1,100), and Yellowstone National Park (1,250) (Hill et al., 1993; Anderson et al., 1994; Bodin and Gomberg, 1994; Gomberg and Bodin, 1994; Roquemore and Simila, 1994).

Two processes are discussed by Hill et al. (1993) as possible mechanisms for remotely triggering slip. Both triggering mechanisms involve brittle slip on favorably oriented faults either due to stress changes sufficient to surpass the frictional strength, or to a decrease in the frictional strength. One mechanism involves static stress changes produced by dislocation along the Landers rupture, and the other mechanism involves dynamic stresses associated with propagating seismic waves generated by abrupt slip along the rupture surface. Modeling static-elastic dislocation in homogeneous media suggests that a static stress mechanism may be responsible for aftershocks within one to two rupture lengths of a fault. Hill et al. (1993) state that “the temporal form and spatial distribution of the remote triggering point—to a class of explanations involving critically loaded faults in a heterogeneous crust, static strain amplification within weak boundaries (fault zones) between crustal blocks, and nonlinear interactions between dynamic stresses in seismic waves and crustal fluids.” Bodin and Gomberg (1994) used

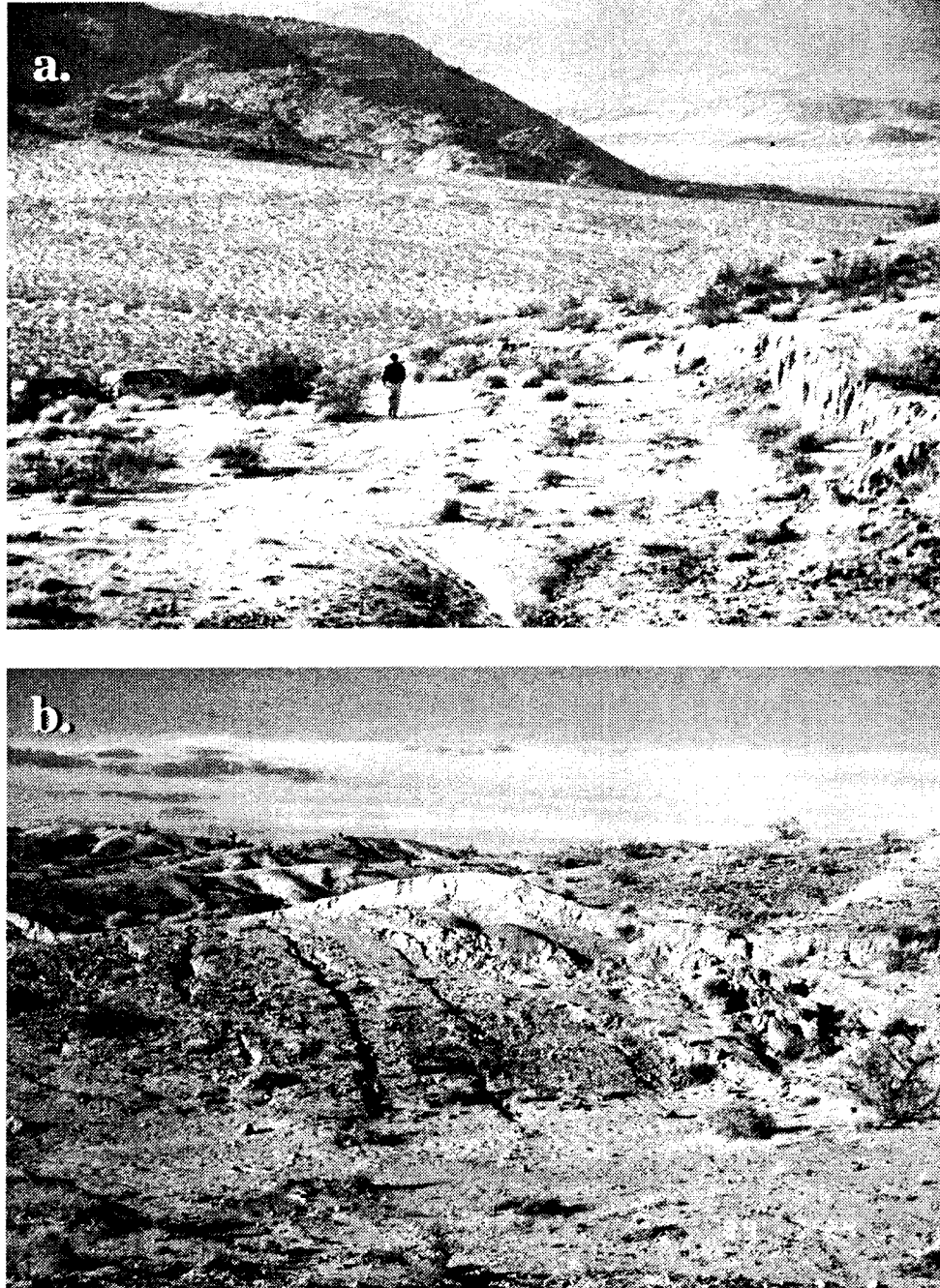


Figure 8-5. Field photographs of Emerson Fault rupture at the Galway Lake Road site. Right-lateral-dominated oblique slip of 7 m was measured at this site. (a) View towards NW displays fault scarp in foreground (1.5–2 m high) and trace of rupture crossing desert toward eastern end of distant ridge. (b) View toward NE shows main scarp (1.5–2 m high) dipping southwestward and subsidiary normal faults that form horsts and grabens in hangingwall of main fault. Photographs taken by D. Ferrill on 24 March 1994.

numerical modeling to test the viability of static stress change as a mechanism for remote triggering of earthquakes. The results of these models suggest that regional fault connectivity can increase the static stress change by about an order of magnitude at distances of at least 280 km, which would include the distance between the Landers mainshock and Little Skull Mountain. Dynamic strain may also be channeled by structure and the direction of rupture propagation, which would, in the case of the Landers sequence, focus generally toward the north and Little Skull Mountain (Figure 8-3) (Bodin and Gomberg, 1994).

Remote triggering like that following the Landers mainshock may serve to release strain in the regions between the most active faults, and may thereby inhibit large strain buildup that could support large earthquakes. The Landers surface rupture includes slip along numerous faults, rather than being restricted to a single major fault or a part of a fault. Though the strain released by the Landers earthquake is attributable to the San Andreas Fault, the earthquake sequence did not occur on the San Andreas Fault. The fact that the earthquake sequence extended from near the San Andreas Fault northward into the Mojave Desert was a surprise and led A. Nur and coworkers (as discussed by Monastersky, 1993) to suggest that the San Andreas Fault system may be changing locations and preparing to avulse to a new position, extending along the Landers earthquake sequence and northward along Owen's Valley on the eastern side of the Sierra Nevada.

8.2.3 Reconnaissance Field Investigations in the Black Mountains and Vicinity

Central Death Valley is a classic pull-apart basin along the DVFC Fault system (Burchfiel and Stewart, 1966). The Black Mountains bound the eastern margin of the pull-apart basin and are in the footwall of the west-dipping, basin-forming normal fault. The Panamint Range bounds central Death Valley on its western side and represents the hangingwall of the Death Valley pull-apart. The Black Mountain block is interpreted to have originated at midcrustal depths between 10–20 km (based on geobarometry) and 30 km (based on structural configuration; Holm and Wernicke, 1990). Denudation by extensional detachment faulting and erosion is interpreted to have resulted in the uplift and tilting of the Black Mountains to their present configuration (Stewart, 1983; Holm and Wernicke, 1990). Detachment-related deformation in the Black

Mountains was first mapped and described by Noble (1941), who referred to it as the "Amargosa Chaos" because of the observed chaotic character of the deformation. Based on the deformation style and the subhorizontal orientation of the Amargosa Chaos, the "chaos" was originally referred to as the "Amargosa Thrust" (Noble, 1941). Based on the younger-over-older relationship across the "chaos" and the regional context, subsequent workers have reinterpreted the Amargosa Chaos to be an extensional detachment fault (Hunt and Mabey, 1966; Stewart, 1983; Burchfiel and Wernicke, 1989; McKenna and Hodges, 1990).

Different amounts of horizontal extension during the Tertiary have been interpreted for the unroofing and uplift of the Black Mountains. Stewart (1983) interpreted that >10 km of uplift of the Black Mountains could not be accounted for by erosion. Stewart instead interpreted that the crustal section now present as the Panamint Mountains originally was located above and somewhat east of the Black Mountains and subsequently moved 80 km northwestward relative to the Black Mountains. McKenna and Hodges (1990) have interpreted 25 to 55 km of post-9 Ma horizontal extension, between the Panamint Mountains and the Black Mountains, at an averaged extension rate of 2.7–6.4 mm/yr. Wright and Troxel (1967) and Prave and Wright (1986a,b) have interpreted substantially less displacement between the Panamint Mountains and the Black Mountains and a more significant role of erosion in the denudation of the Black Mountains. According to McKenna and Hodges (1990) and Stewart (1983), most of the horizontal displacement between the Panamint Mountains and the Black Mountains was accommodated along the Amargosa Chaos.

The Black Mountains are potentially useful for the study of structural and tectonic features and processes that may apply to YM at several scales. Crater Flat Valley, between YM and Bare Mountain, has been interpreted to be a pull-apart basin by Carr (1990). Therefore, interpretations of structures and deformation associated with the central Death Valley pull-apart are important for their potential impact on subregional tectonic models of YM. Listric normal fault geometry has been proposed at depth for the normal fault system exposed in the vicinity of YM (Scott, 1990; Young et al., 1992). The Black Mountains block appears to represent one of the best exposed examples of deep structures associated with detachment faulting of the

type proposed to underlie YM (Scott, 1990; Young et al., 1992). Additionally, listric normal faults that merge with gently west-dipping detachment faults have been described in the vicinity of the Mormon Point turtleback on the west side of the Black Mountains in southern Death Valley (Troxel, 1986) and may provide a model of the intersection of listric faults with the associated detachment surface. Fault zone deformation has been shown to significantly affect the permeability of rocks with respect to fluid flow (e.g., Phillips 1972, Sibons 1986, 1987). The deformation mechanisms in the Paleozoic sedimentary rocks of the Amargosa Chaos are of interest because of the possible effects of either increased or decreased permeability of fault zones with respect to the surrounding rock in the regional carbonate aquifer in the greater Death Valley region, including YM.

Surveys of literature on detachment zone deformation at two localities; namely, the Amargosa Chaos in the southern Black Mountains, California, and the Old Bullfrog Mine in the Bullfrog Hills near Beatty, Nevada, were followed by field reconnaissance at the two areas. Field observations suggest that deformation was dominated by brittle processes. Fault rock textures at the two localities differ dramatically because of the degree of vein infill in the brittle fractures. These differences would have a major impact on the permeability and transmissivity of the faulted rocks and are therefore potentially important for understanding groundwater flow along and across listric faults. These two sites warrant additional study to investigate the structural and geochemical characteristics of detachment zone deformation that may affect groundwater flow in the regional carbonate aquifer.

The erosional remnant of Amargosa Chaos adjacent to Highway 178 near Rhodes Wash in the southern Black Mountains, described by Noble (1941) (Virgin Spring Phase), is visible on the north face of a hill approximately 90 m high. Noble (1941) surmised that present-day thickness of the Amargosa Chaos does not exceed about 610 m (2,000 ft) in the Virgin Spring area of the Black Mountains; however, the chaos is overlain by the Funeral fanglomerate above an erosional unconformity, indicating that the initial thickness was probably greater than the present thickness. From bottom to top, the exposure reveals strongly sheared, autochthonous, older Proterozoic gneisses beneath a subhorizontal fault contact with the overlying chaos; fault-bounded lenses of arkosic sandstone and shale of

the lower Crystal Spring Formation (oldest of the three formations of the Proterozoic Pahump Group); dark green lenses of diabase sill that regionally separate the lower clastic members of the Crystal Spring from its higher carbonate member (dark reddish-brown lenses of dolomite); and yellowish-gray Noonday dolomite at the crest of the hill. Like the Crystal Spring Formation, the Noonday Formation also occurs as fault-bounded lenses in the chaos. The Crystal Spring Formation is ordinarily between 750–1,200 m thick (Troxel and Wright, 1987), but at this location has been attenuated to a thickness of about 60 m. All carbonate units at this locality have been brittlely deformed; however, in spite of the attenuation and fracturing of the units, the exposed lenticular slices retain the proper stratigraphic position of younger over older. It is not clear what factors governed development of thick zones of fracturing adjacent to the detachment surface. As noted by Noble (1941), "every contact between blocks throughout the chaos is a fault" and "blocks in the chaos are so intensely and minutely fractured—that uncracked pieces of rock over 2 in. in diameter are exceptional." This description suggests the potential for considerably increased permeability of brittle units adjacent to major extensional detachment surfaces.

The second example of detachment zone deformation is at the Old Bullfrog Mine. The exposed upper detachment fault separates highly attenuated lower and middle Paleozoic clastic and carbonate rocks of the middle plate from an overlying upper plate sequence of faulted and tilted Tertiary (Miocene) volcanic, volcanoclastic, and sedimentary rocks (McKague et al., 1989). The lower detachment, not exposed at this location, separates the middle plate from a lower plate of Proterozoic, amphibolite grade core complex metamorphic rocks that are tentatively correlated with the Johnnie Formation (McKague et al., 1989) and which are exposed about 1.6 km southwest of the Old Bullfrog Mine. The Tertiary volcanic units are strongly brecciated and contain a stockwork of quartz veining, at least some of which show chalcedony banding. This banding suggests pulses of (low-temperature?) fluid movement rather than single-shot hydrothermal (high-temperature) intrusions. Brecciation is intense, and even the quartz veins show evidence of intense brecciation at a fine scale. This "mini-chaos" appears similar in deformational behavior to the brittlely deformed carbonate observed in the Amargosa Chaos. A difference at this location is that permeation of the fractured mass by silica-rich solutions was ubiquitous,

while no similar veining was noted in the observed exposures of Amargosa Chaos. It is worth noting that the Old Bullfrog Mine was also an area "saturated" with disseminated gold above and below the upper detachment surface, which indicates movement of mineralized solutions at this locale. These associations suggest the system was fractured sufficiently to allow permeation of available fluids into the rocks, although the system now must be at least partially "healed" by precipitation of minerals in fractures. Effects on groundwater flow systems may have occurred because of development of preferential pathways formed by detachment-related fracturing. Such fracturing may be sufficiently extensive to require consideration of potential effects on regional and local hydrology when hydrologic models are being constructed for YM.

Based on the field observations from the extensional detachment deformation in the Amargosa Chaos and at the Old Bullfrog Mine, extensional detachment faulting is capable of producing very high fracture permeability in carbonate sedimentary rocks. The fracture porosity may be filled by veins or may remain open, depending on the presence of fluids, the saturation state of fluids present with respect to soluble minerals, operative deformation mechanisms, and temperature and pressure conditions. Fault zones may act either as conduits or barriers to fluid flow. More thorough field investigations in the southern Black Mountains (planned for FY95) may reveal additional information on style of deformation with respect to structural geometry, finite strain, and displacement magnitude.

8.2.4 Natural Selection of Faults

In a state of homogeneous stress at a point, the equations for normal and shear stress components across any arbitrarily oriented surface imply that the ratio of these two components is a function of the ratio of the principal stresses. Classical fracture analysis predicts that failure or slip or both will occur on a surface when the resolved shear stress component equals or just exceeds some critical value. This value is determined by the "cohesive strength" of the material and the frictional resistance to sliding along that surface. For this analysis, uniformly distributed fractures are assumed to exist in the earth's crust. Thus, cohesion is not considered here.

The functions that describe the stress values are continuous. Although some surfaces are optimally

oriented for failure or slip, there are surfaces with orientations other than those exactly optimal that may also be utilized for slip. This observation is analogous to saying that, for any given environmental/ecological niche, some theoretically perfect biological adaptation may exist, but that in reality some spectrum of organisms can fill the niche.

The equations that give the normal and shear stress components for arbitrarily oriented surfaces in a state of three-dimensional homogeneous stress at a point are (after Ramsay 1967):

$$\sigma = \sigma_1 l^2 + \sigma_2 m^2 + \sigma_3 n^2 \quad (8-1)$$

$$\tau = \sqrt{\{(\sigma_1 - \sigma_2)^2 l^2 m^2 + (\sigma_2 - \sigma_3)^2 m^2 n^2 + (\sigma_3 - \sigma_1)^2 n^2 l^2\}} \quad (8-2)$$

where: σ = normal stress component; τ = shear stress component; $\sigma_1, \sigma_2, \sigma_3$ = maximum, intermediate, and least principal compressive stresses; and l, m, n = direction cosines of the normal to the surface of interest with respect to the principal stress axes.

If we assume that the earth's crust contains a large number of fractures that are evenly (or randomly) distributed both areally and in orientation, then the tendency for any surface to slip is described by the ratio between shear and normal stress components across it:

$$\tau / \sigma = f(\sigma_1, \sigma_2, \sigma_3, l, m, n) \quad (8-3)$$

This slip tendency varies with both stress state, as defined by the principal stresses, and orientation of the surface under consideration. Figure 8-6 graphically illustrates a range of solutions to Eq. (8-3). Figures 8-6 and 8-7 are lower-hemisphere stereographic projections of normals to potential slip surfaces. Dots represent intersections of normals with the lower-hemisphere, as viewed from above. Dots are sized proportional to slip tendency.

For any given stress state, as defined by the principal compressive stresses, any fracture surface will have a slip tendency that varies with the orientation of the surface. The significance of this statement is that real materials will develop a population of slip surfaces that reflect this distribution. In other words, a real fault system developed under conditions approximating a homogeneous state of stress will contain faults with variable orientations and slip amounts. The most

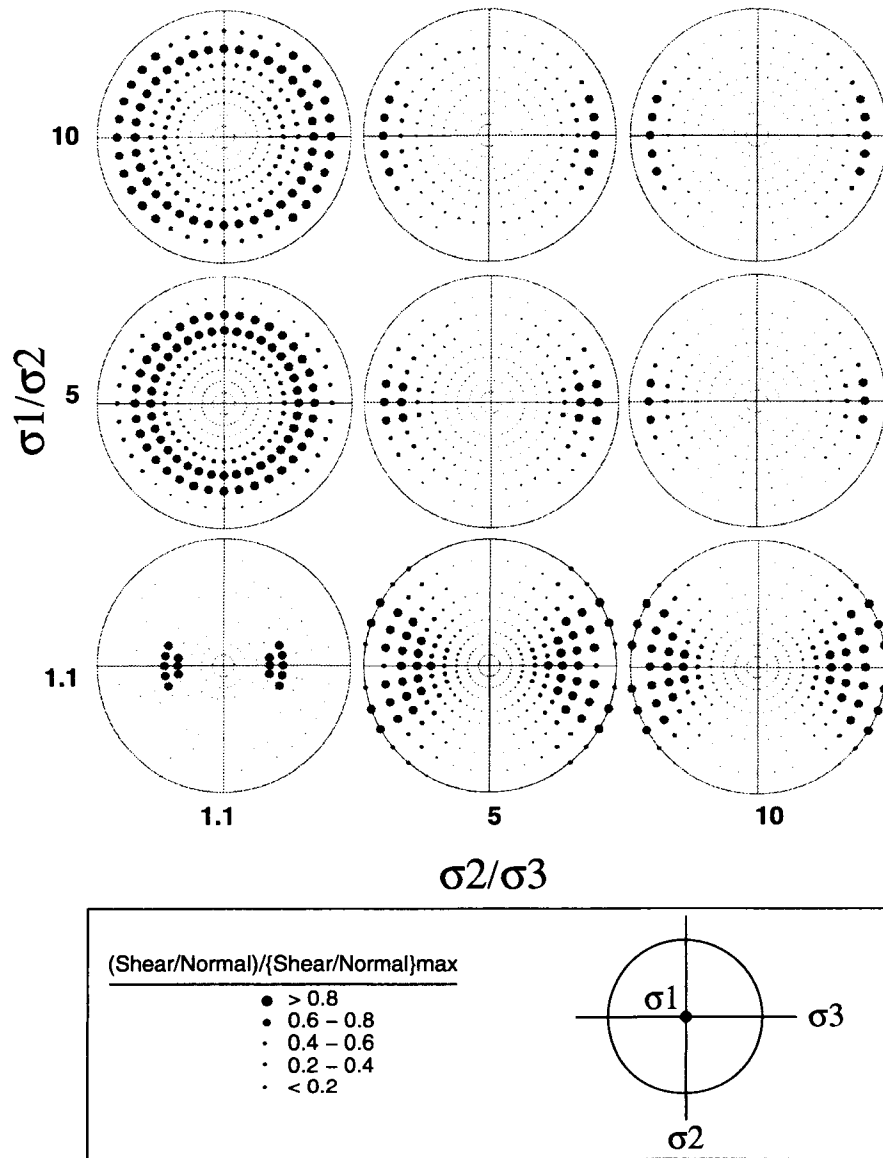


Figure 8-6. Graphical representation of solutions to Eq. (8-3) for the case where σ_1 is vertical, σ_2 is horizontal and oriented N-S, and σ_3 is horizontal and E-W. The inset circles are lower hemisphere, equal-angle stereographic projections of the poles to surfaces in a three-space. The poles are coded according to their slip tendency (τ/σ): the large dots are those surfaces for which the slip tendency exceeds 80 percent of the maximum slip tendency developed in that stress condition; the medium dots are those surfaces for which slip tendency is between 60 and 79 percent of the maximum slip tendency in that stress condition; and the small dots represent surfaces that have slip tendencies lower than 59 percent of the maximum. The stereographic projections are positioned in σ_1/σ_2 , σ_2/σ_3 space appropriately for the stress conditions that they represent.

numerous faults and those with the greatest net slip will be closest in orientation to surfaces optimally oriented for slip (maximum value of slip tendency); however, there will be a range of other fault orientations and slip amounts as indicated by the slip tendency spectrum for the applied stress conditions. Figure 8-7 illustrates the fault population that would develop for one set of principal stress conditions. This approach provides a potential technique for predicting which faults, in a known 3D stress field, are most likely to either have slipped relatively recently or to slip in the future. These predictions could be useful for earthquake hazard analysis and for interpretation of conduits for regional groundwater flow.

8.2.5 Stress, Brittle Deformation, and Effects on Transmissivity

Several recent studies have found that *in situ* stress has an effect on the transmissivity of rock, particularly with respect to oil and gas production from reservoirs with significant fracture permeability, and in investigations of potential geothermal reservoirs (e.g., Cornet and Jones, 1994; Meehan, 1994). Two factors, with respect to regional *in situ* stress and fractures, may contribute significantly to transmissivity anisotropy in fractured rock. First, existing fractures that are at a high angle to the maximum horizontal stress may preferentially be closed by the maximum horizontal stress, thereby reducing transmissivity parallel to the minimum *in situ* stress. Second, new fractures tend to form in orientations that are perpendicular (mode 1 tensile fractures) or at a relatively low oblique angle (<45°; mode 2 shear fractures) to the maximum horizontal stress. In either case, the *in situ* stress exercises direct control on the bulk transmissivity of the rock, and the transmissivity will tend to be relatively higher parallel to the maximum horizontal stress, decreased parallel to the minimum horizontal stress, or both. At relatively shallow depths, subvertical fractures tend to stand open because the confining stress is insufficient to close them. Hydrostatic pressure can open preferentially oriented fractures, and at the Nevada Test Site (NTS) there is some evidence that the weight of the drilling column water was sufficient to overcome the minimum *in situ* stress and cause hydraulic fracturing (Stock et al., 1985).

Regional *in situ* stress data for the Basin and Range Province (Zoback and Zoback, 1980; Zoback et al., 1981; Zoback, 1989) have recently been compiled in

a common format with data from throughout the world as part of the World Stress Map Project (Zoback, 1992; Zoback et al., 1992). *In situ* stress data from the World Stress Map for part of the western Basin and Range Province centered on the YM area are presented in Figure 8-8 and illustrate that the azimuth of the maximum horizontal stress varies around a general NE-SW trend. Normal, strike-slip, and thrust-faulting stress regimes are defined on the basis of the orientation of the maximum (σ_1), intermediate (σ_2), and minimum (σ_3) *in situ* stresses. The normal faulting regime is typified by vertical σ_1 and horizontal σ_2 and σ_3 . The strike-slip faulting regime is characterized by vertical σ_2 , and horizontal σ_1 and σ_3 . The thrust-faulting regime is distinguished by σ_3 being vertical and σ_1 and σ_2 having horizontal orientations. The regional *in situ* stress data for the western Basin and Range Province indicate normal and strike-slip faulting stress regimes.

A comparison of maximum horizontal stress (Zoback, 1992; Zoback et al., 1992) and regional groundwater flow (Wittmeyer et al., 1994) in the YM region is presented in Figure 8-8. The dominant regional groundwater flow is from north to south, as indicated by the arrows in Figure 8-8. Flow is dominantly from the topographically higher areas of recharge in the north to the topographically lower areas of discharge in the south, and is strongly influenced by the structural geometry of the regional aquifer system. The subregional flow arrows locally deviate from the regional pattern and show reasonable agreement with the maximum horizontal stress orientations. Two locations in particular show close agreement between *in situ* stress and the interpreted regional flow pattern: (i) southern Yucca Flat, and (ii) the Death Valley region. A more detailed analysis of stress and flow orientations in Yucca Flat (Figure 10-3), in Chapter 10 on Regional Hydrology Research, involves determining the azimuth of maximum horizontal stress (Figure 10-4) and modeling the effects of anisotropic transmissivity aligned parallel to the maximum horizontal stress (Figures 10-5 through 10-11). These modeling studies show that the interpretation of flow direction can be considerably different when the possible effects of *in situ* stress and resultant transmissivity are included. Death Valley is an important area of discharge for the regional aquifer system. Groundwater flows beneath the Funeral Mountains and the Black Mountains from the Amargosa Valley into Death Valley. Flow directions apparently bend in a clockwise direction as flow crosses the mountain ranges from the east into Death Valley

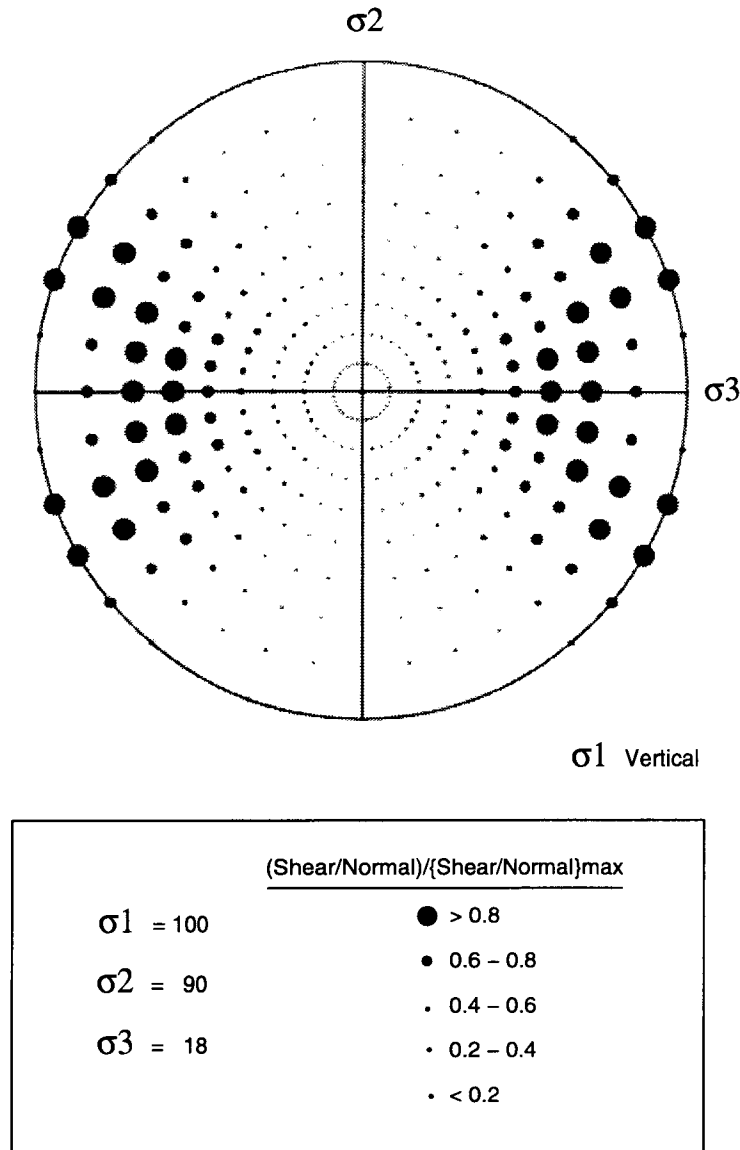


Figure 8-7. Lower hemisphere, equal-angle projection of the poles to surfaces within a three-space representing the solution to Eq. (8-3) for the case where σ_1 is vertical and equal to 100 units; σ_2 is horizontal and oriented N-S, equal to 90 units, and σ_3 is horizontal and oriented E-W, equal to 18 units. The poles are coded according to their slip tendency (τ/σ); large dots are those surfaces for which the slip tendency exceeds 80 percent of the maximum slip tendency developed in that stress condition; the medium dots are those surfaces for which slip tendency is between 60 and 79 percent of the maximum slip tendency in that stress condition; the small dots represent surfaces that have lower slip tendencies than 59 percent of the maximum. Surfaces that have high slip tendencies form a population that includes pure dip-slip normal faults with dips of 60° to 70° trending NS, oblique-slip faults with dips of 70° to 80° trending NW-SE and NE-SW, and vertical strike-slip faults trending WNW-ESE and ENE-WSW.

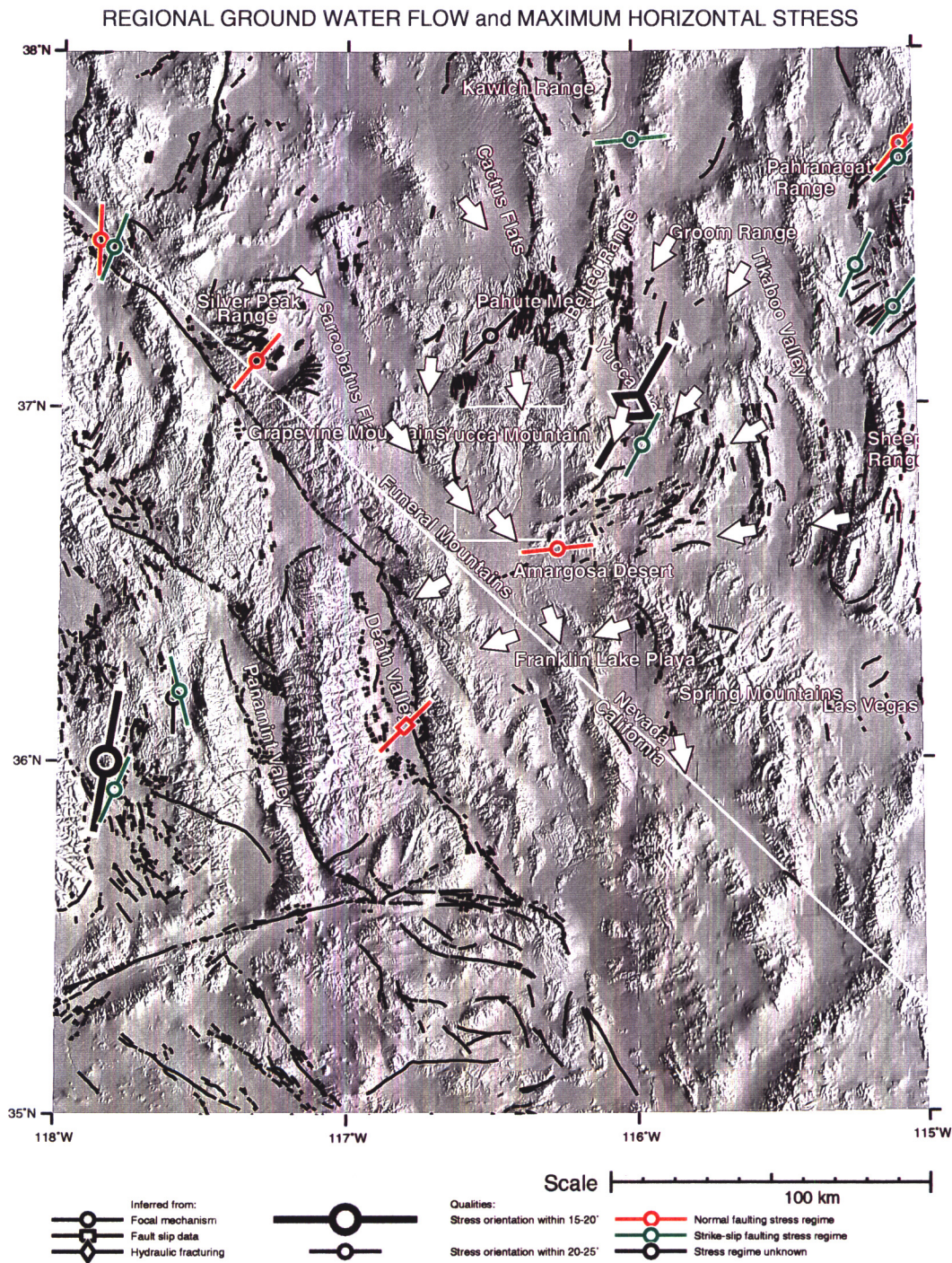


Figure 8-8. Regional groundwater flow and maximum horizontal stress. Flow directions are from Wittmeyer et al. (1994) and are represented by white arrow. Horizontal stress data are from Zoback et al. (1992). Fault traces are from Jennings (1992) in California; and Dohrenwend (1982), Dohrenwend and Moring (1991 a,b,c), Dohrenwend et al. (1991 a-f, 1992 a,b), and Nakata et al. (1982) in Nevada.

(Figure 8-8). Correspondingly, the maximum horizontal stress measurement in Death Valley is rotated clockwise from the more regional pattern of maximum horizontal stress measurements with north-northeast azimuths. Though more detailed study is warranted and underway, the initial comparison of *in situ* stress and groundwater flow shows fairly close agreement between the data sets.

8.3 ASSESSMENT OF PROGRESS TOWARD MEETING PROJECT OBJECTIVES

Compilation of data on tectonics, faulting, and seismicity into the Tectonics GIS and critical review of the compiled tectonic data are proceeding on schedule. Regional data sets compiled into the GIS to date include: digital terrain elevation, Quaternary and Tertiary faults, *in situ* stress, historic earthquakes, conodont color alteration indices, and volcanic fields. Compilation of data on fault activity (e.g., fault orientation, total displacement, slip direction, slip rate, recurrence interval, date of last major earthquake, associated earthquake magnitudes, and length of surface rupture) into the GIS is underway and will be a major emphasis of the next reporting period.

Field work to date has included one trip to the Death Valley region (Black Mountains area), and involvement in the 1993 GPS campaign which was discussed in the last semi-annual report (Young and Stirewalt, 1993). Field work to study possible interaction of faulting and magma migration in the San Francisco Volcanic Field (AZ) is planned for FY94 and 95. Regional tectonic modeling is proceeding at a slower rate than originally scheduled; however, modeling efforts are expected to increase at the beginning of FY95.

Data and references compiled by Tectonics Research project staff have been used to develop Compliance Determination Strategies (CDSs) on Structural Deformation [License Application Review Plan (LARP) No. 3.2.1.5], Evidence of Igneous Activity (LARP No. 3.2.1.9), and Structural Deformation and Groundwater (LARP No. 3.2.2.8). Digital terrain models, geographic data, Quaternary fault coverage, and *in situ* stress data compiled by the Tectonics Research Project, along with visualization methods developed for tectonics research, are also being used in a collaborative effort with the Regional Hydrology Research Project to

study groundwater flow in the regional carbonate aquifer.

8.4 PLANS FOR NEXT REPORTING PERIOD

The efforts of the Regional Tectonics Research Project during the next reporting period will focus on Task 3 (Critical review of compiled tectonic data) and Task 4 (Field investigations). Tasks 3 and 4 are scheduled to end in September 1994. Task 3 is planned to culminate in a NUREG.

Regional tectonic modeling activity will be increased during the next reporting period, with planned emphasis on the deep structural geometry in the greater Death Valley region and the structural geometry and tectonic history of Bare Mountain. Specific activities that are planned to address these issues include: (i) using geometric modeling techniques to interpret deep structural geometry, (ii) using analog modeling to produce 3-D fault geometries that can be analyzed in three dimensions and compared with structures in the greater Death Valley region, and (iii) continuing with fission track and paleomagnetic analyses of Bare Mountain in an attempt to constrain the 3-D displacement paths of Bare Mountain.

Collaboration between the Tectonics Research project, Volcanism Research, and Investigation of Issues Related to Geology and Geophysics for the Division of Waste Management (DWM) is expected to increase during the next reporting period. This collaborative research will initially focus on identifying field examples of demonstrable fault and dike interaction at different depths, including faults and cinder cones coexisting at the surface.

Integrated work between the Regional Tectonics Research and Regional Hydrology Research projects will continue during the next reporting period. The potential effects of *in situ* stress on transmissivity and regional groundwater flow will continue to be investigated in the current collaborative effort. Also, efforts towards building a 3-D model of the regional carbonate aquifer system in the greater Death Valley region will continue.

8.5 REFERENCES

- Anderson, J.G., J.N. Brune, J.N. Louie, Y. Zeng, M. Savage, G. Yu, Q. Chen, and D. dePolo. 1994. Seismicity in the western Great Basin apparently triggered by the Landers, California, earthquake, 28 June 1992. *Bulletin of the Seismological Society of America* 84(3): 863–891.
- Arrowsmith, R.J., and D.D. Rhodes. 1994. Original forms and initial modifications of the Galway Lake Road scarp formed along the Emerson Fault during the 28 June 1992 Landers, California, Earthquake. *Bulletin of the Seismological Society of America* 84(3): 511–527.
- Bodin, P., and J. Gomberg. 1994. Triggered seismicity and deformation between the Landers, California, and Little Skull Mountain, Nevada, earthquakes. *Bulletin of the Seismological Society of America* 84(3): 835–843.
- Burchfiel, B.C., and J.H. Stewart. 1966. "Pull-apart" origin of the central segment of Death Valley, California. *Geological Society of America Bulletin* 77: 439–441.
- Burchfiel, B.C., and B.P. Wernicke. 1989. Spring Mountains breakaway zone, Amargosa Chaos, and the Death Valley pull-apart basin. Extensional tectonics in the Basin and Range Province between the Southern Sierra Nevada and the Colorado Plateau. *Field Trip Guidebook T138. 28th International Geological Congress*. Washington, DC: American Geophysical Union: 39–45.
- Carr, W.J. 1990. Styles of extension in the Nevada Test Site region, southern Walker Lane Belt — An integration of volcano-tectonic and detachment fault models. Basin and Range Extensional Tectonics near the latitude of Las Vegas, Nevada. B.P. Wernicke, ed. *Geological Society of America Memoir* 176: 283–303.
- Cornet, F.H., and R. Jones. 1994. Field evidences on the orientation of forced water flow with respect to the regional principal stress directions. *Rock Mechanics*. Nelson and Laubach, eds. Rotterdam: Balkema: 61–69.
- Dohrenwend, J.C. 1982. *Surficial Geologic Map of the Walker Lake 1° by 2° Quadrangle, Nevada—California. Scale 1:250,000*. U.S. Geological Survey Miscellaneous Field Studies Map MF-1382-C. Reston, VA: U.S. Geological Survey.
- Dohrenwend, J.C., and B.C. Moring. 1991a. *Reconnaissance Photogeologic Map of Young Faults in the Vya 1° by 2° Quadrangle, Nevada, Oregon, and California. Scale 1:250,000*. U.S. Geological Survey Miscellaneous Field Studies Map MF-2174. Reston, VA: U.S. Geological Survey.
- Dohrenwend, J.C., and B.C. Moring. 1991b. *Reconnaissance Photogeologic Map of Young Faults in the Winnemucca 1° by 2° Quadrangle, Nevada, Oregon, and California. Scale 1:250,000*. U.S. Geological Survey Miscellaneous Field Studies Map MF-2175. Reston, VA: U.S. Geological Survey.
- Dohrenwend, J.C., and B.C. Moring. 1991c. *Reconnaissance Photogeologic Map of Young Faults in the McDermitt 1° by 2° Quadrangle, Nevada, Oregon, and Idaho. Scale 1:250,000*. U.S. Geological Survey Miscellaneous Field Studies Map MF-2177. Reston, VA: U.S. Geological Survey.
- Dohrenwend, J.C., M.A. McKittrick, and B.C. Moring. 1991a. *Reconnaissance Photogeologic Map of Young Faults in the Lovelock 1° by 2° Quadrangle, Nevada and California. Scale 1:250,000*. U.S. Geological Survey Miscellaneous Field Studies Map MF-2178. Reston, VA: U.S. Geological Survey.
- Dohrenwend, J.C., M.A. McKittrick, and B.C. Moring. 1991b. *Reconnaissance Photogeologic Map of Young Faults in the Wells 1° by 2° Quadrangle, Nevada, Utah, and Idaho. Scale 1:250,000*. U.S. Geological Survey Miscellaneous Field Studies Map MF-2184. Reston, VA: U.S. Geological Survey.
- Dohrenwend, J.C., C.M. Menges, B.A. Schell, and B.C. Moring. 1991c. *Reconnaissance Photogeologic Map of Young Faults in the Las Vegas 1° by 2° Quadrangle, Nevada, California, and Arizona*.

- Scale 1:250,000. U.S. Geological Survey Miscellaneous Field Studies Map MF-2182. Reston, VA: U.S. Geological Survey.
- Dohrenwend, J.C., B.A. Schell, and B.C. Moring. 1991d. *Reconnaissance Photogeologic Map of Young Faults in the Elko 1° by 2° Quadrangle, Nevada and Utah. Scale 1:250,000.* U.S. Geological Survey Miscellaneous Field Studies Map MF-2179. Reston, VA: U.S. Geological Survey.
- Dohrenwend, J.C., B.A. Schell, and B.C. Moring. 1991e. *Reconnaissance Photogeologic Map of Young Faults in the Lund 1° by 2° Quadrangle, Nevada and Utah. Scale 1:250,000.* U.S. Geological Survey Miscellaneous Field Studies Map MF-2180. Reston, VA: U.S. Geological Survey.
- Dohrenwend, J.C., B.A. Schell, and B.C. Moring. 1991f. *Reconnaissance Photogeologic Map of Young Faults in the Ely 1° by 2° Quadrangle, Nevada and Utah. Scale 1:250,000.* U.S. Geological Survey Miscellaneous Field Studies Map MF-2181. Reston, VA: U.S. Geological Survey.
- Dohrenwend, J.C., B.A. Schell, M.A. McKittrick, and B.C. Moring. 1992a. *Reconnaissance Photogeologic Map of Young Faults in the Goldfield 1° by 2° Quadrangle, Nevada and California. Scale 1:250,000.* U.S. Geological Survey Miscellaneous Field Studies Map MF-2183. Reston, VA: U.S. Geological Survey.
- Dohrenwend, J.C., B.A. Schell, and B.C. Moring. 1992b. *Reconnaissance Photogeologic Map of Young Faults in the Millett 1° by 2° Quadrangle, Nevada. Scale 1:250,000.* U.S. Geological Survey Miscellaneous Field Studies Map MF-2176. Reston, VA: U.S. Geological Survey.
- Doser, D. 1986. Earthquake processes in the Rainbow Mountain-Fairview Peak-Dixie Valley, Nevada, region 1954–1959. *Journal of Geophysical Research* 91(B12): 12,572–12,586.
- Dreger, D.S. 1994. Investigation of the rupture process of the 28 June 1992 Landers earthquake utilizing TERRAscope. *Bulletin of the Seismological Society of America* 84(3): 713–724.
- Gomberg, J., and P. Bodin. 1994. Triggering of the Ms=5.4 Little Skull Mountain, Nevada, earthquake with dynamic strains. *Bulletin of the Seismological Society of America* 84(3): 844–853.
- Hart, E.W., W.A. Bryant, and J.A. Treiman. 1993. Surface faulting associated with the June 1992 Landers earthquake, California. *California Geology* 46(1): 10–16.
- Hill, D.P., P.A. Reasenber, A. Michael, W.J. Arabaz, G. Beroza, D. Brumbaugh, J.N. Brune, R. Castro, S. Davis, D. dePolo, W.L. Ellsworth, J. Gomberg, S. Harmsen, L. House, S.M. Jackson, M.J.S. Johnston, L. Jones, R. Keller, S. Malone, L. Munguia, S. Nava, J.C. Pechmann, A. Sanford, R.W. Simpson, R.B. Smith, M. Stark, M. Stickney, A. Vidal, S. Walter, V. Wong, and J. Zollweg. 1993. Seismicity remotely triggered by the magnitude 7.3 Landers, California, earthquake. *Science* 260: 1,617–1,623.
- Holm, D.K., and B.P. Wernicke. 1990. Black Mountains crustal section, Death Valley extended terrain, California. *Geology* 18: 520–523.
- Hudnut, K.W., Y. Bock, M. Cline, P. Fang, Y. Feng, J. Freymuller, X. Ge, W.K. Gross, D. Jackson, M. Kim, N.E. King, J. Langbein, S.C. Larsen, M. Lisowski, Z.-K. Shen, J. Svarc, and J. Zhang. 1994. Co-seismic displacements of the 1992 Landers earthquake sequence. *Bulletin of the Seismological Society of America* 84(3): 625–645.
- Hunt, C.B., and D.R. Mabey. 1966. *Stratigraphy and Structure, Death Valley, California.* U.S. Geological Survey Professional Paper 494-A: Reston, VA: US Geological Survey.
- Irvine, P.J., and R.L. Hill. 1993. Surface rupture along a portion of the Emerson Fault. *California Geology* 46(1): 23–26.

- Jennings, C.W. 1992. *Preliminary Fault Activity Map of California*. DMG Open-File Report 92-03. The Resources Agency, California Department of Conservation, Division of Mines and Geology; 76. Replaces the 1:750,000 scale Fault Map of California, Bulletin 201, California Department of Conservation, Division of Mines and Geology, and the Fault Map of California with location of volcanoes, thermal springs, and thermal wells (Jennings 1975).
- Kanamori, H., H.-K. Thio, D. Dreger, E. Hauksson, and T. Heaton. 1992. Initial investigation of the Landers, California, earthquake of 28 June 1992 using TERRAScope. *Geophysical Research Letters* 19(22): 2,267-2,270.
- McKague, H.L., P.P. Orkild, and S.R. Mattson. 1989. The geology of the Nevada Test Site and surrounding area. Field Trip Guidebook T186. *28th International Geological Congress*. Washington, DC: American Geophysical Union.
- McKenna, L.W., and K.V. Hodges. 1990. Constraints on the kinematics and timing of late Miocene-Recent extension between the Panamint and Black Mountains, southeastern California. *Basin and Range Extensional Tectonics near the Latitude of Las Vegas, Nevada*. B.P. Wernicke, ed. Geological Society of America Memoir: 176: 363-376.
- Meehan, D.N. 1994. Rock mechanics issues in petroleum engineering. *Rock Mechanics*. Nelson and Laubach, eds. Rotterdam: Balkema: 3-17.
- Monastersky, R. 1993. Lessons from Landers. *Earth* 2 (2): 40-47.
- Nakata, J.K., C.M. Wentworth, and M.N. Machette. 1982. *Quaternary Fault Map of the Basin and Range and Rio Grande Rift Provinces, Western United States*. U.S. Geological Survey Open-File Report 82-579. Washington, DC.
- Noble, L.F. 1941. Structural features of the Virgin Spring area, Death Valley, California. *Geological Society of America Bulletin* 52: 941-999.
- Oldow, J.S. 1992. Late Cenozoic displacement partitioning in the northwestern Great Basin. *Walker Lane Symposium: Structure, Tectonics and Mineralization of the Walker Lane*. Geological Society of Nevada.
- Prave, A.R., and L.A. Wright. 1986a. Isopach pattern of the Lower Cambrian Zabriskie Quartzite, Death Valley Region, California-Nevada: How useful in tectonic reconstructions? *Geology* 14: 251-254.
- Prave, A.R., and L.A. Wright. 1986b. Reply to Comment on "Isopach pattern of the Lower Cambrian Zabriskie Quartzite, Death Valley Region, California-Nevada: How useful in tectonic reconstructions?" *Geology* 14: 811-812
- Phillips, W.J. 1972. Hydraulic faulting and investigation. *Journal of Geological Society of London* 128: 337-359.
- Ramsay, J.G. 1967. *Folding and Fracturing of Rocks*. McGraw-Hill. New York, NY.
- Reheis, M.C. 1994. Holocene faulting along the central Fish Lake Valley Fault Zone, California and Nevada. *Geological Society of America Abstracts with Programs* 26(2), 83.
- Reynolds, R.E. 1993. Road guide Landers: Earthquakes and aftershocks. R.E. Reynolds, ed. *San Bernardino County Museum Quarterly*. San Bernardino, CA: San Bernardino County Museum: 40(1): 7-39.
- Rogers, A.M., S.C. Harmsen, E.J. Corbett, K. Priestly, and D. dePolo. 1991. The seismicity of Nevada and some adjacent parts of the Great Basin. *Neotectonics of North America*. D.B. Slemmons, E.R. Engdahl, M.D. Zoback, and D.D. Blackwell, eds. Boulder, CO: Geological Society of America. 1: 153-184.
- Roquemore, G.R., and G.W. Simila. 1994. Aftershocks from the June 28, 1992, Landers earthquake: Northern Mojave Desert to the Coso Volcanic Field, California. *Bulletin of the Seismological Society of America* 84(3): 854-862.

- Scott R.B. 1990. Tectonic setting of Yucca Mountain, southwest Nevada. B.P. Wernicke, ed. Basin and Range Extensional Tectonics near the Latitude of Las Vegas, Nevada. *Geological Society of America Memoir* 176: 251–282.
- Sibson, R.H. 1986. Brecciation processes in fault zones: Inferences from earthquake rupturing. *Pageoph* 124(1/2): 159–175.
- Sibson, R.H. 1987. Earthquake rupturing as a mineralizing agent in hydrothermal systems. *Geology* 15(8): 701–704.
- Sieh, K., L. Jones, E. Hauksson, K. Hudnut, D. Eberhart-Phillips, T. Heaton, S. Hough, K. Hutton, H. Kanamori, A. Lilje, S. Lindvall, S.F. McGill, J. Mori, C. Rubin, J.A. Spotila, J. Stock, H.K. Thio, J. Treiman, B. Wernicke, and J. Zachariasen. 1993. Near-field investigations of the Landers earthquake sequence, April to July 1992. *Science* 260: 171–176.
- Slemmons, D.B. 1957. Geological effects of the Dixie Valley-Fairview Peak, Nevada, earthquakes of December 16, 1954. *Bulletin of the Seismological Society of America* 47: 353–375.
- Smith, R.B., and W.J. Arabasz. 1991. Seismicity of the Intermountain Seismic Belt. *Neotectonics of North America*. D.B. Slemmons, E.R. Engdahl, M.D. Zoback, and D.D. Blackwell, eds. Boulder, CO: Geological Society of America Decade Map Volume 1: 185–228.
- Sowers, J.M., J.R. Unruh, W.R. Lettis, and T.D. Rubin. 1994. Relationship of the Kickapoo Fault to the Johnson Valley and Homestead Valley Faults, San Bernardino County, California. *Bulletin of the Seismological Society of America* 84(3): 528–536.
- Stewart, J.H. 1983. Extensional tectonics in the Death Valley area, California: Transport of the Panamint Range structural block 80 km northward. *Geology* 11: 153–157.
- Stock, J.M., J.H. Healy, S.H. Hickman, and M.D. Zoback. Hydraulic fracturing stress measurements at Yucca Mountain, Nevada, and relationship to regional stress field. *Journal of Geophysical Research* 90 (B10): 8,691–8,706.
- Topozada, T.R. 1993. The Landers–Big Bear earthquake sequence and its felt effects. *California Geology* 46(1): 3–9.
- Troxel, B.W. 1986. Significance of Quaternary fault patterns, west side of the Mormon Point turtleback, southern Death Valley, California—A model of listric normal faults. Quaternary Tectonics of Southern Death Valley. *Friends of the Pleistocene–Pacific Cell*: 37–39.
- Troxel, B.W., and L.A. Wright. 1987. *Tertiary extensional features, Death Valley region, eastern California*. Geological Society of America Centennial Field Guide, Cordilleran Section: 121–132.
- Wiemer, S., and M. Wyss. 1994. Seismic quiescence (M=7.5) and Big Bear (M=6.5) 1992 earthquakes. *Bulletin of the Seismological Society of America* 84(3): 900–916.
- Wittmeyer, G., W.M. Murphy, and V. Kapoor. 1994. Regional hydrogeologic processes in the Death Valley Region. *NRC High-Level Radioactive Waste Research at the Center for Nuclear Waste Regulatory Analyses, July-December 1993*. CNWRA 93-02S. B. Sagar, ed. San Antonio, TX: Center for Nuclear Waste Regulatory Analyses: 11-1 to 11-19.
- Wright, L.A., T.L. Pavlis, M.A. Ellis, R.A. Thompson, E.H. DeWitt, M.G. Miller, B.W. Troxel, J.K. Otton, and L.F. Serpa. 1991. Cenozoic magmatic and tectonic evolution of east-central Death Valley Region, California. *Geologic Excursions in Southern California and Mexico*. M.J. Walawender and B.B. Hanan, eds. *Geological Society of America: 1991 Annual Meeting Guidebook*. San Diego, CA: 93–127.

- Wright, L.A., and B.W. Troxel. 1967. Limitations on right-lateral, strike-slip displacement, Death Valley and Furnace Creek fault zones, California. *Geological Society of America Bulletin* 78: 933-958.
- Young, S.R., and G.L. Stirewalt. 1993. Tectonics. *NRC High-Level Radioactive Waste Research at the Center for Nuclear Waste Regulatory Analyses, July-December 1993*. B. Sagar, ed. CNWRA 93-02S. San Antonio, TX: Center for Nuclear Waste Regulatory Analyses: 9-1 to 9-20.
- Young, S.R., G.L. Stirewalt, and D.A. Ferrill. 1994. *Project Plan for Research on Tectonic Processes in the Central Basin and Range Region*. CNWRA Project Plan, Rev 0, Change 6. San Antonio, TX: Center for Nuclear Waste Regulatory Analyses.
- Young, S.R., G.L. Stirewalt, and A.P. Morris. 1992. *Geometric Models of Faulting at Yucca Mountain*. CNWRA 92-008. San Antonio, TX: Center for Nuclear Waste Regulatory Analyses.
- Zhang, P., D.B. Slemmons, and F. Mao. 1991. Geometric pattern, rupture termination and fault segmentation of the Dixie Valley-Pleasant Valley active normal fault system, Nevada. *U.S.A. Journal of Structural Geology* 13(2): 165-176.
- Zoback, M.L. 1989. State of stress and modern deformation of the northern Basin and Range Province. *Journal of Geophysical Research* 94(B6): 7,105-7,128.
- Zoback, M.L. 1992. First- and second-order patterns of stress in the lithosphere: The World stress map project. *Journal of Geophysical Research* 97 (B8): 11,703-11,728.
- Zoback, M.L., R.E. Anderson, and G.A. Thompson. 1981. Cainozoic evolution of the state of stress and style of tectonism of the Basin and Range Province of the western United States. *Philosophical Transactions of the Royal Society of London* A300: 407-434.
- Zoback, M.L., and 36 project participants. 1992. World stress map—maximum horizontal stress orientations. *Journal of Geophysical Research* 87 (B8).
- Zoback, M.L., and M. Zoback. 1980. State of stress in the coterminous United States. *Journal of Geophysical Research* 85(B11): 6,113-6,156.

9 FIELD VOLCANISM RESEARCH

by Charles B. Connor and Brittain E. Hill

Investigators: Charles B. Connor and Brittain E. Hill (CNWRA)

NRC Project Officer: L.A. Kovach

9.1 TECHNICAL OBJECTIVES

The Yucca Mountain region (YMR) has been the site of recurring small volume basaltic eruptions during the last 10 m.y. (Crowe et al., 1983a; Smith et al., 1990). This volcanic activity has led to the formation of numerous cinder cones, eight of which are less than 1.6 m.y. old. These volcanoes likely represent a range of eruptive activity from explosive eruptions to comparatively gentle effusive volcanic eruptions (Valentine et al., 1992; Amos et al., 1983; Walker, 1991; 1993). The technical objectives of the Field Volcanism project are to better characterize the effect of this type of volcanic activity on repository performance and, as a result, better constrain probability models of disruption of the repository. This characterization will be possible through investigation of the: (i) mechanics of mafic cinder cone eruptions, (ii) extent and characteristics of shallow hydrothermal systems and diffuse degassing associated with small-volume mafic eruptions, and (iii) nature of mafic intrusive geometries at repository depths. Successful completion of the Field Volcanism project, which began in April 1993, will require study of Plio-Quaternary cinder cones in the western Great Basin and comparison with modern, recently active cinder cones located elsewhere.

Results of the Field Volcanism project will be used to support specific sections of the License Application Review Plan (LARP). Insight into the possible magnitude of volcanic processes likely to occur in the YMR in the event of further volcanic activity, the areas probably affected, and the likely duration of volcanic activity form an integral part of site characterization activities (evidence of igneous activity as a potentially adverse condition, Section 3.2.1.9; and impact of volcanism on groundwater movement, Section 3.2.2.7), and the description of overall system performance (assessment of compliance with the requirement for cumulative releases of radioactive materials, Section 6.1). Compliance Determination

Strategies (CDSs) for these LARP sections have been prepared, and Compliance Determination Methods (CDMs) are currently under development. The CDSs associated with evidence of Quaternary volcanism are of Type 5, indicating that independent research is needed to evaluate Key Technical Uncertainties (KTUs) associated with volcanism and that volcanism poses a high risk to the U.S. Nuclear Regulatory Commission (NRC) of reaching unwarranted conclusions regarding compliance with 40 CFR Part 191 and 10 CFR 60.122(c)(15). For example, until acceptable methods for the characterization of the likely magnitude and duration of eruptive activity and the determination of the impact of this activity on groundwater and geochemical transport are found, it will be difficult to ascertain compliance with 40 CFR Part 191.

To date, three KTUs related to igneous activity have been identified as part of the CDS concerned with evidence of Quaternary igneous activity. These KTUs are:

- Low resolution of exploration techniques to detect and evaluate igneous features (Type 4)
- Inability to sample igneous features (Type 5)
- Development and use of conceptual tectonic models as related to igneous activity (Type 5).

Evaluation of these KTUs will require detailed safety review supported by analyses (Type 4), and detailed safety review supported by independent tests, analyses, and other investigations (Type 5). Additional KTUs related to igneous activity will likely be identified in a forthcoming CDS on rates of tectonic activity. The Field Volcanism project will address each of these KTUs. For example, Task 4 investigations into geophysical techniques for identifying anomalies related

to subsurface igneous dikes will address uncertainties resulting from the low resolution of exploration techniques, a Type 4 KTU. Many problems in eruption dynamics and the extent of volatile degassing following eruptive activity can only be addressed by comparison of earlier eruptions at recently active cinder cones with those of the YMR. Tasks 2 and 3 in the Field Volcanism project are designed to investigate eruptive activity and degassing, providing independent testing, analysis, and investigation addressing the inability to sample igneous features, a Type 5 KTU.

Successful completion of the Field Volcanism Research Project and efficient integration of results into the LARP will require interaction with the Volcanic Systems of the Basin and Range Research Project (Figure 9-1). This project concentrates on probability model development and the structural setting of volcanism in the Basin and Range. The Geologic Setting Task 425, which is being conducted for the Division of Waste Management (DWM), develops the comparison, evaluation and use of probability models in volcanism and performance assessment projects. For example, the Field Volcanism project will provide data that are critical for review of alternative probability models (Figure 9-1). The Field Volcanism project, together with these associated investigations, will form an integral part of volcanism models in Iterative Performance Assessment (IPA). For example, the effects of development of a shallow diffuse degassing system about a cooling cinder cone and estimates of the area likely to be influenced by such a system are not currently part of IPA models. This integration with Performance Assessment (PA) to evaluate the effects of degassing on repository performance has been formalized as a PA research Task which will begin in FY95, a direct outgrowth of volcanism research (Figure 9-1).

9.2 SIGNIFICANT TECHNICAL ACCOMPLISHMENTS

Activities designed to address issues related to the probability and consequences of igneous activity in the YMR that have been initiated or completed during the last 6 mo include:

- Completion of a review of the seismic tomographic and magnetic methods and their application to the study of small-volume basaltic cinder cone fields

- Development of a research strategy to use tomographic and magnetic methods to investigate basaltic cinder cone alignments
- Completion of a simple model for dike-fracture interaction
- Preliminary study of diffuse degassing at Parícutin Volcano, Mexico
- Comparison of xenocrystic and phenocrystic amphiboles in alkaline basalts
- Acquisition of basaltic rocks collected during the 1975–1976 eruption of the Tolbachik cinder cones
- Continuation of major element and petrographic analysis of basaltic lavas of the WGB

These activities resulted in a Major Milestone (MM), Geophysical Topical Report: Application of Seismic Tomographic and Magnetic Methods to Issues in Basaltic Volcanism (Connor and Sanders, 1994), and a poster session, A Simple Model of Dike-Fracture Interaction, presented at the Spring Meeting of the American Geophysical Union (McDuffie et al., 1994). In addition, a staff perspective was prepared during this period on the technical and regulatory basis for the study of recently active cinder cones (CNWRA Staff, 1994), in support of an earlier Intermediate Milestone on this topic (Connor, 1993).

Here, a summary will be provided of findings on three technical topics that have not been presented elsewhere. These topics are: diffuse degassing at Parícutin Volcano, Mexico; and comparison of xenocrystic and phenocrystic amphiboles in alkaline basalts. A summary of the major findings and recommendations of the MM on seismic tomographic and magnetic methods is provided in Section 9.5, Assessment of Progress.

9.3 DIFFUSE DEGASSING AT PARÍCUTIN VOLCANO, MEXICO

9.3.1 Background

In terms of its growth and development, Parícutin is clearly the historically active cinder cone in

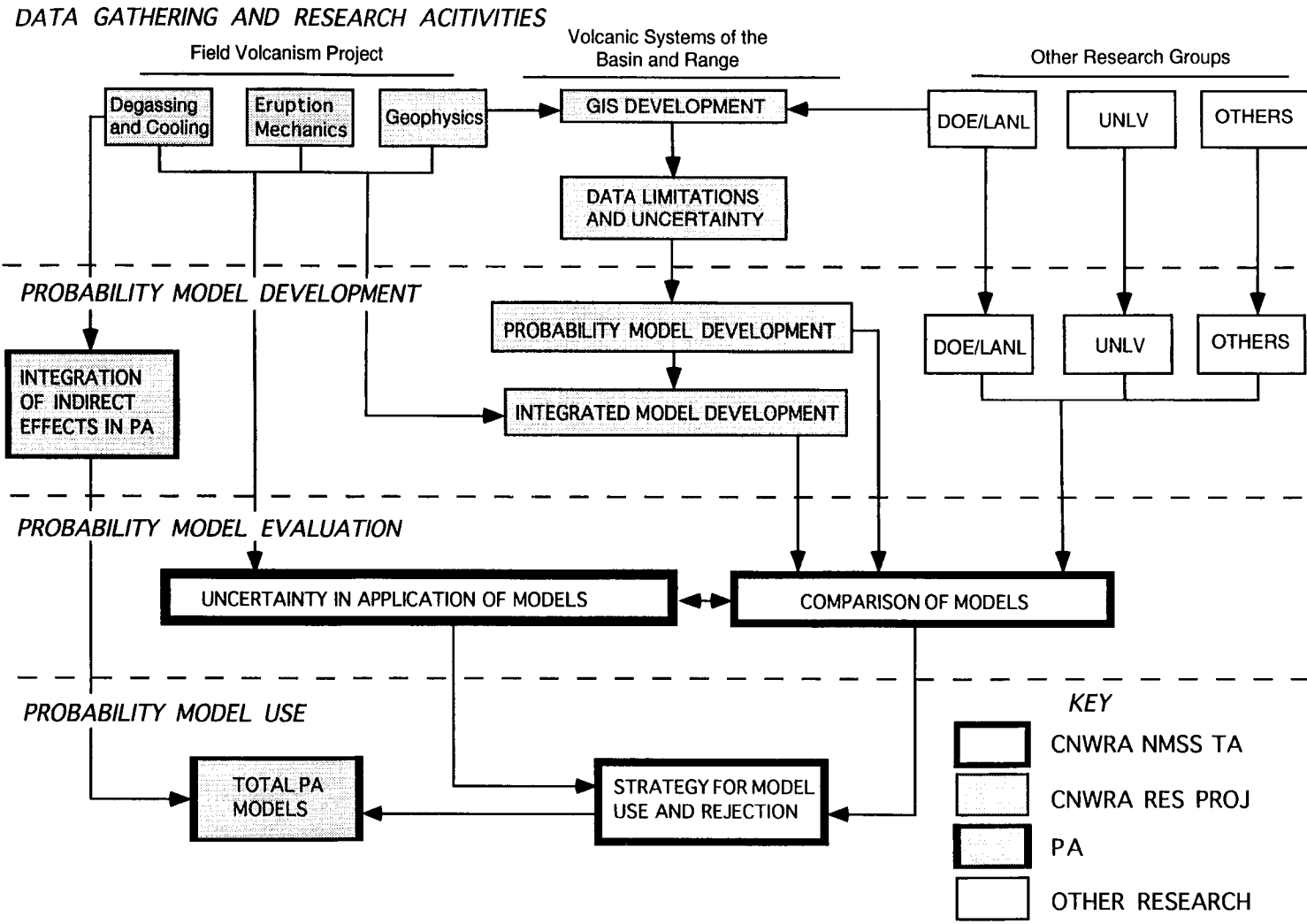


Figure 9-1. Overview of the relationship between tasks in the Field Volcanism Project and other research and technical assistance projects

North America most analogous to those found in the YMR. Parícutin Volcano (19.48°N, 102.25°W) is located in the Michoacán-Guanajuato volcanic field, Mexico, within the TransMexican Volcanic Belt (Williams, 1950; Hasenaka and Carmichael, 1985). There are well over 1,000 cinder cones in this region, in addition to several hundred monogenetic and polycyclic shield volcanoes, composite cones, and maars. Cumulatively, this area is probably the largest active sub-aerial volcanic field on Earth. Parícutin is part of a cluster of approximately 120 cinder cones within the Michoacán-Guanajuato volcanic field (Connor, 1990). All of these cinder cones are believed to be less than 2 m.y. old, and approximately 70 cones in the region are believed to be less than 40,000 yr old, largely based on geomorphic evidence and eight ^{14}C dates (Hasenaka and Carmichael, 1985). Numerous young cinder cones are located in the immediate vicinity of Parícutin (Figure 9-2).

Parícutin formed as a result of eruptive activity that commenced in 1943 and continued through 1952. Details of the Parícutin eruption are summarized by Wilcox (1954). The Parícutin eruption began in February 1943, when hot gases and pyroclastic rocks began erupting from a small fissure in a cultivated field. This pyroclastic activity was preceded by several weeks of seismic activity that was reported to increase in intensity and frequency up until the initiation of the eruptive phase (Wilcox, 1954). Although the eruption lasted 9 yr, most of the central cone was built in the first year of activity, during which time pyroclastic activity was fairly steady (Segerstrom, 1950). During October 1943, a series of new vents formed on a NE-trending line. These vents, located NE and SW of the main cone, were the sites of vigorous explosive and effusive activity, and were alternately active and quiescent until the end of eruptive activity in 1952. According to Wilcox (1954), new satellite vents continued to form as late as 1947. Lava flow effusion ceased at Parícutin in February 1952, and pyroclastic activity declined gradually until it ceased in March 1952. The cinder cone is now approximately 350 m in height, and lava flows from the volcano cover an area of about 24 km². The 9-yr Parícutin eruption produced approximately 1.3 km³ of lava and 0.7 km³ of tephra, a total dense-rock-equivalent volume of 1.32 km³ (McBirney et al., 1987).

The most energetic explosive activity occurred during March–August 1943 (Foshag and Gonzalez, 1956). During this phase of activity, highly convective

ash column heights were maintained at 6 to 8 km above Parícutin and blocks up to 15 m in diameter were ejected from the central crater. During the most energetic explosive activity, ash accumulated to a thickness of 15 cm approximately 6 km from the central cone, and ash fall was reported up to 250 km from Parícutin (Foshag and Gonzalez, 1956). Although the most sustained and intensive pyroclastic activity occurred during the first 2 yr of activity, explosive activity continued through the end of the eruption in 1952.

As is the case with all cinder cone eruptions, volatile content is thought to have been an important control on eruption energetics at Parícutin. Several estimates of the volatile content in Parícutin magmas have been made previously (Fries, 1953; Egger, 1972; Anderson, 1979). Fries (1953) estimated water content exsolved during the eruption by estimating the amount of gas released in the column above the volcano compared with the volume of material erupted. Fries calculated the volatile content to be about 1 wt% using this technique. Egger used phase relations among phenocrysts in Parícutin lavas together with experimental results to estimate water content at about 2.2 percent in Parícutin magmas. Anderson (1979), using melt inclusions in Parícutin lavas, found volatile contents of approximately 1.5 percent by weight. Volatile concentrations of 1 to 2 percent indicate that magmas were likely fragmenting at depths of more than 300 m and ascended as highly erosive gas-magma mixtures from those depths.

Wilcox (1954) reports that xenoliths of gabbro, quartz monzonite, and Tertiary silicic tuffs were common in the eruptive products during the first 2 yr of activity. Parícutin lies on a section of Quaternary basalts of unknown thickness, but likely on the order of several hundred meters thick (Williams, 1950); the thickness of the underlying Tertiary silicic tuffs is also unknown, but is estimated by Williams (1950) to be over 300 m thick in the Parícutin region, based on exposures along the Cupatitzio river about 30 km from Parícutin.

Parícutin continues to degas today, 41 yr after the cessation of eruptive activity. This degassing is extremely weak compared with that observed at many quiescent composite volcanoes, but is also quite sustained, with low mass flow, high-temperature fumaroles remaining stable since at least 1983 (McClelland et al., 1987). Connor (1989) mapped fumaroles and soil Hg anomalies around the main crater

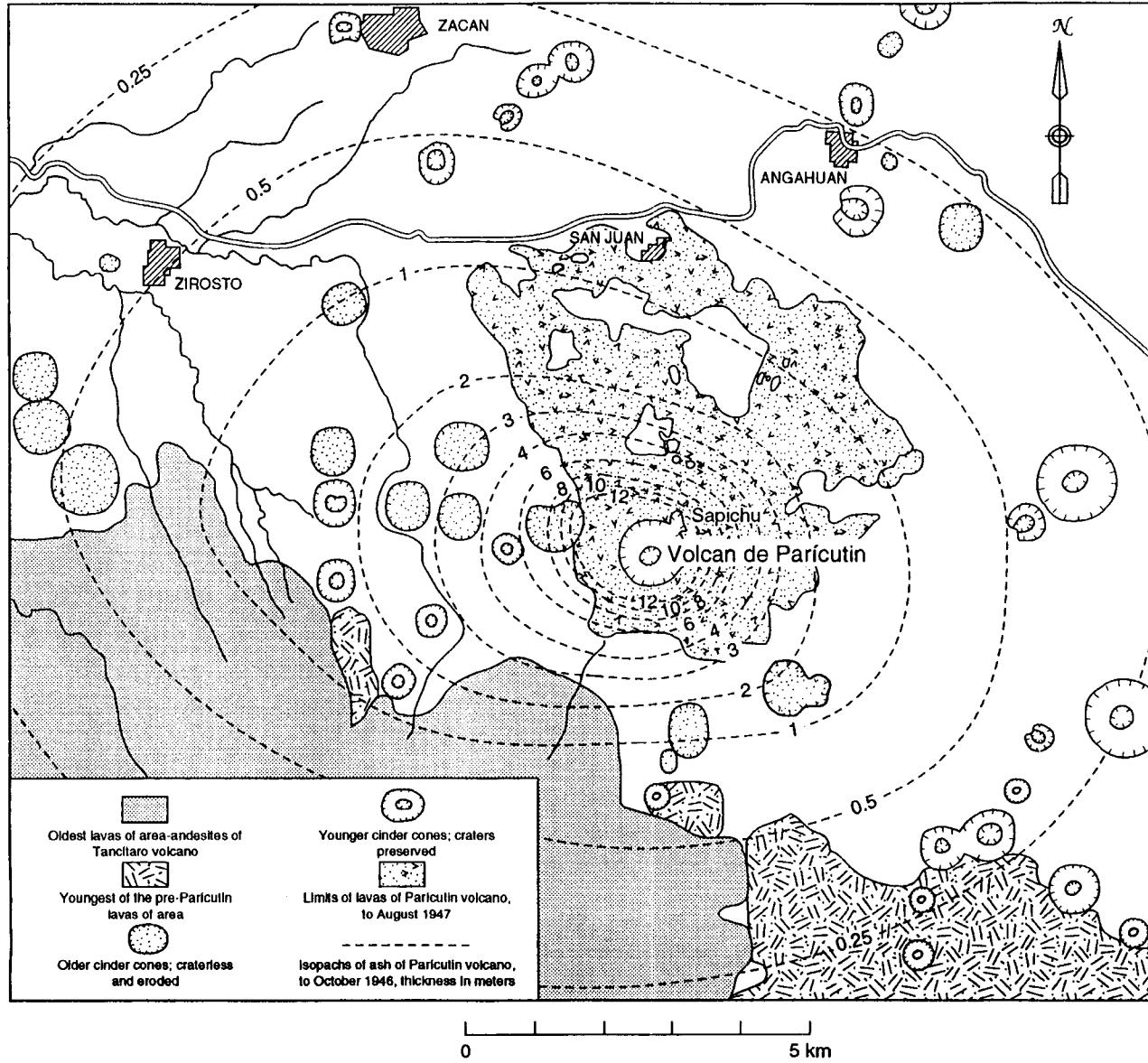


Figure 9-2. Parícutin is surrounded by numerous Quaternary cinder cones. Ash isopachs are in meters.

and Ahuan vent, located SW of the main crater, and the Taqui vent, located NE of the main crater. High-temperature fumaroles are restricted to the Ahuan and Taqui vents. Temperatures at the Ahuan vent have been monitored intermittently since 1983. During this period, temperatures have varied between 473 °C, recorded in November 1985, and 303 °C, recorded in 1991. These fumaroles have low mass flows, and the dominant components of the gas are water vapor, HCl, and Cl₂. A single electrical self-potential traverse across the Ahuan vent, made in 1983, identified a 1.2-volt anomaly. These electrical data, although quite preliminary, may indicate the presence of localized zones of groundwater movement and vaporization in response to high heat flow or the heat flow from the vent, or some combination of the two flow phenomena.

Low-temperature fumaroles (50 to 150 °C) are more widespread, occurring elsewhere on the lava flows, along flow levees, and along the rim of the main crater. Connor (1989) collected approximately 50 soil samples on the SW flank of the volcano, near and around the Ahuan vent. Soil Hg concentrations were found to be anomalously high over an area of at least 1 km² on the SW flank of the volcano, with soil Hg concentrations between 1,200 and 11,000 ppb. These Hg concentrations are comparable to those found in active geothermal systems (e.g., Varekamp and Buseck, 1983; Lescinsky et al., 1987). Mean background concentrations in the Parícutin area, far from the volcano, are 30 ± 24 ppb. Based on Hg distributions, Connor (1989) concluded that convective upwelling of gas occurs over an area of at least 1 km² on and around the SW flank of the volcano. This diffuse degassing is far more widespread at Parícutin than is indicated by the distribution of high-temperature fumaroles or alteration zones, but its areal extent was not determined because of the limited extent of the Hg survey.

9.3.2 Field Work at Parícutin Volcano

Field work was carried out at Parícutin during a 10-day period in late January and early February 1994. The following activities were performed:

- Four fumaroles were monitored continuously during a 4-day period using a Campbell Scientific datalogger
- A total of 84 soil CO₂ samples were collected

- A total of 29 radon stations were established and monitored at intervals over a period of 1 wk
- A total of 16 soil He samples were collected
- 93 soil Hg samples were collected
- An infrared CO₂ analyzer was tested for direct measurement of soil CO₂
- Gas condensates were collected from fumaroles for determination of H and O isotopic composition, and for major element analysis
- Numerous ash samples were collected, primarily from a 2-m deep pit dug in the ash section approximately 800 m from the base of the cone.

Temperature data are shown in Figures 9-3 through 9-5. Temperatures were measured continuously in four fumaroles at the Ahuan vent on the SW flank of the main cone. Temperatures in these fumaroles have been measured to be as high as 473 °C in 1983 and have fallen steadily since that time. The highest temperatures recorded during this field work were about 220 °C (Table 9-1). These fumaroles are located in an alteration zone that measures approximately 100×50 m. The fumaroles do not have a large condensable phase, although flow is audible in these fumaroles. These comparatively high-temperature fumaroles are surrounded by low-temperature fumaroles (40–85 °C) that cover a broad zone around the Ahuan vent, extending up onto the main cone and to some of the surrounding lava flows. These fumaroles appear to emit water vapor. A second zone of higher temperature fumaroles is located at the Taqui vent on the NE flank of the main cone. Fumarole temperatures of up to 280 °C were identified at the Taqui vent. Like the Ahuan vent, these fumaroles are in an extensive alteration zone and surrounded by low-temperature fumaroles. The alteration and sublimate minerals around these fumaroles are sulfur, hematite, sylvite, magnetite, and ilmenite.

Temperatures varied by as much as 40 °C during continuous monitoring (Figure 9-3) and correlated well with atmospheric temperature in some fumaroles. Specifically, temperature variations in the lower temperature fumaroles correlate very well with

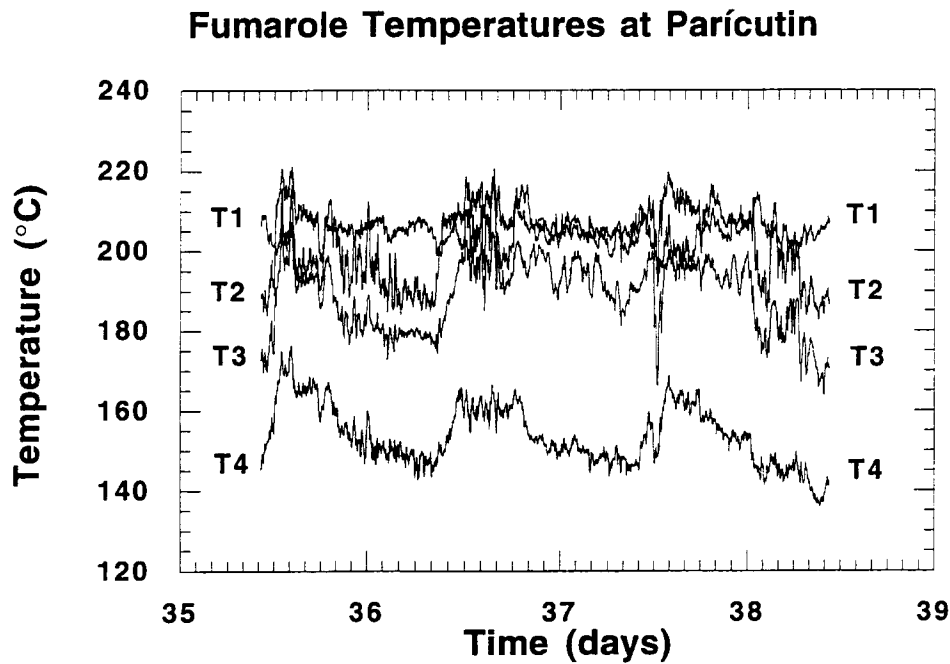


Figure 9-3. Fumarole temperatures measured at the Ahuan vent, Parícutin volcano. Time is in days since January 1, 1994.

atmospheric temperature variation. This correlation was less pronounced in the highest temperature fumaroles located in the central part of the fumarole field (Figure 9-4). Barometric pressure fluctuations have a 12-hr cycle; no large barometric pressure fluctuations occurred during the sample interval. The strong correlation of fumarole temperature and barometric pressure that has been observed at some volcanoes is not observed at Parícutin (Figure 9-5). A preliminary interpretation of this phenomenon is that flow in these fumaroles is driven by a venturi effect, resulting in a good correlation with atmospheric temperature. It is clear from these preliminary results that Parícutin has an active hydrothermal system that is gradually cooling. Additional analysis is planned to clarify the relationship between fumarole temperatures and atmospheric processes.

Soil gas sampling stations were chosen using the following criteria:

- A base station was located far from the volcano in an area thought to be beyond the influence of any hydrothermal activity or diffuse degassing. The base station was located at a campsite, 2 km NW of the

main cone. The location of the base station was determined by Global Positioning Satellite (GPS): 19° 30' 34" N, 102° 16' 1" W.

- Several stations were established on the main cone, at the Ahuan vent, and near the Taqui vent. Samples could not be located on the Taqui vent itself because this blocky vent lacks ash pockets or soil development.
- A sampling traverse was located along a survey line extending southwest from the cone. It was anticipated that soil degassing might be high along this line because of the preferred orientation of vents in a NE-SW trend at Parícutin.
- A sampling traverse was established trending NW orthogonal to the apparent structural control on vent alignment in the area.
- Other stations were established around the base of the cone and extending south and southeast of the cone.

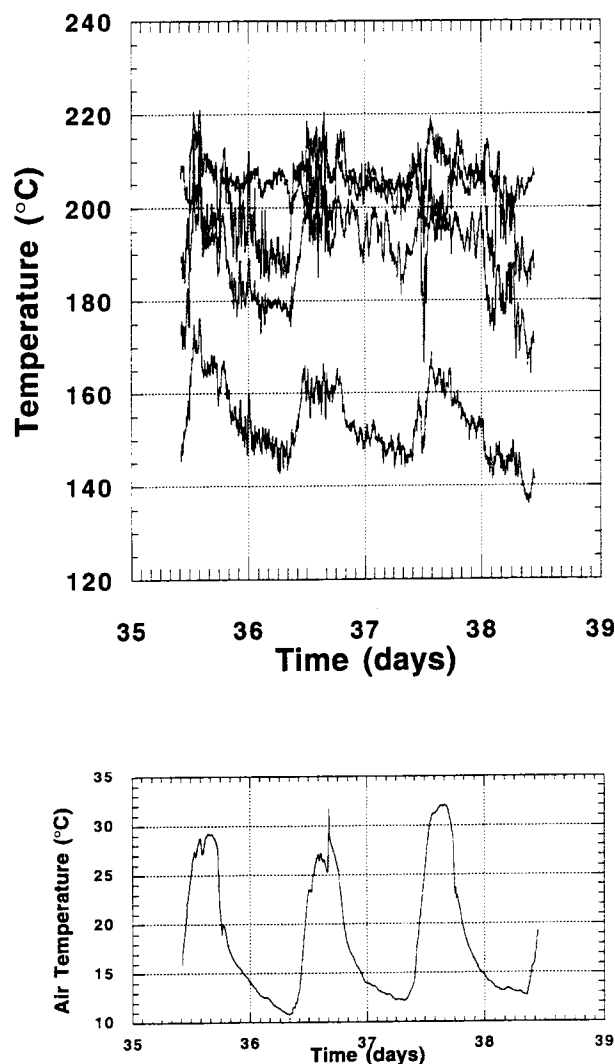


Figure 9-4. Fumarole temperatures (a) correlate with atmospheric temperatures (b), especially in the lower temperature fumaroles

- Sample locations were limited on the N and E sides of the volcano because there is little or no ash covering the late-stage lava flows there. This lack of ash hinders soil gas sampling using these methods.

All sample locations were established using GPS measurements (relative error between stations of ± 50 m). Sample locations were also determined using tape and compass techniques, with the exception of samples collected: (i) on the crater rim; (ii) on the north side of the cone; and (iii) at the base station. Cross checking the station locations indicates that these locations are known to within ± 20 m and most have a relative error of less than 5 m. Sample locations and a

base sketch map were subsequently digitized using the ARC/INFO Geographic Information System (GIS).

Anomalously high He concentrations were identified in samples collected at the Ahuan vent and about 90 m from the Ahuan vent on the flanks of the main cone (Figure 9-6). Soil He concentrations are about 250 ppb in excess of atmospheric concentration; these concentrations are extremely high except in comparison to those observed at active volcanoes. For example, He concentrations at Kilauea Volcano are up to 8,000 ppb at Sulfur Bank. Other samples collected at Parícutin, mostly along a NE-trending traverse, average about 100 ppb in excess of atmospheric He. This concentration indicates active convective upwelling of

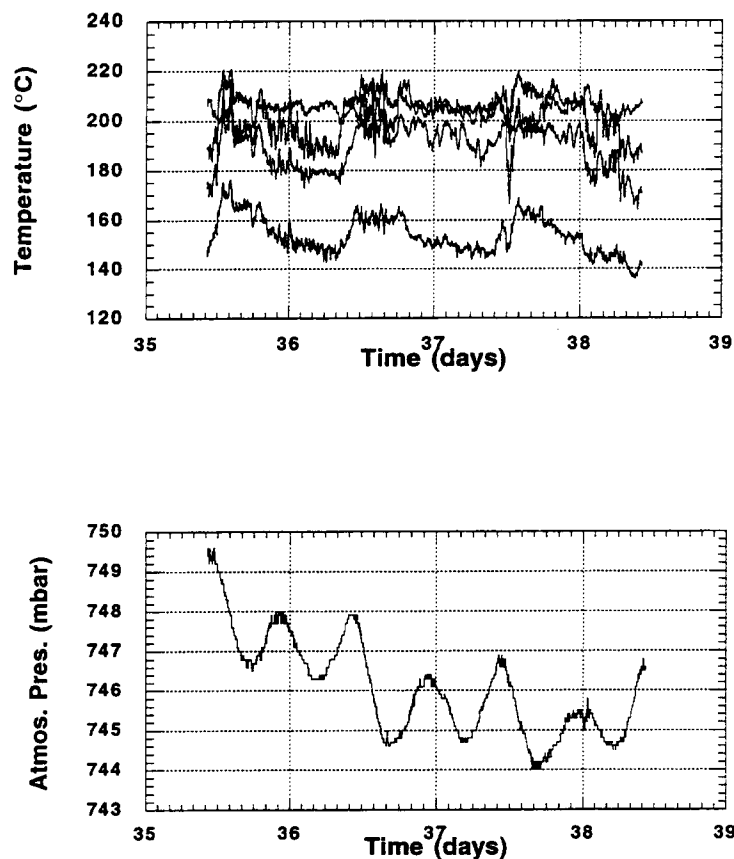


Figure 9-5. Fumarole temperatures (a) do not correlate with atmospheric pressure (b)

He in the area around the cooling cone. These He concentrations are normally thought to originate from decay of isotopes in the crust and indicate migration of excess He from depth.

Radon concentrations were greatest on the cone rim and in the area of the Ahuan vent (Figure 9-7). The highest radon concentration measured was 67 pCi/L, found on the NW rim of the crater. Radon was found to be as high as 20 pCi/L at the Ahuan vent. High radon concentrations, in excess of 10 pCi/L, were also found along the traverse west of the cinder cone (Figure 9-7). Background Rn concentrations in the area are about 2.5 pCi/L. As was the case with the He concentrations, soil radon flux is high in a broad area around the cone and is very high on the main cone rim and at the Ahuan vent. Soil CO₂ concentrations were highest on the main cone (Figure 9-8) and were comparatively high throughout the survey area.

9.3.3 Preliminary Conclusions of the Parícutin Soil Gas Survey and Implications for the Volcanism Disruptive Scenario

This survey at Parícutin provided an overview of current degassing at Parícutin. Several preliminary conclusions include the following.

- Fumaroles remain superheated at the Ahuan and Taqui vents. These vents are separated by a distance of approximately 750 m along a NE trend. Daily temperature variations in these vents are likely the result of atmospheric forcing. These superheated fumaroles have a minimal condensable phase.
- Low-temperature fumaroles (45–85 °C) are found over a broad area at Parícutin, including the entire area between the

Table 9-1. Fumarole temperature at Parícutin

	Baro (mbar)	Air T (°C)	T1	T2	T3	T4
Minimum	744.0	10.8	190.2	182.6	163.9	136.0
Maximum	749.6	32.1	218.5	221.1	207.2	176.3
Range	3.6	21.3	28.3	38.5	43.3	40.3
Mean	746.0	18.4	204.0	203.3	188.8	153.8
Median	746.0	15.7	204.5	205.8	190.9	152.6
Standard Deviation	1.2	6.4	3.85	8.92	8.68	7.58
Variance	1.5	41.1	14.9	79.7	75.4	57.5

Taqui and Ahuan vents, with the exception of the N rim of the main cone, and extending S and SW of the Ahuan vent. These diffuse fumaroles surrounding the high-temperature fumaroles emit water vapor.

- Excess He, radon, and CO₂ flow occur at Parícutin. Highest concentrations occur at the main cone and the Ahuan vent, suggesting forced convective flow of these gases in these areas.
- Elevated Radon and He concentrations are found over an area extending more than 500 m from the Ahuan vent.

Although these data are preliminary, they do indicate some bounds of models for diffuse degassing at cooling cinder cones. Very high-temperature zones are limited in areal extent to former vents, covering areas of several thousand square meters. Even after a long period of time, these vents are superheated; however, there is little or no condensable phase associated with fumaroles in these high-temperature regions, indicating that they act as dry-out zones. The high radon and He fluxes observed in these areas indicate transport from depth with comparatively little mixing. These zones are surrounded by lower temperature regions in which there is high vapor flow at temperatures of 45 to 100 °C. At Parícutin, this region of elevated vapor flow covers 1.5 to 2 km². Gas flow is high throughout this area. A working hypothesis is that these zones are areas of convective upwelling due to the cooling rock beneath

the cone, and that there is very little or no magmatic component to gases at Parícutin. At depth, a broader area is likely affected by convective flow. Modeling of convective flow and cooling is planned, which will be constrained by gas flow and temperature data collected at Parícutin, with the objective of determining the likely areas affected by gas flow during and following cinder cone eruptions.

Future field work at Parícutin will concentrate on several specific issues:

- Additional soil samples should be collected, concentrating on He sampling perpendicular to the NE-trending traverse already collected. This additional sampling will provide an idea of the extent of the diffuse He anomaly.
- In collaboration with local scientists, an effort to determine the depth and configuration of the groundwater table in the region beneath and surrounding Parícutin should be made using drillhole data.
- The map distribution of thermal anomalies is poorly known at this volcano. The United States Geologic Survey (USGS) maps of Parícutin were made in 1946, prior to the end of eruptive activity, and as a result are not accurate. The Ahuan and Taqui vents, for example, had not yet formed in 1946. A topographic map

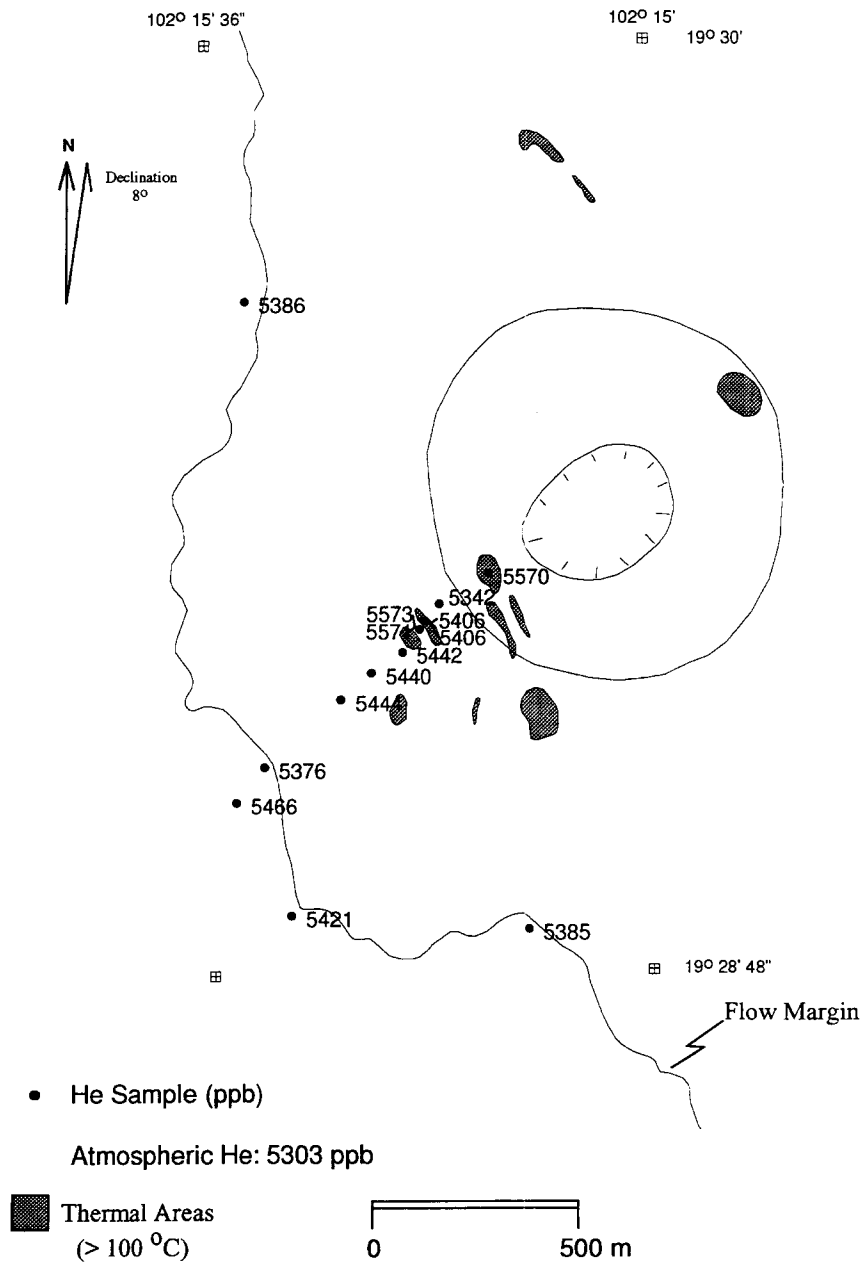


Figure 9-6. Soil He concentrations at Parícutin. Collected during January 1994

should be made of the main cone and the Ahuan and Taqui vents, extending out approximately 200 m from these locations. The simplest approach would be a plane table and alidade survey. As the topography is mapped, alteration zones, fumaroles, and soil temperature profiles can be plotted. The dry-out zones associated with high-temperature

fumaroles and the areal extent of low-temperature fumaroles can then be determined with confidence. This topographic base and geologic map will be very important for accurately modeling the cooling of the cinder cone, especially if flow in the system is related to venturi effects, as initial temperature data indicate.

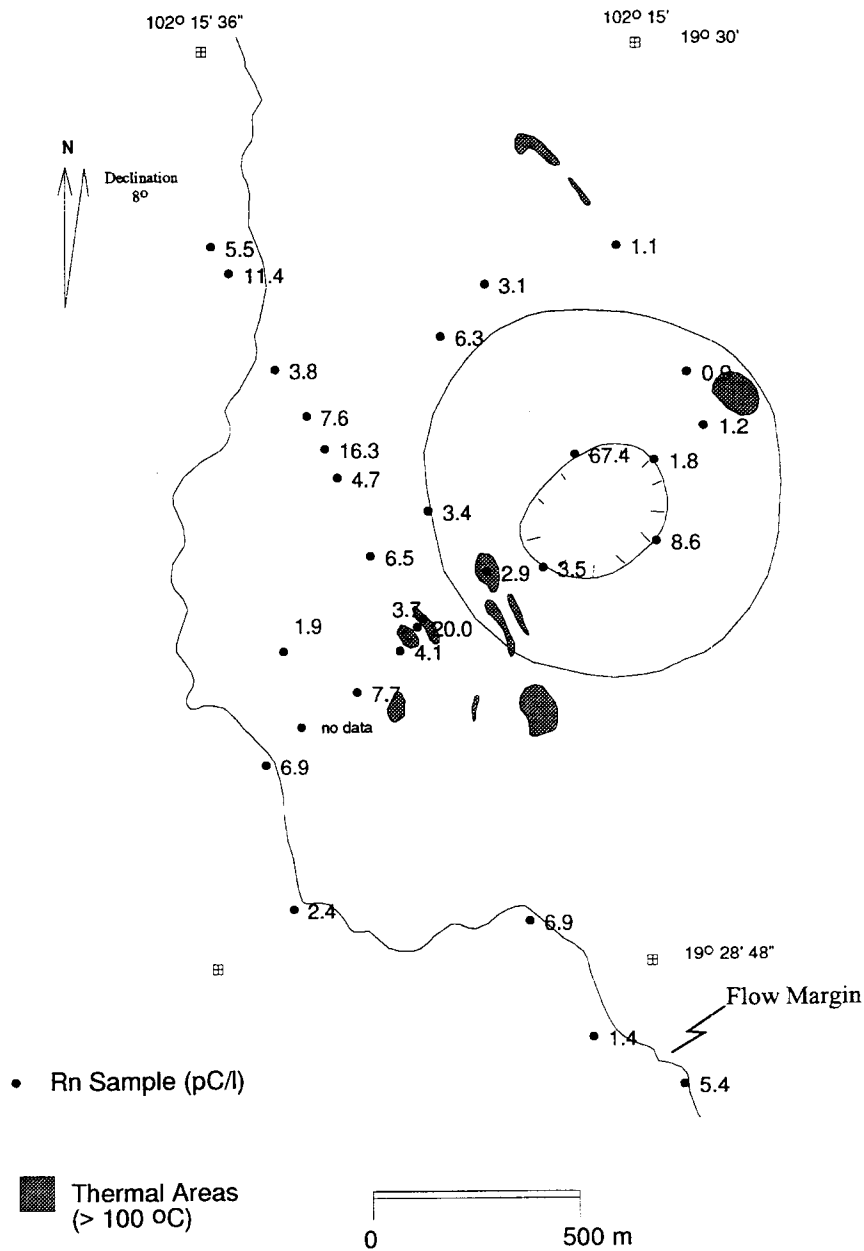


Figure 9-7. Soil Radon concentrations at Parícutin. Collected during January 1994

- Perhaps the most interesting effect observed at Parícutin was the rapid flow of heated water vapor over a broad region at the volcano. This flow should be quantified. Two methods to do this are either by measuring soil temperature gradients through time, using the datalogger, or measuring flow in radon sampling tubes by hot-wire anemometry.

Both methods are currently being explored.

- Future work needs to concentrate to a greater degree on systematic ash sample collection and the mapping of ballistic features and xenoliths on and around the cone (Rowland et al., 1991; Walker, 1993).

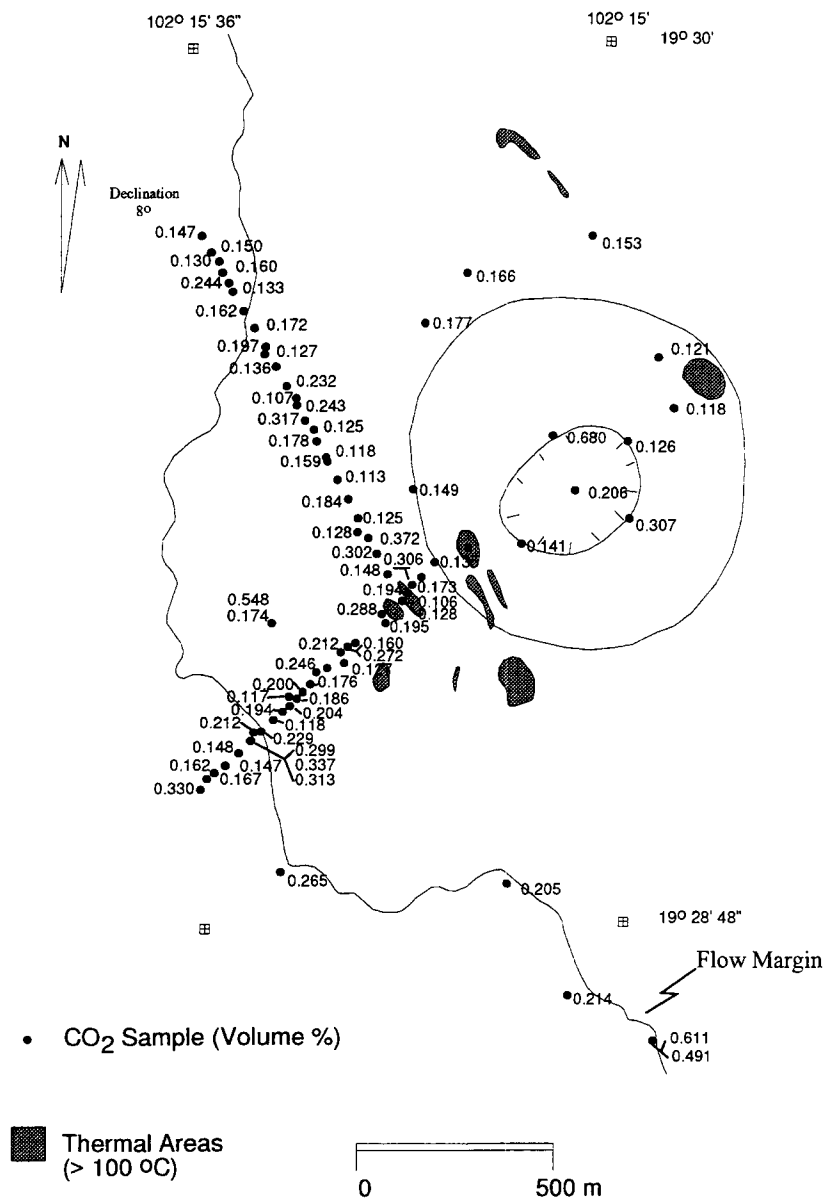


Figure 9-8. Soil CO₂ concentrations at Parícutin. Collected during January 1994

9.4 AMPHIBOLES IN ALKALINE BASALTS

Amphibole occurs in many of the Quaternary and in some Neogene basalts of the YMR (Vaniman et al., 1982; Crowe et al., 1983a). Small, isolated crystals of amphibole with reaction rims of plagioclase, clinopyroxene, and magnetite are rare phases at Sleeping Butte (Crowe et al., 1983a), Red Cone (Vaniman et al., 1982; Smith et al., 1990), Little Cone NE (Vaniman et al., 1982), Little Cone SW,¹ Buckboard Mesa (Crowe et al., 1983a), and Nye Canyon (Crowe et

al., 1983a). A total of four analyses have been published for YMR amphiboles (Vaniman and Crowe, 1981). Vaniman et al. (1982) conclude that amphibole in the Quaternary basalts is of cognate origin, primarily based on evidence of amphibole fractionation in the evolution of the basalts. In contrast, amphiboles in the Nye Canyon basalt are megacrysts (Crowe et al., 1983a) and

1. B.E. Hill, CNWRA, unpublished research, 1994.

Table 9-2. Comparison of Crater Flats with basalts used in hydrous crystallization experiments

	Average LW ¹ (n = 55)	Average CF ² (n = 14)	Hawaiite ³	Basan ⁴	BasAnd ⁵	HI Ol-Th ⁶
SiO ₂	48.41	50.06	52.20	44.82	52.58	46.01
TiO ₂	1.92	1.65	2.54	2.50	2.08	2.10
Al ₂ O ₃	16.61	16.74	16.20	14.73	14.94	13.89
FeO*	10.64	10.10	11.28	11.03	11.49	12.82
MnO	0.17	0.16	0.16	0.19	0.19	0.19
MgO	6.10	5.13	4.45	9.69	5.26	10.04
CaO	8.49	9.11	6.94	10.05	8.49	10.36
Na ₂ O	3.11	3.49	4.18	4.01	3.35	2.59
K ₂ O	1.73	1.72	2.11	1.85	0.97	0.75
P ₂ O ₅	1.18	1.23	1.16	0.94	0.38	0.33
TOTAL	99.53	99.39	101.22	99.81	99.73	99.08
Data Sources:						
¹ Average Lathrop Wells basalt, from Perry and Crowe (1992).						
² Average Quaternary Crater Flat basalt, from Vaniman and Crowe (1981) and Crowe et al. (1986).						
³ Hawaiite (basalt) used in crystallization experiments of Knutson and Green (1975).						
⁴ Basanite (basalt) used in crystallization experiments of Allen and Boettcher (1983).						
⁵ Basaltic andesite used in crystallization experiments of Allen and Boettcher (1983).						
⁶ Hawaiian olivine-tholeiite basalt used in crystallization experiments of Adam et al. (1993).						

likely are not derived from the basalts (Best, 1974; Irving, 1980; Dawson and Smith, 1982).

Amphibole also occurs as a primary phase in hydrous crystallization experiments of some alkaline basalts. The experiments of Knutson and Green (1975) were conducted on basalts that are relatively similar in composition to Quaternary Crater Flat compositions (Table 9-2). In summary, Knutson and Green (1975) observed crystals of amphibole in basalts containing 5 wt% water between 5 and 10 kbars pressure, but amphibole was absent from runs containing only 2 wt% water. Although the composition of the experimental basalt is not identical to Quaternary YMR basalts (Table

9-2), it more closely resembles Quaternary YMR basalt than other relevant experiments. For example, 23-kbar water-saturated experiments on Hawaiian tholeiitic basalt contained amphibole (Allen and Boettcher, 1983), as did 10- to 20-kbar, 8- to 10-wt% water content experiments on a nepheline basanite and basaltic andesite (Adam et al., 1993). However, none of these basaltic compositions more closely represents Quaternary YMR basalt (Table 9-2) than that used by Knutson and Green (1975).

The volatile content of a magma must be determined in order to construct accurate models of basaltic eruptions (Blackburn et al., 1976; Wilson, 1980;

Wilson and Head, 1981; Vergnolle and Jaupart, 1986; Jaupart and Vergnolle, 1988; Head and Wilson, 1989; Jaupart and Tait, 1990). The presence of amphibole phenocrysts in some Quaternary YMR basalts may indicate that water contents were in excess of 2 wt% (Knutson and Green, 1975). This determination is critical to distinguishing amphibole that is derived from the magma (i.e., cognate) from amphibole that is derived from surrounding mantle rocks (i.e., xenocryst).

Although there are few experiments on amphibole crystallization in moderately alkaline basaltic melts, numerous experiments on other types of basalt have shown that amphibole composition is primarily dependent upon melt composition, temperature, and pressure (e.g., Allen and Boettcher, 1983; Hammarstrom and Zen, 1986; Blundy and Holland, 1990; Adam et al., 1993). Amphibole that originated through metasomatism in the upper mantle (e.g., Best, 1974; Boettcher and O'Neil, 1980; Menzies and Murthy, 1980; Dyar et al., 1993) likely would be compositionally distinct from amphibole that crystallized from alkaline basaltic magmas at relatively low (i.e., 10–20 kbars) pressures. Amphiboles from mantle xenoliths or megacrysts thus might be compositionally distinct from amphiboles in basalt crystallization experiments.

The major elements in amphiboles often are distributed among several different sites in the crystal lattice (e.g., Hawthorne, 1981). In order to accurately compare compositional differences between amphiboles, the raw major-element analysis must be converted into lattice site-specific abundances. The recalculation method of Spear and Kimball (1984) provides reasonable estimates of Fe^{3+} and Fe^{2+} abundances (Blundy and Holland, 1990) and provides a straightforward procedure for recalculating major element composition into amphibole structural formulae on the basis of 23-Oxygen. Table 9-3 shows representative amphibole compositions from xenocrysts and phenocrysts in both major element and structural formulae abundances. Using the nomenclature suggested by Hawthorne (1981), amphiboles in xenoliths and megacrysts are generally calcic, with $(\text{Ca}+\text{Na})[\text{M4}]>1.34$ and $\text{Na}[\text{M4}]<0.67$ (e.g., Table 9-3). Calcic amphiboles with $\text{Ti}>0.5$ are referred to as kaersutite, whereas calcic amphibole xenocrysts with $\text{Ti}<0.5$ are generally pargasitic to hastingsitic.

The compositions of 145 amphibole xenocrysts in alkaline basalts were compiled from Wise (1966),

Mason (1968), Best (1970; 1974; 1975), Kesson and Price (1972), Frey and Green (1974), Green et al. (1974), Irving (1974), Wilkinson (1975), Frey and Prinz (1978), Boettcher and O'Neil (1980), Bergman et al. (1981), Bergman (1982), Dyar et al. (1993), and Arana et al. (1994). In addition, amphibole compositions from basalt crystallization experiments were compiled from Allen and Boettcher (1983), and Adam et al. (1993). The compositions of 32 amphiboles from Knutson and Green (1975) were recently reanalyzed by D.S. Draper and T.H. Green, who have generously provided these unpublished data for experiments (5 kbar, 5 wt% H_2O , 1,000 °C; and 10 kbar, 10 wt% H_2O , 1,060 °C). All amphibole compositions in the compilation have been recalculated into structural-formula units utilizing the program AMPREC by Spear and Kimball (1984) with the recalculations based on average Fe^{3+} .

The compiled amphibole compositions are compared with the four amphibole analyses available from Red Cone and Little Cone NE (Vaniman and Crowe, 1981) in Figure 9-9. Crater Flat amphiboles have lower Ti and Al abundances than many xenocrysts and experimental phenocrysts. Best (1974) noted that higher-Ti megacrysts tend to have lower pressure and temperature stability limits than lower-Ti amphiboles, although there is significant variation in Ti content of amphiboles from the same volcano. Experiments by Knutson and Green (1975) and Green (unpublished analyses, 1994) show that an increase in temperature, pressure, and water content also will result in higher Ti abundances along with smaller increases in Al (Figure 9-9). In addition, Ti substitutions in the M4 lattice site also is controlled by several coupled reactions (Hawthorne, 1983). Thus, variations in the Ti content of calcic amphiboles cannot be related to a unique parameter such as pressure. Crater Flat amphiboles do have relatively low Ti and Al contents, but these compositions are measured in some known xenocrysts (Figure 9-9).

Variations in Al(IV) (i.e., tetrahedral coordination in the crystal lattice) and Al(VI) (i.e., octahedral coordination) may indicate that Crater Flat amphiboles originated at pressures or temperatures that are lower relative to other xenocrysts (Figure 9-10). Best (1974) and Dawson and Smith (1982) have noted amphibole xenocrysts that are thought to have formed at relatively higher pressures tend to have higher total Al. Experimental work on silicic magmas by Hammarstrom and Zen (1986), Hollister et al. (1987), and Johnson and

Table 9-3. Compositions of amphiboles from Crater Flat, Lunar Crater, western Grand Canyon Volcanic Fields, and analyses of Green and Draper (unpublished research). Formula units calculated using the method of Spear and Kimball (1984) with average Fe³⁺. Nomenclature of Hawthorne (1981).

Source	1a	1b	2	3	4a	4b
Type	Pargasite	Pargasite	Kaersutite	Kaersutite	Kaersutite	Kaersutite
SiO ₂	40.0	40.8	39.81	40.9	38.57	40.54
TiO ₂	3.94	2.99	6.13	4.45	5.74	4.42
Al ₂ O ₃	12.9	13.8	15.04	13.62	12.78	12.62
Fe ₂ O ₃	—	—	—	6.04	—	—
Cr ₂ O ₃	—	0.08	0.043	0.09	0.1	0.01
MgO	13.9	14.4	12.16	13.82	10.21	11.86
FeO	11.2	11.0	11.61	5.79	15.86	13.81
MnO	0.05	0.09	0.14	0.07	0.15	0.17
CaO	11.8	11.5	10.84	10.08	10.52	9.75
Na ₂ O	2.45	2.55	3.28	2.66	2.51	2.78
K ₂ O	1.0	0.8	1.35	1.6	1.12	1.11
H ₂ O	2.8	2.0	—	0.7	—	—
Cl	—	—	—	—	0.00	0.00
F	—	—	—	—	0.117	0.123
Formula Units (23-O)						
Si	5.94	5.97	5.76	6.12	5.86	6.08
Al(IV)	2.06	2.03	2.25	1.88	2.15	1.92
Al total	2.26	2.38	2.56	2.40	2.29	2.23
Al(VI)	0.20	0.36	0.32	0.52	0.14	0.32
Ti	0.44	0.33	0.67	0.50	0.66	0.50
Fe ³⁺	0.08	0.13	0.00	0.35	—	—
Cr ³⁺	—	0.01	0.01	—	0.01	0.00
Mg	3.08	3.14	2.62	3.08	2.31	2.65

Table 9-3. Compositions of amphiboles from Crater Flat, Lunar Crater, western Grand Canyon Volcanic Fields, and analyses of Green and Draper (unpublished research). Formula units calculated using the method Spear and Kimball (1984) with average Fe³⁺. Nomenclature of Hawthorne (1981).

Source	1a	1b	2	3	4a	4b
Type	Pargasite	Pargasite	Kaersutite	Kaersutite	Kaersutite	Kaersutite
Fe ²⁺	1.32	1.22	1.40	0.38	2.01	1.73
Mn	0.01	0.01	0.02	0.01	0.02	0.02
Ca	1.88	1.80	1.68	1.62	1.71	1.57
Na(M4)	0.00	0.01	0.30	0.54	0.14	0.21
Na total	0.71	0.72	0.92	0.77	0.74	0.81
Na(A)	0.71	0.71	0.62	0.23	0.60	0.60
K	0.19	0.15	0.25	0.31	0.22	0.21
Sum (A)	0.90	0.86	0.87	0.54	0.82	0.81
OH	2.00	2.00	2.00	2.00	1.94	1.94
Cl	—	—	—	—	0.00	0.00
F	—	—	—	—	0.06	0.06
Data Sources:						
¹ Vaniman and Crowe, 1981. (a) Little Cone NE, (b) Red Cone.						
² Bergman, 1982. Xenocryst, Lunar Crater Volcanic Field, NV.						
³ Best, 1970. Xenocryst, western Grand Canyon Volcanic Field, AZ.						
⁴ T.H Green & D.S. Draper, 1994, unpublished research. Experimental conditions: (a) 5 kbar, 5% H ₂ O, 1,000 °C, (b) 10 kbar, 10% H ₂ O, 1,060 °C.						

Rutherford (1989) supports this interpretation. However, Blundy and Holland (1990) also have shown that an increase in temperature results in increased Al(IV), relative to Al(VI), in silicic magmas. This interpretation must be tempered by the fact that the effects of water content and basaltic melt composition on amphibole composition have not been investigated in detail. An increase in pressure from 5 to 10 kbars, water from 5 to 10 wt%, and temperature from 1,000 °C to 1,060 °C¹ results in lower Al(IV) (Figure 9-10).

Although a 50 °C increase in temperature should result in a 0.2 formula unit increase in Al(IV) (Blundy and Holland, 1990), an increase in pressure and water content reverses this effect (Figure 9-10).

The significance of titanian pargasite to ferropargasite amphibole in some Quaternary Crater Flat basalts is difficult to interpret. These amphiboles

1. Green and Draper, unpublished research, 1994.

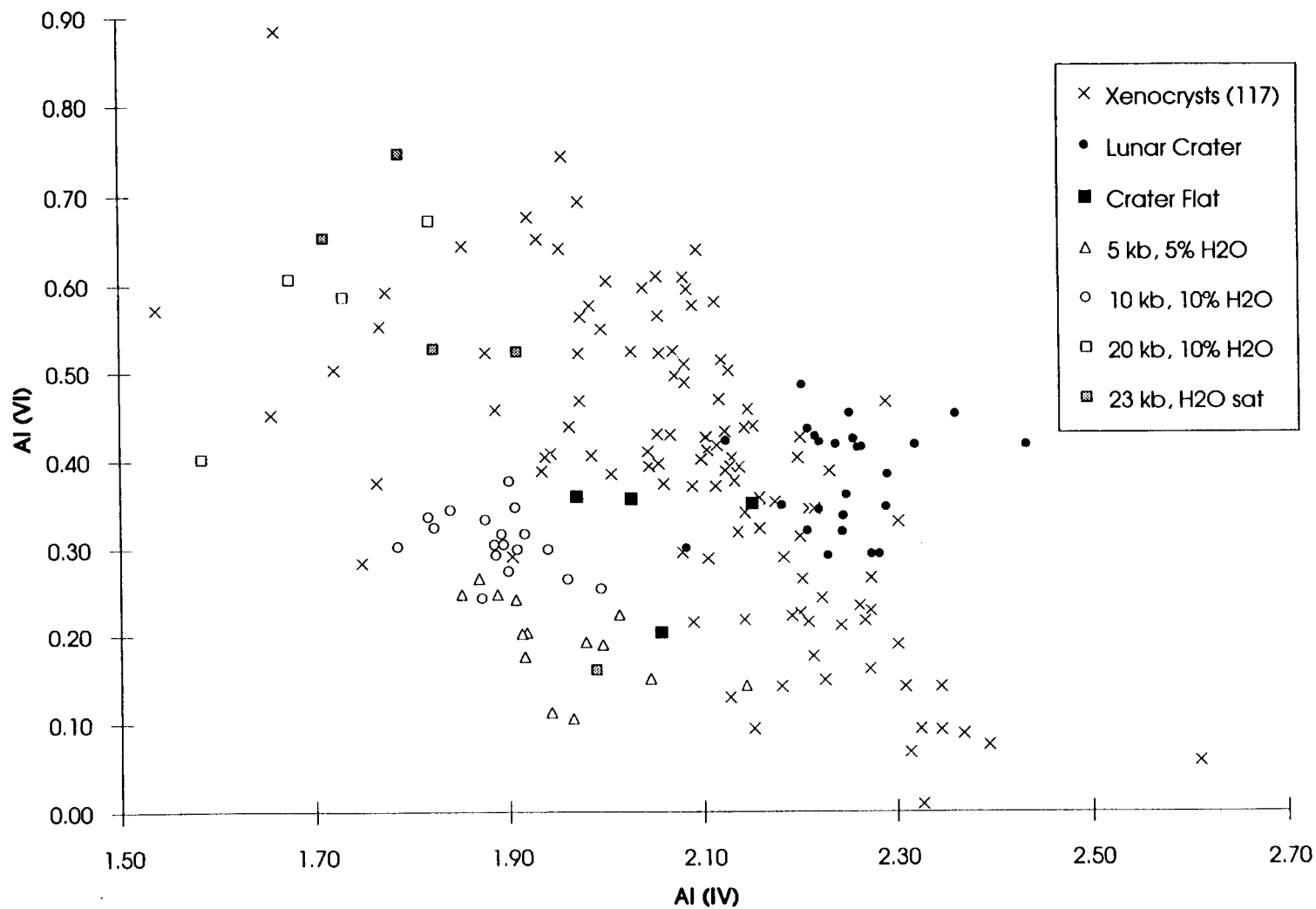


Figure 9-9. Variations in total Al and Ti (formula units) for amphibole from alkaline basalt xenocrysts and basalt crystallization experiments. Amphiboles from 5- and 10- kbar experiments are from Green (unpublished analyses, 1994), 20 kbar from Adam et al. (1993), and 23 kbar from Allen and Boettcher (1983).

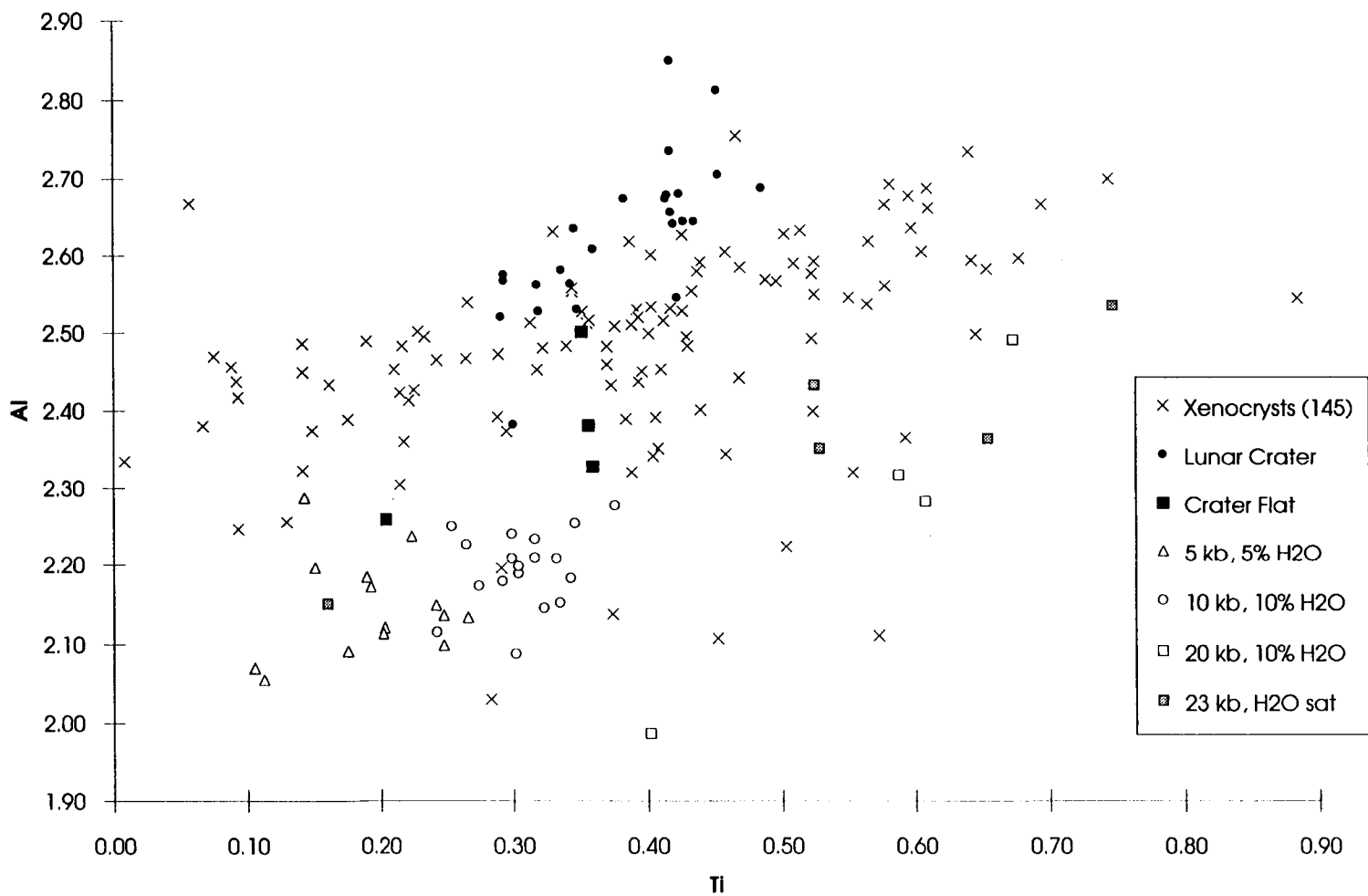


Figure 9-10. Variations in Al(IV) versus Al(VI) in amphiboles are sensitive to variations in temperature, pressure, and water contents. Crater Flat amphiboles appear transitional between experimentally derived and xenocrystic amphiboles. Same symbols as in Figure 9-9.

are reportedly small and not in equilibrium with surficial conditions (Vaniman et al., 1982). They do not occur as megacrysts and apparently are not associated with mantle xenoliths (e.g., Vaniman et al., 1982; Crowe et al., 1983a; 1986). Association with other mantle phases, such as aluminous clinopyroxene, high-magnesium olivine, or aluminous spinels, would be good evidence that the amphiboles originated from disaggregated mantle xenoliths. However, olivine (Fo₇₆₋₇₉) in these basalts was in apparent equilibrium with the host magma (Vaniman et al., 1982). Olivine xenocrysts are generally not in equilibrium with the host basalt (e.g., Bergman, 1982). Clinopyroxene and aluminous or chromian spinels are absent from Quaternary Crater Flat basalts. Based on morphology and mineralogical associations, Crater Flat amphiboles appear to be phenocrysts and not xenocrysts.

The Ti and Al contents of Crater Flat amphiboles are generally lower than measured in other amphibole xenocrysts, although some xenocrysts have similar Ti and Al contents (Figures 9-9 and 9-10). Variations between Al(IV) and Al(VI) may indicate that Crater Flat amphiboles formed at relatively low pressures, but variations in temperature and water content likely obscure this relationship. Amphiboles from alkaline basalt hydrous crystallization experiments have generally lower Ti and Al than Crater Flat amphiboles. Based on the available data, it is unlikely that the Crater Flat amphiboles formed from basaltic magmas with ≥ 5 wt% H₂O and pressures ≥ 5 kbar.

There is a significant amount of compositional variation in the four Crater Flat analyses. Clearly, additional amphibole data are needed to accurately determine the compositional variation in Crater Flat amphiboles. Additional amphibole xenocrysts from other alkaline basalts, especially for the western Great Basin, also are needed to provide more statistically meaningful comparisons to Crater Flat amphiboles. Currently, it is not possible to convincingly demonstrate that Crater Flat amphiboles are xenocrysts. It is, however, highly unlikely that these amphiboles crystallized from basaltic magmas with water contents of ≥ 5 wt%.

9.5 APPLICATIONS OF GEOPHYSICAL DATA TO ISSUES IN BASALTIC VOLCANISM

A major milestone (Connor and Sanders, 1994) summarizes the Center for Nuclear Waste Regulatory Analyses (CNWRA) research conducted during 1993 and 1994 on the applications and limitations of geophysical methods to the study of intrusive or buried extrusive basalts. The objective of this summary is to review the application of geophysical methods in use in the YMR as part of site characterization (e.g., Oliver et al., 1990), discuss the application of these methods in the context of volcanism studies (Crowe et al., 1993; Connor and Hill, 1993; Valentine et al., 1992), and explore the utility and limitations of geophysical methods in volcanism studies through presentation of parametric models and the results of numerical experiments. In the context of volcanism studies in the YMR, geophysical methods to date have been used primarily in the exploration for volcanic features that lack surface expression. These methods have included the use of aeromagnetic and ground magnetic surveys to search for buried basaltic centers in the Amargosa Valley (Langenheim et al., 1993; Ponce et al., 1992) and the use of broadband seismic tomographic methods to characterize the velocity structure of basaltic source regions in the mantle (Evans and Smith, 1992). These two geophysical methods—magnetics and seismic tomography—will likely continue to be used to great extent in site characterization efforts related to volcanism (Crowe et al., 1993). Furthermore, applications of these two methods currently hold the greatest promise of reducing uncertainties related to basaltic volcanism in the YMR. Although both methods have been used primarily for the exploration and identification of features related to basaltic and silicic volcanism (Evans and Smith, 1992; Langenheim et al., 1993), they hold potential for further application to other issues in volcanology, including characterization of intrusion volume and geometry and determination of volumetric intrusion to extrusion ratio in the YMR. As a result, it is critical to understand both the utility and limitations of these two geophysical methods in particular.

Results of this study, presented in detail in Connor and Sanders (1994), indicate that probability models based on the distribution and timing of cinder cone volcanism can be significantly enhanced through the application of geophysical methods. Models of the

impact of volcanism on repository performance can also be improved through geophysical investigations. Therefore, an important consideration in future geophysical research in the YMR should be that this research encompass specific issues in volcanism related to probability and consequence model development. This does not mean that geophysical data, such as tomographic data, need be collected for the use of volcanologists alone, rather that the data should be used to address specific research goals in volcanology and that survey design should consider these issues. Basic areas of research in basaltic volcanism in which geophysical methods may be used to reduce KTUs are:

- Identification and mapping of shallow igneous features that lack surface expression
- Estimation of the volume of rock at repository depths disrupted by magmatic activity
- Demonstration of the relationship between igneous features, such as cinder cones and dikes, to regional tectonic setting and local structures
- Identification and mapping of high-temperature subsolidus or partial-melt zones in the YMR

To date, geophysical methods have been applied to two of these problems: identification and mapping of shallow igneous features that lack surface expression, through the application of aeromagnetic methods (Langenheim et al., 1993; Crowe et al., 1993), and the search for high-temperature subsolidus or partial-melt zones in the YMR, through the application of teleseismic tomographic methods (Evans and Smith, 1992).

Identification of subsurface igneous features is a basic aspect of site characterization. The simulations and parametric studies presented in this report provide some bounds on the capability of seismic tomographic and magnetic surveys for the identification of subsurface igneous features. Some basic conclusions with regard to application of these methods to this identification and mapping process are the following:

- Numerous seismic tomographic studies have demonstrated that this method is capable of resolving high-temperature and

partial-melt zones in the crust and upper mantle. Recognition of these potential source zones for basaltic magma, or increased confidence in their absence, can help resolve uncertainty related to the application of probability models.

- The volume of the velocity anomalies that can be identified depends on survey design, the number of stations deployed and the station spacing, and the depth of the target anomaly.
- Synthetic tomography experiments at the site indicate that 15151-km low-velocity anomalies can be identified at shallow depths (<5 km) using approximately 100 stations in a 100-km² area. The results of such a survey would facilitate characterization of the geology of the site generally, and may help bound the intrusion/extrusion ratio of basalts in parts of the YMR. This detailed survey, coupled with lower resolution, deeper surveys, may have an impact on probability calculations for volcanic disruption of the candidate repository and the results of these surveys should be considered in this context.
- Tomography surveys in other, younger, basaltic fields may provide evidence of the longevity of velocity anomalies related to small-volume basaltic volcanism.
- Ground and aeromagnetic data will not be useful in identifying shallow igneous features in the YMR, except where these features are located in alluvium that is deep with respect to the level of the igneous features. Therefore, recognition and mapping of aeromagnetic anomalies in the Amargosa Valley will not, in itself, indicate that all buried centers or significant intrusive structures have been identified in the YMR.
- Any result or interpretation of the recurrence rate of volcanism in the YMR based on the application of aeromagnetic methods, must address the uncertainty of

the geophysical method employed. Parametric studies summarize the limits of the resolution of the magnetic methods for the identification of basaltic features in various magnetized terrains.

Analyses in this study indicate that specific seismic tomographic and refraction experiments can be designed to investigate the structure of feeder dike systems beneath cinder cone alignments. These experiments could be coupled with aeromagnetic and ground magnetic surveys. In both geophysical methods, the ability to resolve and map intrusion geometries depends on dike volume and contrast with the surrounding media. Traveltime anomalies on the order of 0.01 s, corresponding to dike volumes on the order of several percent, can be resolved using comparatively straightforward experimental designs. Numerous parameters, such as topographic complexity and magnetization contrast, impact the dike geometries that can be resolved using magnetic methods. Resolution of magnetic data can, under some circumstances, be enhanced through the application of frequency domain map enhancement techniques and statistical analysis of magnetic data. Thus, both methods are capable of resolving large shallow dikes or dike swarms that may be related to alignments or polycyclic activity. Conversely, neither of these methods is likely to identify small features, such as individual dikes, at repository depths. In either case, an investigation of a cinder cone alignment, for example the Crater Flat alignment, or a similar feature would place valuable constraints on models of repository disruption due to volcanism. Such data are not currently available. An investigation of this kind would impact volcanism models and performance assessment because: (i) the interpretation of structural controls on alignment evolution and understanding of the dynamics of this process may change; (ii) as a result, probability models may change; and (iii) such an investigation may alter current models of the volume of rock disrupted, and therefore the repository area affected, by igneous activity.

The relationship of basaltic volcanism to regional tectonic setting and structure is also best approached through integrated surveys. Determination of the tectonic setting of volcanic fields should include cross-correlation of LandSat Thematic Mapper (TM) data, long-wavelength geophysical data including gravity and magnetics, topographic information, and geological information. Cross-correlation is best

handled quantitatively on a geographic information system platform. This approach will simplify superposition of disparate data sets such as aeromagnetic anomalies and TM imagery, and the use of map enhancement techniques. Forward or inverse modeling of geophysical data, although valuable in many circumstances, is not likely to be as helpful as quantitative map analysis for establishing relationships between structure and magmatism in basaltic volcanic fields. On local scales, surveys can be designed to search for interaction between individual faults and dikes in the third dimension. Again, the strength of this approach lies in formulation of the volcanological problem rather than in application of geophysical methods.

9.6 ASSESSMENT OF PROGRESS

Overall, research in the Field Volcanism Research Project during the last 6 mo has provided results which address the objectives of this project and are important to licensing activities in the following areas:

- Results of the MM on geophysical methods indicate the limitations and utility of magnetic and seismic tomographic analyses in site characterization. This is important in order to understand and evaluate statements about intrusion to extrusion ratio in the YMR, and the volume of rock likely disrupted at repository depths by magmatic activity, and the relationship between volcanism and tectonism in the YMR.
- Initial results indicate degassing occurs over a broad area at Parícutin. These data help constrain models for the area affected by volcanic activity and the longevity of these effects. These models will be used to better estimate the probability of volcanic disruption of the candidate repository and the consequences of the volcanic disruptive scenario.
- Review of geochemical analyses of amphiboles in basalts from the YMR and elsewhere indicate that the basalts of the YMR that have amphibole analyses do not likely have water contents greater than 5

wt%. This result does not bound models for the consequences of basaltic volcanic activity because magmas having water contents less than 5 wt% may erupt effusively or explosively. However, the review does indicate the range of water contents currently permissible, given available data, and indicates that additional determinations of water content may improve estimates of volatile content and, as a result, models of the consequences of basaltic volcanism in the YMR.

9.7 PLAN FOR NEXT REPORTING PERIOD

The Field Volcanism project utilizes a dual approach to the evaluation of the consequences of potential volcanic activity in the YMR. Clearly, the range of volcanic activity in the western Great Basin, the duration of this activity, and geology of near-surface structures must be evaluated using detailed field studies of specific sites in the region. Also, much can be learned from the study of historically active cinder cones, especially those where eruptions have been rigorously monitored. As described previously, recent work indicates that many physical and conceptual models of cinder cone volcanism do not encompass the range of activity in modern cinder cones. Therefore the dynamics of cinder cone eruptions in the western Great Basin cannot be truly assessed without thorough comparison to monitored cinder cone eruptions. One simple approach adopted in the Field Volcanism project is to compare near vent deposits at YMR volcanoes with those at Parícutin, Tolbachik, and Cerro Negro – volcanoes with well known eruption histories. Furthermore, processes such as diffuse degassing and thermal loading operate on geologically limited time scales, but could have important impact on repository performance. These processes can be studied most directly at recently active cinder cones. This integrated approach, the study of western Great Basin cinder cones and recently active cones, will provide the most comprehensive and defensible basis for evaluation of compliance with 40 CFR Part 191 and 10 CFR 60.122(c)(15). As such, results of the Field Volcanism project will directly support development of the LARP and subsequent determinations of regulatory compliance. Without this type of integration,

consequence studies and their utility in probability model development will become unnecessarily tenuous.

During the next 6 mo, research will focus on studies at the Tolbachik cinder cones, Kamchatka, Russia. These studies will include surveys of diffuse degassing, temperature monitoring, and collection of rock specimens for characterization of eruption mechanisms at these cinder cones. Following field work at Tolbachik, initial surveys of the three cinder cones used for analog studies, Parícutin, Mexico, Cerro Negro, Nicaragua, and Tolbachik, will be complete. During the Fall of 1994, initial modeling studies of the degassing data will be made.

In addition to these activities, it is anticipated that a new task will be developed in the Field Volcanism project. This task will involve seismic tomographic and magnetic investigations of a selected cinder cone alignment for the purpose of delineating intrusion geometry and the relationship of the alignment to regional structure. Based on results from Task 4 (Connor and Sanders, 1994), it is clear that this geophysical investigation will provide an approach to reduction of uncertainty related to exploration of igneous features, especially intrusions at repository depths and the relationship between tectonism and volcanism in the western Great Basin. It is anticipated that, in collaboration with NRC Office of Nuclear Regulatory Research staff, this task will be developed in the next 6 mo.

As described in Section 7 of this semi-annual report, the Field Volcanism Project will be peer reviewed during the next 6 mo. The process of selection of a peer review panel began in June 1994. This peer review is extremely important because of our use of modern analogs in the investigation of volcanic processes that can potentially impact repository performance (Connor and Hill, 1993; CNWRA Staff, 1994). The peer review panel can make objective comments and criticisms of this approach.

All these activities will provide important contributions to the LARP and, particularly, CDM development. In addition, these activities will be coordinated with Volcanic Systems of the Basin and Range research in order to refine probability models on a continuing basis.

9.8 REFERENCES

- Adam, J., T.H. Green, and S.H. Sie. 1993. Proton microprobe determined partitioning of Rb, Sr, Ba, Y, Zr, Nb and Ta between experimentally produced amphiboles and silicate melts with variable F content. *Chemical Geology* 109: 29–49.
- Allen, J.C., and A.L. Boettcher. 1983. The stability of amphibole in andesite and basalt at high pressure. *American Mineralogist* 68: 307–314.
- Amos, R.C., S. Self, and B.M. Crowe. 1983. Pyroclastic activity at Sunset Crater: Evidence of a large magnitude, high dispersal strombolian eruption. *Eos, Transactions of the American Geophysical Union* 62: 1,085.
- Anderson, A.T. 1979. Water in some hypersthenic magmas. *Journal of Geology* 87: 509–531.
- Arana, V., J. Marti, A. Aparicio, L. Garcia-Cacho, and R. Garcia-Garcia. 1994. Magma mixing in alkaline magmas: An example from Tenerife, Canary Islands. *Lithos* 32:1–19.
- Bergman, S.C. 1982. *Petrogenetic Aspects of the Alkali Basaltic Lavas and Included Megacrysts and Nodules from the Lunar Crater Volcanic Field, Nevada, U.S.A.* Ph.D. Thesis. Princeton, NJ: Princeton University.
- Bergman, S.C., K.A. Foland, and F.J. Spera. 1981. On the origin of an amphibole-rich vein in a peridotite inclusion from the Lunar Crater Volcanic Field, Nevada, U.S.A. *Earth and Planetary Science Letters* 56: 343–361.
- Best, M.G. 1970. Kaersutite-peridotite inclusions and kindered megacrysts in basaltic lavas, Grand Canyon, AZ. *Contributions to Mineralogy and Petrology* 27: 25–44.
- Best, M.G. 1974. Mantle-derived amphibole within inclusions in alkalic-basaltic lavas. *Journal of Geophysical Research* 79: 2,107–2,113.
- Best, M.G. 1975. Amphibole-bearing cumulate inclusions, Grand Canyon, Arizona, and their bearing on silica-undersaturated hydrous magmas in the upper mantle. *Journal of Petrology* 16: 212–236.
- Blackburn, E.A., L. Wilson, and R.S.J. Sparks. 1976. Mechanisms and dynamics of strombolian activity. *Journal of the Geological Society of London* 132: 429–440.
- Blundy, J.D., and T.J.B. Holland. 1990. Calcic amphibole equilibria and a new amphibole-plagioclase geothermometer. *Contributions to Mineralogy and Petrology* 104: 208–224.
- Boettcher, A.L., and J.R. O'Neil. 1980. Stable isotope, chemical, and petrographic studies of high-pressure amphiboles and micas: Evidence for metasomatism in the mantle source regions of alkali basalts and kimberlites. *American Journal of Science* 280: 594–621.
- CNWRA Staff. 1994. *CNWRA Perspective on: Identification and Use of Modern Analogs to Basin and Range Volcanism*. CNWRA manuscript, San Antonio, TX: Center for Nuclear Waste Regulatory Analyses.
- Connor, C.B. 1989. Anomalous soil Hg concentrations at Parícutin Volcano, Michoacán-Guanajuato volcanic field, Mexico. *Geofísica Internacional* 28: 1,029–1,042.
- Connor, C.B. 1990. Cinder cone clustering in the Trans-Mexican Volcanic Belt: Implications for structural and petrologic models. *Journal of Geophysical Research* 95: 19,395–19,405.
- Connor, C.B. 1993. *Technical and Regulatory Basis for the Study of Recently Active Cinder Cones*. NRC-02-88-005, Washington DC: Nuclear Regulatory Commission. 48.
- Connor, C.B., and B.E. Hill. 1993. *NRC High-Level Radioactive Waste Research at CNWRA, July 1 Through December 31, 1992. Chapter 10: Volcanism Research*. NRC-02-88-005. Washington, DC: Nuclear Regulatory Commission: 10-1–10-31.
- Connor, C.B., and C.O. Sanders. 1994. *Geophysics Topical Report: Application of Seismic Tomographic and Magnetic Methods to Issues in Basaltic Volcanism*. CNWRA 94-013. San Antonio, TX: Center for Nuclear Waste Regulatory Analyses.

- Crowe, B.M., D.T. Vaniman, and W.J. Carr. 1983a. *Status of Volcanic Hazard Studies for the Nevada Nuclear Waste Storage Investigations*. LA-9325-MS. Los Alamos, NM: Los Alamos National Laboratory.
- Crowe, B.M., K.H. Wohletz, D.T. Vaniman, E. Gladney, and N. Bower. 1986. *Status of Volcanic Hazard Studies for the Nevada Nuclear Waste Storage Investigations*. LA-9325-MS, Vol. 2. Los Alamos, NM: Los Alamos National Laboratory.
- Crowe, B.M., F.V. Perry, and G.A. Valentine. 1993. *Status of Volcanic Hazard Studies for the Yucca Mountain Site Characterization Project*. LA-9325, Vol. 3. Los Alamos, NM: Los Alamos National Laboratory.
- Dawson, J.B., and J.V. Smith. 1982. Upper-mantle amphiboles: A review. *Mineralogical Magazine* 45: 35–46.
- Dyar, M.D., S.J. Mackwell, A.V. McGuire, L.R. Cross, J.D. Robertson. 1993. Crystal chemistry of Fe^{3+} and H^+ in mantle kaersutite: Implications for mantle metasomatism. *American Mineralogist* 78: 968–979.
- Eggler, D.H. 1972. Water saturated and undersaturated melting relations in a Parícutin andesite and an estimate of water content in a natural magma. *Contributions in Mineralogy and Petrology* 34: 261–271.
- Evans, J.R., and M. Smith III. 1992. Teleseismic tomography of the Yucca Mountain Region: Volcanism and tectonism. *Proceedings of the Third International Conference on High-Level Radioactive Waste Management*. La Grange Park, IL: American Nuclear Society: 2,372–2,380.
- Foshag, W.F., and J.R. Gonzalez. 1956. *Birth and Development of Parícutin Volcano, Mexico*. U.S. Geological Survey Bulletin 965-D. Washington, DC: U.S. Geological Survey: 355–389.
- Frey, F.A., and D.H. Green. 1974. The mineralogy, geochemistry and origin of lherzolite inclusions in Victorian basanites. *Geochimica et Cosmochimica Acta* 38: 1,023–1,059.
- Fries, C. 1953. Volumes and weights of pyroclastic material, lava, and water erupted from Parícutin volcano, Michoacán, Mexico. *Transactions of the American Geophysical Union*: 34: 603–616.
- Frey, F.A., and M. Prinz. 1978. Ultramafic inclusions from San Carlos, Arizona: Petrologic and geochemical data bearing on their petrogenesis. *Earth and Planetary Science Letters* 38: 129–176.
- Green, D.H., A.D. Edgar, P. Beasley, E. Kiss, and N.G. Ware. 1974. Upper mantle source for some Hawaiites, Mugearites and Benmoreites. *Contributions to Mineralogy and Petrology* 48: 33–43.
- Hammarstrom, J.M., and E. Zen. 1986. Aluminum in hornblende: An empirical igneous geobarometer. *American Mineralogist* 71: 1,297–1,313.
- Hasenaka, T., and I.S.E. Carmichael. 1985. The cinder cones of Michoacán-Guanajuato, central Mexico: Their age, volume, distribution, and magma discharge rate. *Journal of Volcanology and Geothermal Research* 25: 105–124.
- Hawthorne, F.C. 1981. Crystal chemistry of the amphiboles. *Amphiboles and Other Hydrous Pyriboles*. D.R. Veblen, ed. Reviews in Mineralogy Vol. 9A: Washington, DC: Mineralogical Society of America.
- Hawthorne, F.C. 1983. Crystal chemistry of the amphiboles. *Canadian Mineralogist* 21: 174–481.
- Head, J.W., III, and L. Wilson. 1989. Basaltic pyroclastic eruptions: Influence of gas-release patterns and volume fluxes on fountain structure, and the formation of cinder cones, spatter cones, rootless flows, lava ponds and lava flows. *Journal of Volcanology and Geothermal Research* 37: 261–271.

- Hollister, L.S., G.C. Grissom, E.K. Peters, H.H. Stowell, and V.B. Sisson. 1987. Confirmation of the empirical correlation of Al in hornblende with pressure of solidification of calc-alkaline plutons. *American Mineralogist* 72: 231–239.
- Irving, A.J. 1974. Megacrysts from the Newer Basalts and other basaltic rocks of southeastern Australia. *Geological Society of America Bulletin* 85: 1,503–1,514.
- Irving, A.J. 1980. Petrology and geochemistry of composite ultramafic xenoliths in alkalic basalts and implications for magmatic processes within the mantle. *American Journal of Science* 280: 389–426.
- Jaupart, C., and S. Tait. 1990. Dynamics of eruptive phenomena. *Modern Methods of Igneous Petrology: Understanding Magmatic Processes*. J. Nicholls and J.K. Russell, eds. Reviews in Mineralogy Vol. 24: Washington, DC: Mineralogical Society of America.
- Jaupart, C., and S. Vergnolle. 1988. Laboratory models of Hawaiian and Strombolian eruptions. *Nature* 331: 58–60.
- Johnson, M.C., and M.C. Rutherford. 1989. Experimental calibration of the aluminium-in-hornblende geobarometer with application to Long Valley caldera (California). *Geology* 17: 837–841.
- Kesson, S., and R.C. Price. 1972. The major and trace element chemistry of Kaersutite and its bearing on the petrogenesis of alkaline rocks. *Contributions to Mineralogy and Petrology* 35: 119–124.
- Knutson, J., and T.H. Green. 1975. Experimental duplication of a high-pressure megacryst/cumulate assemblage in a near-saturated Hawaiite. *Contributions to Mineralogy and Petrology* 52:121–132.
- Langenheim, V.E., K.S. Kirchoff-Stein, and H.W. Oliver. 1993. Geophysical investigations of buried volcanic centers near Yucca Mountain, Nevada. *Proceedings of the Fourth International Conference on High-Level Radioactive Waste Management*. La Grange Park, IL: American Nuclear Society: 1,840–1,846.
- Lescinsky, D.T., C.B. Connor, and R.E. Stoiber. 1987. Soil mercury study of thermal areas, Rincon de la Vieja Volcano, Costa Rica. *Geothermics* 16: 159–168.
- Mason, B. 1968. Kaersutite from San Carlos, Arizona, with comments on the paragenesis of this mineral. *Mineralogical Magazine* 36: 997–1,002.
- McBirney, A.R., H.P. Taylor, and R.L. Armstrong. 1987. Parícutin re-examined: A classic example of crustal assimilation in calc-alkaline magma. *Contributions in Mineralogy and Petrology* 94: 4–20.
- McClelland, L., T. Simkin, M. Sommers, E. Nielsen, and T.C. Stein. 1987. *Global Volcanism 1975–1985*. Prentice-Hall. Englewood Cliffs, NJ: 467.
- McDuffie, S.M., C.B. Connor, and K.D. Maher. 1994. A simple 2-D stress model for fault dike interaction. *EOS, Transactions of the American Geophysical Union* 75: 345.
- Menzies, M., and V.R. Murthy. 1980. Nd and Sr isotope geochemistry of hydrous mantle nodules and their host alkali basalts: Implications for local heterogeneities in metasomatically veined mantle. *Earth and Planetary Science Letters* 46: 323–334.
- Oliver, H.W., E.L. Hardin, and P.H. Nelson. 1990. *Status of Data, Major Results, and Plans for Geophysical Activities, Yucca Mountain Project*. U.S. Department of Commerce: National Technical Information Service: Springfield, Va.
- Perry, F.V., and Crowe, B.M. 1992. Geochemical evidence for waning magmatism and polycyclic volcanism at Crater Flat, Nevada. *Proceedings of the Third International Conference on High-Level Radioactive Waste Management*. La Grange Park, IL: American Nuclear Society: 2,356–2,365.

- Ponce, D.A., S.B. Kohn, and S. Waddell. 1992. Gravity and magnetic data of Fortymile Wash, Nevada Test Site, Nevada. *U.S. Geological Survey Open-File Report 92-343*. Washington, DC: U.S. Geological Survey.
- Rowland, S.K., Z. Juardo, and G.P.L. Walker. 1991. El Jorullo, Mexico: The nature of "violent" strombolian eruptions is determined by the yield strength of magma? *EOS, Transactions of the American Geophysical Union* 72:568.
- Segerstrom, K. 1950. *Erosion Studies at Parícutin, State of Michoacán, Mexico*. U.S. Geological Survey Bulletin 965-A. Washington, DC: U.S. Geological Survey: 1-131.
- Smith, E.I., D.L. Feuerbach, T.R. Naumann, and J.E. Faulds. 1990. The area of most recent volcanism near Yucca Mountain, Nevada: Implications for volcanic risk assessment. *High-Level Radioactive Waste Management, International Conference*, April 8-12, 1990. La Grange, IL: American Nuclear Society: 1: 81-90.
- Spear, F.S., and K.L. Kimball. 1984. RECAMP - A FORTRAN IV program for estimating the Fe³⁺ contents in amphiboles. *Computers and Geosciences* 10: 317-325.
- Valentine, G.A., B.M. Crowe, and F.V. Perry. 1992. Physical processes and effects of magmatism in the Yucca Mountain Region. *Proceedings of the Third International Conference on High-Level Radioactive Waste Management*. La Grange, IL: American Nuclear Society and American Society: 2,014-2,024.
- Vaniman, D., and B. Crowe. 1981. *Geology and Petrology of the Basalts of Crater Flat: Applications to Volcanic Risk Assessment for the Nevada Nuclear Waste Storage Investigations*. LA-8845-MS. Los Alamos, NM: Los Alamos National Laboratory.
- Vaniman, D.T., B.M. Crowe, and E.S. Gladney. 1982. Petrology and geochemistry of Hawaiite lavas from Crater Flat, Nevada. *Contributions to Mineralogy and Petrology* 80: 341-357.
- Varekamp, J.C., and P.R. Buseck. 1983. Hg anomalies in soils: A geochemical exploration method in geothermal areas. *Geology* 12: 283-286.
- Vergniolle, S., and C. Jaupart. 1986. Separated two-phase flow and basaltic eruptions. *Journal of Geophysical Research* 91(B12): 12,842-12,860
- Walker, G.P.L. 1991. Origin of vesicle types and distribution patterns in the Xitle pahoehoe basalt, in Mexico City. *Eos, Transactions of the American Geophysical Union* 72: 766.
- Walker, G.P.L. 1993. The pyroclastic deposits of El Parícutin. *50 Años Del Volcán Parícutin, Reunión Internacional Conmemorativa, Programa y Resúmenes*, Uruapan, Michoacán: Mexico City: Instituto de Geofísica.
- Wilkinson, J.F.G. 1975. Ultramafic inclusions and high pressure megacrysts from a nephelinite sill, Nandewar Mountains, northeastern New South Wales, and their bearing on the origin of certain ultramafic inclusions in alkaline volcanic rocks. *Contributions to Mineralogy and Petrology* 51: 235-262.
- Williams, H. 1950. *Volcanoes of the Parícutin Region*. U.S. Geological Survey Bulletin 965-B: 165-279.
- Wilcox, R.E. 1954. Petrology of Parícutin Volcano. U.S. Geological Survey Bulletin 965-B: 281-353.
- Wilson, L., 1980. Relationships between pressure, volatile content, and ejecta velocity in three types of volcanic explosion. *Journal of Volcanology and Geothermal Research* 8: 297-313.
- Wilson, L., and J.W. Head III. 1981. Ascent and eruption of basaltic magma on the Earth and Moon. *Journal of Geophysical Research* 86(B4): 2,971-3,001.
- Wise, W.S. 1966. Zeolitic basanite from southern California. *Bulletin Volcanologique* 29: 235-252.

10 REGIONAL HYDROGEOLOGIC PROCESSES OF THE DEATH VALLEY REGION

by Gordon W. Wittmeyer, William M. Murphy, and David A. Ferrill

Investigators: David A. Ferrill, Christopher J. Goulet, H. Lawrence McKague, William M. Murphy, Kathy Spivey, and Gordon W. Wittmeyer (CNWRA); and D. Brent Henderson (SwRI)

NRC Project Officer: Thomas J. Nicholson

10.1 TECHNICAL OBJECTIVES

Yucca Mountain (YM) has been proposed as a potential high-level nuclear waste (HLW) repository in part because of the favorable geochemical and hydrologic environment provided by its 700-m thick unsaturated zone. Siting the repository in the unsaturated zone may significantly reduce the potential for waste canister corrosion and subsequent dissolution of the waste form. Moreover, the low water flux rates that are presumed to exist in the unsaturated zone reduce the likelihood that radionuclides that are dissolved will be rapidly transported to the accessible environment. Mechanisms that may saturate the repository horizon, and thus compromise favorable conditions provided by the YM site, include rapid infiltration of water from the surface through highly conductive fracture networks and an increase in the elevation of the regional water table. The first mechanism is a site-scale or subregional issue and is not addressed by this research project. Elevation of the water table may occur due to increased recharge to the regional carbonate system along stream channels and mountain fronts in topographically closed basins 100 km to the north and northeast of YM. Even if elevation of the regional water table does not saturate the repository block, the reduced thickness of the unsaturated zone has the potential to diminish travel times within the vadose zone. In addition, travel times in the saturated zone, and the location of potential discharge areas for dissolved radionuclides downgradient from YM are performance-related issues addressed by this research project. The primary objectives of this research project are to: (i) analyze existing conceptual models and develop new conceptual models of the regional hydrogeologic flow regime in the Death Valley region that contains YM, and (ii) construct numerical models of regional flow that may be used to assess the potential for the water table beneath YM to rise in response to wetter climatic conditions.

Predictions made with numerical models will be used by the U.S. Department of Energy (DOE) in its license application to demonstrate that the YM site meets the overall performance standards outlined in 10 CFR 60.112 and the geologic subsystem performance standard defined in 10 CFR 60.113(a)(2). In addition, the DOE may choose to use numerical models to demonstrate the absence or influence of potentially adverse conditions including: the effects of future pumping on the regional flow system [10 CFR 60.122(c)(2)]; the potential for deleterious changes to the hydrologic system [10 CFR 60.122(c)(5)]; the potential for changes to the hydrologic conditions resulting from climate change [10 CFR 60.122(c)(6)]; the potential for water table rise [10 CFR 60.122(c)(22)]; and the presence and influence of favorable conditions, including the clear absence of fully saturated pathways connecting the repository to the water table [10 CFR 60.122(b)(8)(ii)]. Understanding of the regional hydrogeologic system developed from this project will be used to guide the review of the DOE license application and to assess the adequacy of the models used by the DOE to demonstrate compliance with the regulatory requirements and environmental standards.

Understanding of the regional hydrogeologic system gained from this research project will also be used to construct specific Compliance Determination Methods (CDMs) outlined in the License Application Review Plan (LARP) (NRC, 1994). Literature reviews and hydrogeologic data gathered in Task 1 of the project will provide information that may be directly used to assess the description of individual systems and characteristics of the site (LARP Section 3.1) and, in particular, the description of the hydrologic and geochemical systems (LARP Sections 3.1.2 and 3.1.3, respectively). Evidence gleaned from literature reviews and data analysis in conjunction with conceptual and numerical models of the regional flow regime developed in this research project will be directly used

to determine if the applicant has provided convincing evidence of the presence or absence of favorable hydrogeologic conditions and potentially adverse hydrogeologic conditions (LARP Sections 3.2.1.1, 3.2.2.1, 3.2.2.3, 3.2.2.6, 3.2.2.8, 3.2.2.9, 3.2.2.11, and 3.2.4.2). Flow models developed in this project will also be used to confirm that velocity fields and travel times within the saturated zone estimated by the DOE are accurate enough to demonstrate compliance with the Groundwater Travel Time (GWTT) performance objective (LARP Section 3.3).

Compliance Determination Strategies (CDSs) for the LARP sections listed previously have been developed but will not be finalized until a thorough review of the LARP has been conducted. However, the Regional Hydrogeology Research Project will be instrumental in resolving specific technical uncertainties identified during the CDS development process. Key Technical Uncertainties (KTUs) that pose a high risk of noncompliance with the total-system or subsystem performance requirements may require that the Nuclear Regulatory Commission (NRC) conduct independent research to resolve the issue. Development of a conceptual groundwater flow model that is representative of the YM site groundwater system has been identified as a KTU that must be addressed in LARP Sections 3.2.2.1, 3.2.2.9, and 3.3.

The Regional Hydrogeology Research Project has been divided into five tasks: Task 1—Collect and analyze data and existing models; Task 2—Construct alternative conceptual models of key hydrogeologic processes in the Death Valley region of the western Great Basin; Task 3—Construct and calibrate mathematical and numerical models of subsurface flow at local, basin, and regional scales; Task 4—Use geochemical data to evaluate and refine regional flow models; and Task 5—Apply models to analyze problems critical to repository performance. Current plans call for completion of Tasks 1 and 2 during the first 2 years of the project with the remaining tasks to be initiated in the third year and completed by the fourth and final year of the project. Efforts during the past 6 months have primarily been focused on Task 2. The primary technical objectives of Task 2 are: (i) to critically evaluate geologic, hydrogeologic, and geochemical data from the Death Valley region; and (ii) use data compiled in the computerized Geographic Information System (GIS) to construct alternative conceptual models of flow in the Death Valley Region.

10.2 SIGNIFICANT TECHNICAL ACCOMPLISHMENTS

During the past 6 months, research has focused on collecting and analyzing hydraulic, hydrostratigraphic, geochemical, and structural data in order to critically evaluate existing conceptual models of interbasin flow in the Death Valley region, as well as to develop new conceptual flow models. These efforts have been closely focused on the issue of flow channeling within the Paleozoic rocks, that hydraulically connect the topographically closed basins at depth, and the fractured welded tuff aquifer in the vicinity of YM. Understanding the potential for, and consequences of flow channeling is essential for evaluating the potential for future climate changes to affect the performance of the repository. Local hydrogeologic studies of the Paleozoic carbonate aquifer suggest that channeling does occur along solution-widened faults and fracture zones. Research presented here suggests that the contemporary regional stress may control the hydraulic properties of fractures and fault zones and lead to anisotropy of the transmissivity. Incorporating anisotropy into flow maps of Yucca Flat shows that the direction of the Darcy flux differs significantly from the direction of the driving force. Anisotropy will be used in computational models to quantitatively demonstrate the effects of flow channeling. Chemical concentration measurements from waters in the tuffaceous aquifer near YM show undersaturation with respect to calcite. Since these tuffaceous rocks are known to contain calcite, the existence of zones or channels of water flow is suggested. Isolation of tuffaceous rocks containing calcite from the flow system is also supported by carbon isotope data and qualitative permeability data.

10.2.1 Relation of Geologic Structure to the Regional Carbonate Aquifer

The eastern two-thirds of the Great Basin, which includes the Death Valley region, is underlain by thick sequences of clastic and carbonate rocks that were deposited in shallow seas that covered most of western North America during Precambrian and Paleozoic times. In the vicinity of the Nevada Test Site (NTS), the Precambrian and Middle Cambrian strata are chiefly composed of quartzite and siltstone while the Middle Cambrian to Upper Devonian strata are primarily limestones and dolomites (Winograd and Thordarson, 1975). Reports by Dettinger (1989, 1992) and Burbey

and Prudic (1991) suggest that this description of the Precambrian to Upper Devonian rocks is generally accurate throughout the eastern two-thirds of the Great Basin. This portion of the Great Basin is commonly referred to as the Carbonate-Rock Province due to the strong hydraulic control exerted by the complexly deformed Paleozoic carbonate aquifer on movement of water between topographically closed basins. Burbey and Prudic (1991) note that the depositional thickness and lithology of the Paleozoic rocks are remarkably homogeneous throughout the province, however, post-depositional episodes of regional compression, extension, and igneous activity have significantly altered the current distribution and thickness of these strata. Dettinger (1992) notes that thinning of the carbonate-rock section in southern Nevada due to uplift and erosion, and extensional faulting, and denudation has been so extreme that in some areas the entire carbonate-rock section is missing. Within the Death Valley region, the thickness of the Paleozoic carbonate sequence is estimated to vary from more than 7,600 m in northwestern Pahranaagat and southeastern Tikaboo Valleys to less than 3,000 m in Pahute Mesa, Oasis Valley, Gold Flat, and Sarcobatus Flat (Dettinger, 1992).

Within the NTS, the Paleozoic carbonate aquifer is compartmentalized along normal faults by its juxtaposition with less permeable sequences of clastic rocks of Precambrian to Middle Cambrian, and Upper Devonian to Mississippian age, which are locally referred to as the lower clastic aquitard and upper clastic aquitard, respectively. Winograd and Thordarson (1975) have used the presence of a steep hydraulic gradient from Emigrant Valley (Groom Lake and Papoose Lake) to northeastern Yucca Flat to infer compartmentalization of the carbonate aquifer. Based on conceptual models developed by Wernicke et al. (1984), Dettinger (1992) has constructed a map delineating Tertiary extensional features in the southeastern portion of the carbonate province. This map indicates that Yucca Flat lies in an area relatively underformed during Tertiary extension while immediately to the northeast, across a north-trending shear zone, Emigrant Valley lies in an area where the carbonate-rock sequences have been broken by extreme extension. Understanding the continuity of the carbonate sequences is essential for understanding the regional movement of groundwater flow. Juxtaposition of broken terranes and stable terranes may produce some compartmentalization. Flow within broken terranes may be extremely complex, and

exact flow directions may be impossible to determine without an extensive network of boreholes.

10.2.2 Hydraulic Properties of the Paleozoic Carbonate Aquifer

Summaries by Winograd and Thordarson (1975) of outcrop studies of the Paleozoic carbonate strata suggest that, while the intercrystalline porosity of these rocks is extremely small, most outcrops are highly fractured and brecciated. According to Winograd and Thordarson (1975), "most outcrops exhibit three or more sets of joints, one or more high-angle faults, and one or more brecciated zones." Joints and faults observed in outcrops are predominantly high-angle fractures, and brecciation is typically observed adjacent to faults with only a meter or less of displacement. While the dip of most fractures is near vertical, the strike of major fracture sets varies considerably from area to area. According to Winograd and Thordarson (1975), the dominant strike of 933 high-angle fractures mapped within the Yucca Flat area ranged from N 20–30° W to N 20–30° E. By contrast, the dominant strikes of 384 faults mapped by Burchfiel (1965) in the Specter Range varied from about N 75° E to N 45° W. Unpublished studies cited by Winograd and Thordarson (1975) indicate that the density of joint or fracture sets is closely related to rock type. Within fine-grained carbonate rocks, joints are spaced from 1 to 5 cm, while in medium-grained carbonate rocks, joints are spaced from 5 to 30 cm, and within coarse-grained carbonate rocks, joints are spaced from 15 to 60 cm.

The intercrystalline porosity and permeability of rock cores from formations within the Paleozoic carbonate aquifer also are very small (Winograd and Thordarson, 1975). Measured effective porosities range from 0.0 to 9.0 percent, and measured hydraulic conductivities range from 2.1×10^{-10} to 1.0×10^{-6} m/s. The strike and aperture of major, high-angle fractures cannot be easily determined from these rock cores since most were obtained from vertical boreholes. In addition, only fractures that had been filled with breccia or clayey gouge, or had been partly filled or sealed with calcite, dolomite, or other minerals, remained intact during coring.

Pumping tests conducted in the Paleozoic carbonate aquifer demonstrate that its transmissivity varies greatly between formations. Estimated transmissivities range from 3 m²/s in the middle Cambrian Carrara Formation to 2.1×10^{-3} m²/s in the lower

Ordovician Pogonip Group (Winograd and Thordarson, 1975). The corresponding hydraulic conductivities for these tests are 6.0×10^{-2} m/s in the Carrara Formation and 9.2×10^{-6} m/s for the Pogonip Group. For both pumping tests, the estimated hydraulic conductivity greatly exceeds the minimum hydraulic conductivity determined from core samples, suggesting that fractures control the transmissive properties of the Paleozoic carbonate aquifer. Drill-stem tests conducted by swabbing open or packed-off intervals were used to identify water-bearing fracture zones within the borehole. According to Winograd and Thordarson (1975), the fracture transmissivity of the carbonate aquifer varies greatly with depth in each of the boreholes tested, but no uniform increase or decrease in transmissivity was observed. Winograd and Thordarson (1975) assert that transmissivity does not vary randomly within the region but is strongly controlled by structural features. Five wells that tap the upper plate of a low-angle thrust fault in the Paleozoic carbonates probably have higher than average transmissivities due to the intense fracturing that is commonly seen in thin thrust plates observed in outcrops. Winograd and Thordarson (1975) also state that variations in structure appear to have a more pronounced effect on the transmissivity than do changes in lithology.

Although solution features such as caves have been observed in outcrops of the Paleozoic carbonates, there is no direct evidence, such as the presence of buried sinkholes or karst features below the Tertiary unconformity, to suggest that large solution features control the hydraulic properties of the regional carbonate aquifer. The only major solution feature in Paleozoic strata within the Death Valley region, Devils Hole, is believed to be controlled by a nearly vertical fault and thus cannot be used to infer the presence of extensive solution channels within undisplaced, fractured carbonate rock masses. According to Winograd and Thordarson (1975), no major caverns have been encountered during drilling into the Paleozoic carbonate strata within Yucca Flat and the southeastern Amargosa Desert, although two of the test holes did encounter small (less than 1 m) voids as detected by lost drilling fluid circulation or rapid dropping of the drill-string. As evidence that fault zones, rather than solution-widened joints, are the principal water-bearing fractures within the lower carbonate aquifer, Winograd and Thordarson (1975) note that water pumped from one borehole in the upper Cambrian Nopah formation was muddy, although drilling mud had not been used during

construction, suggesting that gouge had been washed from an adjacent fault zone.

10.2.3 Evidence of Local Channeling in the Paleozoic Carbonate Aquifer

An in-depth hydrogeologic study of the Ash Meadows flow system was conducted by Dudley and Larson (1976) to evaluate the effect of increased irrigation pumping on the habitat of the endangered Devils Hole desert pupfish (*Cyprinodon Diaboli*) and other less endangered desert pupfish that inhabit the springs and outlet channels in the Ash Meadows area. Ash Meadows is a major discharge area for an extensive regional hydrogeologic system that is believed to receive recharge from the Belted Range, Groom Range, and Pahranaagat Range to the north, the Sheep Range to the northeast, and from the Spring Mountains to the immediate southeast. At Ash Meadows, approximately $58,000 \text{ m}^3$ of water discharges daily from 30 springs that lie along a line extending 16 km N 20–25° W from the north end of the Resting Spring Range. Approximately 35 percent of the flow is discharged from Fairbanks, Soda, Rogers, and Longstreet Springs along the northwestern portion of the spring line, 28 percent from Crystal Pool in the central region, and 29 percent from King, Point-of-Rocks, Jack Rabbit, and Big Springs at the southeastern end. Although all of these springs, except for one small discharge point at Point-of-Rocks, discharge through Pleistocene lake deposits, spring discharge is believed to be conveyed from the lower carbonate aquifer along a series of northwest-trending faults that juxtapose less-permeable Tertiary lake beds and bedded tuffs against the permeable Paleozoic carbonate aquifer. According to Winograd and Thordarson (1975), a gravity survey in the Ash Meadows area indicates that the Pre-Tertiary surface is downdropped 600 m along an inferred fault that lies 1.6 km to the west of the Ash Meadows spring line.

Dudley and Larson (1976) note that although the hydraulic properties of carbonate aquifers may appear to be homogeneous at a large scale, the behavior of the flow regime becomes "quite capricious" as the scale of observation is decreased due to the effects of channeling. Dudley and Larson (1976) point out that the development of highly conductive channels in carbonate rocks by chemical dissolution is controlled by: (i) the areal pattern of recharge, (ii) the position and orientation of structural discontinuities, and (iii) the position of the

area of discharge. By constructing a conceptual model that incorporates channeling and interpreting the effects of pumping in the Spring Meadows area, Dudley and Larson (1976) have attempted to explain the flow pattern from the regional carbonate aquifer to the discharge points in Ash Meadows. The concentrations of major ions and temperatures of water from wells and springs upgradient of Ash Meadows and from the Ash Meadows springs were also used to infer the existence of separate flow paths from the carbonate aquifer to discharge points in Ash Meadows. The flow paths identified by Dudley and Larson (1976) appear to coincide with two major sets of faults or lineations. One set of faults strikes northwest, subparallel to the Ash Meadows spring line and the other set, observed in the Paleozoic units that outcrop to the northeast of the spring line, strike N 20–30° E.

Large-scale channeling of flow in the carbonate aquifer at Ash Meadows has also been inferred by Winograd and Pearson (1976) from an anomalously large measured value of ^{14}C in Crystal Pool. The ^{14}C content averages 2.35 percent modern carbon in the other springs at Ash Meadows while at Crystal Pool the ^{14}C content is 11.1 percent modern carbon. Winograd and Pearson (1976) suggest that the difference in apparent ages indicated by the difference in ^{14}C content is the result of recharge from separate pluvial periods being advected along distinct flow paths at different velocities.

10.2.4 Flow in Fractured Rock and the Effect of *In Situ* Stress

Maps depicting the direction of flow through the Paleozoic carbonate aquifer have been constructed by assuming that the direction of flow is perpendicular to the potentiometric contours. However, the direction of flow and the direction of the driving force (negative gradient) are only parallel if the transmissive properties of the aquifer are isotropic. Invoking the assumption of isotropic transmissivity without carefully assessing its validity may lead to erroneous estimates of the direction of local and regional flow. No multiwell pumping tests have been conducted in the Paleozoic carbonate aquifer to quantitatively determine if it is hydraulically anisotropic. However, geologic evidence indicates that flow in the aquifer is primarily conducted through solution-widened fractures and fault zones, systems that are hydraulically anisotropic.

10.2.4.1 Conductivity and Transmissivity of Fractured Rock Masses

The formal mathematical relationships shown below between the geometry of idealized sets of fractures and the effective hydraulic properties of the fractured rock mass clearly illustrate the potential for anisotropic horizontal stress regimes to induce anisotropy of transmissivity. For flow of water in the Stokes regime (Reynolds number ≤ 10), the hydraulic conductivity of an assemblage of smooth-walled, parallel fractures, equally spaced a distance d , with identical apertures a , is given by

$$K = a^3 \frac{\rho g}{12\mu d} \quad (10-1)$$

where ρ is the density of the fluid, g is acceleration due to gravity, and μ is the dynamic viscosity. Note that Eq. (10-1) defines the hydraulic conductivity of the composite rock mass parallel to the fracture set.

Consider the two fracture sets shown in Figure 10-1. Fracture set α with constant fracture aperture a_α and fracture spacing d_α is oriented at an angle θ with respect to fracture set β , which has constant fracture aperture a_β , and fracture spacing d_β . The hydraulic conductivity of fracture set α parallel to its orientation and the hydraulic conductivity of fracture set β parallel to its orientation are given by

$$K_\alpha = a_\alpha^3 \frac{\rho g}{12\mu d_\alpha} \quad (10-2)$$

and

$$K_\beta = a_\beta^3 \frac{\rho g}{12\mu d_\beta} \quad (10-3)$$

respectively. By using elementary vector geometry, Maini and Hocking (1977) showed that the angle of the x_1 axis of the principal coordinates of the hydraulic conductivity tensor with respect to fracture set α is given by

$$\psi_1 = \frac{1}{2} \text{atan} \left(\frac{\sin 2\theta}{\cos 2\theta (K_\alpha/K_\beta)} \right) \quad (10-4)$$

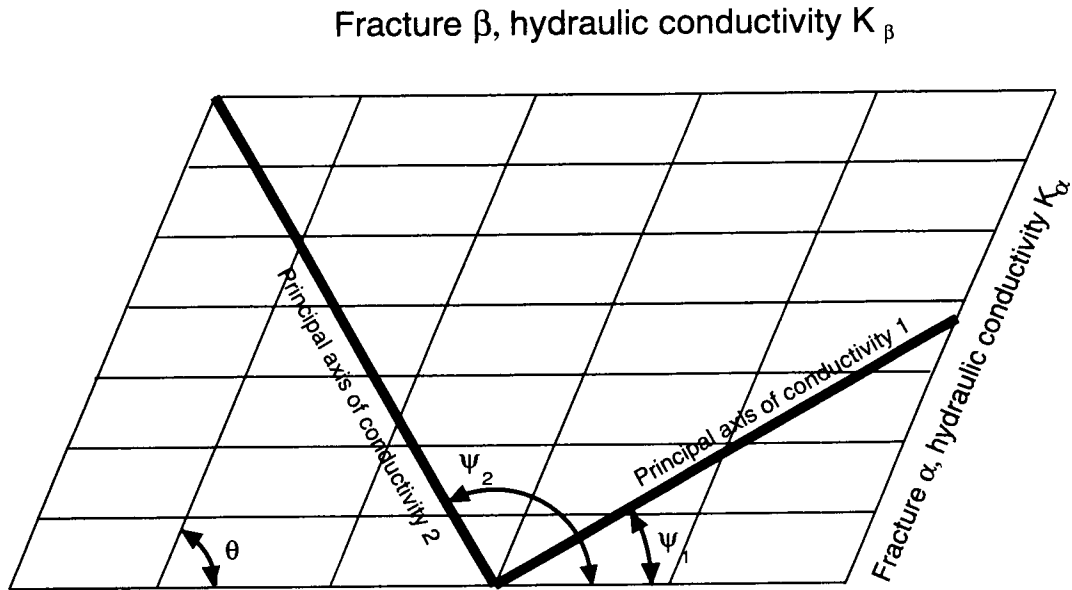


Figure 10-1. Orientation of the principal axes of anisotropy in a fractured medium in two dimensions (After Maini and Hocking, 1977)

The angle of the x_2 axis with respect to fracture set α is given by $\psi_1 + \frac{\pi}{2}$. The principal hydraulic conductivities are given by

$$K_1 = \frac{K_\alpha K_\beta \sin^2 \theta}{K_\alpha \sin^2 \psi + K_\beta \sin^2 (\theta - \psi_1)} \quad (10-5)$$

and

$$K_2 = \frac{K_\alpha K_\beta \sin^2 \theta}{K_\alpha \sin^2 \left(\psi + \frac{\pi}{2} \right) + K_\beta \sin^2 \left(\theta - \psi_1 - \frac{\pi}{2} \right)} \quad (10-6)$$

The hydraulic conductivity tensor for the working coordinate system with x'_1 axis parallel to fracture set α is given by

$$K' = A^T K A \quad (10-7)$$

where

$$K = \begin{bmatrix} K_1 & 0 \\ 0 & K_2 \end{bmatrix} \quad (10-8)$$

and

$$A = \begin{bmatrix} \cos \psi & \sin \psi \\ -\sin \psi & \cos \psi \end{bmatrix} \quad (10-9)$$

In order to simplify the mathematical expressions given above, only two fracture sets were assumed to exist. However, this development may be extended to incorporate any number of fracture sets with any strike and dip that would lead to the construction of a three-dimensional (3D), second rank hydraulic conductivity tensor. Within much of the lower carbonate aquifer, vertical gradients are assumed to be small relative to the saturated thickness of the aquifer. This assumption allows the 3D flow equation to be vertically

integrated and the conductance of the aquifer described by its transmissivity

$$T = \begin{bmatrix} z_u & z_u \\ \int K'_{11}(x) dx_3 & \int K'_{12}(x) dx_3 \\ z_l & z_l \\ z_u & z_u \\ \int K'_{21}(x) dx_3 & \int K'_{22}(x) dx_3 \\ z_l & z_l \end{bmatrix} \quad (10-10)$$

where x_3 is the vertical coordinate, $x = (x_1, x_2, x_3)$, z_1 is the elevation of the bottom of the aquifer, and z_u is the elevation of the top of the aquifer if confined, or the elevation of the water table if the aquifer is unconfined.

Note that for two fracture sets the hydraulic conductivity tensor [Eq. (10-8)], and thus the transmissivity tensor [Eq. (10-10)], is anisotropic for the case where the fractures are orthogonal and the mean apertures and spacing of the fracture sets are not equal, and for the case where the mean apertures and spacing of the fracture sets are equal and the fracture sets are non-orthogonal. It is apparent that there are an infinite number of combinations of fracture aperture, fracture spacing, and fracture orientation that will produce either isotropic or anisotropic hydraulic conductivity fields for two fracture sets.

10.2.4.2 Effect of *In Situ* Stress on Transmissivity

An isolated rock mass dissected by two orthogonal, vertically oriented fracture sets with identical fracture spacing and apertures has an isotropic transmissivity field. If the rock mass is now confined by equal horizontal compressional loads, the fracture apertures of both sets will be equally reduced and the transmissivity of each fracture set will be correspondingly reduced. As long as the state of horizontal stress in the rock mass is isotropic, the transmissivity tensor for the rock mass will remain isotropic. However, if the state of stress is anisotropic, fractures that are normal to the maximum principal stress will have smaller apertures than those parallel to the maximum principal stress. Note that in the case where the major and minor horizontal stresses bisect the angle of intersection of two sets of fractures with equal densities and apertures, the resulting transmissivity will

remain isotropic. This simple conceptual model becomes more complex when the fracture sets are nonorthogonal. Estimates of the relative change in fracture apertures can be determined by transferring the stresses to the fracture planes and computing the composite normal component of stress on each fracture set.

For the simple model presented above, the relationship between the anisotropy of the transmissivity for a fractured rock mass and the state of stress of the rock mass is easily seen. However, the spacing, orientation, and aperture size of actual rock fractures exhibit considerable variability, thus making the relationship between the composite hydraulic character and the state of stress less apparent. The concept may be readily tested in the field by performing one or more multiwell pump tests to determine the full transmissivity tensor, and comparing the orientation of its principal components to measurements of the orientation of the maximum and minimum *in situ* horizontal stresses. The principal directions of *in situ* stress may be determined from direct measurements of the stress tensor by overcoring, or inferred from borehole breakout orientations and fracture orientations obtained from hydro-fract tests.

Although the data on *in situ* stress are abundant at the NTS, no multiwell hydraulic tests have been performed in either the lower carbonate aquifer or the highly fractured, welded tuff aquifer. However, cross-hole pumping tests are planned at the C-well complex located in the welded tuff aquifer at the north end of Bow Ridge east of YM. Several multiwell pumping tests have been performed in the fractured Culebra Dolomite at the Waste Isolation Pilot Plant (WIPP) site in southeastern New Mexico (Figure 10-2) and several measurements of contemporary *in situ* stress in elastic rocks are available for areas near the WIPP (Zoback, 1992).

The WIPP is a mined geologic repository for transuranic waste located in the Permian Salado formation, which is composed primarily of highly plastic rock salt with minor beds of anhydrite and clayey to silty clastics (Brinster, 1991). The Salado is overlain by the Rustler formation, which is composed of five members. These members are, in ascending order, the unnamed lower member, the Culebra Dolomite Member, the Tamarisk Member, the Magenta Dolomite Member, and the Forty-Niner Member (Brinster, 1991). The hydrology of the Culebra Dolomite Member has

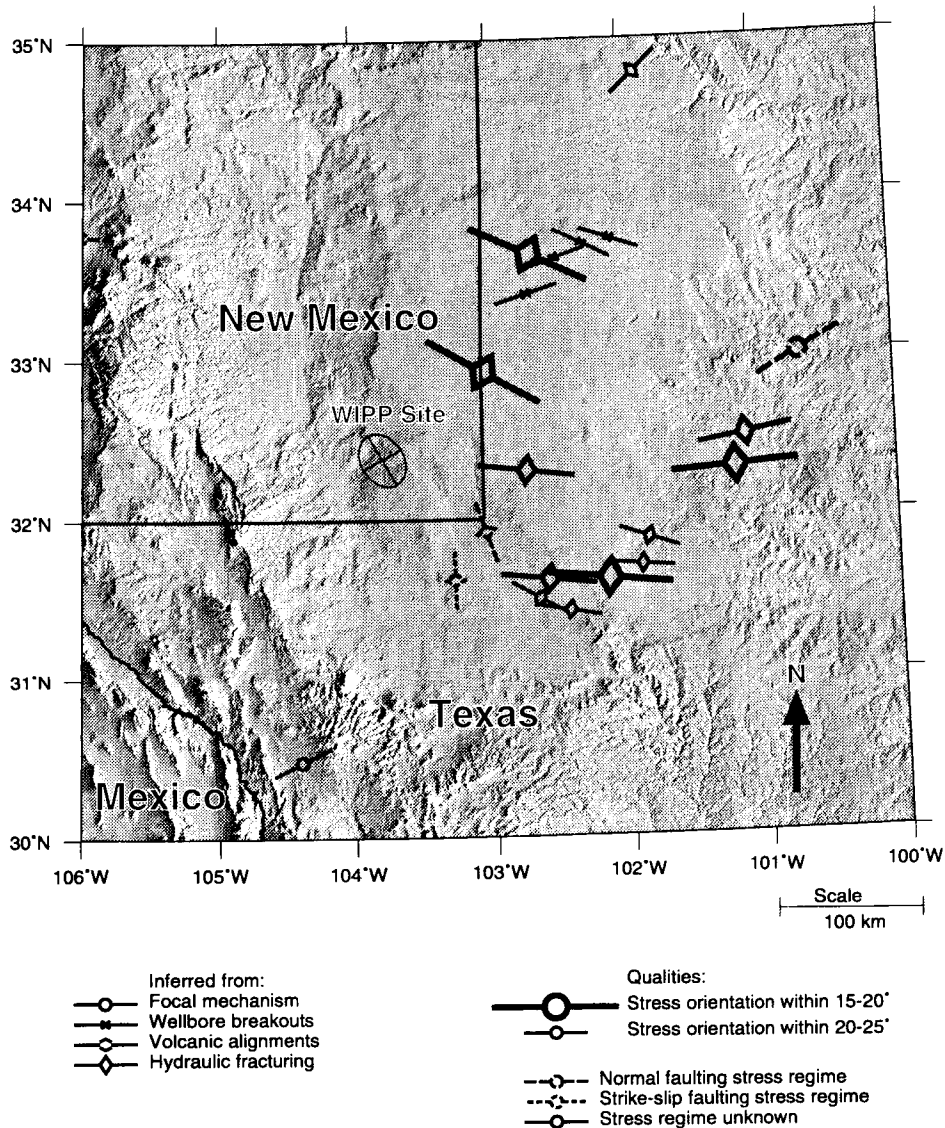


Figure 10-2. Physiography of the WIPP Site, New Mexico, with directions of inferred maximum horizontal *in situ* regional stress

been extensively investigated because it is believed to be one of the most likely paths for radionuclides released from the repository to reach the accessible environment. The thickness of the Culebra Dolomite ranges from 4.8 to 11.0 m, and the hydraulic conductivity ranges from 1×10^{-10} to 1×10^{-4} m/s (Brinster, 1991).

Procedures for determining the transmissivity tensor from four wells, one pumped with drawdown

recorded in the remaining three, have been developed by Papadopoulos (1965), Hantush (1966), and Way and McKee (1982). Neuman et al. (1984) developed a procedure for determining the transmissivity tensor with only three wells if a minimum of two pumping tests are performed with the pump located in a different well for each test. Neuman et al. (1984) applied their method to pumping test data obtained from the H-6 well-pad at the WIPP site. The three boreholes at the H-6 well-pad all penetrate the highly transmissive Culebra Dolomite.

Analysis of the drawdown data indicated that the principal transmissivities are $T_1=1.0 \times 10^{-4}$ and $T_2=5.4 \times 10^{-5}$ m²/s, and the maximum principal transmissivity is oriented N 29.6° W (Neuman et al., 1984). The transmissivity ellipse corresponding to the estimates obtained by Neuman et al. (1984) is shown in Figure 10-2. Other multiwell pumping tests have been conducted in the Culebra Dolomite at the H-3, WIPP-13, and H-11 well-pads (Brinster, 1991). Beauheim (1987) presents detailed information on two pump tests conducted at the H-3 drillpad. In Test 1, borehole H-3b3 was pumped, and drawdown was monitored in the two other wells that form the H-3 hydropad. In Test 2, borehole H-3b2 was pumped with drawdown monitored in 11 other boreholes located from 27 to 5,126 m away. Data from Test 1 are not suitable for employing either the Neuman et al. (1984) procedure for three boreholes or other interpretation methods that require a minimum of four boreholes. Data from Test 2 could be interpreted using any of the three procedures requiring one pumping and three observation wells. The report by Beauheim (1987) does not indicate that anisotropic pump test interpretation methods were used for Test 2; however, in summarizing the directional transmissivity data, Beauheim (1987) notes that the transmissivities appear to be highest from H-3 toward the southeast. This observation appears to be in basic agreement with the analysis by Neuman et al. (1984). Brinster (1991) constructed a plot of the change in transmissivity as a function of azimuth from H-3 for Test 2. This plot also indicates that transmissivity increases toward the southeast (112 to 138°).

Wawersik and Stone (1989) conducted hydraulic fracturing tests within the bedded salts in the Salado Formation to assess the utility of this method for determining *in situ* stress in inelastic rock. Although creep and stress relaxation in the salt appear to complicate the analysis of the hydraulic fracturing, Wawersik and Stone (1989) conclude that the virgin *in situ* stress in the bedded Salado Formation at the WIPP is isotropic. It seems incorrect, however, to conclude from these results that the virgin *in situ* stress within the dolomite beds in the overlying Rustler Formation is also isotropic. The tendency for salt to deform plastically under load suggests that salt should not, in general, be in the same state of stress as an overlying or underlying elastic rock unit subject to the same loads.

Regional *in situ* stress measurements near the WIPP site compiled by Zoback (1992) and Zoback et al.

(1992) are shown in Figure 10-2. Orientations of the maximum horizontal *in situ* stress made by various methods in elastic rock located east of the WIPP site show an overall northwest trend. The mean orientation of the four stress measurements nearest to the WIPP site is N 42° W, with an estimated error of plus or minus 19–24°. This orientation is fairly close to the orientation of the principal transmissivity determined by Neuman et al. (1984) and the orientation of the maximum transmissivity determined by Beauheim (1987). While this close agreement does not prove the hypothesis, it certainly lends credence to the basic conceptual model presented here.

10.2.5 Effect of Anisotropy on Flow in the Paleozoic Carbonate Aquifer in Yucca Flat, Death Valley Regional Flow System

Although the potential for flow channeling, as well as its effects on conceptual models of the hydraulic properties of the Paleozoic carbonate aquifer, appear to be well understood, there have been no published reports in which the effects have been incorporated into the construction of large-scale hydrogeologic maps. Incorporating the anisotropic effects of channeling in fracture networks has the potential to alter current conceptual models of the orientation of flowpaths connecting recharge and discharge zones. Measured hydraulic head data are sparse within the Death Valley region. However, at the NTS, extensive networks of boreholes for measuring hydraulic head have been established in areas where weapons testing has been conducted and where site characterization activities for the proposed HLW repository are taking place. Hydraulic head measurement networks exist on Pahute Mesa, YM, Frenchman Flat, and Yucca Flat. However, only within Yucca Flat do a large number of boreholes penetrate the Paleozoic carbonate aquifer. In addition, as noted previously, there are numerous measurements of the orientation of the minimum horizontal *in situ* stress within Yucca Flat [Springer et al. (1984), Gillson (1993)].

10.2.5.1 Geologic and Hydrogeologic Setting of Yucca Flat

Figure 10-3 shows the surficial exposure of the major hydrostratigraphic units within Yucca Flat, 50 m topographic contours, the location of boreholes in which 40 percent or more of the screened section occurs in Paleozoic units, and the location and orientation of the

maximum horizontal stress determined from borehole breakout measurements. Yucca Flat is bounded on the west by Mine Mountain and Syncline Ridge, on the northwest by the Eleana Range, on the north by Rainier Mesa, Quartzite Ridge, and Oak Spring Butte, on the northeast and east by the Halfpint Range, and on the south by French Peak, and Massachusetts Mountain. Most units exposed in Mine Mountain, Syncline Ridge, the Eleana Range, and Quartzite Ridge are from the Eleana Formation, which is composed of Devonian to Mississippian argillite and quartzite. The Eleana is the primary formation in the upper clastic aquitard defined by Winograd and Thordarson (1975). Rainier Mesa is composed of a sequence of Tertiary bedded and welded tuffs. Rocks exposed in Oak Spring Butte are granodiorite and quartz monzonite from Permian to Cretaceous granitic stocks. According to Winograd and Thordarson (1975), these granitic stocks form a local aquitard. Rocks exposed in the northwestern portion of the Halfpint Range consist of quartzite, siltstone, shale, and limestone of Precambrian to Cambrian age. These Precambrian to Cambrian rocks form the regionally extensive lower clastic aquitard. Rocks exposed in the southeastern portion of the Halfpint Range, French Peak and Massachusetts Mountain are predominantly limestones and dolomites of Cambrian to Devonian age. These carbonate units together comprise the regionally extensive Paleozoic carbonate aquifer. The Paleozoic carbonate units also crop out along the eastern flanks of Shoshone Mountain and the Eleana Range, along the western flank of the Halfpint Range, and west of Oak Spring Butte. Within the central portion of Yucca Flat, the Paleozoic carbonate aquifer is successively overlain by the Tertiary tuff aquitard, Tertiary bedded and welded tuff aquifer, and the Quaternary valley-fill aquifer.

Water recharged along the flanks of the mountains bounding Yucca Flat is presumed to discharge as underflow from Yucca Flat through the Paleozoic carbonate aquifer. According to Winograd and Thordarson (1975), boreholes drilled through Cenozoic deposits and into the Paleozoic carbonate units generally show a decrease in hydraulic head with depth, suggesting that water flows downward through the alluvium and tuffs, and into the lower carbonate aquifer. The great depths to water measured throughout the eastern portion of Yucca Flat and the fact that Yucca Lake is a dry playa further support the hypothesis that water leaves Yucca Flat through the lower carbonate aquifer. On the basis of estimated hydraulic gradients,

water leaving Yucca Flat through the lower carbonate aquifer is presumed to enter Frenchman Flat to the south, although the location at which the flow enters Frenchman Flat is unknown.

10.2.5.2 Contemporary *In Situ* Stress in Yucca Flat

The orientations of the maximum horizontal stress inferred from borehole breakout data and hydraulic fracturing experiments are shown in Figure 10-3. The data used to construct this plot were obtained from Gillson (1993) and Springer et al. (1984). Data obtained by overcoring from the tuffs penetrated by the Rainier Mesa tunnel complex and from the granite in the Climax Mine, are more apt to reflect the effects of topographic relief than those obtained within the valley floor and are not included. A rose diagram depicting the direction of maximum horizontal stress is shown in Figure 10-4. The mean azimuth of the maximum horizontal stress, based on the five largest azimuth classes (20–30, 30–40, 40–50, 10–20, and 50–60°), is N 39° E. Orientations that differ greatly from the mean azimuth are presumed to reflect local topographic or structural effects.

10.2.5.3 The Effect of Anisotropic Transmissivity on Flow in Yucca Flat

Figure 10-5 shows hydraulic head contours based on measurements made in 25 boreholes in which 40 percent or more of the screened interval penetrates Paleozoic rocks. Analysis of the well hydrographs for the 25 selected boreholes was complicated by not having each borehole's detailed drilling history. In the absence of drilling history information, steady-state hydraulic heads were estimated by computing the average for the longest horizontal portion of each hydrograph. In the eastern portion of Yucca Flat, the primary Paleozoic hydrostratigraphic unit penetrated by the wells is the lower carbonate aquifer, while in the western portion of Yucca Flat, the primary hydrostratigraphic unit is the upper clastic aquitard. Relatively flat gradients measured in the lower carbonate aquifer in the eastern portion of Yucca Flat suggest that flow is primarily horizontal and the associated contours are fairly accurate. Contours constructed from wells penetrating the lower permeability Eleana Formation in the west are probably less reliable.

If the equipotential lines depicted in Figure 10-5 are assumed to be vertical, and the

Hydrostratigraphic Map of Yucca Flat

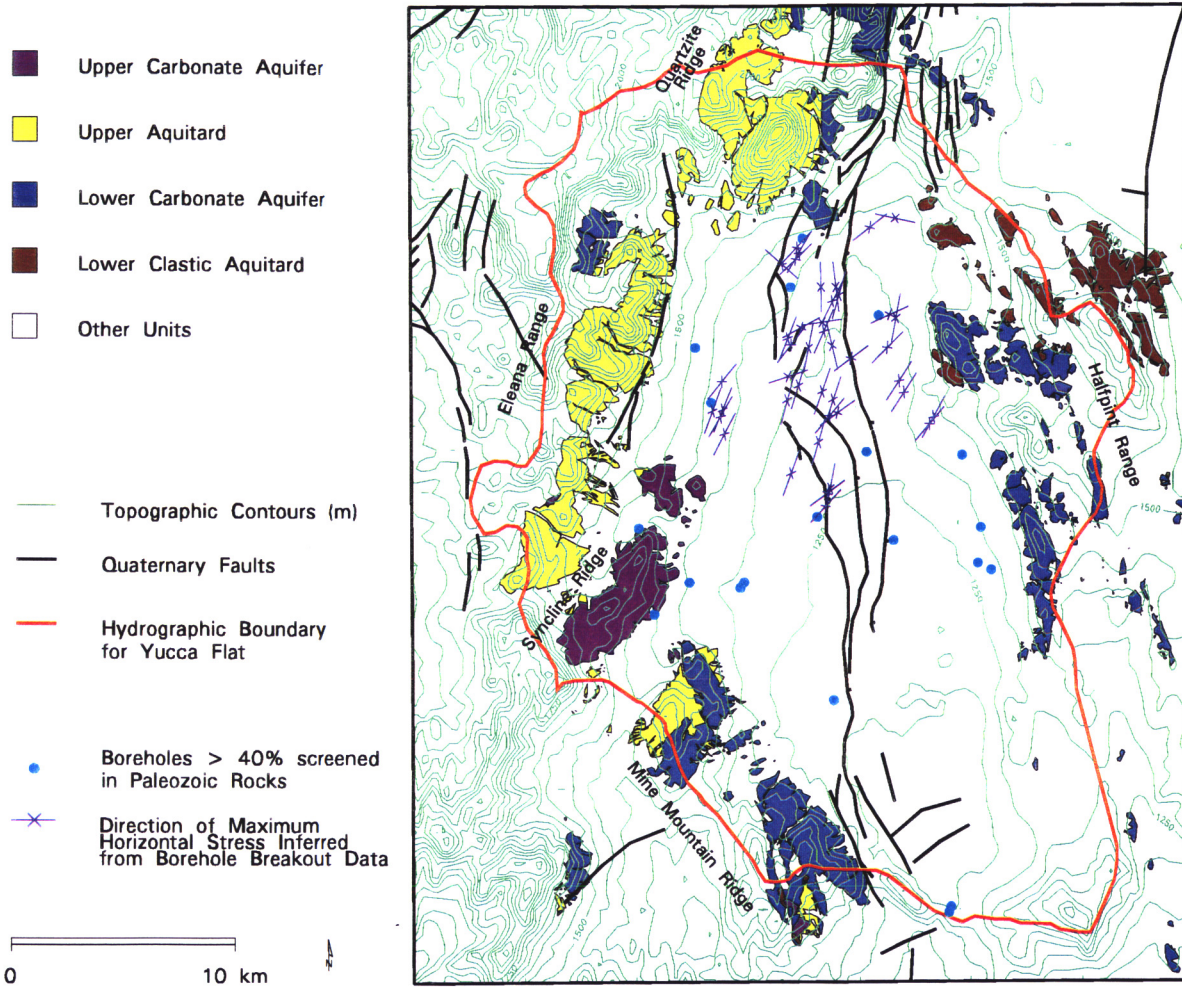


Figure 10-3. Hydrostratigraphic map of Yucca Flat with topographic contours (m), locations of boreholes with water level measurements in the Paleozoic rocks, inferred orientation of maximum *in situ* horizontal stress, and Quaternary faults.

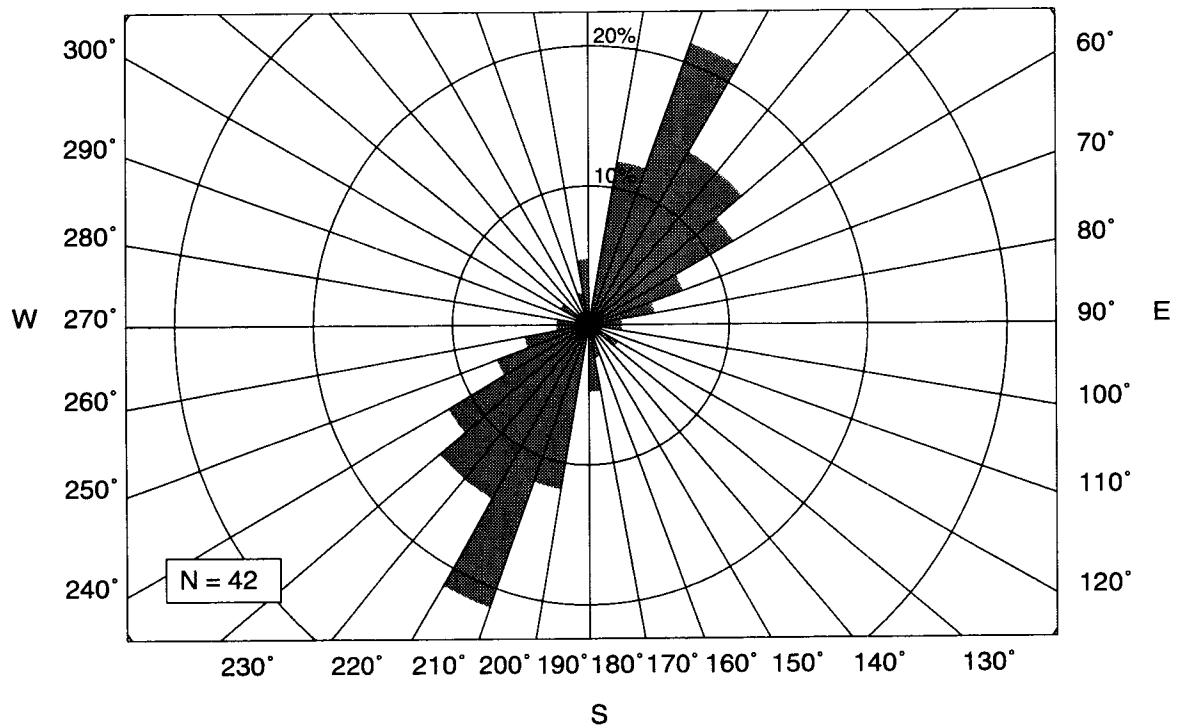


Figure 10-4. Rose diagram of orientation of inferred maximum horizontal *in situ* stress at Yucca Flat, Nevada

transmissivity is assumed to be homogeneous and isotropic, the arrows shown in Figure 10-5 depict the direction of flow within the carbonate aquifer. If it is assumed that transmissivity within Yucca Flat is anisotropic with maximum principal component parallel to the direction of maximum horizontal stress (N 39° E), the actual flow direction will be deflected from that shown in Figure 10-5. Figures 10-6 through 10-9 show the orientation of the driving force (short arrow) and the orientation of the resulting flow (long arrow) for anisotropy ratios $T_x/T_y = 2, 3, 4,$ and $5,$ respectively, where the x_1 axis is parallel to the major semi-axis of the transmissivity ellipse shown in the upper righthand corner of each figure. These anisotropy ratio values were selected only to illustrate their effect on the actual flow direction. Although there are no data from Yucca Flat that may be used to support or refute transmissivity ratios as large as 5, the data from WIPP suggest that transmissivity ratios of 2 are not unreasonable in fractured rock. It is readily apparent that, in areas where the driving force is not parallel to the maximum horizontal stress, incorporating the effect of anisotropic transmissivity changes the estimated direction of flow in the lower carbonate aquifer. In northern Yucca Flat, where a cluster of measurement locations makes the

head contours fairly accurate, increasing the anisotropy ratio changes the flow direction from east to northeast between Banded Mountain to the south and the Smoky Hills to the north. Flow in east central Yucca Flat, where head contours are also fairly accurate, is deflected from the south to the southwest. Note, however, that flow from the area near Syncline Ridge and Mine Mountain toward central Yucca Flat is unaffected. Figure 10-10 (a) through (d) show the angle between the hydraulic driving force and the flow direction corresponding to transmissivity anisotropy ratios of 2, 3, 4 and 5. These figures clearly show that the greatest effects of incorporating anisotropy occur in the northern, southwestern and eastern portions of the contoured region. Figures 10-11 (a) through (d) show the angle between the orientation of maximum horizontal stress and the direction of the Darcy flux corresponding to transmissivity anisotropy ratios of 1, 2, 3 and 5. In Figures 10-11 (a) through (d), the light shaded zones indicate areas in which the angle between the flux direction and the orientation of the maximum horizontal stress is relatively small while the dark shaded zones indicate areas where this angle is relatively large. These figures show that as the degree of anisotropy increases, the flow direction becomes increasingly parallel to the

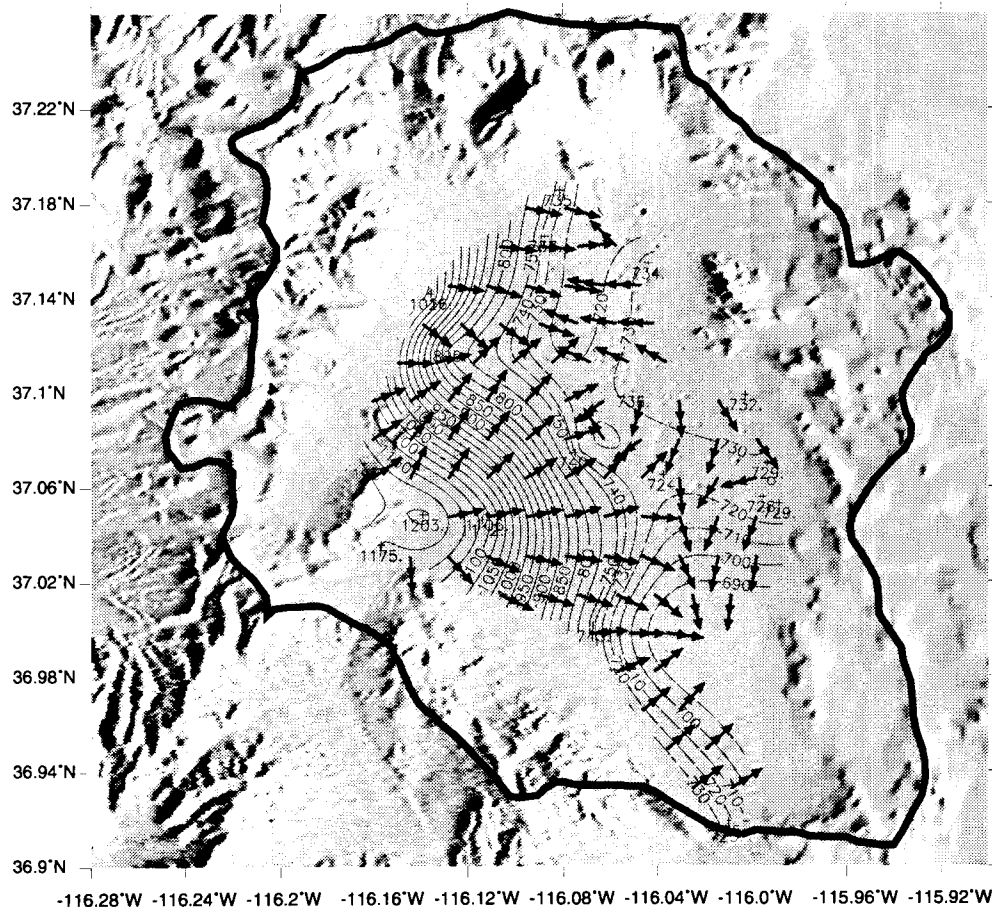


Figure 10-5. Contours of hydraulic heads (interval is 50 m except in southeastern portion where interval is 10 m) measured in Paleozoic units with orientation of driving force depicted by arrows

direction of maximum horizontal stress. Caution should be exercised in using Figures 10-5 through 10-9 to draw firm conclusions about flow in Yucca Flat since, as noted earlier, the steady-state head contours were constructed without detailed information on each borehole's drilling history.

10.2.6 Implications of Stress and Transmissivity Anisotropy on Conceptual Models of Regional Flow

Figures 10-5 through 10-9 should not be used by themselves to construct alternative conceptual models of flow between Yucca Flat and adjoining hydrologic basins, since the contours do not reflect head measurements in the adjoining basins. However, it is readily apparent that incorporating transmissivity

anisotropy into regional contour maps may alter conceptual models of interbasin transfer of water.

Conceptual models of the Death Valley region flow system have been developed by Rush (1971), Winograd and Thordarson (1975), Waddell (1982), Waddell et al. (1984), and Burbey and Prudic (1991). The hydrographic basins and flow boundaries included in the Death Valley regional flow systems defined by Rush (1971), Winograd and Thordarson (1975), Waddell (1982), and Waddell et al. (1984) are similar. Although there are minor differences in the author's definitions, each of these conceptual models includes three groundwater systems: (i) Ash Meadows, (ii) Oasis Valley, and (iii) Alkali Flat-Furnace Creek. The Ash Meadows system, previously discussed in Section 10.2.3, is generally believed to receive recharge in the northeast from the Pahranaagat, Timpahute, and Sheep

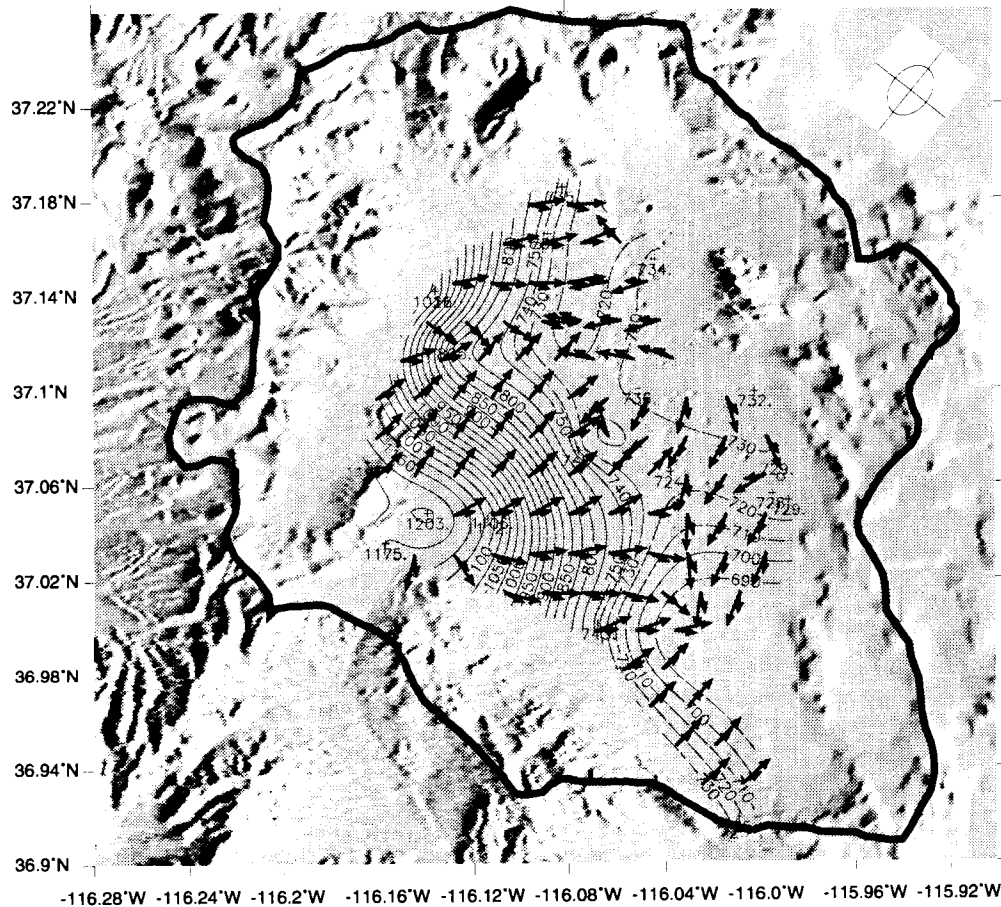


Figure 10-6. Orientation of Darcy flux for transmissivity anisotropy ratio $T_x/T_y=2$ shown by long arrow. Orientation of driving force is shown by short arrow.

Ranges, and from underflow from Pahrnatag Valley, and in the east from the Spring Mountains (see Figure 8-8). Most of the water in the Ash Meadows system discharges from the spring line at Ash Meadows, although there may be some underflow through Cenozoic aquifers from Ash Meadows to the Alkali Flat-Furnace Creek system to the west. The Oasis Valley system receives recharge from western and central Pahute Mesa. Most water discharges from the Oasis Valley system north of Beatty along a series of springs in Oasis Valley. Some water exits the Oasis Valley system as underflow to the Alkali Flat-Furnace Creek system through the Amargosa Desert. Recharge to the Alkali Flat-Furnace Creek System comes from the Cactus, Reveille, and Kawich Ranges to the north. This system discharges by evapotranspiration at Alkali

Flat (Franklin Lake Playa) and through springs located near Furnace Creek in Death Valley.

The boundaries for the Death Valley regional flow system defined in the Regional Aquifer System Analysis (RASA) of the carbonate-rock province in the Great Basin conducted by Burbey and Prudic (1991) differ markedly from those of previous studies. Burbey and Prudic (1991) exclude from their model Tikaboo Valley, which is bounded on the east by the Sheep and Pahrnatag Ranges and on the west by the Groom and Pintwater Ranges, and Northern Three Lakes Valley, which is bounded on the east by the Sheep Range and on the west by the Pintwater Range. Instead, within the vicinity of the NTS, the eastern boundary of the flow system is formed by the Groom and Pintwater Ranges. The northern extent of the Death Valley flow system has

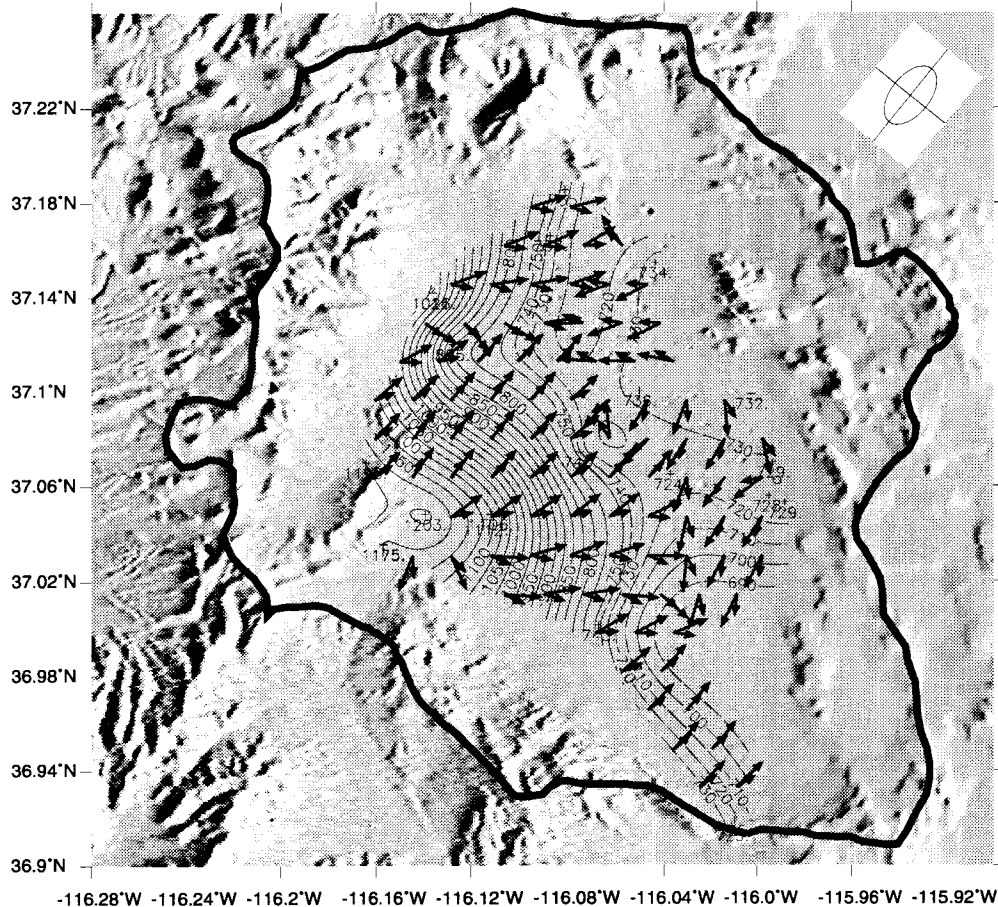


Figure 10-7. Orientation of Darcy flux for transmissivity anisotropy ratio $T_x/T_y=3$ shown by long arrow. Orientation of driving force is shown by short arrow.

been considerably expanded to the north to include recharge from the Hot Creek, Monitor, Toiyabe, and Toiyabe Ranges. Southward flow of groundwater from these more northern ranges is inferred from the relatively "light" deuterium values ($\delta D = -110\text{‰}$) found in Reveille Valley, which suggests this water was recharged farther to the north (Burbey and Prudic, 1991).

A preliminary regional groundwater flow map which includes measurements of the maximum horizontal stress in the Death Valley region is discussed in Chapter 8 on research performed in collaboration with the research project on Tectonic Processes of the Central Basin and Range. This map, shown in Figure 8-8, indicates that while regional flow is primarily topographically driven from areas of increased recharge in the north toward discharge areas

at lower elevations in the south, there is a fairly strong correlation between the patterns of regional maximum horizontal stress and the predominant flow direction. Until computational models are developed, it is difficult to assess how the changes to the conceptual model developed by Burbey and Prudic (1991) will affect flow near YM. However, prior to the development of new computational models, additional analysis should be performed to determine the effect of anisotropy on flow directions in the typical flow model of the Death Valley region by Waddell et al. (1984) and the newer flow model developed by Burbey and Prudic (1991). In addition to testing the effect of anisotropy on the regional flow system, the methods introduced herein should be applied to flow in the fractured, welded-tuff aquifer near YM, with particular emphasis on the nature of the steep hydraulic gradient north of YM. As shown

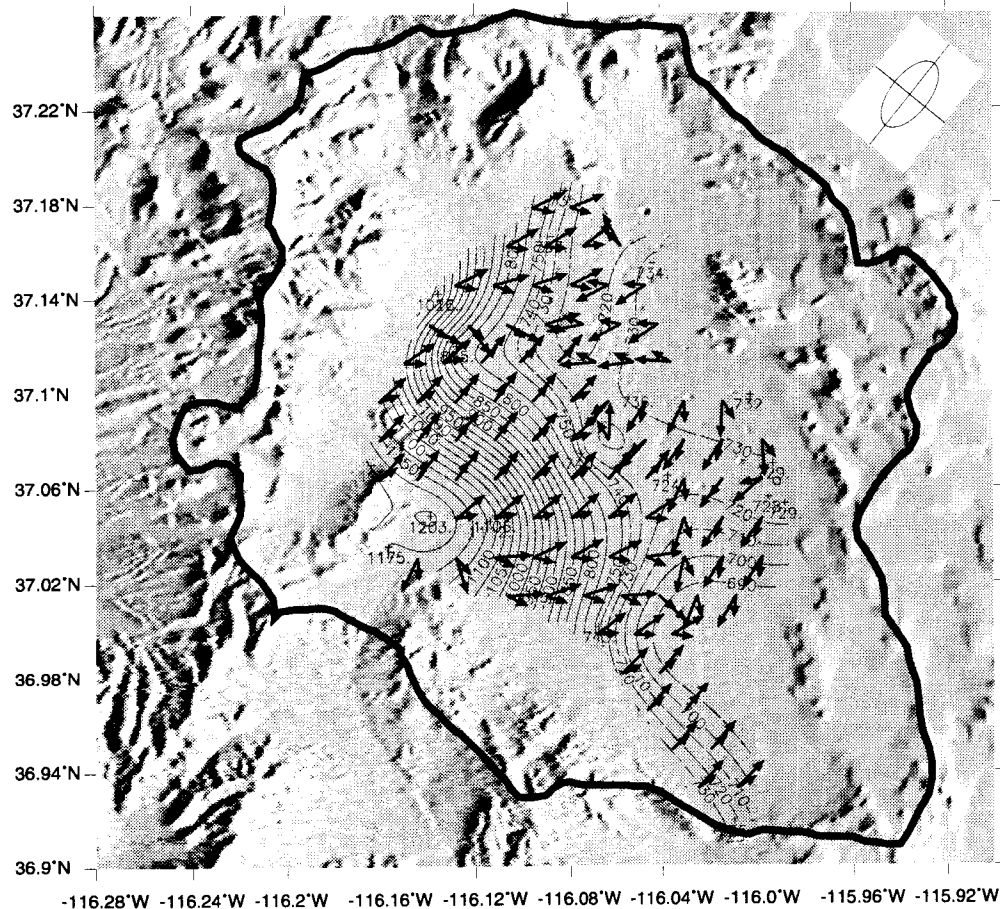


Figure 10-8. Orientation of Darcy flux for transmissivity anisotropy ratio $T_x/T_y=4$ shown by long arrow. Orientation of driving force is shown by short arrow.

below, geochemical evidence suggests that channeling does occur in the tuffaceous aquifer at YM.

10.2.7 Calcite and Channeling in the Tuffaceous Aquifer Near Yucca Mountain

Calcite is a common mineral in tuffaceous rocks from the vicinity of YM, although it is not generally abundant or ubiquitous (e.g., Carlos, 1987; Bish and Chipera, 1989). Calcite is a predominate mineral in Paleozoic rocks underlying the tuffs. Examination of the occurrence and isotope chemistry of calcite in the YM region provides a variety of indications concerning regional groundwater flow. Oxygen isotope analyses of calcite from Devils Hole dated by uranium series analyses reveal variations that correlate to climatic variations (Winograd et al., 1992). The resolution of the variations at a scale of 10,000 yr or

less precludes variable travel times on this scale or greater for waters from different sources to Devils Hole. Calcite dated by uranium series methods from spring deposits in Crater Flat indicates episodic discharge over the last 50,000 yr at levels that are up to 116 m above the present regional water table (Paces et al., 1993). Calcite occurring in fractures in the unsaturated zone at YM has been interpreted to record paleohydrologic pathways (Whelan et al., 1994). In contrast, the occurrence of calcite in the saturated zone tuffaceous aquifer in the vicinity of YM is an indication that groundwater flow is channelized and that portions of the rock are effectively isolated from present water circulation. This conclusion is supported by the isotopic composition of the calcite in comparison to that of the groundwater and underlying Paleozoic carbonate rocks, the chemical saturation state of the groundwater with

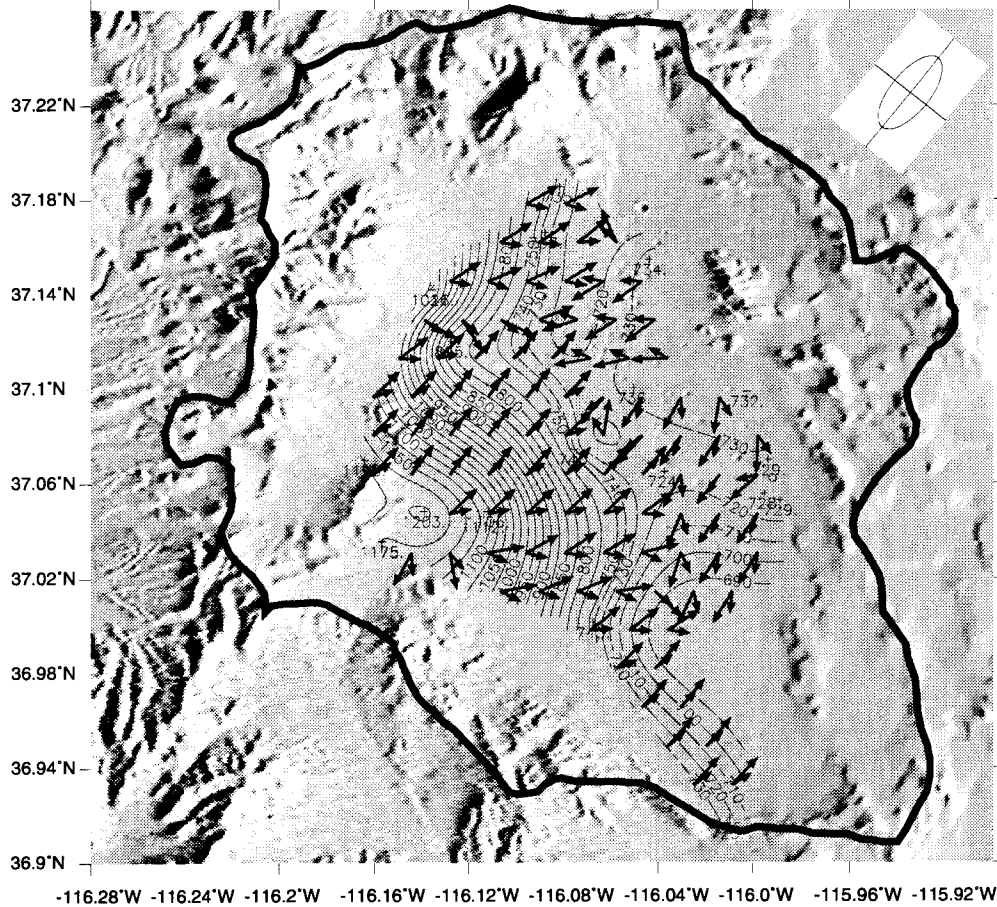


Figure 10-9. Orientation of Darcy flux for transmissivity anisotropy ratio $T_x/T_y=5$ shown by long arrow. Orientation of driving force is shown by short arrow.

respect to calcite, and relations between calcite occurrence and permeability.

Calcite in tuffaceous rocks from below the water table in the vicinity of YM occurs as milky veins and replacement cements (Broxton et al., 1987). It is particularly abundant in borehole USW G-2 (Bish and Chipera, 1989) where there is mineralogic evidence of hydrothermal alteration, which has been dated at approximately 10 to 11 Ma (Bish and Aronson, 1993). A variety of contrasts between unsaturated and saturated zone calcites led Whelan et al. (1994) to propose that calcite in the saturated tuffaceous rocks in the vicinity of YM generally formed during this hydrothermal event. The carbon isotopic composition of calcite from greater than 300 m depth below the water table ($\delta^{13}\text{C} = -2$ to 5‰) is generally compatible with precipitation from water that presently occurs in the regional aquifer in

Paleozoic carbonate rocks ($\delta^{13}\text{C} = -5.2$ to -2.3‰), which contrasts with water presently in the tuffaceous aquifer ($\delta^{13}\text{C} = -11.4$ to -4.9‰) (Whelan and Stuckless, 1992).

Computations were performed with EQ3NR version 7.1 with database DATA0.COM.R16 (Wolery, 1992) using the temperatures of the water samples at the time of collection, which are generally between 25 °C and 40 °C. Temperature and chemical analysis data were taken from Kerrisk (1987) for water samples from boreholes J-12, J-13, UE-25b#1, UE25c#1, UE-29a#2, USW G-4, USW H-1, USW H-4, USW H-5, USW H-6, and USW VH-1. Data from boreholes USW H-3 and UE-25p#1 were not included because the chemical analyses and aqueous speciation calculations indicate relatively poor charge balance, and because water from UE-25p#1 is likely to be a mixture of tuffaceous and

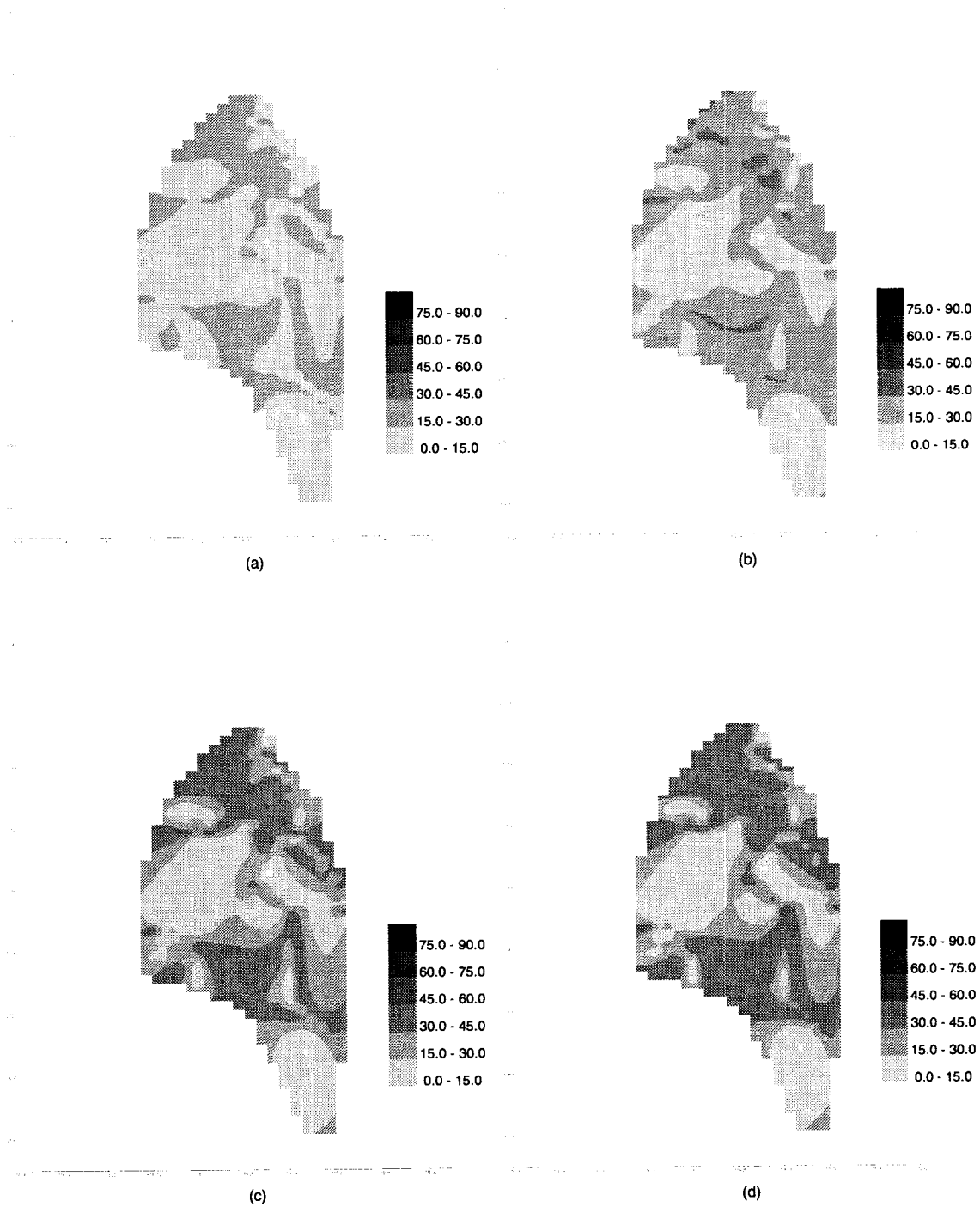


Figure 10-10. Angle between direction of driving force and direction of resulting Darcy flux in Paleozoic aquifer in Yucca Flat for: (a) anisotropy ratio of 1, (b) anisotropy ratio of 2, (c) anisotropy ratio of 3, and (d) anisotropy ratio of 5

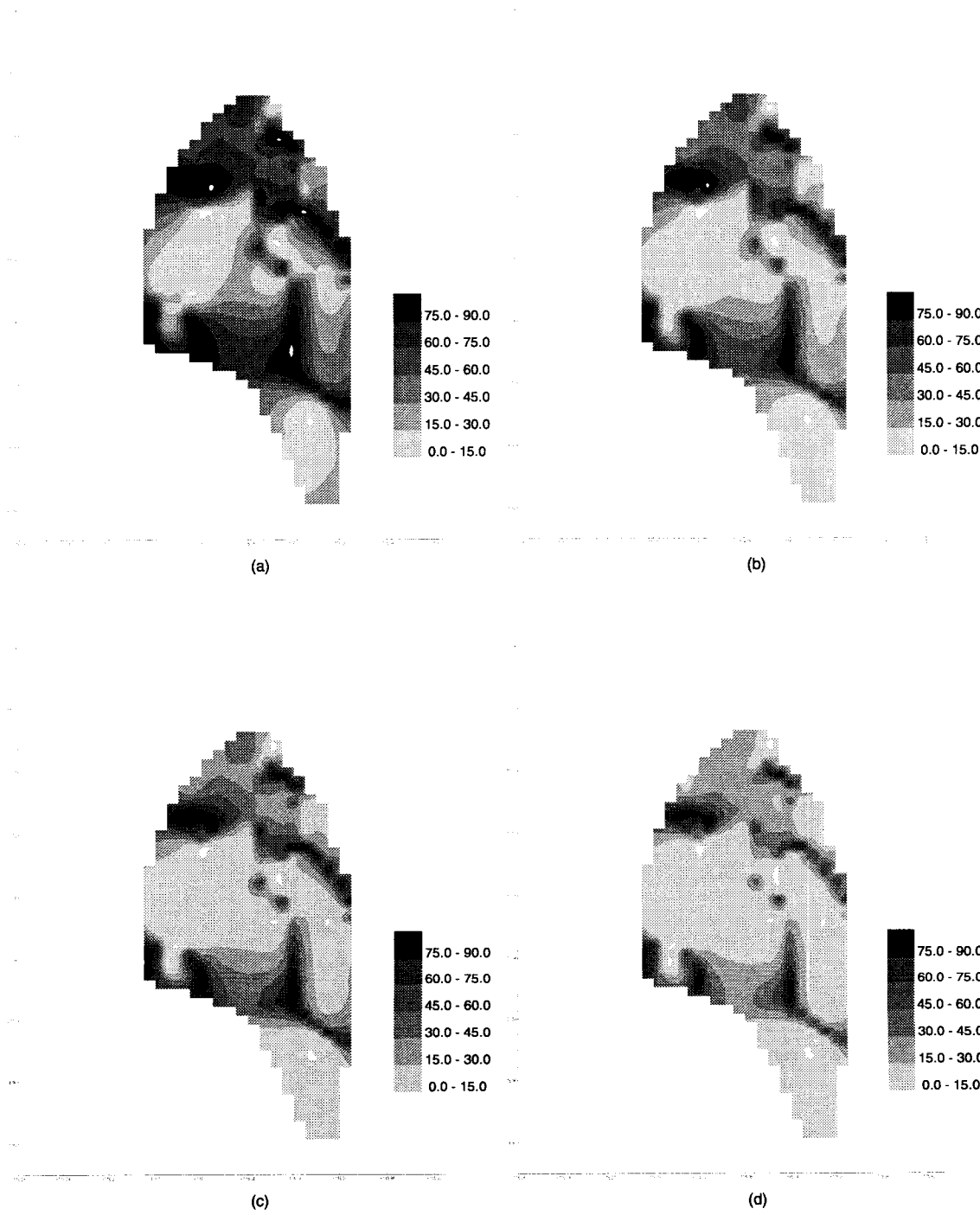


Figure 10-11. Angle between Darcy flux direction in Paleozoic carbonate aquifer and orientation of maximum horizontal stress in Yucca Flat for: (a) anisotropy ratio of 1, (b) anisotropy ratio of 2, (c) anisotropy ratio of 3, and (d) anisotropy ratio of 5

carbonate aquifer waters. Calcite solubility can be represented by the reaction



with an equilibrium constant

$$K = \left(a_{\text{HCO}_3^-} \right)^2 \left(a_{\text{Ca}^{2+}} \right) / f_{\text{CO}_2} \quad (10-12)$$

for unit activity of calcite and H_2O , where a_i is the thermodynamic activity of species i , and f_{CO_2} denotes the fugacity of CO_2 in the aqueous phase. Lines in Figure 10-12 correspond to the logarithm of (10-12) using data from DAT0.COM.R16. Conditions below the lines in Figure 10-12 are undersaturated with respect to calcite and conditions above the lines are supersaturated. The figure illustrates that all water samples from the tuffaceous aquifer in the vicinity of YM are undersaturated with respect to calcite.

Thermodynamic calculations of the equilibrium aqueous speciation of groundwaters from the saturated zone tuffaceous aquifer in the vicinity of YM indicate that samples are chemically undersaturated with respect to calcite (Figure 10-12). Dissolution kinetics of calcite at groundwater temperatures and pH are generally rapid (e.g., Sjöberg and Rickard, 1984), so calcite cannot persist together with chemically undersaturated water, particularly over geologic time scales.

In summary, calcite in saturated zone tuffaceous rocks at YM is apparently old. Its isotopic composition is compatible with precipitation from water derived from the Paleozoic carbonate aquifer, not the present tuffaceous aquifer water. Furthermore, the present tuffaceous aquifer waters are chemically undersaturated with respect to calcite. Together these observations indicate that calcite is isolated from the flow system that presently supplies water to wells in the tuffaceous aquifer. Saturated zone flow in the tuffaceous aquifer appears to be channelized, bypassing zones containing calcite. This conclusion is supported by comparisons of zones containing calcite (Bish and Chipera, 1989) and permeable zones (Benson et al., 1983). For example, in well UE-25b#1, permeable zones have been identified in the lower Calico Hills

Beds and in the upper Bullfrog Member where calcite is absent or sparse. In contrast, the Tram Member from UE-25b#1 is relatively impermeable and rich in calcite.

An implication of this conclusion is that the occurrence of calcite may be an indicator of impermeable zones in the saturated zone tuffaceous aquifer. Permeability at the top of the aquifer beneath the proposed repository site and down the hydraulic gradient is of particular interest because it is a potential path for radionuclide migration. A comparison of potentiometric levels for this area (Ervin et al., 1994) with calcite occurrences (Bish and Chipera, 1989) shows no calcite near the top of the aquifer. However, cores were not continuously sampled in generating the Bish and Chipera (1989) compilation, so calcite may have been missed. Notably, in compilations of isotopic data for calcite from numerous boreholes in the vicinity of YM (Whelan and Stuckless, 1992; Whelan et al., 1994), data were reported for the upper 100 m of the saturated zone for only one borehole, USW G-4. The isotopic character of this calcite resembles calcites from the unsaturated zone (Whelan and Stuckless, 1992), unlike most calcite below the water table, which appears to have affinities with Paleozoic aquifer water. An additional implication of channelized flow in the tuffaceous aquifer is that travel times are shorter than in the case of homogeneous porous medium flow for a given flux. The likely role of fracture transmissivity in controlling channelized flow also indicates that the anisotropic stress field would affect flow directions in the tuffaceous aquifer.

10.3 ASSESSMENT OF PROGRESS

Structural, hydrostratigraphic, and geochemical evidence has been analyzed to assess the occurrence and effects of flow channeling within the regional Paleozoic carbonate aquifer and the local tuffaceous aquifer near YM. Studies near Ash Meadows indicate that high-angle fault zones control the complex "feeder" system through which water flows from the carbonate units to springs. Flow channeling in the densely welded, fractured tuffaceous aquifer near YM has been inferred from chemical undersaturation of pore waters with respect to calcite. The transmissive properties of faults and fracture zones are affected by the state of *in situ* regional stress. The hydraulic properties of fractured rocks become anisotropic when the ratio between the major and minor principal horizontal *in situ* stress is greater than one. Most local

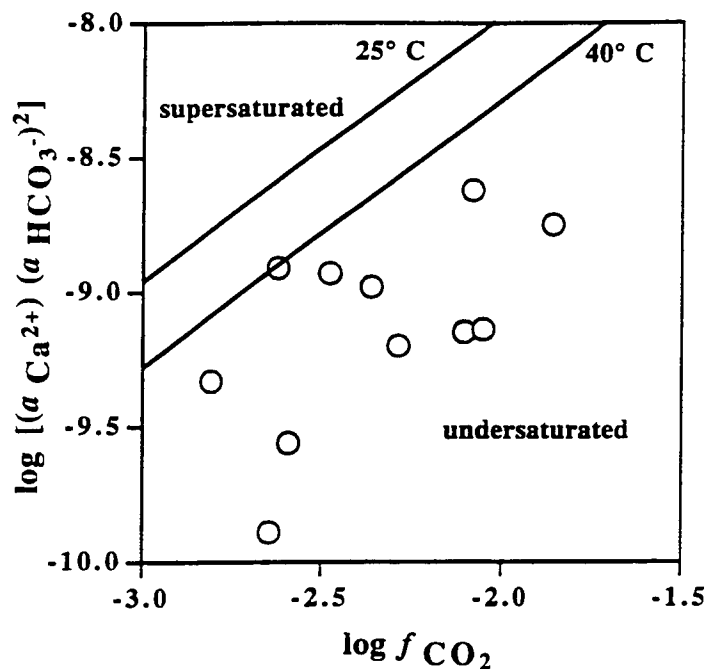


Figure 10-12. Calcite solubility limits for water samples from the tuffaceous aquifer at YM

and regional groundwater flow maps for the Death Valley region have been constructed assuming that the transmissivity of the units is isotropic. Using borehole breakout data to determine the direction of maximum horizontal stress and orientation of the maximum principal component of the transmissivity tensor, flow maps for Yucca Flat were constructed assuming different transmissivity anisotropy ratios. These flow maps suggest that incorporating the effect of anisotropy may considerably alter existing conceptual models of interbasin flow and thereby has the potential to change predictions of the magnitude of water table fluctuations at YM due to changes in recharge.

Hydrogeologic information compiled in Task 1 and conceptual flow models developed in Task 2 have not yet been used to revise CDSs or construct CDMs, or evaluate study plans submitted by the DOE. However, information gathered during the first year of this project is being used in the review of Sandia National

Laboratory's 1993 Total System Performance Assessment for the proposed HLW repository at YM.

10.4 PLAN FOR NEXT REPORTING PERIOD

During the next reporting period, work will continue on the development of a 3D hydrostratigraphic model of the Death Valley region. As part of collaborative work conducted with the research project on Tectonic Processes, *in situ* stress measurements from other hydrographic basins will be used to estimate the direction of the maximum principal transmissivity. Water level maps of other hydrographic areas will then be re-interpreted using estimates of the orientation and anisotropy ratios of the transmissivity tensor. These new conceptual models of groundwater flow will be used to develop computational models from the Death Valley region.

10.5 REFERENCES

- Beauheim, R.L. 1987. *Analysis of Pumping Tests of the Culebra Dolomite Conducted at the H-3 Hydropad at the Waste Isolation Pilot Plant (WIPP) Site*. SAND86-2311. Albuquerque, NM: Sandia National Laboratories.
- Benson, L.V., J.H. Robison, R.K. Blankennagel, and A.E. Ogard. 1983. *Chemical Composition of Ground Water and the Locations of Permeable Zones in the Yucca Mountain Area, Nevada*. Open-File Rept. 83-854. Washington, DC: U.S. Geological Survey.
- Bish, D.L., and J.L. Aronson. 1993. Paleogeothermal and paleohydrologic conditions in silicic tuff from Yucca Mountain, Nevada. *Clays and Clay Minerals* 41: 148-161.
- Bish, D.L., and S.J. Chipera. 1989. *Revised Mineralogic Summary of Yucca Mountain, Nevada*. Report LA-11497-MS. Los Alamos, NM: Los Alamos National Laboratory.
- Brinster, K.F. 1991. *Preliminary Geohydrologic Conceptual Model of the Los Medanos Region Near the Waste Isolation Pilot Plant for the Purpose of Performance Assessment*. SAND89-7147. Albuquerque, NM: Sandia National Laboratories.
- Broxton, D.E., D.L. Bish, and R.G. Warren. 1987. Distribution and chemistry of diagenetic minerals at Yucca Mountain, Nye County, Nevada. *Clays and Clay Minerals* 35: 89-110.
- Burbey, T.J., and D.E. Prudic. 1991. *Conceptual Evaluation of Regional Ground-Water Flow in the Carbonate-Rock Province of the Great Basin, Nevada, Utah, and Adjacent States*. Geological Survey Professional Paper 1409-D. Washington, DC: U.S. Government Printing Office.
- Burchfiel, B.C. 1965. Structural geology of the Specter Range quadrangle, Nye County, Nevada. *Geological Society of America Bulletin* 76(2): 175-191.
- Carlos, B.A. 1987. *Minerals in Fractures of the Saturated Zone from Drill Core USW G-4, Yucca Mountain, Nye County, Nevada*. Report LA-10927-MS. Los Alamos, NM: Los Alamos National Laboratory.
- Dettinger, M.D. 1989. *Distribution of Carbonate-Rock Aquifers in Southern Nevada and the Potential for their Development*. Program for the Study and Testing of Carbonate-Rock Aquifers in Eastern and Southern Nevada—Summary Report No. 1. Carson City, NV: U.S. Geological Survey.
- Dettinger, M.D. 1992. *Geohydrology of Areas Being Considered for Exploratory Drilling and Development of the Carbonate-Rock Aquifers in Southern Nevada—Preliminary Assessment*. Water Resources Investigations Report 90-4077. Denver, CO: U.S. Geological Survey.
- Dudley, W.W., and J.D. Larson. 1976. *Effect of Irrigation Pumping on the Desert Pupfish Habitat in Ash Meadows, Nye County, Nevada*. Geological Survey Professional Paper 927. Washington, DC: U.S. Government Printing Office.
- Ervin, E.M., R.R. Luckey, and D.J. Burkhardt. 1994. *Revised Potentiometric-Surface Map, Yucca Mountain and Vicinity, Nevada*. USGS Water-Resources Investigations Report 93-4000. Denver, CO: U.S. Geological Survey.
- Gillson R.G. 1993. *Analysis of Borehole Elongation in Yucca Flat and Pahute Mesa, Nevada Test Site, Nevada, Using the Digital Downhole Surveyor*. Unpublished Master's Thesis. Little Rock, AR: University of Arkansas.
- Hantush, M.S. 1966. Analysis of data from pumping tests in anisotropic aquifers. *Journal of Geophysical Research* 72: 1,709-1,720.
- Kerrisk, J.F. 1987. *Groundwater Chemistry at Yucca Mountain, Nevada, and Vicinity*. Report LA-10929-MS. Los Alamos, NM: Los Alamos National Laboratory.
- Maini, T., and G. Hocking. 1977. An examination of the feasibility of hydrologic isolation of a high level waste repository in crystalline rock. *Geo-*

- logic Disposal of High-Level Radioactive Waste Session—Annual Meeting*. Seattle, WA: Geological Society of America
- Neuman, S.P., G.R. Walter, H.W. Bentley, J.J. Ward, and D.D. Gonzalez. 1984. Determination of horizontal aquifer anisotropy with three wells. *Ground Water* 22(1): 66–72.
- Nuclear Regulatory Commission. 1994. *License Application review Plan for the Review of a License Application for a Geologic Repository for Spent Nuclear Fuel and High-Level Radioactive Waste Yucca Mountain Site, Nevada*. NUREG-1323. Washington, DC: Nuclear Regulatory Commission.
- Paces, J.B., E.B. Taylor, and C. Bush. 1993. Late Quaternary history and uranium isotopic compositions of ground water discharge deposits, Crater Flat, Nevada. *Proceedings of the Fourth International High-Level Waste Conference*. La Grange Park, IL: American Nuclear Society: 1,573–1,580.
- Papadopoulos, I.S. 1965. Nonsteady flow to a well in an infinite anisotropic aquifer. *Proceedings of the Dubrovnik Symposium on the Hydrology of Fractured Rocks*. International Association of Scientific Hydrology: 21–31.
- Rush, F.E. 1971. *Regional Ground-Water Systems in the Nevada Test Site Area, Nye, Lincoln and Clark Counties, Nevada*. Water Resources-Reconnaissance Series Report 54. Denver, CO: U.S. Geological Survey.
- Springer, J.E., R.K. Thorpe, and H.L. McKague. 1984. *Borehole Elongation and Its Relation to Tectonic Stress at the Nevada Test Site*. UCRL-53528. Livermore, CA: Lawrence Livermore National Laboratory.
- Sjöberg, E.L., and D.T. Rickard. 1984. Temperature dependence of calcite dissolution kinetics between 1 and 62 °C at pH 2.7 to 8.4 in aqueous solutions. *Geochemical et Cosmochemical Acta* 48: 485–493.
- Waddell, R.K. 1982. *Two-Dimensional, Steady-State Model of Ground-Water Flow, Nevada Test Site and Vicinity, Nevada-California*. Water Resources Investigations Report 82-4085. Denver, CO: U.S. Geological Survey.
- Waddell, R.K., J.H. Robison, and R.K. Blankenagel. 1984. *Hydrology of Yucca Mountain and Vicinity, Nevada-California, Investigative Results through Mid-1983*. Water Resources Investigations Report 84-4267. Denver, CO: U.S. Geological Survey.
- Wawersik, W.R., and C.M. Stone. 1989. A characterization of pressure records in inelastic rock demonstrated by hydraulic fracturing measurements in salt. *International Journal of Rock Mechanics* 26(6): 613–627.
- Way, S.C. and C.R. McKee. 1982. *In-situ* determination of three-dimensional permeabilities. *Ground Water* 20(5): 594–603.
- Wernicke, B., P.L. Guth, and G.J. Axen. 1984. Tertiary Extension in the Sevier Thrust Belt of Southern Nevada. J. Lintz Jr., ed. *Western Geological Excursions*. Reno, NV: University of Nevada-Reno, Mackay School of Mines: 4: 473–510.
- Whelan, J.F., and J.S. Stuckless. 1992. Paleohydrologic implications of the stable isotopic composition of secondary calcite within the Tertiary volcanic rocks of Yucca Mountain, Nevada. *Proceedings of the Third International High-Level Waste Conference*. La Grange Park, IL: American Nuclear Society: 1,572–1,581.
- Whelan, J.F., D.T. Vaniman, J.S. Stuckless, and R.J. Moscati. 1994. Paleoclimatic and paleohydrologic records from secondary calcite: Yucca Mountain, Nevada. *Proceedings of the Fifth International High-Level Waste Conference*. La Grange Park, IL: American Nuclear Society: 2,738–2,745.
- Winograd, I.J., and W. Thordarson. 1975. *Hydrogeologic and Hydrochemical Framework, South-Central Great Basin, Nevada-California, with Special Reference to the Nevada Test Site*.

Geological Survey Professional Paper 712-C.
Washington, DC: U.S. Government Printing
Office

- Winograd, I.J., and F.J. Pearson, Jr. 1976. Major carbon 14 anomaly in a regional carbonate aquifer: Possible evidence for megascale channeling, South Central Great Basin. *Water Resources Research* 12: 1,125–1,143.
- Winograd, I.J., T.B. Coplen, J.M. Landwehr, A.C., Riggs, K.R. Ludwig, B.J. Szabo, P.T. Kolesar, and K.M. Revesz. 1992. Continuous 500,000-year climate record from vein calcite in Devils Hole, Nevada. *Science* 258: 255–260.
- Wolery, T.J. 1992. *EQ3/6, A software package for geochemical modeling of aqueous systems: Package overview and installation guide (version 7.0)*. UCRL-MA-110662 PT 1. Livermore, CA: Lawrence Livermore National Laboratory.
- Zoback, M.L. 1992. First- and second-order patterns of stress in the lithosphere: The World Stress Map Project. *Journal of Geophysical Research* 97(B8): 11,703–11,728.
- Zoback, M.L. and 36 Project Participants. 1992. The World Stress Map—Maximum horizontal stress orientations. *Journal of Geophysical Research* 87(B8).